Drying droplets as a template for multi-component solid particles : experimental study and modeling at the droplet scale

Roger Williams de Souza Lima

THÈSE

en vue de l'obtention du

DOCTORAT DE L'UNIVERSITÉ DE TOULOUSE

délivré par
IMT – École Nationale Supérieure des Mines d'Albi-Carmaux

présentée et soutenue par
Roger Williams DE SOUZA LIMA
le 22 janvier 2020

Drying droplets as a template for multi-component solid particles: experimental study and modeling at the droplet scale

Acknowledgements

First of all, I would like to thank my supervisors, Maria-Inês Ré and Patricia Arlabosse, for allowing me to work on such an interesting project, such as the drying of droplets. You have taught me a lot, not only on the physics related to our project, but the critical thinking, rigor and patience necessary for completing a complex task. You have supported me throughout this project and I am deeply grateful. I changed for the better.

I would also like to thank the members of my thesis committee, Catherine Bonazzi, Stéphane Desobry, Stephan Drusch, Andreas Braeuer and Jean-Eudes Vendeville, for the honor of having my work evaluated by you. I would like to thank particularly Andreas Braeuer for our work at ITUN, in Freiberg. It was a very nice experience and it has deeply contributed to the originality of this thesis project. And, of course, I would like to thank all the colleagues that I met in Freiberg, specially Simon, Christine, Tijana, Michael, Mirko, Zheng, Matthias, Martin, Medhanie, Marina, André, Roland and Kerstin.

This thesis project was developed at RAPSODEE Center. I could not ask for a better place to be. I am glad to have met such incredible people. Many thanks to Ange, Fabienne, Suênia, Mickaël, Pierre, Denis, Sylvie, Céline, Philippe, Laurent, Laurène, Angélique, Antoine, Anne-Marie, Chrystel, Valérie and the list of course goes on!

I could not forget to mention all the Ph.D. researches and interns at RAPSODEE Center who contributed to make this experience greater. Special thanks to Ana, Bhianca, Rababe, Lori, Margot, Tina, Marwa, Felipe, Janine, Gaëtan, Marine, Martin, Karline, Ludovic, Pauline, Carla, Thomas, Gweni, Sagar, Laura, Razac, Lina, Léa and many more. Thank you all!

I would also like to thank all my friends back in Brazil, Millene, Luiz, Jéssica, Iêda and Tahyná. Even across the ocean, I could still count on you. I love you. Many thanks to Audrey, Marion, Stevan and Hamilton as well. Also, I want to thank my two families for their support. Your emotional suport was vital specially during the writing period. My deepest gratitude to Thomas. Concluding this thesis project was much lighter with you.

Thank you,

Roger Williams de Souza Lima

Summary

Introduction

Liquid droplets, which are afterwards solidified by physical or chemical transformations, is one of the major means of generation of solid particles with controlled properties like shape (predominantly spherical), size, chemical surface composition, porosity or density. These properties impact other targeted functional solid properties such as reactivity, dissolution and release profiles, taste masking, flowability or wettability, which are the main issues for applications including pharmaceutical, food, catalysis, development of new materials and other fields. Liquid droplets as templates for solid formation are encountered with a variety of industrial processes, among them, spray drying.

The spray drying process is related to the application of a driving force to a liquid feed (such as pressure, centrifugal or ultrasonic energy) through an atomizing device to produce finely dispersed droplets. The liquid droplets, subsequently in contact with a hot gaseous phase, are dried resulting in the fast production of fine solid particles. By modifying the liquid feed characteristics (such as nature of components and concentration), the atomizing device (which impacts the droplet formation) and the drying gas characteristics (temperature, flow rate, water vapor concentration), such interplay generates different particle solid structures, which affect the powder material properties, such as the bulk density, the particle size distribution, the porosity, the moisture content and the flowability.

Drying was the central objective in the early applications of this process. However, such perception evolved over the years driven by an increasing demand for particles with engineered end-use solid structures (i.e. multi-layer composite coating, controlled porosity, low density particles with controlled morphology and hierarchically distributed nanoparticles) for targeted applications, such as dissolution and release profiles, taste masking, reactivity, wettability and coating. As a result of the continuous targeting for producing such crafted particles, the spray drying process became more associated with the perception of a particle engineering tool. Nowadays, despite the clear interest of the use of spray drying as a particle engineering process, it is still lacking a number of scientific advances in specific subjects such as detailed descriptions of the spatial distribution of the components inside a multi-component droplet/wet particle during the drying process, which has firstly a major impact on the particle surface chemistry. Additionally, the development of a model capable of predicting different particle morphologies based on the drying conditions would help accelerate the development of new solid products.

In order to overcome such scientific challenges, experimental and modeling approaches were established in the literature to comprehend the mechanisms of solid formation from multi-component drying droplets. Both approaches are developed either on the spray scale, which corresponds to a reproduction of the spray drying process, or on the droplet scale, which corresponds to a simplification of such process. In experimental works at the spray scale, the drying conditions (e.g. air temperature and absolute humidity)

and the liquid formulation characteristics (e.g. solutes concentration and droplet size) are related to the final solid particle properties (e.g. porosity, bulk density, surface composition). Even though the studies at the spray scale allow an observation of the influence of drying conditions and liquid formulations on the formation of the solid particles, studies have been performed for monitoring the drying process at the scale of a single drying droplet. For this purpose, the droplet may be held in place through the physical support of a solid material, the so-called invasive methods, or by lifting the droplet with the help of physical forces or letting it freely fall in a drying chamber, the non-invasive methods.

Regarding the modeling approach, the description of the spray drying process has been developed at the spray scale, where the flow field of the drying gas is coupled to the physics related to the drying of droplets, as well as the description of the processes related to the collision of the droplets to the drying chamber walls or the inter-particle interactions. Even at the spray scale, the development of a model describing the drying of a droplet becomes necessary. As a result, the models related to the droplet scale may be developed with an empirical approach, with simple implementation and entirely based over a set of experimental data, or with a deterministic approach, based on the physics related to the drying of the droplet through the use of more complex equations and more computational effort. Naturally, this approach needs to be supported by experimental data.

The present thesis has the aim to bring together the experimental and the modeling approaches at the droplet scale to contribute to the scientific understanding of the mechanisms involved in solid particles formation from multi-component drying droplets.

The experimental work was firstly carried out at the spray scale in order to generate the particle morphologies and powder properties (e.g. porosity, density, etc.) serving as a reference picture for two chosen drying ternary systems: dextran-sucrose-water and lactose-whey protein isolate-water. Next, an experimental apparatus allowing the drying of a single droplet under controlled drying conditions was designed and constructed. With such set-up, the mass and the visual aspect of the droplet were monitored during drying, allowing the investigation of the influence of the mass content of solutes and the drying gas properties on the dried particle characteristics.

A second experimental set-up was also implemented in order to provide more information about droplet changes during drying, such as the mass content profile of individual solutes within the droplet over time. To achieve this, an *in situ* Raman technique was employed on acoustically levitated droplets containing the same ternary systems studied with the first experimental set-up.

The experimental observations acquired throughout the thesis were used for helping the conception and validation of a two-dimensional droplet drying model using computational fluid dynamics – CFD, until the formation of the solid crust. Through the use of a microscopic definition, the model allows the assessment of moisture evolution of the ternary mixture droplet under convective air flow until the period of a solid surface formation, as well as tracking the spatially distributed mass content profiles of each solute and other variables, such as the evaporation flux, the water activity or the droplet temperature. Also, a sensitivity analysis was performed in order to evaluate the influence of the experimental conditions on the simulated drying kinetics and the spatial distribution of the components in the droplet, particularly the composition obtained at

the surface of the droplet and the eventual influence of varying the liquid formulation on the appearance of the solid crust.

The organization of this thesis is as follows:

Chapter 1 provides the background related to the different steps composing the spray drying process (e.g. droplet formation, drying process and powder collection) and gives a qualitative view on the different solid structures obtained from this drying process. Next, the different experimental and modeling studies carried out at the spray and at the droplet scales for the former and at the droplet scale for the latter are presented.

The first part of the Chapter 2 introduces the two ternary systems chosen for this thesis. In the second part, the study performed in a spray drying with the two ternary systems is presented, with special emphasis on the solid particle characteristics obtained from different liquid compositions.

Chapter 3 covers the study of a single droplet drying at the tip of a glass filament. A detailed description is given on the design of the droplet-suspension set-up, along with the definition of the experimental plan and the steps taken for ensuring the validity of the drying data. Two global and independent droplet properties (mass and external aspect) are combined for giving insight into the drying phenomena and the solid particle formation from the two selected ternary liquid systems.

Chapter 4 focuses in the second experimental study performed with an *in situ* Raman technique on an acoustically levitated drying droplet. It covers the corresponding treatment of the acquired data in order to provide information on the mass content profiles of the solutes present in the droplet, with a special focus on the component spatial distribution induced by a modification of the liquid formulation and the mass composition.

Chapter 5 presents the physical and mathematical description of the droplet drying model and its implementation on a CFD software, which covers the definition of the ternary mixture physicochemical properties, the coupling of the underlying physics and the moving mesh implementation. The simulated results are compared with experimental data, with a focus on the drying kinetics and component spatial distribution, and provide, with the sensitivity analysis, an overview of the influence of the experimental conditions on droplet drying behavior.

Finally, the thesis is terminated with the conclusion of the work presented and suggestions for future work.

Background

In this chapter, a first introductory overview is given about the spray drying operation, which will serve as a foundation for the rest of the present work. Thus, it aims at showing the rich possibilities of solid particle structures that can be produced by spray drying, which turned this drying process into an instrument for finely designing solid structures. In order to deal with the still present scientific challenges, the experimental and modeling complementary approaches developed in the literature are presented on two distinct, but related, observation scales: from the spray scale to the focus of the present thesis, the droplet scale.

1.1 Spray drying operation overview

Spray drying is a well-established industrial operation used for rapidly producing fine particulate material with controlled properties from liquid feeds. Therefore, the spray drying process has been applied to a variety of industrial fields, such as food and dairy processing [9, 153], pharmaceuticals [128, 170], ceramics [164], base chemicals [122], painting [167] and magnetic and optical materials [70]. Recent advances have improved the use of such operation to that of a tool for engineering solid particle structures, which means that the resulting particulate material is designed for attaining specific end-use powder properties [170]. This section is dedicated to present an overview of the main steps related to the spray drying process, as presented in Figure 1.1, which are the liquid feed atomization, the droplet drying and particle formation and finally the powder recovery.

1.1.1 Atomization step

The first step of the spray drying process is related to the generation of finely dispersed droplets from a liquid feed. The liquid feed to be introduced in the equipment is previously prepared by mixing the solvent with the desired organic or inorganic molecules to form pumpable solutions, emulsions or suspensions. Next, the liquid feed is sent to a device, the nozzle, responsible for the atomization step. Different nozzles have been presented in the literature and they differ in the technical sophistication, the physico-chemical properties of the employed liquid feed, the driving force for atomization, the
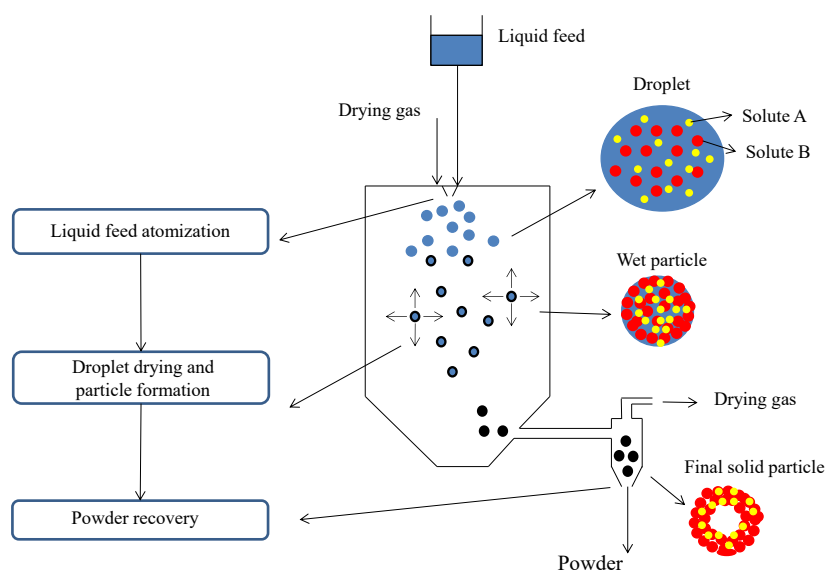
Figure 1.1 – Schematic representation of the main steps in the spray drying process: atomization of the liquid feed, droplet drying and formation of the solid particles and powder recovery. As a result, the solute-containing liquid droplets are converted into solid particulate material

mean droplet size, the throughput and the scale-up ability, as described in [97]. Different mechanisms for producing the droplet are presented hereafter, with a classification based on the number of fluids passing through the nozzle. Accordingly, the atomization step may be accomplished with single-fluid nozzles, where the droplets are generated from the energy applied to the liquid only, two-fluid nozzles, where the compressed gaseous medium is responsible for the droplets production, finally less common nozzle types are three-fluid nozzles and four-fluid nozzles, depending on the number of feeds passing through the nozzle devices. For these last two nozzle types, the reader is invited to consult the work in [118] and [76].

Single-fluid nozzle

As presented in Figure 1.2, the single-fluid nozzles commonly found in the literature are the rotary disk, the hydraulic nozzle and the ultrasonic nozzle [15, 118]. In the rotary disk (Figure 1.2-A), the liquid feed is centrifugally accelerated into a spinning disk to high velocities (on the order of hundreds of meters per second), before being discharged into the drying chamber. Here, kinetic energy is the mechanism of action for disintegrating the liquid film exiting the rotary disk. The mean droplet size obtained with this kind of nozzle is in the order of 200 µm, but it may be adjusted by controlling the revolution speed of the nozzle and the liquid feed rate. However, a special attention is needed when varying the droplet size, as the spray of droplets leaves almost horizontally from the rotary disk. Consequently, the collision of the droplets to the walls of the drying chamber should be avoided.

For the hydraulic nozzle (Figure 1.2-B), the liquid feed is pumped under pressure to the nozzle. This pressure-energy is converted into kinetic energy as the fluid approaches the

(A) Rotary disk (B) Hydraulic nozzle (C) Ultrasonic nozzle

Figure 1.2 – The production of a spray of droplet with single-fluid nozzles may be achieved through kinetic energy (A), pressurized liquid feed (B) or ultrasonic vibration of the nozzle tip (C). Adapted with permission from [118]
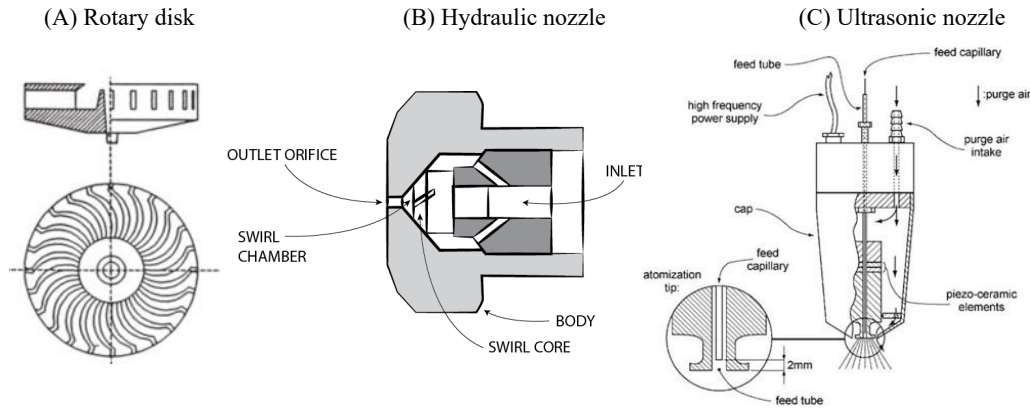
tip of the nozzle. Accordingly, higher feed pressure leads to the production of smaller droplets (adjustable droplet size ranging from 10 µm to 400 µm). Even though the use of this nozzle is restricted to feeds with low viscosities, the lower energy consumption attract the use of this device [132]. Finally, regarding the ultrasonic nozzle (Figure 1.2-C), which is adapted for laboratory-scale productions, this nozzle generates the spray of droplets by using an oscillatory piezoelectric transducer, which vibrates at ultrasonic frequencies. The droplet size is dependent on the working frequency and very small droplets may be obtained (20 µm to 100 µm) [132]. Also, bigger apertures may be used regarding the tip of the nozzle, which reduce the risk of clogging. The main drawbacks is related to the capital expenditure costs.

Two-fluid nozzle

Regarding the two-fluid nozzle, both drying gas and liquid feed are pumped into the nozzle and their contact may happen still inside of the nozzle or at its tip, as presented in Figure 1.3. The droplets are generated due to a high frictional force from the compressed drying gas over the liquid surface. The resulting droplet size depends then on the liquid properties (e.g. viscosity and surface tension) and the drying air characteristics (e.g. velocity and density). As a result, a wide range of droplet size may be obtained (from 10 µm to 1000 µm), depending on the liquid-to-gas feed ratio (LGR). For a LGR inferior to unity, the compressed gas can readily cause the necessary turbulence and energy transfer to form a highly homogeneous spray of droplets. On the other hand, with a higher LGR, the atomization is incomplete with a percentage of liquid remaining in the center of the spray.

Three-fluid and four-fluid nozzles

For the three-fluid and four-fluid nozzle, a schematic representation is shown in Figure 1.4. The main difference between these designs is related to the position of the fluids in the nozzle. In the three-fluid nozzle, the fluids are injected concentrically for atomization. Such configuration is not the case for the four-fluid nozzle and the drying gas follows
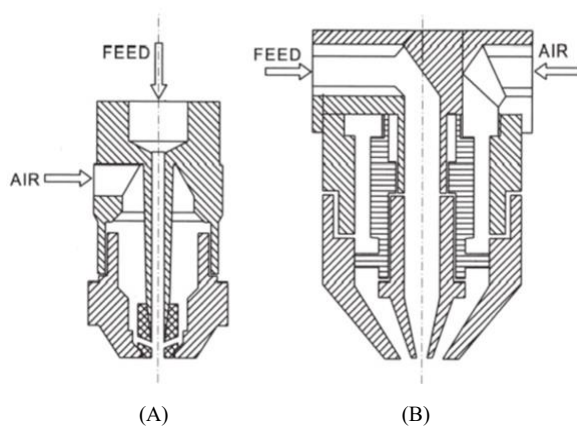
Figure 1.3 − Schematic representation of a two-fluid nozzle. Here, the liquid feed and the drying gas are sent into the nozzle and their contact may take place at the tip of the nozzle or at its interior. The production of a spray of droplets results from the frictional force of the compressed gas over the liquid feed. Adapted with permission from [118]

two passages. The nozzles presented in Figure 1.4 are specifically designed to create droplets containing liquids with different polarities. These designs are also useful for the mixture of two different solutes, dissolved in separate solvents, without the need for finding a common solvent [76].
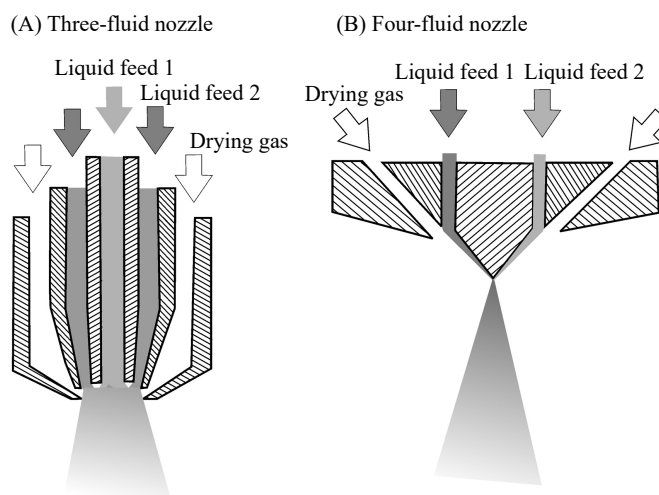
Figure 1.4 − Schematic representation of a (A) three-fluid nozzle and a (B) four-fluid nozzle. With this kind of nozzle, different liquid feed can be mixed together and subsequently atomized with the drying gas. Adapted with permission from [176]

From the nozzles presented previously, it is possible to observe the variety of mechanisms that can be employed for generating the spray of droplets, with different forces acting upon the liquid jet and various levels of complexity. It should be noted that the atomizing

devices do not create a spray of monodispersed droplets. In fact, a polydispersed, but narrowly distributed, spray of droplet is generated. In order to maintain uniform dried product characteristics, it is essential that the droplets leaving the nozzle present a initial size as uniform as possible. Also, it should be mentioned the key impact of the atomization step on the production of fine, dry powder, since the size of the resulting powder, which affect its application[1], is directly linked to the initial droplet size. Some authors have created correlations for estimating the powder particle size, based on the type of nozzle and operating conditions (e.g. feed rate, inlet air velocity, feed viscosity) as described in the review from O'Sullivan et al. [118]. However, as mentioned in [118], a direct relationship between the initial droplet size and the final solid particle size is not always easy to obtain, due to disturbances during the drying step, such as particle agglomeration.

1.1.2 Droplet drying

The drying step is very complex as it brings together coupled mass, energy and momentum transfers between the dispersed liquid phase and the surrounding drying gas during the short residence time of the droplets in the drying chamber. The droplets coming from the atomization step present a high surface area-to-volume ratio, as a result, extremely high evaporation rates are obtained and the droplets are rapidly converted into solid particles. Indeed, this step takes place in only a few seconds [114]. The simultaneous fast removal of a solvent and the formation of a solid particle is a unique feature of the spray drying process.

The continuous gas phase used for drying the droplets is generally air, but nitrogen, carbon dioxide, argon or water vapor can be used as well, depending on the molecules present in the liquid phase [116]. In the present work, the description of the drying process is presented with air as continuous gas phase and water as the main solvent in the dispersed phase.

The drying process is related to the transfer of water at a molecular scale between the sample and the surrounding drying air. Additionally, the intensity of such process is linked to the departure from thermodynamic equilibrium. For the discussion of the drying process here, it is important to firstly present a few definitions related to the drying gas and the droplet. In these definitions, the term moisture will be related to the water in the droplet and wet particle[2] only. For the drying air phase, the term water vapor will be employed.

Water vapor in the humid air

Before entering in the drying chamber, the air stream is set to the appropriate drying conditions, which are the inlet temperature, the flow rate and the absolute humidity. The latter is a measure of the quantity of water vapor present in the air stream. This

---

[1]In pharmaceutical drug delivery applications, extremely small solid (around 5 micrometers) particles are needed for penetrating in the lungs, for example.

[2]This nomenclature is used to represent the intermediate stage between a liquid droplet and a completely solid particle. A denser solid phase (frequently referred as a crust) is already present at the surface of the droplet, while its core is still liquid

variable is expressed in terms of mass of water vapor to the mass of dry air, as written in Equation 1.1 (with the ideal gas law),

$$Y \text{ (water/dry air)} = \frac{m_v}{m_{da}} = \frac{MM_w}{MM_{da}} \frac{P_v}{(P - P_v)} \tag{1.1}$$

Where Y stands for the absolute humidity, m_v the mass of water vapor, m_{da} the mass of dry air, MM_w the molar mass of water, MM_{da} the molar mass of the dry air, P_v the water vapor pressure and P the total stream pressure.

For the sake of fast perception of the water vapor content in the gas phase, another parameter, the relative humidity, may be used. The relative humidity is defined as the ratio between the water vapor pressure in the gas phase and the water vapor saturation pressure, for a given temperature T (Equation 1.2). The relative humidity may vary from zero, when the air is completely dry, to one, when the air is saturated with water vapor, which means that any additional mass of water in the gas phase will be converted into liquid, for a given temperature and total pressure.

$$HR = \frac{P_v}{P_v^{sat}(T)} \tag{1.2}$$

Where HR is the relative humidity and P_v^{sat} is the water vapor saturation pressure, at a given temperature T.

The driving force for the mass transfer is the difference between the water vapor pressure P_v in the drying air and the water vapor pressure $P_{v,d}$ in equilibrium with the droplet/wet particle at a given moisture content. The term $P_{v,d}$ is linked to the concept of water activity of the droplet/wet particle, as presented hereafter.

Water in the drying droplet

In drying processes, the description of the moisture content of a sample can be related to the mass of dry solids[3] (a moisture content on a dry basis), since they are constant throughout the process, or to the mass of the whole product (a moisture content on a wet basis). For this thesis, the moisture content in each droplet will be presented on a dry basis. Such parameter is calculated as presented in Equation 1.3.

$$X(\text{kg water/kg dry solids}) = \frac{m_{drop} - m_{ds}}{m_{ds}} \tag{1.3}$$

Where X stands for the dry basis moisture content, m_{drop} the mass of the droplet and m_{ds} the mass of dry solids. The mass of dry solids can be easily measured with gravimetric methods.

As mentioned previously, the water vapor pressure $P_{v,d}$ in equilibrium with the sample at a given moisture content X can be expressed in terms of the water activity a_w of the sample as follows,

$$P_{v,d}(X,T) = a_w P_v^{sat}(T) \tag{1.4}$$

---

[3]In the case of the drying droplets, dry solids is used here as a general term to represent the mass of the compounds (other than water) present in the droplet, whether dissolved in the liquid droplet, as solutes, or present in solid state at the final solid particle

From Equations 1.2 and 1.4, it is possible to observe that at equilibrium conditions, the water activity of the product is equal to the relative humidity of the drying air.

As long as the water activity is equal to unity, the moisture is said to be "unbound" and is treated as pure water in the drying process. The energy required for leading the water molecules from the liquid to the gas state is similar to the vaporization enthalpy of pure water, at the temperature of the sample. As the water activity becomes inferior to unity, the moisture is said to be "bound", chemically or physically adsorbed to the substances present in the sample. The addition of solutes in the water always lowers the water activity as they bind the solvent molecules through molecular interactions (hydrogen bonds, Van der Waals, etc). As the water activity decreases, more energy is necessary for taking the water molecules to the vapor state. Such increase in the vaporization enthalpy depends on the product being dried. Finally, the water activity is an important parameter in the food industry, for example, since microbial activity is related to the water activity in the produced solid material [118].

Drying kinetics

The discussion of the drying kinetics is linked to the presentation of the different rates at which the moisture is removed from the droplets/wet particles crossing the drying chamber. These drying rates are associated to drying phases or periods. Indeed, the drying rate is modified across the drying chamber due to a modification in the water activity of the droplets/wet particles, which has an influence in the water vapor pressure gradient $(P_{v,d} - P_v)$ between the drying air and the droplets/wet particles. Such variation in the water activity also has an effect in the temperature gradient for the heat transfer. When the droplets are injected into the drying chamber, they may possess a water activity value at unity, thus the water vapor pressure gradient between the dispersed phase (droplets) and the continuous phase (drying air) is the highest. As mentioned previously, the energy required for evaporating the water molecules is similar to that of pure water.

In Figure 1.5, the evolution of the moisture content of a droplet/wet particle, on a dry basis, is plotted through the drying time. Also, three periods of drying were distinguished in Figure 1.5, which correspond to the initial droplet heat-up (going until the point A), the first drying stage or constant-rate period (comprised in the line A-B) and the second drying stage or falling-rate period (comprised between the line B-C). The point C represents the solid particle at equilibrium conditions, for illustrating purposes. In order to better visualize these different drying periods, the plot of the moisture content in Figure 1.5 may be complemented by the plot of the drying flux with the droplet moisture content, on a dry basis, as shown in Figure 1.6. As a matter of fact, the drying flux is calculated (for each droplet) from the drying rate, dX/dt, multiplied by the mass of dry solids, m_{ds}. This results in the evaporated mass of water per time. Since the exchange area of the droplets/wet particles is not constant with time, the drying rate is divided by the surface area of the droplets/wet particles (Equation 1.5).

$$N_v = -\frac{m_{ds}}{S}\frac{dX}{dt} \qquad (1.5)$$

Where N_v represents the drying flux, dX/dt the drying rate ($\mathrm{kg\,s^{-1}\,kg^{-1}}$), m_{ds} the mass of solutes (kg) and S is the surface area of a sphere representing the droplet/wet particle ($\mathrm{m^2}$).
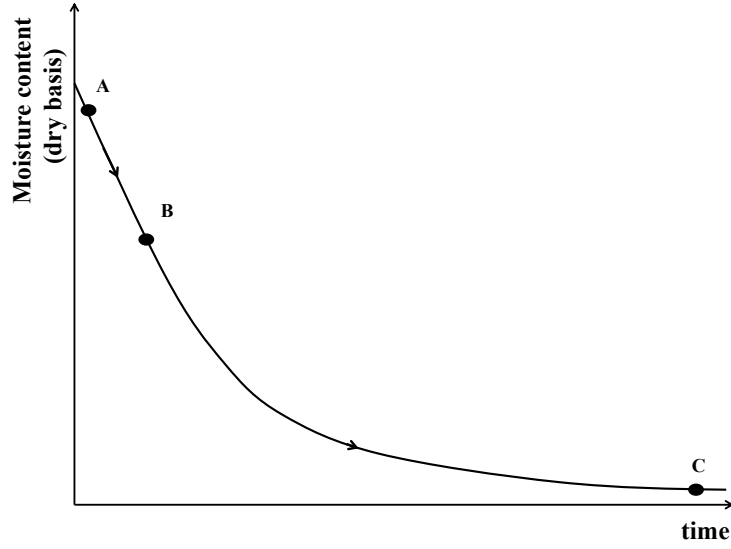
Figure 1.5 – Schematic representation of the evolution of the droplet moisture content, on a dry basis, over time. The main drying phases are presented in the figure: (A) End of the initial droplet heat-up; (B) End of the first drying stage; (C) End of the falling-rate period

The period ending in point A in both Figures 1.5 and 1.6 corresponds indeed to a brief period (on the order of a tenth of a second for a 300-µm droplet at industrial conditions [119]) where the droplet temperature and drying rate are strictly unsteady and evolve to attain the conditions related to the first drying stage. The droplet drying rate increases to attain the value found in the constant-rate drying period and the droplet temperature may increase or decrease depending on the droplet initial temperature and its temperature at the first drying stage.

The first drying stage comprised in the line $A - B$ is characterized by a constant drying flux, compared to the subsequent falling-rate period and the moisture removal takes place at the surface of the droplet. At this stage, the water activity at the surface of the droplet is unity and the droplet behaves then as an evaporating pure water droplet. Regarding the droplet temperature, heat is transferred from the drying air to the droplet due to the temperature gradient between these two phases. A steady state is attained between the heat received by the droplet and that used for evaporation. The resulting temperature is called wet bulb temperature. As long as enough moisture is supplied to the droplet surface at a rate sufficient to maintain saturated conditions, the droplet surface temperature remains at the wet bulb temperature. In this phase, the drying process is limited by the heat and mass transfers at the boundary layer around the droplet. It is also interesting to note that if the drying flux, N_v, at the first drying stage, is constant, the evaporation rate $\mathrm{d}X/\mathrm{d}t$ is not, it decreases linearly through time due to a reduction in the droplet surface area.

The transition between the first drying rate and the falling-rate period happens at the so-called critical moisture content. In Figure 1.6, such transition was represented by a single moisture content value, X_c, over which the drying period changes. However, as stated in [72], the transition may not be as strict as a single critical moisture content
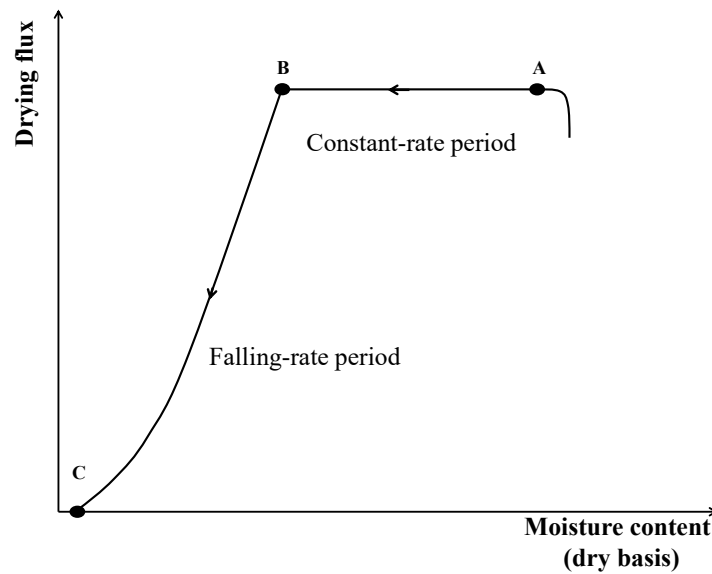
Figure 1.6 – Schematic representation of the evolution of the droplet drying flux (calculated from the drying rate, dX/dt, per unit of surface area). The main drying phases are presented in the figure: (A) End of the initial droplet heat-up; (B) End of the first drying stage; (C) End of the falling-rate period

point, but rather a range of moisture content values over which the droplet enters in the falling-rate period. Such period is also accompanied by the formation of the solid surface of the droplet (frequently named crust) [106].

In the falling-rate period, as mentioned previously, the driving force for the mass and the heat transfers are reduced throughout this drying stage. With a progressive reduction in the drying flux from the decrease in the wet particle water activity, the temperature of the wet particle increases. The moisture removal in the falling-rate period becomes limited by the transport of moisture from the center to the surface of the wet particle. The heat transfer is limited by its conduction throughout the solid structure, from the surface to the center. Depending on the drying conditions, an important temperature gradient may be found in the wet particle [169]. Such increase in temperature should be taken into account depending on the molecules initially present in the liquid formulation, as to avoid thermal degradation. Finally, the limit for the drying process is represented by C in Figures 1.5 and 1.6. At this point, the solid particle would be in thermal equilibrium with the surrounding air and the solid particle water activity would be equal to the drying air relative humidity. The equilibrium found in the point C depends on the drying air properties (temperature and relative humidity).

Drying air flow pattern

The overall trend in the droplet moisture content evolution in the drying chamber has been introduced (the Section 1.2 will again present the drying of the droplet but with a particular focus on the solutes present in the liquid phase). At the present, one last point should be considered in the droplet drying step, which is the way in which the spray of droplet enters in contact with the air stream.

Three main forms are employed in the literature (as depicted in Figure 1.7) : cocurrent, countercurrent and mixed flow. The cocurrent flow is the most common configuration, where the spray of droplets will flow in the same direction as the gas phase towards the bottom of the drying chamber. Consequently, the droplets leaving the atomizer come into contact with the hottest air. However, the droplet liquid formulation is protected from the high temperature thanks to the droplet dynamic equilibrium at the wet bulb temperature. Later in the drying process, when the wet particles are formed and their overall temperature starts to increase, the surrounding air temperature is already colder (compared to the inlet stream). In that way, this configuration is preferred for the drying of heat-sensitive substances.
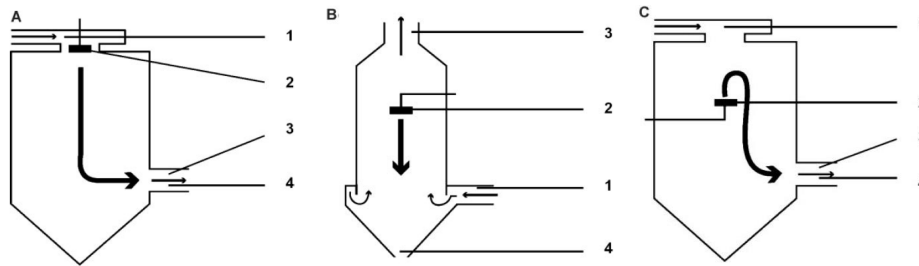

Figure 1.7 – Schematic representation of the different air flow configurations in the spray drying process. (A) Cocurrent flow; (B) Countercurrent flow; (C) Mixed flow. And, (1) drying gas inlet; (2) nozzle; (3) Air outlet; (4) Powder outlet. Image adapted from [15]

For the countercurrent configuration, the continuous and the dispersed phase will flow in opposite directions. The coldest air leaving the drying chamber is in contact with the spray of droplets leaving the atomizer. In this configuration, a better energy performance is obtained, compared to the cocurrent configuration, as the hottest air is in contact with the spray of solid particles and can provide more energy for moisture removal at the particles lower water activity. The countercurrent flow can be used for example for the drying of ceramic materials, as this kind of formulation will not suffer degradation from the hottest air stream.

The mixed flow configuration combines some features of the past two configurations. The spray of droplets are fed upward from a middle point in the chamber, which is a countercurrent movement relative to the air stream. Then, the wet particles move downward, following the motion of the gas phase. It allows a higher thermal efficiency with a maximized particle residence time while employing small drying chambers.

Regarding the air pattern, the cocurrent configuration allows the production of a laminar or a turbulent, swirling gas motion inside of the drying chamber. While the former is used only in combination with nozzles [15] and are used for stress-sensitive substances, which need relatively small drying rates (as a consequence, higher drying chambers are necessary), the latter is used in combination with any type of atomized and produces a higher drying rate.

1.1.3 Powder recovery

Once the desired particle moisture content is obtained, the produced powder must be separated from the humid gas stream. This is accomplished through the use of cyclones

(the separation is based on the difference between the powder and the air densities), a bag filter or an electrostatic precipitator [15]. The choice of the recovery system depends on the powder density, diameter and the substances present in it.

The content presented hereafter has been published in *Powder Technology*. "R. de Souza Lima, M.-I. Ré, P. Arlabosse, Drying droplet as a template for solid formation: A review, Powder Technology 359 (2020)" (https://doi.org/10.1016/j.powtec.2019.09.052).

1.2 Drying droplet as a template for solid formation

As mentioned in the previous section, the first feature that attracts attention to the use of a spray dryer is the simultaneous fast removal of solvent from a liquid feed and the formation of solid particles. Different air properties may be varied to control the drying process, namely the air inlet and outlet temperatures, the air pressure inside the drying chamber, the flow rate and the air absolute humidity. Also, different atomizer designs have a key impact on the drying process, such as the type of atomizer, the diameter and the liquid and atomizing gas pressures.

Naturally, the resulting spray-dried particles are influenced by the liquid formulation as well. Through the use of a wide range of feed streams, as solutions, emulsions or suspensions, the generated droplets will act as a template, a confined space where the solid structure will be built. These liquid templates are frequently multi-component mixtures and the interplay between the process conditions and the formulation characteristics give rise to an ample range of solid structures. In Section 1.1.2, the notion of drying of a droplet was mainly focused on the moisture removal. For the present section, a particular focus on the liquid formulation is given regarding the different solid particles that may be obtained from spray drying. It should also be noted that the main objective here is not to assemble an exhaustive number of similar findings in the literature, but rather present representative solid particle structures obtained from the process in question.

As mentioned previously, in the spray drying process, evaporation firstly takes place at the surface of the droplet. In that way, the solvent molecules inside the liquid phase will move from the core of the droplet to its surface. The other substances present in the droplet are equally carried by this outward motion. Thus, the solvent removal leads to a solute enrichment at the surface of the droplet, until a solid phase (crust) begins to form. As the solvent removal progresses, the crust thickens and grows towards the center of the liquid phase.

One important parameter that arises when dealing with the process of particle formation is the capillary pressure, which is derived from the difference in the pressure inside and out the droplet and is related to the surface tension (a force that acts upon reducing the surface area of the droplet). At the beginning of drying, the droplet shrinks and the internal pressure increases as a result from solvent removal. However, once the crust is formed, the reduction in the droplet volume is hindered. As a consequence, a growing pressure will be applied over the new-formed crust for balancing the internal droplet pressure. The crust at the droplet surface may be rigid or flexible, depending on the solutes molecular size, viscoelastic properties and molecular interactions [63, 147]. Thus,

depending on the mechanical properties of the crust, the increase in capillary pressure will play a fundamental role on the definition of the final aspect of the resulting solid particle.

Typical visual aspects or particle morphologies of spray-dried solid structures are shown in Figure 1.8. The particles may present a dense [32, 170] or a hollow core [33, 34, 163], a wrinkled surface [82, 157, 170] or they may acquire the shape of a doughnut [7, 116] or a raspberry [116, 186]. The generated structure may also be highly porous [116, 170] or have a "hairy" surface [116]. The reasons for these differences are discussed hereafter.
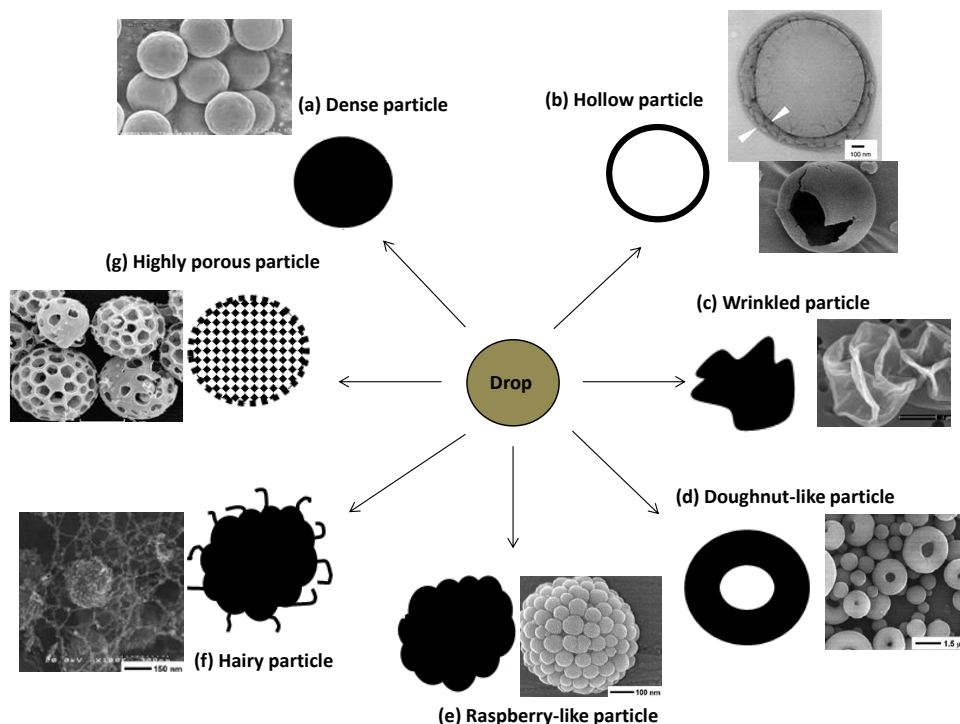

Figure 1.8 – A schematic representation of the possible particle morphologies obtained from the drying of a droplet: (a) solid core, (b) hollow core, (c) wrinkled particle, (d) doughnut-like particle, (e) raspberry-like particle, (f) hairy particle, (g) highly porous particle. Adapted with permission from [116, 170, 173]

As already said, the particles obtained via spray drying may have a dense (Figure 1.8-a) or a hollow core (Figure 1.8-b). When the evaporation flux from a liquid droplet is removed faster than the solute enrichment at the droplet surface, the formation of a solid crust in the droplet surface is delayed and the resulting solid particle may present a solid core (frequently referred as dense in the literature). On the other hand, if the solvent is removed from the droplet faster than the compounds diffusion towards the center of the droplet, a hollow core is most likely to appear [107]. As a result, the particles obtained via spray drying may have a dense (Figure 1.8-a) or a hollow core (Figure 1.8-b), even though the hollow core particle is more easily obtained due to the fast solvent removal rates employed in this process.

A smooth spherical hollow core particle is formed when the mechanical strength of the crust formed during drying can sustain the inward capillary pressure, driven by

the moisture evaporation [95]. If the resultant capillary pressure does not deform the crust, this could lead to a reduction in the wet particle's internal pressure, which could promote the formation of a bubble [127]. Upon further removal of solvent, this centrally located bubble would increase in diameter until the inner particle surface is solidified. If the pressure difference across the crust deforms it, a wrinkled (Figure 1.8-c) or doughnut-like (Figure 1.8-d) morphologies will probably be obtained after drying [147]. In addition, crust inhomogeneities can induce the buckling phenomenon as well, as shown by Bahadur et al. [7]. The phenomenon of the particle surface deformation has been mainly studied on the drying of colloidal suspension systems [20, 95, 127, 146].

Raspberry-like particles (Figure 1.8-e) are the result of the drying of a liquid suspension. The nano- or microparticles in the liquid phase also follow the drying mechanisms as described previously, such as the surface enrichment, but lead to the formation of a rough surface due to the their bigger size, which can go as high as 650 nm [186]. Correspondingly, the hairy-particle (Figure 1.8-f) are generally produced from suspensions under some specific conditions as described by Nandiyanto et al. [116], where a carbon nanotube catalyst (CoPd nanoparticles) and boron nitride nanoparticles were immersed into an ethanol droplet. Without the catalyst, the boron nitride and ethanol mixture would form raspberry-like particles. The addition of the CoPd causes the decomposition of ethanol and formation of carbon nanotubes on the particle's surface.

As described by Vehring [170], highly porous particles (Figure 1.8-g) are the result of the drying of an emulsion, where the dispersed phase (acting as the porous template) evaporates slower than the continuous phase. A stabilizing agent is generally necessary to avoid coalescence of the dispersed phase during drying in order to generate the structure shown in Figure 1.8-g.

The first scientific effort to study spray-dried particle morphologies was done by Charlesworth et al. [16]. These authors performed a series of single-solute solution droplet drying experiments in order to give a set of different particle morphologies. This experimental approach was later applied by Walton et al. [173], with the drying of single-solute solutions, suspensions and multi-component emulsions. Furthermore, the same authors highlighted the production of particles with a hollow or a dense core, a smooth or wrinkled surface, depending on the initial liquid formulation and drying conditions. A comprehensive review was written by Nandiyanto et al. [116] on the subject, with the production of different particle morphologies by varying the initial liquid formulation.

Regarding the application of the different morphologies presented in Figure 1.8, Shah et al. [155] stated the use of particles with wrinkled surface for enhancing the aerosol perfomance in inhalation drug delivery systems due to a reduction in the attractive interparticle interactions. Such improvement in the pulmonary delivery efficiency could also be obtained from the low-density hollow core particles [170]. For the highly-porous particle (Figure 1.8-g), according to Vehring [170], the design of such particle with very low porosity have been applied for pulmonary delivery of small molecules and have been suggested for vaccination purposes.

The particle structures obtained via spray drying are strongly connected to the physico-chemical properties of the substances being dried and the drying conditions. This section presented the rich possibilities of particle morphologies that can be produced. For this reason, the perception of the spray drying process changed. From its first conception, the

process was viewed as solely a drying operation to produce large amounts of powder, to remove most of the feed's solvent and to enhance product storage and stability. However, this approach evolved over the years driven by the increasing demand for particles with engineered end-use properties (Figure 1.9), that is to say particles with improved properties like dissolution and release profiles, reactivity, taste masking, flowability, wettability, compactibility and coating. Therefore, nowadays spray drying is used as an useful system to design particles with engineered structures (low density particles with controlled surface morphology, particles with multi-layer composite coating or particles comprising smaller sub-units, such as nanoparticles, or controlled porosity).

Despite the recent advances in particle engineering, some major scientific obstacles are still present regarding the spray drying operation. That is to say a detailed description of the components distribution inside the droplet/wet particle during drying and further the capability of predicting the final particle structure based on the initial liquid formulation and drying conditions. In order to overcome such challenges, experimental and modeling approaches were established in the literature, as will be discussed in the next sections. Both approaches are developed either on the spray scale, which means working with a pilot- or lab-scale spray dryer, or with a simplified version of this operation, which is the single droplet scale.
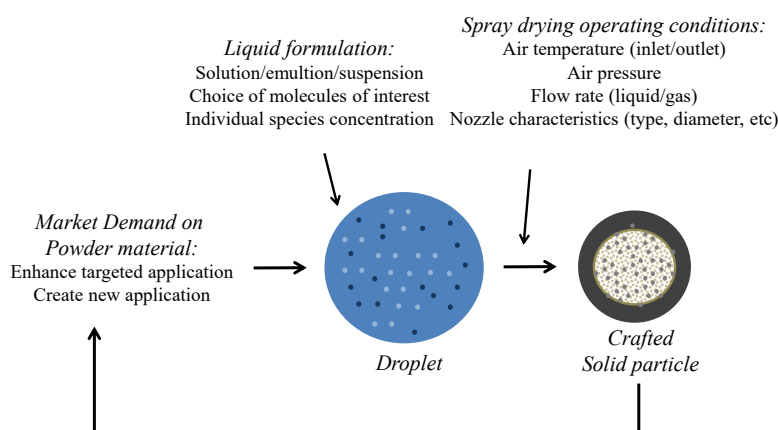
Figure 1.9 – The development of engineered solid particles is a result of an interplay between the liquid formulation and the drying conditions and its creation is impelled by a growing demand for better end-use powder properties

1.3 Experimental approach

In order to deal with the still present scientific challenges in the spray drying operation, two experimental approaches have been developed to study the drying of liquid droplets: either the experiments are focused on the spray of droplets, as in the industrial drying operation, or they are executed on a simplified version of the process, which means working with a single droplet.

1.3.1 Spray scale

Experimentally, understanding the drying mechanisms for a spray of droplets is based on the ability to relate the droplet properties before drying (e.g. droplet size, concentration)

and the air properties (e.g. air inlet temperature, air flow), to the dried particle properties (e.g. particle apparent density, surface composition, porosity, morphology and inner component distribution), as shown in Table 1.1. The present approach is commonly accomplished with pilot- or lab-scale spray dryers [153]. Thus, the initial drying conditions are changed and the resulting effect on the final particle solid structure is analyzed by means of techniques like scanning electron microscopy, Raman spectroscopy, pycnometry and X-ray photoelectron spectroscopy. The main drawback of such approach is the lack of *in situ* monitoring to track changes in the composition of the droplets through the whole drying operation. This would require a technique sophisticated enough to follow the thousands of droplets of various sizes produced by the atomizer, transported by the air flow and dried in only a few seconds.

Table 1.1 – Some representative studies related to the effect of drying conditions and liquid formulations on particle properties at the spray scale

Authors	Compounds	Objective	Outcome
Poozesh et al. [133]	Solution of felodipine and polyvinylpyrrolidone in methanol.	Qualitative analysis of the influence of the spray-dried particle size (produced from different solid loads, i.e. 0.63 %wt and 2.4 %wt) on particle morphology and porosity.	Larger particles (diameter greater than 20 µm) presented a porous structure with an important spatial dispersion of components. Smaller particles (diameter inferior to 10 µm) were more evenly distributed in composition and less porous.
Munoz-Ibanez et al. [115]	O/w emulsion. Sunflower oil as dispersed phase and acacia gum and maltodextrin as wall material.	Influence of the emulsion size (0.1 and 1 µm) and rotary atomizer speed (33 200 rpm and 3270 rpm) on the particle morphology and component distribution.	The morphology changed from hollow and wrinkled to hollow and smooth by decreasing the atomizer speed. Oil droplets evenly distributed, in general, in the particle crust. Increasing the atomizer speed had a positive effect of the wall material spatial distribution.
LeClair et al. [80]	Aqueous solution of mannitol, dextran and adenovirus expressing Escherichia coli β-galactosidase.	Influence of spray drying parameters (air inlet temperature, gas flow rate, liquid feed flow rate and initial solute concentration) on powder yield, particle size fraction below 5 µm and viral vector activity loss.	Loss in viral activity was affected mainly by an increase in the air inlet temperature and gas flow rate. A reduction in powder yield and the desired particle size fraction was the result of increasing the air inlet temperature, the liquid feed flow rate and the initial solute concentration. An increase in the gas flow rate had no significant effect on the powder yield, but increases the desired particle size fraction (5 µm).

Table 1.1 : Continued

Authors	Compounds	Objective	Outcome
Bahadur et al. [7]	Colloidal dispersion of silica and a polymer (polyethylene glycol) with two different molecular weights (PEG400 or PEG1450).	Investigation of the particle morphology by changing the polymer and its concentration (0.5, 1.0, 2.0 and 3.0 % wt).	Pure silica particle had a doughnut shape. Adding 0.5 % wt of PEG400 led to a spherical particle with a small dimple. Higher concentrations resulted in spherical particles. Using PEG1450 at 0.5 % wt resulted in spherical particles. Higher concentrations generated wrinkled particles.
Li et al. [82]	O/w emulsion. Vitamin E as oil phase. Wall materials : whey protein, maltodextrin, gum arabic, Nutriose, Kleptose or Cleargum.	Analysis of pure wall material morphology and size distribution. Effect of adding vitamin E to the morphology and size distribution of whey protein, as model wall material. Investigation of the size of the vitamin E nanodroplets before and after spray-drying.	The pure wall materials produced wrinkled particles with size ranging from 1.5 µm to 2.0 µm. The wrinkled particle of pure whey protein became a smooth spherical particle by the addition of vitamin E. Changing the vitamin E concentration from 21.4 % to 17.6 % wt reduced the particle size from 2.0 µm to 500 nm. The vitamin E nanodroplets doubled in size after spray-drying compared to the initial emulsion size.
Elversson et al. [33]	Aqueous solutions of lactose, mannitol and sucrose/dextran.	Investigation of the influence of feed concentration (ranging from 1 % wt to the corresponding saturation concentration) on particle size and apparent density. The effect of changing the dissolved solids on particle morphology was also examined.	Higher solid contents resulted in bigger particles and lower apparent density. Lactose and sucrose/dextran originated hollow amorphous particles. Mannitol alone produced crystalline porous particles.
Steckel et al. [163]	Oil-in-water emulsion. Aqueous phase composed of salbutamol sulphate, poloxamer (or phosphatidylcholine) and lactose (or a cyclodextrin derivative). Oil phase composed of HPCD (2-hydroxypropyl-beta-cyclodextrine) or HPCD + dichloromethane.	Creation of particles with low apparent density for pulmonary drug delivery by changing the volatility of the emulsion oil phase.	Particles with an apparent density of $0.04\,\mathrm{g\,cm^{-3}}$ were obtained with only HPCD in the oil phase. Particles were hollow with a thin shell and a blow-out hole. Adding dichloromethane to the oil phase reduced the particle apparent density to $0.02\,\mathrm{g\,cm^{-3}}$. The new particles presented a highly porous structure.

Authors	Compounds	Objective	Outcome
Elversson et al. [34]	Aqueous solution of lactose	Effect of nozzle diameter (1.5 mm and 2.0 mm), atomization air flow (from 20.6 L min^{-1} to 35.7 L min^{-1}) and feed solid content (from 1 % wt to 20 % wt) on droplet and particle size	Droplet size controlled by nozzle diameter and air flow. Particle size increased by higher nozzle diameter and feed concentration.

In order to follow the drying of the droplets, Pearce [129] presented a sampling device containing liquid nitrogen to flash frozen the droplets at different positions in the drying chamber. For each trial, the sampling device collected around 50-100 g of droplet/wet particles in a couple of minutes. The moisture content of the frozen sample was measured afterwards. Furthermore, air bulk properties, e.g temperature and humidity, can be measured from thermocouples and humidity sensors placed at different positions in the drying chamber, to obtain a discrete evolution of both air characteristics [87]. However, the droplet bulk properties measured with the device described by Pearce [129], along with the discrete evolution of the air characteristics, would give only a general idea about the drying history. In order to engineer solid particles from complex liquid formulations, a finer experimental evaluation of the solid formation mechanisms is required.

Hence, the drying of a single liquid droplet has been proposed as an alternative path to study the spray drying process. In that way, the structural evolution can be monitored and changes in the droplet properties can be quantified due to the use of bigger droplets, longer drying times and laboratory apparatus allowing the *in situ* follow-up [11, 144]. A literature overview regarding the single droplet is the subject of the next section.

1.3.2 Droplet scale

Changing the observation scale, from a spray of droplets to a single droplet, has become an interesting route to understand the mechanisms of component interaction and distribution inside the liquid droplet and the formation of the solid structure. As presented in Figure 1.10, the single droplet will clearly not experience the same drying conditions as it would in the industrial drying chamber – especially with the increase in droplet diameter (achieving droplet sizes ten times bigger than that in the industrial chamber) [64] and drying time (from seconds in the industrial chamber to minutes in the single drop experiment) and the suppression of the disturbances related to the spray drying process (e.g. droplet-to-droplet interaction, droplet-to-wet particle interaction, droplet-chamber wall collision) [11]. Nevertheless, single droplet experiments can still be used to reproduce particle morphologies that would be obtained from the industrial process [42, 147].

Many devices have been presented in the literature to follow the drying of a single droplet (Figure 1.11). Some use an intrusive material to hold the droplet in place, like a filament [83, 84, 117, 151] or a hydrophobic surface [94, 123, 131, 182]. Others maintain the droplet's position by means of an acoustic field [50, 52, 110, 184] or an air stream [3, 65, 177]. A droplet can also be let to freely fall through a small chamber [8, 37, 139].
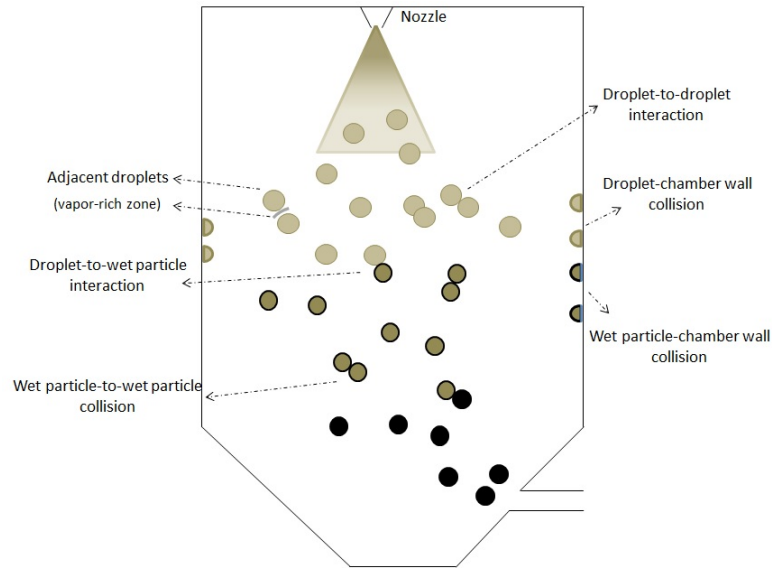
Figure 1.10 – Representation of the disturbances that occur during the drying of the droplets in the spray-drying chamber
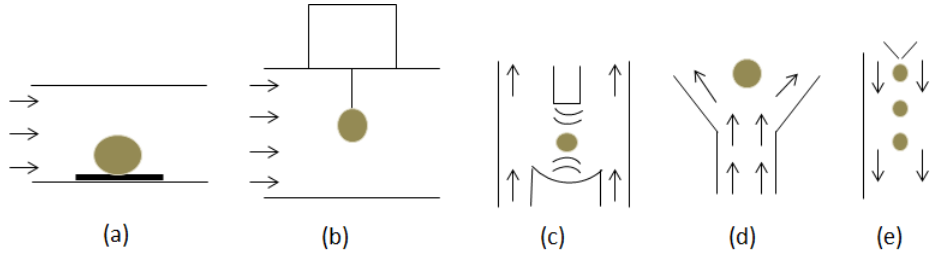

Figure 1.11 – Single droplet drying techniques: (a) droplet on a hydrophobic surface; (b) droplet hanging on by filament; (c) droplet levitated in a acoustic levitator; (d) droplet levitated by an air flow; (e) free-fall technique

Less common methods consist of placing the droplet between plates [145] or making it levitate on a thin layer of its own vapor (the Leindenfrost effect) [95].

The proposed devices tend in their ways to reproduce the environment encountered by the droplets in the industrial drying chamber, apart from the collisions. As a consequence, they are useful to give detailed technical information but also have inherent limitations, as summarized in Table 1.2. The choice of the method will depend on the researcher's judgment in weighting the suitability of the method to the goal of the study.

Table 1.2 – Single droplet drying techniques: an overview

Non-invasive methods			*Invasive methods*	
Chain of droplets	**Aerodynamic levitation**	**Acoustic levitation**	**Thin filament**	**Hydrophobic surface**
Available information				
Diameter evolution tracking	Diameter evolution tracking	Diameter evolution tracking	Diameter evolution tracking	Diameter evolution tracking
Radial composition measurement	Radial composition measurement	Radial composition measurement	Radial composition measurement	Radial composition measurement
-	Droplet temperature assessment	Droplet temperature assessment	Droplet temperature assessment	Droplet temperature assessment
-	-	-	Droplet mass determination	Droplet mass determination
-	-	-	-	Crust growth observation
-	-	-	-	Droplet's internal structure visualization
Technical limitations				
No direct temperature measurement	-	-	-	-
No direct mass measurement	No direct mass measurement	No direct mass measurement	-	-
-	-	Droplet position control	Droplet position control	-
-	-	Droplet size ($300\,\mu m$ - $1\,mm$)	Droplet size ($500\,\mu m$ - $9\,mm$)	Droplet size ($150\,\mu m$ - $2\,mm$)
-	-	Droplet deformation	-	Droplet deformation
-	-	-	Lack of free rotation	Lack of free rotation
-	-	Parasite heat transfer	Parasite heat transfer	Parasite heat transfer
-	Solute nucleation zone	Solute nucleation zone	Solute nucleation zone	Solute nucleation zone

Suspension by a filament

Regarding the method of droplet suspension by a filament, the droplet mass variation over time can be accurately measured by attaching the filament to a precision balance, provided that special attention is given to the air flow disturbances on the mass recording.

The filament method has been used for droplets containing dissolved salts [35, 83, 143], dissolved sugars [1, 60, 151], functional oils [174, 175], pharmaceutical compounds [44, 48] or droplets containing milk components [21, 38, 41, 43, 84, 85]. A thermocouple may be inserted in the droplet in order to assess its temperature, as accomplished by Al-Mubarak et al. [113] and Lin et al. [84]. This adds another intrusive material in the interior of the liquid phase, which can interfere in the drying of the droplet. To overcome the use of a thermocouple, Saha et al. [149] used an infrared camera with a droplet levitated by acoustic waves, but only the droplet surface temperature could be measured.

The intrusive material used to hold the droplet in place must cause the least possible disruption to the drying of the droplet. In that way, Han et al. [55] et Fu et al. [42] examined the effect of the suspension filament on the energy transferred by conduction to the droplet during drying. They showed that the presence of a glass filament only contributes to approximately 1 % of the total heat transferred to a 1 mm droplet. However, this low energy input could still be considered as a parasite heat transfer [4]. Regarding the effect of the filament on the mass transfer, the presence of scratches on the surface may promote heterogeneous nucleation, which offers a smaller energy barrier for phase transition. In that way, the particle solid structure may be formed sooner than in the case without the filament. Thus, it may influence the final particle diameter and at a lesser extent the distribution of the components in the solid structure.

In an industrial drying chamber, the air flowing around a droplet presents homogeneous temperature and vapor content profiles due to the turbulent flow. In that way, heat and mass transfers are more symmetrical over the surface of the droplet. However, in the single droplet methods, the air flows in a laminar regime. Thus, the heat and mass transfers are greater on the droplet side facing the air flow and lower on the wake region. To adress this issue, Hassan et al. [63] et Al-Mubarak et al. [113] used a rotating capillary to homogenize the mass and energy transfers, but the impact of the revolving speed on the evaporation rate was not investigated.

On a hydrophobic surface

The other intrusive drying method consists of placing a droplet on a flat surface covered with a hydrophobic substance, like polydimethylsiloxane (PDMS) [123, 148], polypropylene [13] or teflon [182], so that a high contact angle can be obtained between the droplet and the surface. To increase even further the contact angle, Al-Shehri et al. [159] used a spinning hydrophobic surface to obtain a perfectly spherical droplet. This single droplet method has been used for investigating the inactivation of a bioactive substance during drying [131], surface buckling [13, 20, 127, 146], vacuole formation and mechanical properties of milk particles [145, 148], organisation [54], movement [92, 93, 165], agglomeration [94] of nanoparticles during drying and also droplet bouncing on hydrophobic surfaces [24, 74, 75].

Sadek et al. [148] placed an optical microscope in fluorescent mode near the hydrophobic surface to observe the solid structure formation inside the droplet containing a fluorescent dye. The images captured by the microscope corresponded to a horizontal plan 60 μm away from the hydrophobic surface.

Like the filament method, the hydrophobic surface may transfer heat by conduction to the droplet. According to Perdana et al. [131], this energy input is smaller than

5 % of the total heat transferred to the droplet. The hydrophobic surface may also present preferential sites for solid nucleation. Perdana et al. [131] also highlighted the modification of the air streamlines around the droplet (due to the presence of the surface) and the importance of appropriately adjust heat and mass transfer coefficients.

Acoustic levitation

To avoid using an intrusive material to hold the droplet in place, an acoustic field can be created by a transducer and a reflector. A droplet inserted in this field will not move due to an equilibrium between the droplet weight and the upward acoustic radiation force [4]. It means that the droplet can move upwards due to moisture loss if the pressure radiation force is kept constant [184]. This vertical displacement can be used to generate the droplet drying curve [52]. The use of such method may not be appropriate for the falling drying rate period, where the droplet mass loss becomes smaller and thus the change in droplet position is less discernible. To reduce the effect of acoustic streaming generated by the acoustic field around the droplet, some authors have adapted the acoustic levitator so that an air flow could be used [4, 50, 52, 53]. In that way, the moisture vapor would not be retained at the droplet's boundary layer. The droplet position on the acoustic levitator could become unstable if the air flow rate were increased to suppress the effect of the acoustic streaming on the droplet drying rate. The acoustic levitation has been used for studying the structural behavior of proteins during drying [23], particle mechanical strength [77, 111], droplet velocity field [92, 150] and surface buckling [126]

Aerodynamic levitation

The aerodynamic levitator, as presented by Adhikari et al. [3], is another non invasive method used for the drying of single droplets. In this case, an air flow is created to suspend and dry the droplet. This method is rarely applied for drying droplet studies, due to the difficulties in maintaining the droplet in place, which makes the image capture and mass and temperature measurements difficult. However, in the field of physics, Weber et al. [177] and Hennet et al. [65] have used the aerodynamic levitation to study molten materials using synchrotron x-ray.

The free-fall technique

The single droplet drying method that resembles the most the spray drying operation is the free-fall technique – or chain of droplets technique, when more than one droplet is produced during the experiment [37]. This method does not enable the direct measure of mass or temperature of the falling droplet. Image analysis has to be used to assess the evaporation rate, as demonstrated by Baldelli et al. [8]. The main advantage of the chain of droplets technique is the small size of the droplets (compared to the other single droplet drying methods) and the creation of monodisperse droplets. For example, Baldelli et al. [8] produced particles as small as 30 µm from an acetone droplet containing cellulose acetate butyrate. Regarding the particle size distribution, Rogers et al. [139] produced 100 µm particles with size variation smaller than 10 µm. In that way, the droplets generated will experience the same drying history and produce the same solid structures [138, 180]. A few grams of powder can then be produced and used for the evaluation of powder bulk properties, like water content and solubility [138].

From the single droplet drying methods, droplet average parameters like mass, temperature and concentration can be obtained. Image analysis may also give evaporation rate from the isotropic shrinkage, if any, and external visualization of crust formation and evolution. To understand the mechanisms of component distribution during drying, many studies relate the changes in the initial droplet properties to the final particle properties, as shown in Table 1.3. This approach was previously discussed on the section dedicated to the spray of droplets. The studies with *in situ* droplet components distribution measurement are presented in the next section.

Table 1.3 – Some representative examples of single droplet studies relating the changes in drying conditions to the final particle properties

Authors	Method	Compounds	Objective	Outcome
Osman et al. [121]	Acoustic levitation.	Colloidal suspension. Silica nanoparticles in water.	Investigation of the particle morphology by varying the size of the silica nanoparticles from 46 nm to 2.5 µm.	Drying the 46 nm silica resulted in a dense spherical particle, while the microsized silica originated a particle with a shape resembling the human red blood cells.
Fu et al. [44]	Thin filament.	Suspension of silica nanoparticles and Eudragit RS 30D containing either Rhodamine B or sucrose as model drug.	Investigation of the final particle solid structure (porosity, component distribution, surface visual aspect) by changing the concentration of the model drug in the formulation (0, $5\,\mu g\,mL^{-1}$ or $1.5\,mg\,mL^{-1}$)	The particle solid structure with no model drug presented a porous region rich in Eudragit RS near the particle surface and a denser region rich in silica towards the core of the particle. The visual aspect of these two regions was not modified by the addition of the model drug. However, Rhodamine B was more concentrated at the porous region, while the sucrose was more homogeneously distributed. All the formulations resulted in a particle smooth surface, except the formulation with a high loading of Rhodamine B, which presented small wrinkles on the particle surface.

Table 1.3 : Continued

Authors	Method	Compounds	Objective	Outcome
Shamaei et al. [157]	Thin filament.	O/w emulsion. Walnut oil as dispersed phase. Skim milk solution as continuous phase.	Investigation of the effects of drying air temperature (80 °C - 140 °C), total solid content (12 % - 30 % wt) and oil/wall material mass content (0.25 - 1 wt) on the particle size and surface morphology.	The particle surface became less wrinkled with increasing temperature and oil/wall ratio. A reduction in surface roughness was obtained with higher total solid content. Bigger particles were obtained by increasing the studied parameters.
Sadek et al. [145]	Hydrophobic surface.	Two aqueous solutions were prepared : one with whey protein isolate (WPI), and the other with native phosphocaseinates (NPC).	Analysis of the particle morphology and crust properties (buckling time and compression behavior) under the same drying conditions (air temperature at 20 °C and relative humidity at 2 %).	The WPI particle had a hollow morphology with a smooth surface while the NPC particle presented a wrinkled morphology. The surface of the NPC particle started to buckle after 11 min of drying and the crust tends to deform under stress. On the contrary, the WPI particle crust started to buckle after 30 min and it tends to fracture under stress.
Mondragon et al. [112]	Acoustic levitation.	Colloidal suspension. Silica nanoparticles in water.	Inluence of the solid mass content (0.02 wt - 0.2 wt), drying temperature (80 °C - 120 °C), droplet initial volume (0.3 µL - 0.8 µL), pH value (2 - 10) and salt concentration ($0\,\mathrm{mol\,L^{-1}}$ - $0.05\,\mathrm{mol\,L^{-1}}$) on the final particle size, shell thickness and mechanical strength.	The solid mass content and the initial droplet volume had a positive effect on the final particle size, on the particle shell thickness and on the mechanical strength. The pH value had a positive effect on the particle mechanical strength only at high solid mass content. The other tested parameters did not have any important influence on the particle size, shell thickness and mechanical strength.

Table 1.3 : Continued

Authors	Method	Compounds	Objective	Outcome
Mondragon et al. [111]	Acoustic levitation.	Porcelain tile suspensions (45 % clays, 6 % sand and 49 % feldspars) in water.	Influence of varying initial solid mass content (0.65 wt - 0.70 wt), flocculation state (flocculated - deflocculated), porcelain tile size (1.95 µm - 3.25 µm), air temperature (70 °C - 100 °C) and initial droplet volume (0.4 µL - 0.7 µL) on the particle porosity and mechanical strength.	The porcelain tile size and the initial solid mass content had a negative effect on the porosity but a positive effect on the particle mechanical strength. Increasing the air temperature also had a positive effect on the mechanical strength but not a relevant importance for the porosity. The deflocculated porcelain tiles improved the particle porosity and may improve the particle mechanical strength if a high initial solid mass content is used.
Rogers et al. [138]	Free-fall technique	Reconstituted skim milk and milk protein concentrated powders	Influence of varying the air inlet temperature (from 77 °C to 180 °C) on the solubility of the final particle.	The temperature had a negative impact on the solubility of the dried particles. Indeed, an increase in the air temperature produced insoluble material in the droplet liquid phase during drying.

In situ component distribution evaluation

In order to assess the internal droplet composition profile without disturbing the drying process, it is important to use experimental techniques that interfere the least with the droplet compounds. The techniques in this section rely mainly on the electromagnetic waves emitted from the compounds present in the droplet to give information about their distribution in the liquid.

The research group of Quiño et al. [135] has developed an experimental set-up that enables the acquisition of a one-dimensional concentration profile inside the droplet using Raman spectroscopy[4]. A droplet containing a mixture of acetone and water was levitated through an acoustic levitator and a Nd:YVO4 laser operating at 532 nm was horizontally directed to the droplet. A CCD camera coupled with an spectrometer captured the Raman light scattered at an angle of 90° from the incident laser beam. Even though no solid particle was formed during the experiment, the set-up developed

---

[4]Raman light arises from an inelastic interaction between light and matter. As a matter of fact, a photon carries a certain electromagnetic energy that is inversely proportional to its wavelength. When such photon enters in a molecule, the light-matter interaction may be elastic, where the incident light does not change the energy state of the molecule after leaving it, or it may be inelastic, the photon exchanges a tiny amount of energy with the matter and this fraction of energy is scattered with a different wavelength from the original photon (i.e. the Raman shift). The inelastically scattered light, or Raman light, is a typical feature of each functional group in the molecule. As a result, the Raman light can be used to identify the molecules present in a sample [14].

was still useful for seeing how the acetone concentration was distributed across the droplet (Figure 1.12). The data were obtained every second and the concentration points were spaced at intervals of 120 μm. Enhancing the concentration profile near the droplet surface by increasing the number of measured concentration points is a complicated task due to light distortion near the liquid-air interface. The same group also used the Raman technique for measuring a concentration profile of a supercritical drying gel placed on a high-pressure chamber [136] and the composition of a pendant liquid droplet confined in a supercritical carbon dioxide environment [14].
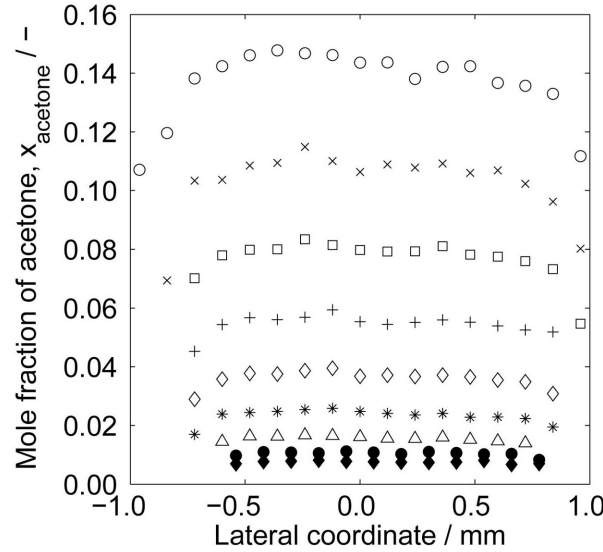
Figure 1.12 – Temporal evolution of radial composition profiles of a water-acetone droplet measured with the *in situ* Raman technique. From the lateral coordinate axis, the droplet initial diameter is about 2 mm and the final diameter is 1.3 mm. The acetone mole fraction difference between the droplet surface and center reduces over time. Adapted with permission from [135]

When a laser beam is focused on the droplet, only a small percentage of the incident light is reflected as Raman light. As a result, very sensible detectors have to be used in order to quantify the weak signal as a compound concentration. Increasing the laser power to reduce measurement errors may induce liquid evaporation. This would deviate the drying experiment from the spray drying process.

Apart from the Raman technique, Lemoine et al. [81] also presented an optical technique, called the Rainbow refractometry, which is based on the droplet's refractive index. According to the authors, the dependence of the refractive index with the droplet's temperature and composition should be known. The main drawback of this technique is the need of a transparent droplet. For this reason, this method would not be useful for the main dried systems, like emulsions and solid suspensions, as the presence of undissolved solids in the droplet would alter the liquid refractive index. Therefore, obtaining a concentration profile from the refracted light in such dispersion would be a quite complex task. Additionally, the formation of a solid crust, if not transparent, could impede the light from entering the droplet.

In the same publication [81], the use of laser-induced fluorescence to characterize the internal flowfield was also reported. Manukyan et al. [92] and Saha et al. [150] visualized the internal flow in a droplet deposited on a hydrophobic surface and a droplet acoustically levitated, respectively, by adding tracer nanoparticles in the droplet (copolymer [92] or polystyrene [150] microspheres). The former was interested in analyzing the effect of the initial contact angle and the pinning effect on the internal flow and the latter studied the effect of droplet size and viscosity on the internal flow. Even though this method does not give a direct measure of the component concentrations, it is a helpful technique to evaluate, for example, if the liquid streams could evenly homogenize the component concentrations, provided that the tracer employed does not disturb the drying process. According to Manukyan et al. [92], the weakening of the liquid streams after the crust formation could also be visualized.

Griffith et al. [51] employed nuclear magnetic resonance spectroscopy to study the drying of a detergent droplet suspended by a glass filament. A $10\,\mu$L-droplet (diameter around $1.6\,$mm) was excited at discrete times and the obtained spin echo profiles were translated into a water distribution profile. Despite its great potential, the use of this technique is not widespread due to capital expenditure costs.

To evaluate the components distribution and the chemical surface composition of a droplet over discrete drying times, Foerster et al. [38] stopped the drying process by flash-freezing the droplet with a vial containing liquid nitrogen. Two model milk emulsions were studied, with different fat contents. The chemical surface composition of the frozen droplet was measured by X-ray spectroscopy, while the component distribution was assessed by confocal laser scanning microscopy. For the latter, the protein molecules were labelled with a red fluorescent dye and the fat with a green one. Then both were excited by respective laser lights. Compared to the methods presented in this section, flash-freezing the droplet is a rapid way to stop the drying process and to allow a subsequently ex-situ measurement of the droplet component distribution.

1.4 Modeling of the drying process

The representation of the drying process through models is an important tool to improve the knowledge about spray-dried particle formation. However, due to the complexity of the process, the model results have to be supported by experimental observations in order to be validated [1]. To adequately represent the drying of a multi-component droplet, a rigorous description of the component diffusive fluxes should be used, since the final component distribution strongly depends on how the substances are being transported in the liquid phase. The process of crust formation and development should be equally well described so that the models can properly represent the drying process of a droplet and then be scaled-up to represent the drying process at the industrial or commercial spray dryer scale.

The drying of a droplet has been illustrated through the use of an empirical or a deterministic approach. For the empirical approach (Section 1.4.1), experimental observations are used for describing the evolution of the droplet over time with average droplet properties (no spatial distribution). On the other hand, the deterministic approach (Section 1.4.2) uses spatially-resolved variables for representing the drying of the droplet, thus giving a much finer insight into the droplet variable changes.

1.4.1 Empirical modeling approach

Three main empirical approaches have been used in the study of a single droplet drying: the characteristic drying curve (CDC) approach [17, 78, 124], the reaction engineering approach (REA) [17, 19, 46, 71, 124, 125, 183] and a Peclet number based analysis (PNA) [21, 121].

The CDC and the REA approaches give fast information about the droplet drying kinetics. They are relatively simple to implement because they use lumped variables and the results can be quickly calculated. The parameters obtained with these two methods depend on the system dried and they do not give information about the particle morphologies [17]. More details about the CDC and REA models can be found in [124]. Mezhericher et al. [105] coupled the water vapor density at the surface of the droplet given by the REA approach to a continuous species transport approach (description in the next section) to model the drying of a skim milk droplet. A good agreement was found between the model and the experimental results.

On the contrary, the PNA has been used to distinguish the final morphology of the dried particle. According to the value of the Peclet number, a dense core solid particle (Peclet inferior to 1) or a hollow core particle (Peclet superior to 1) is expected. Indeed, the Peclet number takes into account the speed in which the droplet compounds diffuse in the droplet during drying and the speed at which the evaporation front recedes, that is to say a measure of the solid accumulation at the droplet surface [171]. Despite its relevance, this dimensionless parameter cannot be used to predict the formation of all the morphologies presented previously, since it does not give information about component distribution. Also, the Peclet number is calculated from the initial drying conditions, but its value may vary during the drying process because the diffusion coefficients and the evaporation front receding speed taken into account may change throughout the drying period. This approach was used by Chew et al. [22] on a series of experiments with a skim milk droplet suspended on the tip of a glass filament. From the plots of normalized particle diameter on the moisture content, the authors observed a deviation from the ideal shrinkage behavior (formation of dense core particle) for high calculated Peclet numbers, indicating the formation of hollow core particles.

1.4.2 Deterministic modeling approach

Two main deterministic approaches have been used in the literature: the continuous species transport (CST) approach [49, 100–102, 105, 109, 142, 143, 158, 181] and the CST approach coupled with a population balance [57–59, 154].

The CST approach gives information about what happens inside the droplet during drying, since it uses spatially distributed variables. Even though this approach uses more complex equations and needs more time to give the results, the CST approach can be used to predict particle morphology [100]. The modeling of the first drying stage – where the activity coefficient of the solvent can be considered equal to one at the surface of the droplet – has been well supported by experimental data [58, 100, 105, 143, 158]. The droplet is considered to remain spherical, with no temperature gradient between its surface and the core and with an ideal shrinkage. The droplet properties are calculated only on the radial direction and the effect of the internal convection is often neglected [58, 107, 158]. Furthermore, the diffusion coefficient of the components

in the droplet is expressed in terms of the Stokes-Einstein equation, which is a simpler equation valid for binary mixtures in infinite dilution. Such estimation may give a first idea of the value of the coefficient of diffusion for a higher water content, however as the concentration in the droplet increases, the values given by the Stokes-Einstein equation may be some orders of magnitude higher than a finer coefficient estimation [91, 100].

Nevertheless, the description and experimental validation of the crust formation and growth are more challenging. The process of solid generation is generally overlooked by considering that the crust is formed once a certain saturation value [105, 158] or a maximum packing fraction [107] are obtained. Handscomb et al. [59] considered a series of shell buckling and shrinkage events due to capillary forces on the droplet suspended solutes. This formation process takes place in only a few seconds, which makes experimental validation difficult.

The main morphologies represented in the literature with the CST approach are the dense and hollow morphologies with a rigid crust. The compounds present in the droplet are either solids in suspension or salts in solution. In that way, the crust formation comes from the agglomeration of the undissolved solids or through crystallization of dissolved crystal-forming compounds. To our knowledge, there is a lack when it comes to the description of the formation of an amorphous crust[5] from substances completely dissolved in the liquid phase and the representation of wrinkled surfaces (apart from the description of the buckling process to form a doughnut-like particle).

Grasmeijer et al. [49] and Sadafi et al. [142, 143] used the CST approach to model the drying of a dense core particle. The glass transition temperature[6] was used by Grasmeijer et al. [49] to determine the formation of a solid structure from a droplet containing a protein and a sugar. The droplet was subdivided in multiple subshells from the center of the droplet to its surface. Additionally, each subshell possessed homogeneous concentration. The obtained results were not experimentally validated. Due to recent advances in computer processing speed, this kind of model may be replaced by a more rigorous one. A different parameter is used by Sadafi et al. [142, 143] to set the crust formation. They considered a critical concentration value for the crystallization of sodium chloride in water. The development of the crust on the surface of the droplet is calculated by blending the equations for the constant evaporation rate period and the falling rate period through a weighting factor. This factor varies from zero (no solid formed at the droplet surface) to one (surface covered by the solid surface). The modeling results were compared to experimental data obtained by the same team. The droplet evaporation rate was slightly underestimated compared to the experimental results.

---

[5]The best way to present the difference between crystalline and amorphous solids is their structure. In a crystalline solid, the molecules composing it are organized with a well-defined network, on a repeating pattern over a long range. Such network is called a crystal lattice, while the unit cell is the smallest repeating unit having a full symmetry in the crystal. The amorphous solids, on the other hand, do not present such organized molecular arrangement, with no unit cell or lattice. In spray drying, due to the high drying rates, the generated solid particles might in most cases present an amorphous structure, since no time is allowed for the formation of the crystalline network.

[6]The glass transition temperature (T_g) is an important property of an amorphous material. Below this temperature, the substance presents itself in a rigid and brittle state with little particle mobility. On the other hand, when the substance is submitted to temperatures above its glass transition temperature, it turns into a viscous or a rubbery state. This property is highly influenced by the material moisture content, by the molecular mass, etc.

The other particle morphology modeled by the CST approach is the hollow core particle with rigid crust. It has been studied with the drying of a droplet containing silica nanoparticles in suspension [100–102, 105, 109]. Unlike the modeling of the dense core particle, internal and external pressures across the wet particle are calculated during the formation of the solid crust for the hollow morphology. Indeed, at the surface of the droplet, liquid bridges between the nanoparticles create compressive tangential and radial stresses, leading to the formation of a crust when a maximum packing fraction value is reached. Once the crust is formed, the water vapor transfer through the pores of the crust is only dependent on the vapor concentration, because the pore size is considered to be much greater than the vapor molecular mean free path. Furthermore, Maurice et al. [102] state that the production of a hollow core particle is possible when the solid crust generated at the surface of the droplet induces a reduction in the droplet internal pressure and thus the formation of a bubble, which may grow driven by the liquid evaporation. The model results concerning the bubble growth period was not validated by lack of experimental data.

Also on the formation of a hollow core particle, Handscomb et al. [59] implemented a population balance in the CST approach to model the drying of a droplet containing a dissolved salt (with the hypothesis that one crystal seed is already present in the liquid phase) and nanoparticles in suspension and surrounded by stagnant air. The use of a population balance allowed the description of nanoparticle agglomeration, dissolved solid crystallization and the radial position of the suspended particles. The formation of the hollow core particle could follow two routes from the developed model: a first one where the evaporation front recedes and water vapor diffuses through the pores of a dry crust, and a second one where the internal bubble growth keeps the evaporation front at the surface of the wet crust. Fickian diffusion was used for representing the movement of the compounds inside the droplet. Finally, a good agreement with experimental data was obtained from the modeling results.

1.5 Summary of the chapter

This chapter firstly presented the different steps composing the spray drying operation, i.e the atomization, the droplet drying and particle formation and the powder separation. In that way, different devices were shown for generating the spray of droplets, along with an introduction to the physics related to the drying process. Additionally, it was possible to see that the use of different liquid formulations and air properties can originate solid particles with a variety of physical structures. Due to this interdependency between the operating conditions and the product properties, the spray drying process has become a tool for producing particles with engineered end-use properties from multi-component droplets. However, there is still scientific and technological challenges regarding the detailed description of the components distribution inside the droplet during drying.

Experimental and modeling approaches at the spray and the droplet scales were developed in the literature to help understanding the mechanisms of solid formation from the drying droplets. Experimental studies related to the spray of droplets only acquire information about the beginning and the end of the drying operation, with no follow-up of what occurs during the process. Single droplet methods have been developed to allow monitoring a simplified drying process, without any disturbances due to collisions. Those methods allow a measurement of the droplet average properties under well controlled

drying conditions. They are capable of providing quantitative kinetic and morphological information necessary for the improvement of the drying models. Models have also been developed to demonstrate the evolution of the droplet properties and the appearance of two main solid morphologies: a dense and a hollow core particle. In the models, the presence of compounds in the droplet is often limited to solids in suspension or crystal-forming substances.

Considering the observation scales developed in the literature, the present thesis focus on a coupled experimental and modeling approaches at the droplet scale to help meeting the aforementioned challenges. Two set-ups are employed for following the droplet properties over the drying time. Furthermore, the experimental observations are used to support the development of a droplet drying model, until the period of solid surface (crust) formation. Trials are also performed at the spray scale, which will support the findings at the droplet scale.

Study at the spray scale

In this chapter, the design of different solid structures is carried out at the spray scale for two drying systems constituted by dextran-sucrose (system 1) and lactose-whey protein isolate (system 2) as solutes. Such approach is employed in order to portray the particle structures that might be obtained from these two aqueous formulations by spray drying. Different characterization techniques (e.g. microscopy, pycnometry, BET) were employed to give details about the particles surface and core aspects and porosity of the particle.

2.1 Motivation

The work developed during this thesis starts at the spray scale. Through the use of different liquid formulations, the powder generated at the spray scale presents the possible particle structures for the selected drying systems. Given the difficulties in following the process of particle formation at this scale, the role of the particles obtained here is to support the studies of particle formation at the droplet scale in the subsequent chapters. Indeed, considering the different duration at which the solid particles are obtained in the spray and droplet scales, such link becomes useful for stating the validity of the studies developed at the droplet scale.

2.2 The choice of the drying systems

This section is dedicated to present the reasons leading to the choice of the drying systems employed in this thesis, with a brief overview of the works in the literature guiding the choice, the physicochemical properties of the selected components and their industrial application. The criteria for the selection were:

1. regarding the liquid formulation, the choice was targeted on an aqueous solution containing two solutes;

2. a droplet from such multi-component mixture should generate amorphous particles, instead of crystal-forming compounds used in the literature;

3. it should be possible to find, from such drying systems, experimental evidence of some modification in the physical structure of the dried particles;

4. the components in the liquid formulation should present different molecular sizes and diffusion coefficients;

5. it should be noted that the design of the solid structures in the present thesis was not intended to fulfill a specific application, which is why the drying systems were also chosen in order to limit the exposure to hazardous substances.

Regarding the modeling studies, from the literature survey executed in Chapter 1, it was possible to see the common simulation of droplets containing silica nanoparticles (in suspension) as a drying system for the acquisition of drying kinetics, shrinkage kinetics, the droplet temperature and the nanoparticles volume fraction profiles through time [101, 106, 109, 178]. The formation of dense and hollow core particles were simulated with the crust being formed through a maximum packing of hard spheres and water vapor leaving the wet particle through the crust pores. Multi-component emulsions were also often studied, such as the milk droplets, with the crust formed after a critical moisture content and further drying taking place at a porous medium. Regarding the droplet solutions, most of them were binary mixtures where the resultant solid particle was formed by a crystal-forming compound.

Regarding the experimental studies, it is interesting to note that the use of droplet suspensions containing silica nanoparticles as a drying system is also very common [7, 111, 121]. Such liquid formulation is often used for studies related to the buckling of the wet particle surface (other applications may be found on the modification of the particle morphology, porosity and mechanical strength). Regarding the emulsions, common applications are related to encapsulation, and consequently the protection, of the compounds of interest by the solid matrix. Milk droplets may also be found in the experimental studies for assessing the particle morphology and drying kinetics [43, 85].

As a result from the common liquid formulation used in the literature, the choice of the drying systems was targeted toward the multi-component droplet solutions (with two solutes present in the liquid phase) and the resulting particles presenting an amorphous structure. The following drying systems were found, considering the criteria (1, 2, 4 and 5) given above: lactose-casein, whey protein isolate-maltodextrin, trehalose-bovine serum albumin, lactose-whey protein isolate, sucrose-dextran. From these options, it was possible to validate the criterion 3 with two aqueous systems containing two different solutes: dextran-sucrose and lactose-whey protein isolate (WPI).

2.2.1 Dextran-sucrose

The choice of a solution containing sucrose and dextran was based upon the results from [32]. Using a cocurrent laboratory-scale spray dryer, two aqueous solutions of sucrose and dextran (with a mass proportion of 4 to 1) and total solute of contents $20\,\%$ wt and $50\,\%$ wt were dried with air. The air inlet temperature was maintained at $200\,^{\circ}\mathrm{C}$ and the oulet temperature was kept at $90\,^{\circ}\mathrm{C}$. The liquid feed rate was $5\,\mathrm{mL\,min^{-1}}$ and the drying air flow was $0.8\,\mathrm{m^3\,min^{-1}}$. In order to estimate the production of particles with dense or hollow cores, the authors used a light microscope with the particles immersed in oil for the direct visualization of the particles interior. Also, an indirect estimation of

the particles' morphology was achieved through gas pycnometry [1], where the sample density was compared to the density of the unprocessed material (the production of hollow core particles would have the effect of lowering the sample density).

The powder obtained from the solution with total solute content of 20 % wt presented a density of $1.52\,\mathrm{g\,cm^{-3}}$. Considering the density of the unprocessed sucrose/dextran mixture at $1.59\,\mathrm{g\,cm^{-3}}$, the authors stated that indeed the sample density is close to that of the unprocessed material and, consequently, particles with dense core were obtained from this liquid formulation. On the contrary, the particles obtained from the more concentrated solution (50 % wt) presented a density of $1.33\,\mathrm{g\,cm^{-3}}$. Thus, the authors stated that hollow core particles were obtained from this sample. From the optical microscope as shown in Figure 2.1, in the powder produced from the experiment with the solution at 50 % wt, it was possible to observe the hollow core. A fair majority of the particles presented in Figure 2.1 presented a hollow core, even if the presence of particles without the dark spots in the core is also observed.
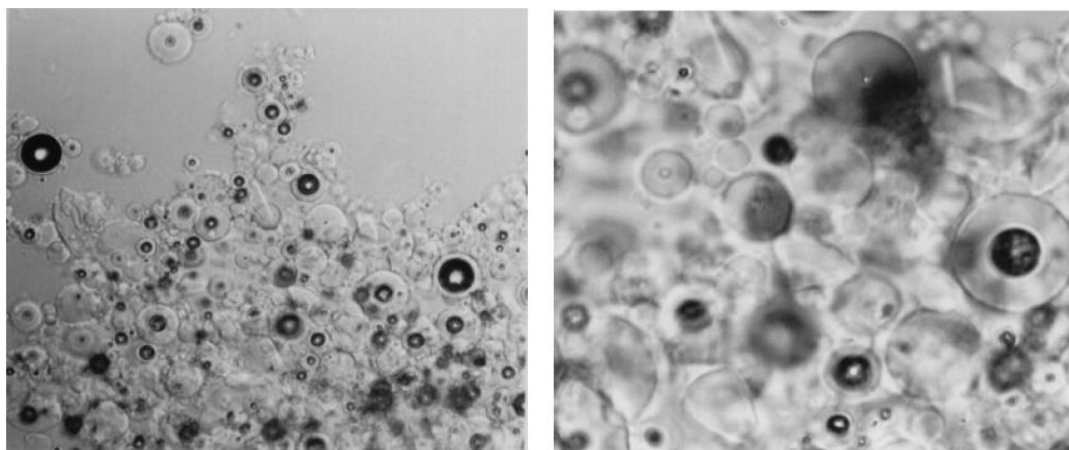
Figure 2.1 – Spray-dried particles produced in [32] from an aqueous solution containing sucrose and dextran (4:1) at 50 % wt of total solute content. With a light microscope, the hollow core particles could be observed (dark spots). However, in the same sample, particles without the dark spots can also be found. Adapted with permission from [32]

2.2.2 Lactose-whey protein isolate

Regarding this time the liquid formulation containing lactose and whey protein isolate, the choice of this drying system was based on the works developed in [168] and [62]. In [168], a single droplet was dried using the thin filament method. The liquid droplet containing 22.5 % wt total solute (15 % wt lactose and 7.5 % wt whey protein isolate) was suspended at the tip of a polyamide wire and dried at different air inlet temperatures (60 °C, 100 °C, 140 °C, 160 °C). The air velocity was kept at $0.021\,\mathrm{m\,s^{-1}}$ and the absolute humidity was maintained at $4\,\mathrm{g\,kg^{-1}}$. The authors have also dried droplets containing only lactose or whey protein isolate. For the ternary mixture, they presented results only from the drying at 140 °C. At this air temperature, a central bubble was created

---

[1]This method will be presented in Section 2.5.

inside the droplet, which expanded upon further removal of moisture from the wet particle and gave place to a hollow core in the final particle.

The authors in [62] also used the thin filament method for drying one single droplet containing lactose and whey protein isolate. Using a constant air velocity $(0.5\,\mathrm{m\,s^{-1}})$ and air relative humidity $(2.5 \pm 0.5\,\%)$, different lactose-to-WPI mass proportions were used (i.e. 0-100, 10-90, 20-80, 30-70, 40-60 wt, on a dry basis) for two drying air inlet temperatures $(65\,°\mathrm{C}$ and $80\,°\mathrm{C})$. However, the evolution of the droplet morphology was only presented for the experiment with the air at $80\,°\mathrm{C}$ and lactose-to-WPI mass proportions at 20-80 and 30-70 (on dry basis). The reason is that the published work was more focused on the evaluation of the denaturation of the protein with the drying process than the evolution of the particle morphology. In Figure 2.2, the evolution of the drying process is presented for the droplet containing $2\,\%$ wt lactose, with the initial liquid droplet shown to the left in the Figure at $t = 0\,\mathrm{s}$ and the final solid particle shown to the right at $t = 500\,\mathrm{s}$.
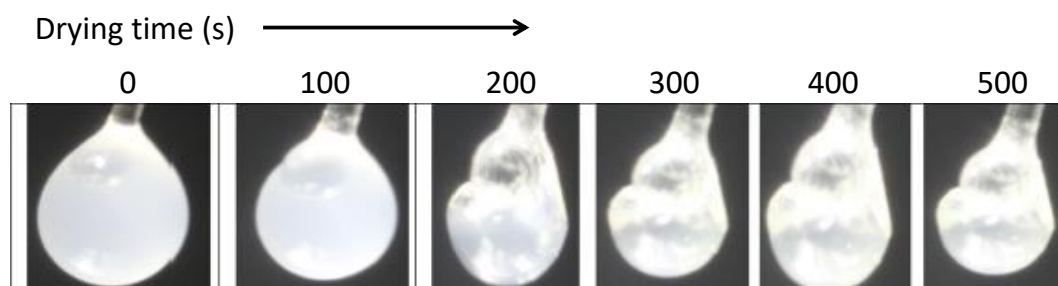
Figure 2.2 – Morphological evolution of the single droplet containing lactose and whey protein isolate (20:80), $10\,\%$ w/v total solids and dried with air at $80\,°\mathrm{C}$ in [62]. Adapted with permission from [62]

With such liquid formulations, it was expected to find experimental evidence of the formation of dense and hollow core particles under a narrow set of experimental conditions, which represents a starting point for the design of different solid structures in the present thesis. Naturally, it is possible to deepen the experimental analysis of such ternary mixtures as, for example, scarce data can be found about the drying kinetics of the mixture water/dextran/sucrose or modifications in the solid structure by altering the initial solute mass content and the air properties. Accordingly, it is possible to complement the data already present on the water/lactose/WPI system by following the approach developed in the present thesis.

2.2.3 Physicochemical properties of the chosen solutes

Considering the physicochemical properties of each solute in the model ternary systems, sucrose (Figure 2.3-A) is a disaccharide formed by a glucose and a fructose unit with chemical structure $C_{12}H_{22}O_{11}$ and molecular mass $342.297\,\mathrm{g\,mol^{-1}}$. This substance is frequently obtained from sugarcane as a white odorless crystalline solid. The water solubility, the density and the Stokes radius[2] of sucrose are presented in Table 2.1. These values were found in [33, 99].

---

[2]The Stokes radius is a rough estimation of the radius of a molecule considering it a hard sphere and dictated by the diffusion of this molecule in a medium, mainly water.
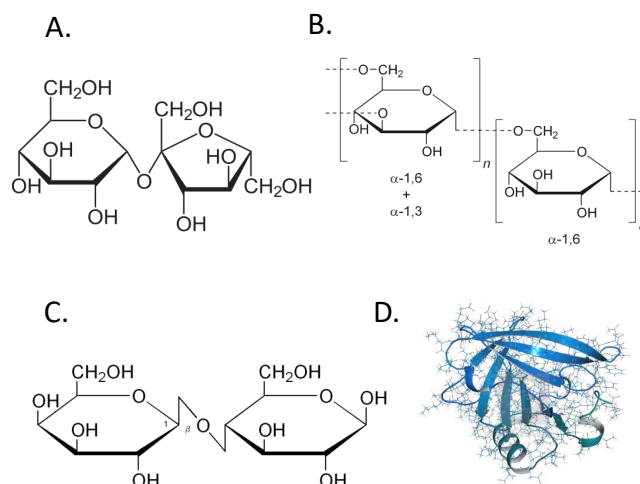
Figure 2.3 – Molecular structures of the compounds used in the present work: (A) Sucrose; (B) Dextran; (C) Lactose; (D) β-lactoglobulin, the main component of whey protein

Dextran (Figure 2.3-B) is a polymer of varying molecular weight produced from the fermentation of glucose ($C_6H_{12}O_6$). The structural aspect of such compound is that of a long chain of glucose units with scarce branches composed of one of two glucose molecules, distributed in a regular fashion. The branching degree of this polymer is around 5% [140]. The molecular mass of dextran depends on its size, or fraction, as the current nomenclature. Thus, it can be $1000\,\mathrm{g\,mol^{-1}}$ (denoted T1) up to $2\,000\,000\,\mathrm{g\,mol^{-1}}$ (T2000). In the present work, the fraction T40 was employed, as in the work from Elversson et al. [33]. For this fraction, the Stokes radius, the density and the solubility were found in [33, 140] and are presented Table 2.1.

Lactose (Figure 2.3-C) is a disaccharide formed by a galactose and a glucose unit and whose chemical structure is $C_{12}H_{22}O_{11}$ and consequently with the same molecular mass as sucrose. Lactose is the main sugar present in milk and can be bought as a white hard crystalline powder. The relatively low solubility, the density and Stokes radius were found in [33, 134] and are also given in Table 2.1.

Table 2.1 – Some physicochemical properties of the drying systems

Molecule	Water solubility ($\mathrm{g\,g^{-1}}$)	Density ($\mathrm{g\,cm^{-3}}$)	Stokes radius (nm)
Sucrose	0.67[a]	1.6	0.49
Dextran (T40)	0.50[a]	0.96	4.45
Lactose	0.20[a]	1.52	0.43
Whey protein isolate	0.20[b]	1.43	2.75

[a] at $25\,°\mathrm{C}$

[b] at $20\,°\mathrm{C}$

Whey protein is a mixture of proteins isolated from the liquid generated as a by-product in the cheese production. The main component in the whey protein is β-lactoglobulin (around 65% of the whey fraction) and is represented in Figure 2.3-D, followed by

α-lactalbumin (around 25 %) and bovine serum albumin. These three globular proteins will be treated as one single component in the studies developed further in this thesis. Depending on the processing conditions, whey protein might be commercially available in two main forms : whey protein concentrate (WPC) and whey protein isolate (WPI, the fraction employed in the present work). The difference in both fractions is the total amount of protein in the product, compared to the other by-products, such as lactose, minerals (calcium, magnesium, phosphorus, etc) and fat. For the WPC, the protein content stands between 50 and 75 %, while for WPI the protein content is superior to 95 %. One important characteristic regarding proteins is their structure. The native proteins present a 3-dimensional, globular structure that is maintained through thousands of noncovalent bonds between amino acids [89]. This native state can be disrupted by various external stresses, such as temperature, water removal, presence of metal ions and shear rate. The unfolding of such structure into a random, misfolded shape is called denaturation. Such a process is to be avoided since it has an impact in the protein biological activity, nutritional efficacy and other functional properties [27]. Whey proteins undergo irreversible heat denaturation at temperatures above 65 °C [61]. The degree of injury will depend on the exposure time to the thermal conditions. For instance, Haque et al. [61] stated that, upon 600 s of isothermal heating, 10.8 % of WPI was denaturated at 65 °C, against 90 % at 80 °C. Regarding other whey protein properties, the relatively low water solubility, the density and the Stokes radius were taken from [18] and are given in Table 2.1.

The chosen drying systems may be found in food and pharmaceutical applications. Whey protein is an important ingredient in formulated food products [130]. Naturally, the product originated from the drying of a liquid formulation containing only the protein would present some degree of protein denaturation, which would impact the solid properties and further applications. Thus, a protecting agent is added to the liquid formulation in order to generate a solid matrix for preserving the protein native structure. The most common agent is lactose [62]. This disaccharide may also be found in the pharmaceutical applications in compressed tablets and capsules for protecting active drugs [2]. Nevertheless, due to the fact that some people might be intolerant regarding the digestion of this compound, an alternative protecting agent is necessary. Sucrose may be used to replace lactose [2]. The main drawback for the use of sucrose comes from its low glass transition temperature (it can go from $T_g = 66.85\,°C$ in the anhydrous form to $T_g = 40.85\,°C$ with the addition of only 2 % wt of water and can be decreased to $T_g = 33.15\,°C$ with 4 % wt of water [39]). With such low glass transition temperature, the wet particles in the drying chamber can easily exceed the T_g before enough moisture is removed for the formation of a non-sticky solid structure. In other words, the particles produced then are sticky and may adhere to the drying chamber walls, reducing drastically the process yield. As a solution, a molecule with high molecular mass can be added to the liquid formulation for increasing the glass transition temperature. Accordingly, dextran, for example, whose anhydrous form presents a T_g around 220 °C [33], can be used in order to make the production of a dried powder become possible.

2.3 The lab-scale spray dryer

The experiments at the spray scale were carried out with a laboratory-scale spray dryer (B-290 advanced, Büchi, Switzerland), shown in Figure 2.4. Through a peristaltic pump,

the liquid feed is sent to the two-fluid nozzle for the atomization step (the contact between the liquid feed and the drying gas takes place inside the nozzle) with a dried air stream. In a cocurrent configuration, the spray of droplets are dried in the glass chamber and the generated powder is captured by a collecting vessel.
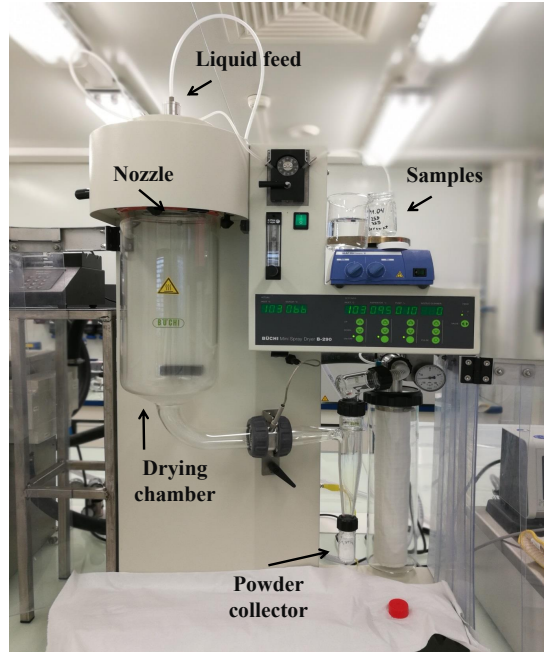

Figure 2.4 – Spray drying device employed in this chapter (Buchi B-290 advanced). From a two-fluid nozzle and the cocurrent configuration, the liquid samples are converted into powder material from the desired experimental conditions

The equipment characteristics are as follows,

- Inlet air temperature: may be varied up to $200\,°C$;

- Air flow rate: up to $35\,m^3\,h^{-1}$;

- Liquid feed rate: up to $30\,mL\,min^{-1}$

- Evaporating capacity : $1\,L\,h^{-1}$ of water;

- Nozzle tip diameter: $0.5\,mm$, $0.7\,mm$, $1.4\,mm$, $2.0\,mm$;

- Drying chamber dimensions: $33.0\,cm$ high and $15.0\,cm$ in diameter;

2.4 Experimental conditions

The experiments were planned expecting to modulate the structure of the solids generated from the two liquid systems. For doing so, the individual solute mass contents were varied in order to present an evolution of the influence of one solute over the other on the particle morphology. In that way, the experiments initiated at each pure solute in the liquid phase and converged into the ternary mixture with equal solute mass contents. So, on dry basis, the selected mass proportions are as follows,

- Lactose and WPI: 100-0, 80-20, 75-25, 50-50, 25-75, 20-80, 0-100;

- Dextran and Sucrose: 100-0, 83-16, 75-25, 50-50, 25-75, 16-83, 0-100;

Regarding the preparation of the solutions with the desired individual solute mass contents, dextran T40 (Alfa Aeser, Thermo Fisher, Germany) and sucrose (Merck, France) were stirred in demineralised water until complete dissolution.

For the second system, lactose (Alfa Aeser, Thermo Fisher, Germany) is first gravimetrically added to demineralised water and then stirred at 65 °C until complete dissolution. In that way, the time for preparing such solution reduces considerably. With the lactose dissolved in water, the solution is brought to ambient temperature before the addition of WPI (this product was kindly provided by Lactalis, France). Then, for dissolving the protein, the solution is kept at a very mild agitation (around 30 rpm) for 8 hours, in order to preserve the protein structure with a minimal addition of shear stress from the magnetic agitator. In Figure 2.5, it is possible to observe the visual aspect of the solution prepared under the described methodology. As can be seen, the solution presents a limpid aspect without the presence of foam, as may be formed from the denaturation of proteins [185].

Figure 2.5 – Visual aspect of the solution produced from the mixture between lactose and whey protein isolate

Regarding the drying conditions set at the lab-scale spray dryer for conducting the experiments, the inlet air temperature, the air flow, the liquid feed rate and the outlet air temperature are presented in Table 2.2. This set of drying conditions were employed for both chosen drying systems. A summary of the selected liquid formulations is presented in Table 2.3. It should be mentioned that for the ternary mixtures at 50-50, on a dry basis, the total solute mass content was varied in order to present the effect of different solute loads on the particle structure, for the same components mass proportion.

2.5 Characterization methods

In this section, the methods chosen for characterizing the powder material are presented. The main goal is to obtain from all the samples produced from the lab-scale spray-dryer

Table 2.2 – Drying conditions set in the lab-scale spray-dryer

Variable	Setpoint
Inlet air temperature (°C)	103
Air flow rate (m^3 h^{-1})	33.3
Liquid feed rate (mL h^{-1})	4
Outlet air temperature (°C)	70
Nozzle tip diameter (mm)	7

Table 2.3 – Summary of the different liquid formulations employed in this study

Variable	lactose-WPI system				dextran-sucrose system			
Solute mass proportion (% wt - dry basis)	100-0	80-20	75-25	50-50	100-0	83-16	75-25	50-50
Solute mass content (% wt)	20	20-5	15-5	5-5/10-10/ 13-13	20	25-5	15-5	2.5-2.5/5-5/ 10-10/15-15
Total solute content (% wt)	20	25	20	10/20/26	20	30	20	5/10/20/30

a direct observation of the external surface and the core aspects of the solid particles. For a few selected samples, other characterization techniques were employed in order to give an indirect assessment of the volume of occluded air within the particles and the crust porosity. Additional information is given regarding the distribution of particle size and the final moisture content present in the particles for the drying conditions used here.

2.5.1 Microscopy

The Scanning Electron Microscopy (SEM - ESEM FEG Philips, Holland) was employed for the visualization of the external surface and core aspects of the powder material. With this technique, a high-energy beam of electrons was directed to the sample. The signal resulting of the interaction electron-sample was collected by detectors to form the image. A better visualization was achieved when the sample is coated with a thin layer of metal. Since the SEM shows the sample surface, the particle had to be broken in order to see the interior of the powder material. This was accomplished by hitting the samples with a scalpel. The resultant material was placed on an adhesive carbon tape and sputter-coated with platinum. Next, the samples were placed in the SEM, which operated under vacuum. For the image acquisition, an acceleration voltage of 8 kV was used.

2.5.2 Pycnometry

Two different versions of the pycnometry analysis (i.e. gas pycnometry and liquid pycnometry) were combined in order to give an indirect estimation of the volume of occluded air in the particles.

In the gas pycnometry, the volume of the sample can be measured by first injecting an inert gas (here, helium is employed) into the measuring cell with known volume and then expanding the inert gas into a reference cell. The pressures observed upon filling the measuring cell and later the reference cell allow the calculation of the sample volume. The main advantage of employing helium as an inert gas here is related to its very small atomic radius, which is around $0.031\,\mathrm{nm}$. As a result, the helium atoms can diffuse through the solid structures of the particles composing the sample. Therefore, the true volume of the sample can be estimated as well as the particles true density, provided that the sample mass is known. For avoiding any interference in the pressure measurement, the powder is previously placed in an oven under vacuum for $48\,\mathrm{h}$ for eliminating any residual moisture. For the equipment protocol, a 1-cm^3 measurement cell is filled to two thirds with the powder material and placed in the pycnometer. The air is firstly purged with helium 25 times before performing a measurement with 25 cycles (each cycle is composed of a filling and a depressurizing step). The equipment shows then the average value between these cycles. The measure of the particle true density is carried out at least three times for each sample, in order to assure a repeatability of the given density.

The principle of the liquid pycnometry relies on the volume displacement (within a container with precise volume) caused by the addition of the powder material into an immiscible liquid. Firstly, the glass pycnometer, whose volume is equal to $10\,\mathrm{cm}^3$, is carefully filled with isopropanol (which is a molecule immiscible to the powder material produced here) up to the tip of the pycnometer stopper and the resulting mass is measured. Next, the pycnometer is cleaned up and approximately $2\,\mathrm{g}$ of the powder is added. After weighting the solid, the rest of the volume of the pycnometer is filled with isopropanol and the resulting powder/isopropanol mass is measured. Since the volume of the bottle is constant and known, these steps allow the calculation of the volume of the powder and thus the powder density. It should be noted that, unlike the previous gas pycnometry where the volume of the solid is measured, the liquid pycnometry gives an apparent powder density, due to the fact that the air entrapped in the solid particles also contribute to the volume of the sample. A schematic representation of the difference in these two pycnometry methods is shown in Figure 2.6.

Now, using the values of true (ρ_{true}) and apparent (ρ_{app}) densities for a given sample, it is possible to estimate the volume of air entrapped in the particles by using the notion of porosity (denoted Φ in Equation 2.1), which corresponds to the volume of "empty" spaces (V_{void}) in the material to the total volume of the material (V_{tot}),

$$\Phi = \frac{V_{\mathrm{void}}}{V_{\mathrm{tot}}} = \frac{V_{\mathrm{tot}} - V_{\mathrm{ds}}}{V_{\mathrm{tot}}} \tag{2.1}$$

where the subscript ds stands for dry solids. Equation 2.1 can be written as shown in Equation 2.2 by neglecting the mass of air in the particle crust,

$$\Phi = \frac{\frac{1}{\rho_{\mathrm{app}}} - \frac{1}{\rho_{\mathrm{true}}}}{\frac{1}{\rho_{\mathrm{app}}}} = \frac{\rho_{\mathrm{true}} - \rho_{\mathrm{app}}}{\rho_{\mathrm{true}}} \tag{2.2}$$
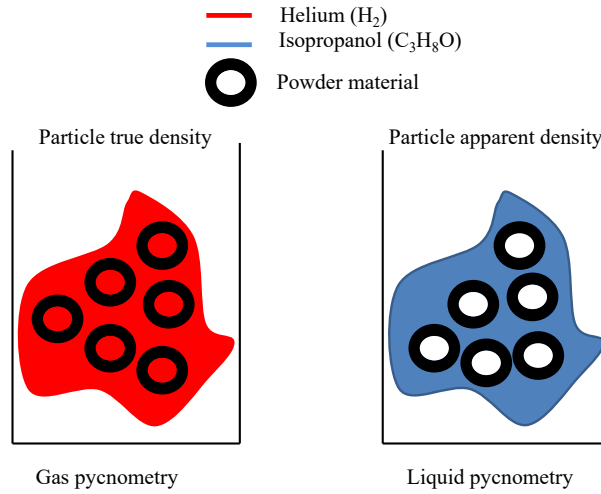
Figure 2.6 – Schematic representation of the gas and liquid pycnometry methods. In the gas pycnometry, the true sample density can be measured because the air inside the powder sample is replaced by the measuring gas. In the liquid pycnometry, on the other hand, the air entrapped inside the powder material is also considered in the density estimation

Finally, the volume of occluded air (V_{oa}) in the solid particles, by gram of powder material, can be derived from the porosity calculated in Equation 2.2,

$$V_{oa} = \Phi V_{tot} = \Phi \frac{1}{\rho_{app}} \qquad (2.3)$$

2.5.3 Specific surface area analysis

The basic principle related to this technique is the adsorption of gas molecules to the exposed surface of the sample, which depends on the temperature, the gas pressure and the strength of the interactions between the gas and the sample. As a matter of fact, the sample is firstly preconditioned to remove physically adsorbed impurities and to remove residual water from the sample surface (degassing step). Next, the gas molecules are injected at an increasing pressure in the chamber containing the sample (a relative pressure is often used in the analysis). As the gas pressure increases, so does the quantity of adsorbed gas at the sample surface, until a first monolayer is formed (the surface of the solid is completely covered by a layer with a width of one gas molecule). Additional molecules are adsorbed to the sample surface (multilayer formation) as the pressure increases, until all the pores (if any) are filled and any further increase in the gas pressure will not increase the quantity of adsorbed gas. The quantity of adsorbed gas and later the calculation of the surface area is accomplished with the BET (Brunauer, Emmett and Teller) theory, which takes into account the quantity of adsorbed gas when the monolayer is formed and the pressure of the gas. The specific area is found by dividing the surface area to the sample mass. Here, the specific surface area is analyzed with a Tristar II 3020 (Micromeritics, U.S.A.) with nitrogen (due to its availability as a pure gas and strong interaction with most solids) at its boiling temperature, 77 K, in

order to increase the interactions between the solid and the gas molecules. The sample is firstly degassed at 40 °C during 1 h (at 10^{-6} bar), and then at 50 °C during 20 h before the beginning of the analysis. The results are given for a relative pressure between 0.1 and 0.3, which covers the domain of validity of the BET equation.

2.5.4 Final moisture content analysis

For the measure of the powder final moisture content, the sample is put into an oven functioning under vacuum at 30 °C for 48 h. The weight of the sample is measured before and after the use of the oven with the help of a balance (Sartorius 221S, Goettingen, Germany) with a precision of 0.1 mg.

2.5.5 Laser diffractometry

Finally, the last characterization technique used for this chapter is the laser diffraction analysis (Malvern Spraytec with Helium-Neon laser, Malvern Instruments Ltd., Malvern, UK), which allows the assessment of a distribution of particle size. In order to do so, the particles are firstly dispersed into a gas or a liquid phase. Then, a laser beam is directed to the dispersed solid particles and the intensity and the angle of the light reflected by the particles as they pass through the beam is captured by a sensor. Light is reflected at a smaller angle and at a higher intensity the smaller the particles. The relation between the reflected light angle and the particle size is calculated using the Mie theory. Before the analysis, the particles were dispersed in isopropanol and then placed in a ultrasonic bath (with a frequency of 35 kHz) for helping disrupting any eventual particle agglomerates. The particle size distribution is represented by three percentages (10, 50 and 90) of particles having at most a given diameter. A mean diameter (d4.3), on a volume basis, is also calculated.

2.6 Results

2.6.1 Particle morphology

In the following discussion, the SEM images of the spray-dried particles produced from the liquid ternary systems are organized in two ways to show:

- firstly, the effect of changing each solute mass content on the particle morphology;

- and thus, the effect of the total solute content on the particle morphology.

Lactose-whey protein isolate

Figure 2.7 shows SEM images of lactose-WPI spray-dried particles obtained from aqueous solutions containing different mass proportions of lactose and WPI.

For a droplet containing only lactose or WPI (Figures 2.7-A and 2.7-D, respectively), the spray-dried particles presented a fairly smooth surface. The particles produced from WPI were easily broken, which allowed the observation of a hollow core. However, in the case of lactose, the interior of the spray-dried particles were not shown in Figure 2.7 because it was not possible to break them with the scalpel. It is interesting to note here

(A) 20L

(D) 20WPI

(B) 20L -5WPI

(E) 5L -20WPI

(C) 15L -5WPI

(F) 5L -15WPI
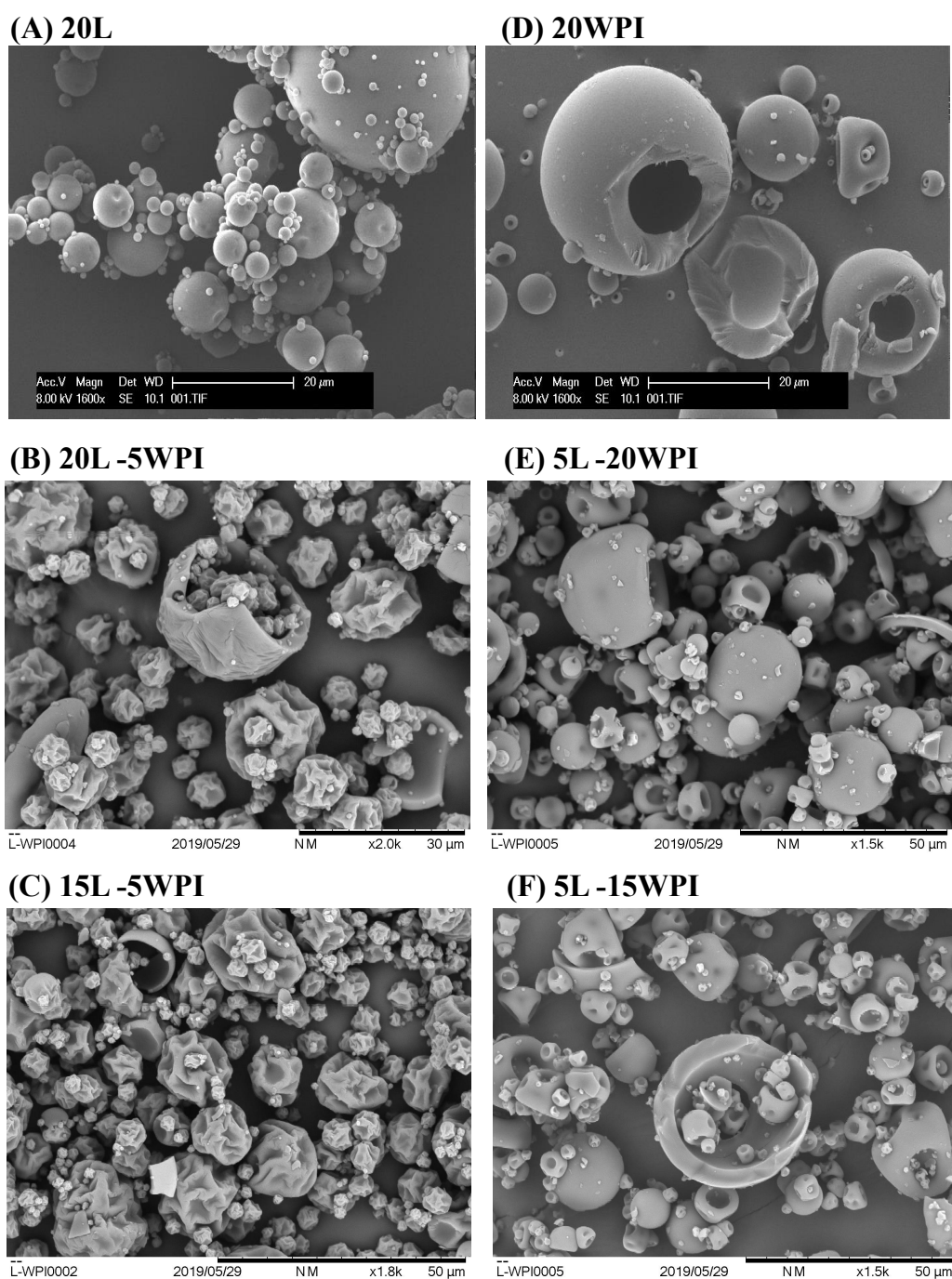
Figure 2.7 − Evolution of the particle morphology by varying the proportion between lactose and WPI in the liquid formulation. The images in the left represent the particles with higher concentration of lactose. The images in the right display the particles with higher whey protein isolate concentrations. The mass content (% wt) between the two solutes in the initial liquid formulation are as follows: (A) Pure lactose (L); (B) 20L-5WPI; (C) 15L-5WPI; (D) Pure WPI; (E) 5L-20WPI; (F) 5L-15WPI

that spray-dried particles with hollow cores were produced in [33] under similar lactose concentration and nozzle diameter, with a higher air inlet temperature.

The ternary lactose-WPI-water mixture resulted in wrinkled spray-dried particles with a hollow core. When lactose is the component in majority (20L-5WPI and 15L-5WPI, in Figures 2.7-B and 2.7-C, respectively), the particle surface presented a higher folding degree than the particles produced when WPI was the component in majority (5L-20WPI and 5L-15WPI in Figures 2.7-E and 2.7-F, respectively). The presence of the folding on the particles produced from the lactose-WPI mixture suggests changes on the mechanical properties of the solid structure composed by the ternary blend, compared to those produced from the pure components, lactose or WPI.

It is also interesting to note in Figure 2.7 the presence of particles with different sizes within the same sample, irrespective of the mass proportion between the solutes. For the mixture 20L-5WPI (Figure 2.7-B), the wrinkled aspect was not influenced by the size of the particle. However, with a higher WPI mass proportion, as in 5L-20WP (Figure 2.7-E), the bigger particles presented a smoother surface while the smaller particles showed big dimples. This difference can be related to the compressive pressure experienced by the droplet during drying. This parameter is inversely proportional to the diameter of the droplet, so it can be assumed that the pressure exerted on the developing particle crust is higher with the smaller droplets, which leads to the deformation of the crust.

Regarding now the effect of the total solute content, it can be seen in Fig 2.8 that the morphology was not modified for 50-50 (on dry basis) spray-dried lactose-WPI particles produced from solutions containing different total solute contents (from 10 to 26 % wt). All the particles presented a wrinkled surface with a hollow core. A quantitative analysis of the effect of the total solute mass content in the initial solutions is shown later in this chapter from the results of other analyses (laser diffraction analysis and pycnometry).

Dextran-sucrose

For the experiments with dextran (D) and sucrose (S) in solution, trials were not performed with sucrose alone or 20D-80S (on dry basis). This was due to the difficulty in spray-drying this compound, as stated in [156], which is related to the low glass transition temperature of sucrose (at 66.85 °C in the anhydrous form [39]) and thus the production of sticky particles. In that way, the morphology of pure spray-dried sucrose presented in Figure 2.9-D arose from the work of Shakiba et al. (the particles were generated with an air inlet temperature at 110 °C). For the sample 20D-80S (on dry basis), the particles presented in Figure 2.9-E were obtained in the work from Elversson et al. [33], with an air inlet temperature at 200 °C. The mass content used in the formulation was not clear.

Starting from an analysis on the left-hand column in Figure 2.9, it can be seen that dextran particles (Figure 2.9-A) presented a wrinkled surface, which still prevailed in the spray-dried particles obtained from dextran-sucrose mixtures even decreasing the dextran-to-sucrose ratio from 5 (25D-5S, Figure 2.9-B) and then to 3 (15D-5S, Figure 2.9-C) in the ternary mixture.

Now observing the right-hand column in Figure 2.9, the 5D-15S spray-dried particles produced in this work presented a smooth surface, very similar to those found in the
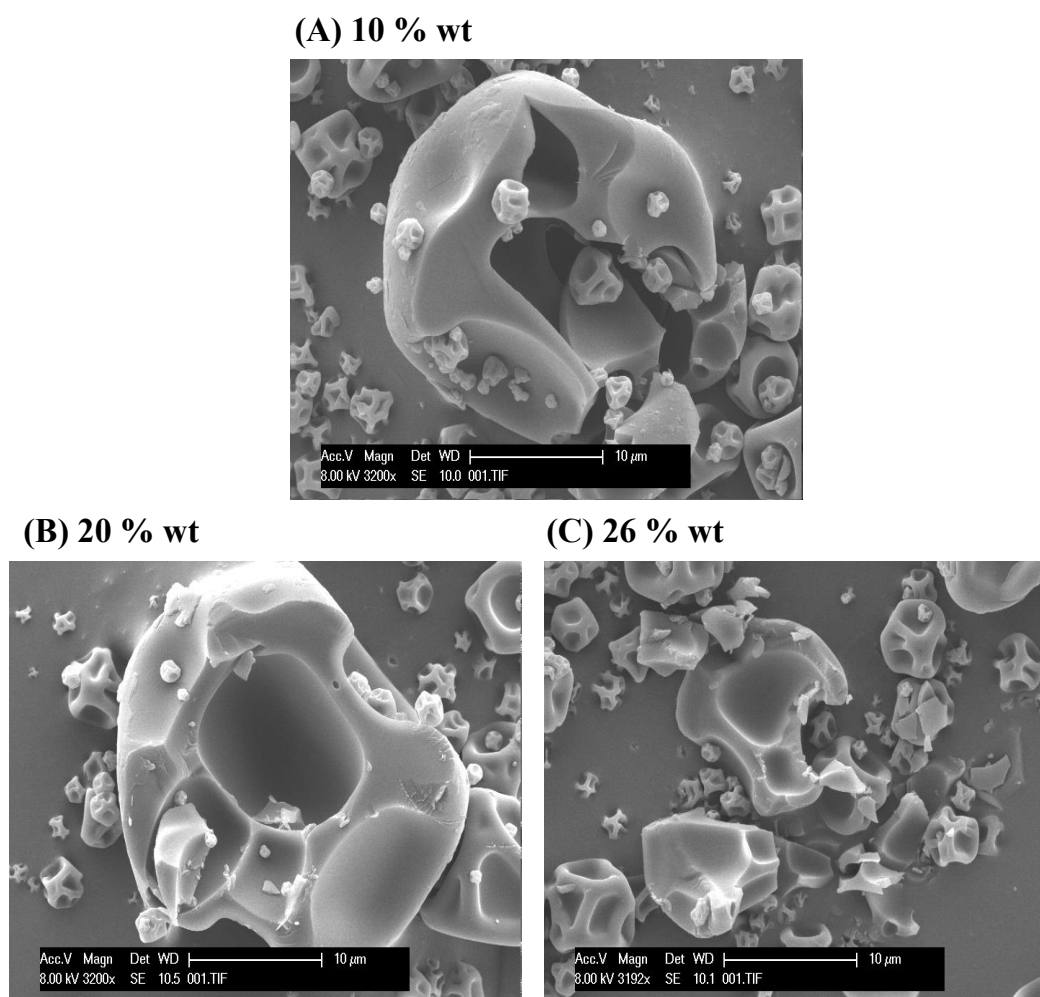
(A) 10 % wt

(B) 20 % wt

(C) 26 % wt

Figure 2.8 – SEM micrographs obtained from 50:50 (on dry basis) spray-dried lactose-WPI particles produced from solutions with different total solute contents. From left to right: (A) 10 % wt; (B) 20 % wt; (C) 26 % wt

literature for spray-dried sucrose (Figure 2.9-D) and for spray-dried particles generated from a sucrose-dextran solution containing 20D-80S (on dry basis) (Figure 2.9-E).

In short, this SEM image analysis shows that, in the case of the aqueous solution containing a dextran-sucrose mixture of solutes, the spray-dried particles combines the surface aspect of both solutes dried as pure components, where the final surface aspect depends on the mass proportion of the solutes employed.

Regarding the effect of the total solute content in dextran-sucrose solutions, it can be seen in Figure 2.10 that the morphology was not modified for 50-50 spray-dried dextran-sucrose particles produced from solutions containing different total solute contents (from 5 % to 30 % wt). All the particles presented light dimples on the surface, with again no important difference in the morphology obtained from these trials.

It is also interesting to note the dextran-sucrose solutions produced polydispersed particles in size, but with no apparent influence on the particle morphology related to the particle size.

(A) 20D

(B) 25D -5S

(C) 15D-5S

(D) 10S (from the literature)

(E) 20D-80S (dry basis - from the literature)

(F) 5D-15S
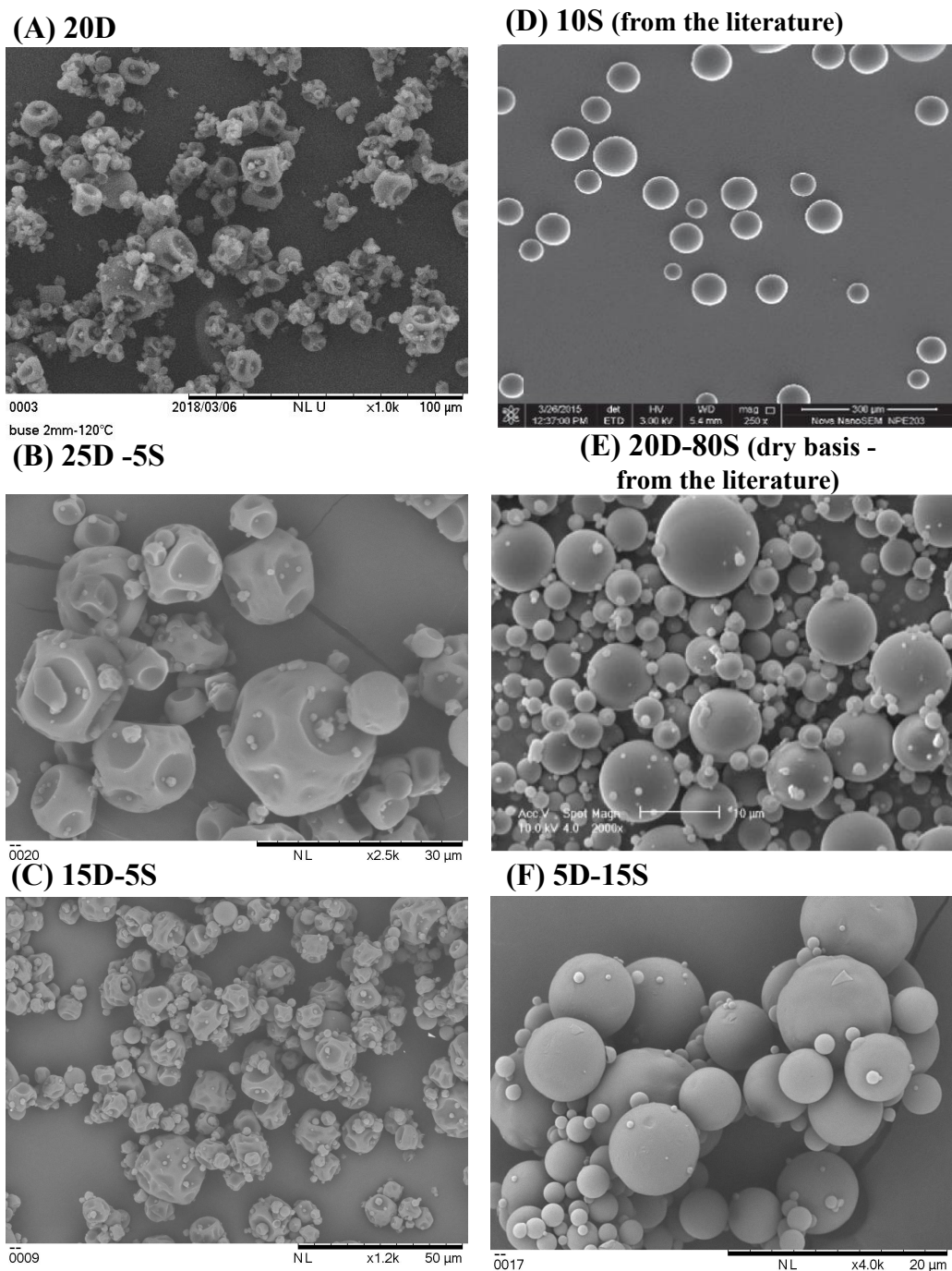
Figure 2.9 – SEM images of spray-dried particles generated from initial solutions containing different mass proportions between sucrose and dextran. For the images in the left, dextran is in majority. For the images in the right, sucrose is in majority. Mass proportion in the solution are as follows: (A) Pure dextran; (B) 25D-5S; (C) 15D-5S; (D) Pure sucrose, from [156]; (E) 20D-80S (on dry basis), from [33]; (F) 5D15S. (D) and (E) were reprinted with permission from [156] and [33], respectively

(A) 5 % wt
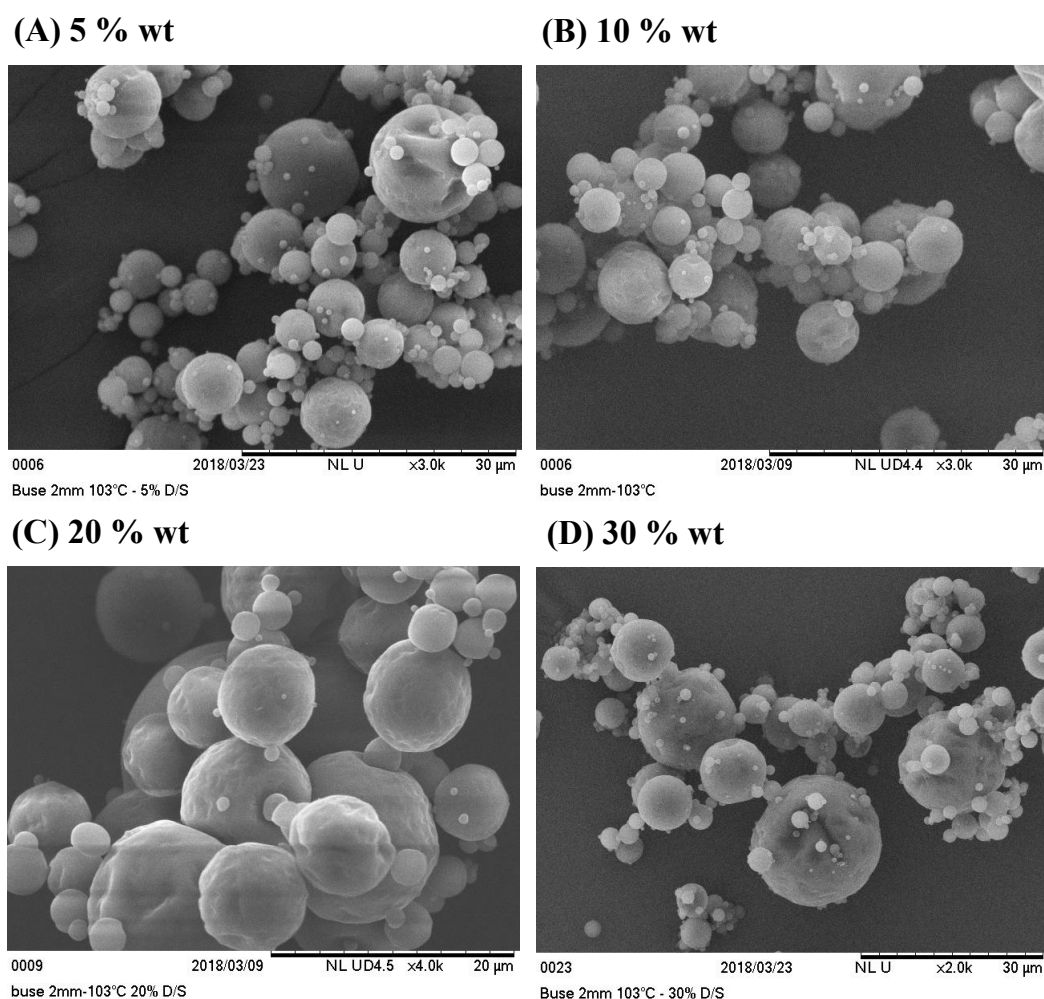
(B) 10 % wt

(C) 20 % wt

(D) 30 % wt

Figure 2.10 – SEM micrographs obtained from 50-50 spray-dried dextran-sucrose particles produced from solutions with different solute contents. From left to right: (A) 5 % wt; (B) 10 % wt; (C) 20 % wt; (D) 30 % wt

2.6.2 Volume of occluded air

Gas and liquid pycnometry analyses were performed on the proportion 50-50 (on dry basis) for lactose-WPI and dextran-sucrose spray-dried particles. The samples produced from the solutions with different total solute contents (10 %, 20 % and 26 % wt for lactose-WPI and 5 %, 10 %, 20 % and 30 % wt for dextran-sucrose) were analyzed. The intent of such analyses was to put in evidence the volume of occluded air in the particles in order to obtain an indicator on the formation of particles with dense or hollow cores.

Table 2.4 provides the measured values of apparent and true densities, the porosity (Φ, Equation 2.2) and the calculated volume of occluded air in the spray-dried particles (V_{oa}, Equation 2.3). For the lactose-WPI system, a neat difference between the apparent particle density (ρ_{app}) and the true density (ρ_{true}) was found. For the dextran-sucrose system, on the other hand, the difference between the apparent and true densities was found to be very low.

Table 2.4 – Pycnometry measurements with the proportion 50-50 (on dry basis) for lactose-WPI and dextran-sucrose spray-dried particles

Drying system	Total solute content in the initial solution (% wt)	Apparent density (g cm^{-3})	True density (g cm^{-3})	Porosity (-)	Volume of occluded air (cm^3 g^{-1})
Lactose-WPI	10.0	0.81 ± 0.01	1.37 ± 0.001	0.41	0.50
	20	0.88 ± 0.01	1.30 ± 0.001	0.32	0.36
	26.0	0.92 ± 0.01	1.25 ± 0.001	0.26	0.28
Dextran-Sucrose	5.0	1.45 ± 0.01	1.56 ± 0.001	0.07	0.05
	10.0	1.54 ± 0.01	1.58 ± 0.001	0.02	0.01
	20.0	1.45 ± 0.01	1.54 ± 0.001	0.06	0.04
	30.0	1.46 ± 0.01	1.47 ± 0.002	0.01	0.01

For the sake of visualization, the difference between the apparent and true densities was translated in terms of volume of occluded air per gram of powder. As a result, the calculated volume of occluded air for the lactose-WPI system is ten times higher than that of the dextran-sucrose system. The difference in the volume of occluded air values from Table 2.4 is better visualized in Figure 2.11 on a logarithmic scale.
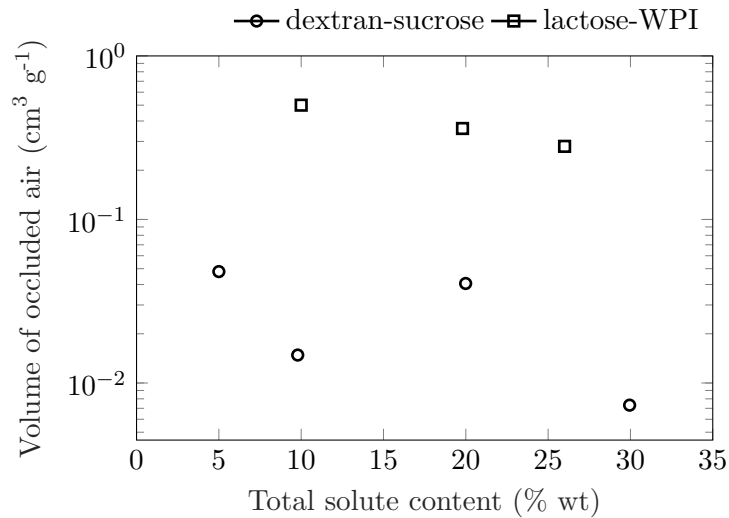
Figure 2.11 – Evolution of the volume of occluded air (log scale) with the proportion 50-50 (on dry basis) for lactose-WPI and dextran-sucrose spray-dried particles generated from aqueous solutions containing different total solute contents.

Since a small number of total solute contents were tested, no clear relation can be drawn for the evolution of the volume of occluded air with the total solute content within the same drying system.

It is also possible to find in the literature examples of the effect of the different liquid formulations on the volume of occluded air in the particles for example for the lactose-WPI model system studied here. The values of V_{oa} found in [166, 172] have fallen in the range 0.3-0.7 cm^3 g^{-1}, similar in magnitude to those obtained in this thesis.

Knowing from the SEM analysis that the lactose-WPI spray-dried particles presented a hollow core, it is possible to presume that the dextran-sucrose system has generated in this study particles with dense core.

2.6.3 Particle size distribution

The laser diffraction analyses were performed to give an order of magnitude of the size of the particles produced at the spray scale and to indicate an eventual impact of the total solute content on the spray-dried particle size. The characteristic diameters are presented in Table 2.5 in volume fractions. The particle size distribution is represented by three percentages of particles having at most the indicated diameters (apart from the d-4.3, which is a volumetric mean diameter). The value span giving an idea of the distribution width is calculated as follows,

$$span = \frac{d_{90} - d_{10}}{d_{50}} \qquad (2.4)$$

Table 2.5 − Particle size measurements from laser diffraction with the proportion 50-50 (on dry basis) for lactose-WPI and dextran-sucrose spray-dried particles

Drying system	Total solid content (% wt)	d-4.3 (µm)	d-10 (µm)	d-50 (µm)	d-90 (µm)	span
Lactose-WPI	10.0	9.1	2.6	8.9	15.4	1.43
	20	10.5	2.8	10.3	17.9	1.47
	26.0	12.3	2.6	12.1	21.8	1.59
Dextran-Sucrose	5.0	8.9	1.7	8.1	16.8	1.86
	10.0	8.1	1.7	8.0	14.3	1.58
	20.0	10.4	2.0	10.2	18.5	1.62
	30.0	9.6	2.1	9.4	16.8	1.56

For the lactose-WPI system, the fine fraction, which corresponds to the d-10 values, gives the same particle size for all three trials tested. For the d-50 values, a slight increase can be found with increasing the total solute content. This tendency is also found in the d-90 values. Droplets possessing a higher solids content will have their diameter locked sooner in the drying process than the more diluted droplets. This is due to the time required for attaining a saturation concentration, which is shorter for the more concentrated droplets. However, the results given in Table 2.5 show that only a small difference in the external diameter could be found. The values of span are very close for all particles. The particle size distributions for the lactose-WPI trials are presented in the top graph in the Figure 2.12.

Regarding the dextran-sucrose system, the fine particle fraction (d-10) remains constant throughout the four trials performed. By regarding the values given by the d-50 and d-90, no clear tendency of increase was identified. The difference between the particle diameter with increasing total solute content is even smaller than that found in the lactose-WPI system. The four trials are represented in the middle graph from Figure 2.12.

Also, in Figure 2.12, the particle size distribution is plotted for the trials at 20 % wt total solute content for both drying systems. The measured particle size diameter are similar.
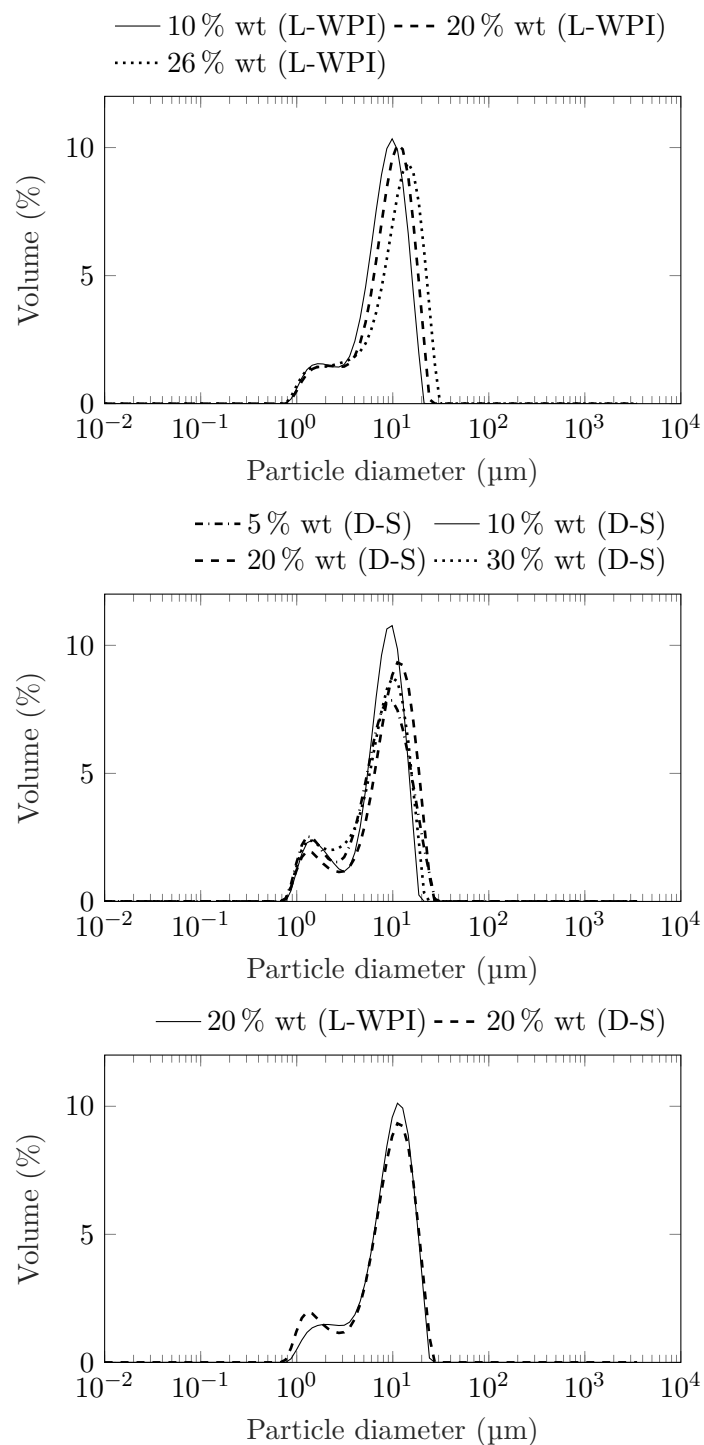
Figure 2.12 – Volumetric distribution with the proportion 50-50 (on dry basis) for both drying systems. From top to bottom: lactose-WPI particles with total solute contents from 10 to 30 % wt; Dextran-sucrose particles with total solute contents from 5 to 30 % wt; Comparison between the particle volumetric distribution between the two systems at 20 % wt

2.6.4 Specific area

The evaluation of the specific area of a powder using BET was performed to give an indirect indication about the particle porosity. This analysis can be used to identify the presence of micropores (pore diameter inferior to $2\,\mathrm{nm}$) or mesopores (pore diameter between $2\,\mathrm{nm}$ and $50\,\mathrm{nm}$). BET measurement was performed with the proportion 50-50 (on dry basis) spray-dried lactose-WPI particles produced from a total solute content of $10\,\%$ wt. The volume of adsorbed nitrogen in the relative pressure range of 0.1 and 0.3 increased up to $0.5\,\mathrm{cm}^3\,\mathrm{g}^{-1}$. The specific area given by the BET equation was $3.17\,\mathrm{m}^2\,\mathrm{g}^{-1}$ (the BET constant C was equal to 36.24). A sample presenting microporous structure would give a specific area one or two orders of magnitude higher [6] than the one found for the lactose-WPI powder. It is also possible to observe, in the SEM micrographs presented previously, that the particles generated from lactose-WPI present a rather compact structure, with no clear signs of a porous structure. Because of the low specific surface area value given above, this technique was not employed for other samples.

2.6.5 Final moisture content

The discussion of the final moisture content in the powder is given hereafter with the proportion 50-50 spray-dried lactose-WPI powder obtained from solutions with $10\,\%$, $20\,\%$ and $26\,\%$ wt of total solute content. The results are presented in Table 2.6. The moisture content is calculated by the ratio [water loss / mass of dry solids], which corresponds to the mass obtained after drying the sample in the oven to remove the residual water.

Table 2.6 – Moisture content from the lactose-WPI with different total solute content and the same initial solute proportion

Total solute content (% wt)	Mass of powder before oven (g)	Mass of powder after oven (g)	Water loss (g)	Moisture content ($\mathrm{g\,g}^{-1}$)
10	2.0065	1.8742	0.132	0.071
20	2.2480	2.1709	0.0771	0.036
26	3.5218	3.4258	0.096	0.028

Table 2.6 shows an amount of residual water with the proportion 50-50 spray-dried lactose-WPI particles was in the range $0.028\,\mathrm{g\,g}^{-1}$ to $0.071\,\mathrm{g\,g}^{-1}$, depending on the solute concentration in the initial solution. Considering that the residence time of the droplet/wet particles and the drying conditions are the same, the droplets presenting the highest initial moisture content (the trial at $10\,^\circ\mathrm{C}$) will accordingly present the highest moisture content in the final particles.

2.7 Summary of the main findings of the chapter

In this chapter, the experimental work is carried out at the spray scale with two drying systems, dextran-sucrose and lactose-WPI aqueous solutions. Using different

solution compositions (mass proportion between constituents) and total solute contents, variations in the solid structures were expected. Different techniques were employed to evaluate physical characteristics of the spray-dried particles (particle size, density, porosity, volume of occluded air, moisture content, morphological aspects).

Regarding the particle size distribution, no important difference between the two drying systems could be observed. Also, a modification in the total solute content in both solutions did not really impact the final size of the particles. Regarding the final moisture content, the droplets presenting the highest initial moisture content also generated solid particles with high moisture content.

Now, in relation to the particle morphology, the different liquid formulations employed here provided an interesting picture of the possible particle morphologies for both dextran-sucrose and lactose-WPI systems. For the lactose-WPI system, the particles presented a wrinkled or smooth surface depending on the mass proportion between lactose and WPI in the initial solution. The presence of a hollow core could be observed for this system with the help of SEM images. In the dextran-sucrose system, the surface aspect could also be modified between wrinkled or smooth depending on the mass proportion between dextran and sucrose in the initial solution. Regarding the interior of the dextran-sucrose particles, the presence of a dense core could be assumed based on the values of the volume of occluded air. As a matter of fact, the volume of occluded air in the dextran-sucrose system was ten times lower than the one in the lactose-WPI system (hollow core particles).

Despite the findings presented above, it was not possible to follow the drying process and the formation of the solids in the spray of droplets. The investigation of such phenomena has to be accomplished at the droplet scale. Consequently, the focus of the subsequent chapters is the tracking of the multi-component droplets drying process with two set-ups of drying droplets. The particle morphologies identified in this chapter for both drying systems will serve as a link, a means of comparison between the solids generated at the spray and at the droplet scales.

Single droplet drying with a glass filament

In this chapter, the work carried out at the droplet scale is presented. Thus, it starts with the presentation of the design of an experimental apparatus for drying a single droplet, as this step covers an important role in the present thesis. After the creation of an experimental strategy, a step is performed for ensuring the reliability of the drying data obtained from the proposed set-up. Then, the drying systems presented in the previous chapter are dried under different experimental conditions. The droplet morphological changes assessed from the camera are used as a complement to the mass data obtained from the weighing balance to help describing the phenomenon of drying of a single droplet, with an emphasis on the period of the solid crust formation.

3.1 Motivation

As described previously, the experimental methods developed at the droplet scale can provide experimental evidence of the transformation of the liquid droplet into a solid particle. Also, the evolution of the droplet characteristics, such as mass or temperature, can be obtained as well. The assessment of these data contributes to a better understanding of the process of particle formation occurring in the spray drying process. In order to study the drying of the droplet, an experimental set-up has to be used to hold the droplet in place, as shown in Section 1.3.2. For the present thesis, the choice of the set-up was based particularly upon the direct acquisition of the droplet mass evolution. The non-invasive methods presented in Section 1.3.2 (chain of droplets, aerodynamic levitation and acoustic levitation) give an indirect measure of the droplet mass loss through the variations in the droplet diameter, considering that the evaporation rate is proportional to the reduction in volume of the spherical droplet. However, this method is no longer suitable once the wet particle diameter is locked, so the small evaporation rate towards the end of the drying process cannot be computed anymore. Likewise, a deviation from the spherical shape due to the surface buckling phenomena can also lead to errors in the mass loss evaluation through the diameter-based method. In that way, the choice of the set-up rested upon the

hydrophobic method and the thin-filament method. For the latter, the contact area between the droplet and the intrusive material is presumably smaller compared with the hydrophobic surface method, which could interfere to a lesser degree to the drying of the droplet. Also, with the thin filament method, it is possible to initiate the drying process with a spherical droplet, similar to the droplet shape at the spray scale. Thus, the thin filament method was chosen for holding the droplet in place. Besides the mass acquisition, recording the droplet surface aspect with a camera should also be possible with the developed set-up.

3.2 The droplet-suspension set-up

This section is dedicated to the presentation of the different parts composing the set-up designed during this thesis and also a summary of the range of operation of the set-up. Firstly, the set-up proposed here should allow the measurement of the drying kinetics of a droplet suspended at the tip of a thin filament under well controlled drying conditions. The control of the air properties for the drying kinetics, such as temperature, absolute humidity and velocity, are achieved through different zones in the set-up. A schematic representation of the set-up developed here is presented in Figure 3.1 (the details are shown in Section 3.2.1). With such apparatus, it is possible to control the absolute humidity of the air stream between $0.03\,\mathrm{g\,kg^{-1}}$ and $10\,\mathrm{g\,kg^{-1}}$ by mixing a dry air stream (whose absolute humidity value corresponds to the lower limit of the range presented here) and an air stream saturated in water vapor (at $20\,^{\circ}\mathrm{C}$, this corresponds to $14.7\,\mathrm{g\,kg^{-1}}$). The velocity of the air stream in the wind tunnel may be varied between $0.06\,\mathrm{m\,s^{-1}}$ and $0.5\,\mathrm{m\,s^{-1}}$. This velocity range corresponds to a dry air volumetric flow rate between $4\,\mathrm{L\,min^{-1}}$ and $48\,\mathrm{L\,min^{-1}}$, at standard conditions, and the control of this dry air flow rate is achieved with two mass flow meters (which are also used for the control of the air absolute humidity). The air stream temperature may be varied between $20\,^{\circ}\mathrm{C}$ and $140\,^{\circ}\mathrm{C}$ with the help of a heating element. Also, the set-up should provide information related to the evolving aspect of the sample surface and allow the assessment of the sample diameter over time. Thus, a camera is placed in front of the droplet-suspension zone for the image acquisition.

3.2.1 Set-up designing

Dehydration column

The first element of the set-up is presented in Figure 3.1-a, which corresponds to a dehydration column and a pressure regulator. As a matter of fact, the compressed air stream (at $4\,bar$) used here possesses a low level of water vapor (in terms of absolute humidity, this represents $1.4\,\mathrm{g\,kg^{-1}}$), which should be removed for the next steps regarding the control of the air absolute humidity. As a result, a column filled with silica gel (silicon hydroxide, $\mathrm{Si(OH)_4}$) is used for removing the residual humidity of the compressed air stream. Regarding the design of such dehydration column, the required mass of silica gel had to be calculated for removing the moisture content of the compressed air stream over a duration of $6\,\mathrm{h}$ (estimated time of the daily operation of the set-up). The maximum quantity of water adsorbed to the silica gel is found with the help of a sorption isotherm, where the relative humidity of the air stream is plotted against the equilibrium water mass adsorbed to the silica gel. With this adsorbed mass
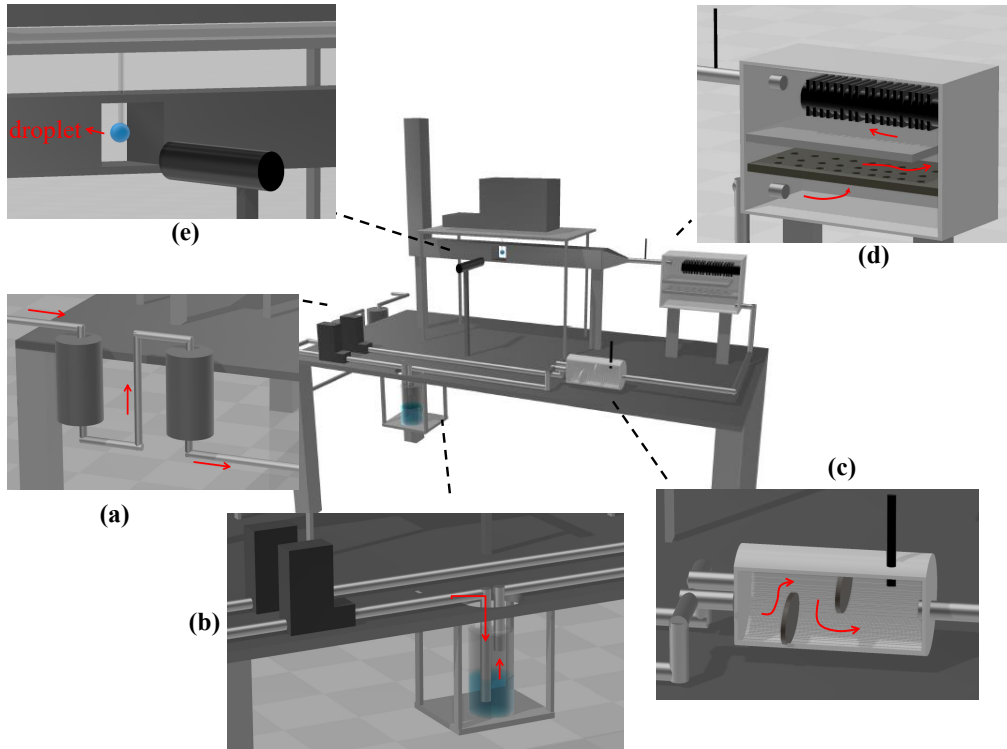
Figure 3.1 – Schematic representation of the set-up developed in the present work for drying a single droplet suspended by a filament. Set-up parts presented counterclockwise: (a) a column filled with silica gel and a pressure regulator; (b) two mass flow meters (in black) and a glass column with distilled water; (c) a chamber for mixing the dry and saturated air flows; (d) air heating section by the heating element; (e) droplet suspended at the tip of a thin filament and a camera placed in front of it. The red arrows indicate the sense of the air flow

value and the mass of water vapor in the air stream over 6 h, the minimum mass of silica gel required for the dehydration step corresponds to 95 g. In order to assure a longer autonomy of the column, 200 g of silica gel were used. After exiting the dehydration column, the compressed air passes through a pressure regulator for a decrease in pressure to 2 *bar*.

Air flow

The next step regards the control over the air flow (Figure 3.1-b), which is important for a modification in the air stream velocity in the wind tunnel, but also for the air stream absolute humidity. After exiting the pressure regulator, the air stream may follow two paths: one where the dry air stream stays at approximately no water vapor content (the air absolute humidity is $0.03 \, \mathrm{g \, kg^{-1}}$) and another where the air stream is injected as bubbles into a column filled with distilled water for saturating the air with water vapor (the details of the humidification column are given in the next step). For both cases, a mass flow meter (model SLA5860, Serv' Instrumentation, Ivigny, France) assures the desired air flow passing into each of these paths.

The choice of the air flow range used in the set-up was a result of an iterative process between the desired air velocity range in the drying zone with the respective cross-sectional area and the flow range measured by the mass flow meters. The idea was to provide an ample range of air velocities for the drying experiments. The design converged to a wind tunnel with cross-sectional area equal to $4\,\text{cm}\times4\,\text{cm}$ and measurable air velocity going from $0.5\,\text{m}\,\text{s}^{-1}$ to a minimum of $0.06\,\text{m}\,\text{s}^{-1}$. This corresponds to a dry air volumetric flow ranging between $48\,\text{L}\,\text{min}^{-1}$ to $4\,\text{L}\,\text{min}^{-1}$, respectively. As a consequence, this air flow range could be measured by a mass flow meter operating from $0.003\,\text{L}\,\text{min}^{-1}$ to $50\,\text{L}\,\text{min}^{-1}$. Otherwise, an increase in the air velocity over $0.5\,\text{m}\,\text{s}^{-1}$ would require another model of mass flow meter not adapted for air flows smaller than $15\,\text{L}\,\text{min}^{-1}$ (which corresponds to approximately $0.2\,\text{m}\,\text{s}^{-1}$ in the wind tunnel).

The control over the mass flow is done with the desired values of temperature, absolute humidity and velocity of the air in the wind tunnel. The setpoint for the humid mass flow in the wind tunnel is calculated as follows,

$$\dot{m}_{\text{ha}}^{\text{sp}} = u^{\text{sp}} A \rho_{\text{ha}}^{\text{sp}}(Y^{\text{sp}}, T^{\text{sp}}) \tag{3.1}$$

Where the superscript sp corresponds to the setpoint, the subscript *ha* stands for the humid air, $\dot{m}$ stands for the mass flow, u the velocity, A the cross-sectional area and ρ the air density, which depends on the absolute humidity and temperature. The humid air flow arriving at the wind tunnel is a result of the summation of the air streams crossing the paths presented in Figure 3.1-b and can be written as shown in Equation 3.2 (where 1 and 2 correspond to the dry air stream and the saturated air stream leaving the humidification column, respectively)

$$\begin{aligned}\dot{m}_{\text{ha}}^{\text{sp}} &= \dot{m}_{\text{da},1}^{\text{sp}} + \dot{m}_{\text{ha},2}^{\text{sp}} \\ &= \dot{m}_{\text{da},1}^{\text{sp}} + \dot{m}_{\text{da},2}^{\text{sp}} + \dot{m}_{\text{da},2}^{\text{sp}} Y^{\text{sat}}\end{aligned} \tag{3.2}$$

The subscript *da* stands for the dry air. In Equation 3.2, the mass flow of humid air leaving the humidification column (stream 2) is written in terms of its dry air and water vapor fractions. The mass flow of water vapor can be calculated with the help of the absolute humidity (since it represents a mass of water vapor per mass of dry air). Here, Y^{sat} corresponds to the absolute humidity at saturation, attained with the help of the humidification column.

After performing a mass balance over the dry air and the humid air streams, and considering the setpoint for the absolute humidity in the wind tunnel, the setpoints given to the mass flow meters (for the streams 1 and 2) can be written as shown in Equations 3.3 and 3.4. These equations are easily written as a function of the dry air flow thanks to the dehydration step.

$$\dot{m}_{\text{da},1}^{\text{sp}} = \frac{\dot{m}_{\text{ha}}^{\text{sp}}(Y^{\text{sat}} - Y^{\text{sp}})}{Y^{\text{sat}}(1 + Y^{\text{sp}})} \tag{3.3}$$

And,

$$\dot{m}_{\text{da},2}^{\text{sp}} = \frac{Y^{\text{sp}} \dot{m}_{\text{da},1}^{\text{sp}}}{Y^{\text{sat}} - Y^{\text{sp}}} \tag{3.4}$$

Humidification column

Regarding the humidification of the dry air stream in Figure 3.1-b, the gaseous phase is injected near the bottom of the column filled with distilled water and dispersed in the form of bubbles with the help of a fritted glass filter. As the air bubble rises to the top of the humidification column, water vapor is transferred from the surface of the bubble (which is saturated in water) to its center. For the design of the humidification column, the air bubbles are considered to become saturated at the top of the column and no bubble coalescence occurs. The design of the column was based on the dry air flow at $48\,\mathrm{L\,min^{-1}}$. The column diameter was fixed as an inlet variable and the air and water temperatures were supposed to remain constant (i.e. overlooking the effect of the evaporative cooling). Considering an infinitesimal control volume with height $\mathrm{d}z_\mathrm{w}$ and cross-sectional area equal to that of the column, the increment in the absolute humidity within the air bubbles comes from the total area of the bubbles in the infinitesimal volume and can be written as shown in Equation 3.5.

$$\dot{m}_\mathrm{da}\mathrm{d}Y = K\alpha_\mathrm{b}A_c\mathrm{d}z_\mathrm{w}(\rho_\mathrm{v}^i - \rho_\mathrm{v}) \tag{3.5}$$

Where the left-hand side of equation 3.5 represent the small increase in the absolute humidity in the air stream. In the right-hand side, K is the mass transfer coefficient $(\mathrm{m\,s^{-1}})$, α_b is the specific area of the bubbles $(\mathrm{m^2\,m^{-3}})$ and can be calculated from the gas hold-up as described in [86], A_c stands for the cross-sectional area $(\mathrm{m^2})$ and the last term is the difference between the mass vapor concentration at the interface and at the center of the air bubble. Given the bubble column diameter equal to 5-cm, the necessary height of liquid water z_w in the column to saturate the dry air stream was estimated as 6 cm. Thus, the total height of the bubble column was fixed at 10 cm.

The saturated air stream leaving the humidification column is mixed with the dry air stream inside a horizontal cylinder containing a series of baffles for helping in the mixing process (Figure 3.1-c). A hygrometer (Model HC2-SM stainless steel, Michell Instruments, France) is placed at the end of the mixing cylinder for a measure of the air temperature and relative humidity, which are used for calculating the air stream absolute humidity and consequently are used by the mass flow meters for the control of the mass flow of air. After the mixing cylinder, two on-off valves were placed in order to guide the air flow either to the droplet-suspension zone or to the exterior. This by-pass was created as to allow the droplet mass to be recorded under stagnant air. The experiments are carried out with cycles of air flow in the wind tunnel and air flowing outwards.

Heating zone

After the mixing cylinder, the humid air stream is sent to the heating zone (Figure 3.1-d). A heating element (Model ASI, Chromalox, Pennsylvania, U.S.A.) with an output power of 250 W is used for heating the air stream from $20\,^\circ\mathrm{C}$ up to $140\,^\circ\mathrm{C}$. The design of the heating zone as presented in Figure 3.1-d is intended to provide a homogeneous heating to the humid air stream. A thermocouple (Type K) is placed at the exit of this zone. The temperature setpoint is manually added to a digital controller, whose value is used for regulating the air heating rate according to the temperature measured by the thermocouple.

For the selection of the heating element, the energy necessary for increasing the air stream temperature from 20 to 140 °C had to be calculated. This was done by considering the difference in enthalpy before and after the passage over the heating element, as shown in Equation 3.6 (and neglecting the heat losses and the effect of the pressure on the enthalpy).

$$\dot{Q} = \dot{m}_{\mathrm{ha}}(h_{\mathrm{ha}}^{\mathrm{out}} - h_{\mathrm{ha}}^{\mathrm{in}}) \tag{3.6}$$

Where $\dot{Q}$ stands for the output power in W, $\dot{m}_{\mathrm{ha}}$ the humid air mass flow and h is the specific enthalpy. The specific enthalpy can be calculated as a summation of the specific enthalpies related to the dry air and to the water vapor (here the reference point is dry air at $T_0 = 0\,°C$ and liquid water at $T_0 = 0\,°C$)

$$h_{\mathrm{ha}}(T, Y) = C_{p_{\mathrm{da}}}(T - T_0) + Y[h^{\mathrm{l}\to\mathrm{g}}(T_0) + C_{p_{\mathrm{v}}}(T - T_0)] \tag{3.7}$$

Where C_p ($\mathrm{J\,K^{-1}\,kg^{-1}}$) is the heat capacity, T the temperature (K) of the stream and $h^{\mathrm{l}\to\mathrm{g}}$ is the water vaporization enthalpy at $0\,°C$ ($\mathrm{J\,kg^{-1}}$).

The required output power is 120 W. A heating element (17 cm×5 cm) with 250 W was chosen (the minimal output power model available from the supplier).

Droplet-suspension zone

After passing through the heating zone, the humid air stream with the desired air properties is sent to a flow straightener (i.e. a honeycomb) in order to minimize any swirling motion in the air stream caused by the passage through the set-up. The rectangular cross-section of the honeycomb, 4 cm×4 cm, corresponds to that of the pipeline where the drying process takes place. The zone where the droplet is suspended at the tip of the thin filament (Figure 3.1-e) is 30 cm away from the exit of the flow straightener. The interior of this zone may be accessed through a small opening door (3 cm×5 cm, stainless steel) in the lower side of the pipeline, but also through a lateral glass window (3 cm×5 cm). A second sealed lateral glass window (3 cm×5 cm) allows then the passage of light around the suspension zone for the image acquisition from a camera placed in front of the droplet (Sentech America, U.S.A.). The details of the camera are given in the next section. Regarding the filaments used for suspending the droplet in the present work, they were manually produced by heating a glass stick and pulling it by the extremities. Thin capillaries (with a length of approximately 5 cm) were then obtained this way. A knob at the tip of the glass filament was created by slightly heating the tip of the filament. With a light microscope, the diameter of the filaments and their knob could be estimated. The filament diameter varied from 160 µm to 430 µm, with an average of 250 µm. The knob diameter varied from 304 µm to 770 µm, with an average of 460 µm. The thin filament produced here could be hanged under the precision balance (Sartorius Genius Series ME215S, Goettingen, Germany) with the help of a a rectangular device (1.5 cm×3 cm) containing a pressure disk at the center and a screw at the top (a 2-mm hole was perforated in the wind tunnel). One droplet could then be placed at the tip of the thin glass filament using a micropipette (model 0.5 ± 0.02 µL/10 ± 0.05 µL, Ergonomic High-Performance Pipettor, VWR International, USA). The mass of the droplet could be obtained thanks to the ability of the balance

to allow mass measurements of samples suspending under it. The humid air stream, after passing around the droplet, leaves the set-up at the "elbow"-shaped pipe (34 cm long and 57 cm high).

Image acquisition

Regarding the image acquisition, a monochrome camera (MB133USB, Sentech America, U.S.A.) with a resolution of 1290×960 pixels is coupled to a zero distortion macro lens (MC100, Sentech America, U.S.A.). The resultant association provides a field of vision of 4.8 mm×3.6 mm, where each pixel has a dimension of 3.75 µm×3.75 µm. The camera needs to be placed at 87 mm away from the center of the suspended droplet.

3.2.2 Summary of the set-up range of operation

The admitted experimental conditions in the droplet-suspension set-up is summarized below,

- Employed dry air flow rate: from $4\,\mathrm{L\,min^{-1}}$ to $48\,\mathrm{L\,min^{-1}}$;

- Absolute humidity: from $0.03\,\mathrm{g\,kg^{-1}}$ to $10\,\mathrm{g\,kg^{-1}}$;

- Employed air velocity: from $0.06\,\mathrm{m\,s^{-1}}$ to $0.5\,\mathrm{m\,s^{-1}}$;

- Air temperature: from $20\,^{\circ}\mathrm{C}$ to $140\,^{\circ}\mathrm{C}$;

- Wind tunnel cross-sectional area: $4\,\mathrm{cm}\times4\,\mathrm{cm}$;

- Precision balance: from $0.01\,\mathrm{mg}$ to $220\,\mathrm{g} \pm 0.01\,\mathrm{mg}$

Given the elements presented in this section, the set-up created for this thesis is presented in Figure 3.2.

3.3 The experimental strategy

This section is dedicated to the presentation of the experimental strategy used with the droplet-suspension set-up introduced previously. The section starts with a brief definition of the design of experiments (DoE) approach and the model adopted in order to create a matrix containing a combination of the drying conditions. The variable of interest for the DoE approach here, the Peclet number, is presented afterwards. The value of this variable helps in the definition of the experimental matrix. It should be noted that the DoE approach is used for guiding the choice of the experimental conditions to be tested. However the analysis of the drying results are carried out with an analytical viewpoint, with a focus on the influence of each parameter (air temperature and solute mass content, for example) on the solid formation.
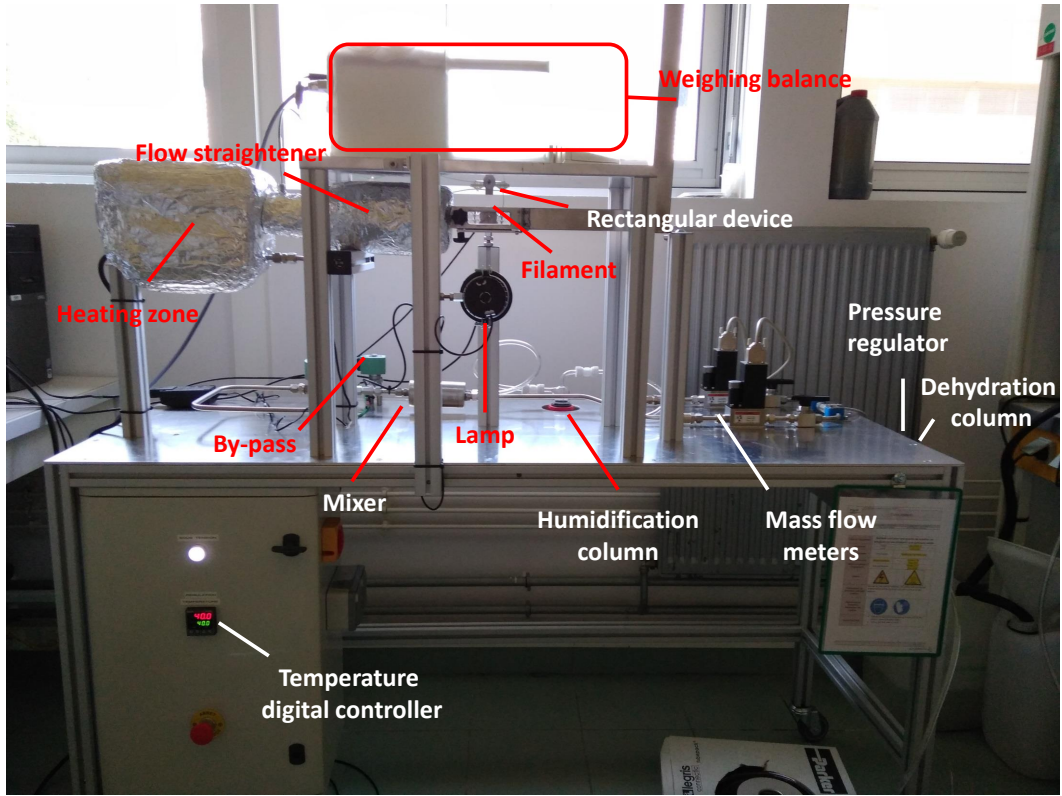
Figure 3.2 – The droplet-suspension set-up developed in the present work for drying a single droplet suspended by a filament

3.3.1 The design of experiments approach

The design of experiments is a tool used to maximize the information acquired from a field of minimum experimental conditions. In order to do so, the input variables or the factors that influence the outcome of the experiments, should be listed. As presented in [79], different kinds of models can be employed to generate the matrix of experimental conditions, which contains a combination of the input variables. The simplest case is produced when only two values, or levels, are attributed to each input variable. Thus, a set of 2^k experiments is created, where k is the number of input variables. This corresponds to a two level full factorial design. However, with such representation, the number of experiments to be performed can rise quickly, depending on the value of k. Consequently, a special category of the two level design can be performed by excluding a fraction of the generated experimental combinations, which gives place to the two level fractional factorial design and is written as 2^{k-q}, where the experimental matrix is divided by 2^q (the value of q depends on the researcher's judgment). Two experimental matrices arising from two models are combined in this chapter: an experimental matrix from a full factorial design from Chapter 4 and an experimental matrix from a fractional factorial design developed for this chapter.

Regarding the independent variables with an effect on the drying of the droplet, six input variables were identified for each drying system: the mass contents of both solutes present in the liquid phase, the droplet size, the air inlet temperature, the air stream absolute humidity and the velocity of the air stream in the drying tunnel. With respect

to the droplet size, the initial droplet diameter used throughout the experiments was approximately the same (i.e. 1.5 mm, which corresponds to a 2-µL-droplet from the micropipette). Consequently, only five input variables will be varied in the experimental matrix and their values are presented in Table 3.1.

Table 3.1 − Range of the variables used in the fractional factorial design

Variable	level −1	level 1
ω_i (% wt)	5	15
ω_j (% wt)	5	15
u_{ha} (m s^{-1})	0.2	0.5
Y_{ha} (g kg^{-1})	3.5	9.0
T_{ha} (°C)	40	80

Regarding each solute mass content ω, the levels are set at 5 % wt and 15 % wt, which would lead to a total solute content ranging between 10 % wt and 30 % wt (considering the solute proportion at 50:50, on dry basis), which are common total solute content found in industrial applications [41, 97, 118]. The air velocity is set at either 0.2 m s^{-1} or 0.5 m s^{-1}. As stated in [10], the higher air velocity employed here may be found in industrial towers operating with a laminar air flow. As for the air absolute humidity, it may vary between 3.5 g kg^{-1} or 9 g kg^{-1}, where the lower value was chosen according to the absolute humidity employed in the acoustic levitator (Chapter 4). Regarding the air temperature, it was set at 40 °C or 80 °C. This parameter was limited to 80 °C due to the difficulties found when conducting the experiments at higher temperatures, such as keeping the air temperature around the droplet as near as possible to the setpoint and the acquisition of a fair amount of drying kinetics data, in order to effectively see all the drying phases.

The outcome of the experiments, or the variable of interest, is the Peclet number here (the details of this parameter calculation are presented in the next section). For the values presented above, a Peclet number superior to unity is obtained. The full factorial design arising from the combination of these five variables is presented in Table 3.2, using the dextran-sucrose system as an example. For the lactose-WPI system, the Peclet number would be different from the ones presented in Table 3.2. The fractional factorial design commented previously is a fraction of these 32 combinations and is shown in the next section. The full factorial design used in Chapter 4 is composed of 4 experiments for each drying systems. Additionally, the Peclet number derived from these experiments is inferior to unity. The experimental matrix coming from Chapter 4 is also presented in the next section.

3.3.2 The Peclet number based selection

From the experimental matrix presented in Table 3.2, only a fraction of these combinations will be performed in the drying trials with the glass filament. The choice of the submatrix containing only 2^{5-2} combinations (for each drying system) is guided by the value of the Peclet number and a fair variability of the experimental conditions.

Table 3.2 – Experimental matrix for the dextran/sucrose system using the two level full factorial design. The corresponding Peclet number is also presented for each combination of experimental conditions

Dextran mass content (% wt)	Sucrose mass content (% wt)	Air temperature (°C)	Air velocity ($\mathrm{m\,s^{-1}}$)	Air absolute humidity ($\mathrm{g\,kg^{-1}}$)	Peclet number
5	5	40	0.2	3.5	3.78
				9.0	2.74
			0.5	3.5	5.89
				9.0	4.27
		80	0.2	3.5	6.51
				9.0	5.75
			0.5	3.5	10.08
				9.0	8.90
	15	40	0.2	3.5	4.36
				9.0	3.16
			0.5	3.5	6.79
				9.0	4.92
		80	0.2	3.5	7.5
				9.0	6.62
			0.5	3.5	11.62
				9.0	10.25
15	5	40	0.2	3.5	10.64
				9.0	7.71
			0.5	3.5	16.58
				9.0	12.02
		80	0.2	3.5	18.30
				9.0	16.16
			0.5	3.5	28.36
				9.0	25.02
	15	40	0.2	3.5	10.96
				9.0	7.95
			0.5	3.5	17.08
				9.0	12.38
		80	0.2	3.5	18.85
				9.0	16.64
			0.5	3.5	29.20
				9.0	25.77

As described in Chapter 1, the Peclet number (Pe) is a measure of the droplet shrinkage rate over the diffusion of the solutes in the liquid phase, as shown in Equation 3.8.

$$Pe = \frac{d_0 \frac{dr}{dt}}{D_{\mathrm{mix}}} \tag{3.8}$$

Where d_0 is the initial droplet diameter, dr/dt is the shrinkage rate and D_{mix} is the diffusion coefficient of both solutes in water.

The diffusion coefficient of the solute mixture is calculated as a weighted mean from the diffusion coefficients of each solute, D_i, calculated with the Stokes-Einstein equation and their respective mass contents, w_i, as shown in Equation 3.9.

$$\frac{1}{D_{\text{mix}}} = \frac{w_i}{D_i} + \frac{w_j}{D_j} \tag{3.9}$$

To calculate the shrinkage rate, it is considered that all the energy provided by the air stream is used for the evaporation of the droplet and that the droplet surface remains saturated with water (first drying stage). The macroscopic representation of the droplet evaporation through a global heat transfer coefficient is shown in Equation 3.10,

$$J_{\text{tot}} h^{\text{l}\rightarrow\text{g}}(T_h) = h_t S(T_{\text{ha}} - T_h) \tag{3.10}$$

Where J_{tot} is the global droplet evaporation rate, $h^{\text{l}\rightarrow\text{g}}(T_h)$ is the latent heat of vaporization at the droplet surface temperature, h_{t} ($\text{W m}^{-2}\,\text{K}^{-1}$) is the heat transfer coefficient, S is the droplet surface area over which the heat and mass transfers take place, T_{ha} the temperature of the surrounding air and the temperature of the droplet surface T_h, which corresponds to the wet bulb temperature of saturated air.

In Equation 3.10, the evaporation rate can be written in terms of the shrinkage rate dr/dt through the use of the droplet density (which is considered to be constant, as the shrinkage rate is calculated for the first moments of drying) and considering the volume of a sphere (Equation 3.11)

$$J_{\text{tot}} = \rho_{\text{drop}} \left(4\pi r^2 \frac{dr}{dt} \right) \tag{3.11}$$

Combining Equations 3.10 and 3.11, the final equation for the shrinkage rate is then,

$$\frac{dr}{dt} = \frac{h_t(T_{\text{ha}} - T_h)}{h^{\text{l}\rightarrow\text{g}}(T_h)\rho_{\text{drop}}} \tag{3.12}$$

The heat transfer coefficient h_t is calculated as a function of the dimensionless Nusselt number, Nu, which is used for a convective heat transfer, the mean thermal conductivity $\bar{\kappa}$ ($\text{W m}^{-1}\,\text{K}^{-1}$), and the initial droplet diameter, d_0, (Equation 3.13). The value of $\bar{\kappa}$ presented in this equation is the mean value between the thermal conductivity of the humid air (away from the droplet surface) and the thermal conductivity of the saturated humid air at the droplet interface. The Nusselt number (Equation 3.14) is calculated as a function of the Reynolds numbers, Re, (a ratio of the inertial-to-viscous forces within a fluid, Equation 3.15) and the Prandt number, Pr, (a relation between the momentum transport and the thermal transport capacity of a fluid, Equation 3.16) [29]. This relation presented in Equation 3.14 was created for estimating the mean heat transfer coefficient between a spherical surface and a flow of fluid and is valid for $0.71 \leq Pr \leq 380$, $3.5 \leq Re \leq 7.6 \times 10^4$ and $1.0 \leq \mu_{\text{ha}}/\mu_{\text{s}} \leq 3.2$.

$$h_t = \frac{Nu\,\bar{\kappa}}{d_0} \tag{3.13}$$

$$Nu = 2 + \left[\left(0.4 Re^{0.5} + 0.06 Re^{0.667} \right) Pr^{0.4} \left(\frac{\mu_{\mathrm{ha}}}{\mu_{\mathrm{s}}} \right)^{0.25} \right] \tag{3.14}$$

$$Re = \frac{\rho_{\mathrm{ha}} u_{\mathrm{ha}} d_{\mathrm{h}}}{\bar{\mu}} \tag{3.15}$$

$$Pr = \frac{\bar{\mu} \bar{C} p}{\bar{\kappa}} \tag{3.16}$$

Where μ_{ha} is the viscosity of the humid air away from the droplet, μ_{s} is the viscosity saturated humid air at the surface of droplet, ρ_{ha} is the humid air density, u_{ha} is the air velocity in the wind tunnel, d_{h} is the wind tunnel hydraulic diameter (the rectangular cross-section of the wind tunnel is translated into a cylinder with this parameter), $\bar{\mu}$ and $\bar{C}_{\mathrm{p}}$ are the mean viscosity and the mean heat capacity, respectively, between the humid air away from the droplet and the saturated humid air at the droplet surface.

Given the above correlations for calculating the Peclet number, this dimensionless number was evaluated for all the combinations presented in Table 3.2. As mentioned previously, the experimental matrix created from the fractional factorial design contains 2^{5-2} combinations (displayed in Table 3.3 for both drying systems) with a Peclet number superior to unity from Table 3.2. This submatrix is firstly composed of the experimental combinations leading to the highest Peclet number (trials 1 and 9 in Table 3.3). Secondly, only the effect of the drying air temperature was sought, which allows the comparison between the trials 1 and 2 or 9 and 10. Next, two more experimental combinations were chosen with the same Peclet number (trials 3 and 6 or 11 and 14 in Table 3.3). The other combinations were chosen in order to see the effect of changing the solute proportion and the total solute content at different temperatures.

Now, regarding the experimental matrix from Chapter 4, the experiments were carried out at low Peclet number. Indeed, they were executed at mild drying conditions, i.e. with an air temperature at $19\,^{\circ}\mathrm{C}$ and no air flow. The resulting Peclet numbers are presented in Table 3.4. In these experiments, the total solute contents were varied between $10\,\%$ wt or $30\,\%$ wt. In two trials, the proportion of the solutes was kept at 50:50, while for the other two, the effect of a small quantity of a given solute to the mixture was sought.

Finally, it should be noted that the experimental conditions presented in Tables 3.3 and 3.4 will be carried in *duplicata*, since each trial produces only one solid particle and, consequently, two particles are needed for the characterization methods presented in the next Section.

3.4 Characterization methods

The solid particles generated from the droplet-suspension set-up were chosen in order to give information about the particle moisture content, which is afterwards used for assuring the validity of the drying results, the solid structure (whether crystalline or amorphous) and the particle morphology.

Table 3.3 – Experimental conditions with Peclet number superior to unity. These conditions are a submatrix from Table 3.2

Trial number	Lactose mass content (% wt)	WPI mass content (% wt)	Air temperature (°C)	Air velocity (m s^{-1})	Air absolute humidity (g kg^{-1})	Peclet number
(1)	15	15	80	0.5	3.5	28.34
(2)	15	15	40	0.5	3.5	17.54
(3)	5	15	40	0.2	9.0	21.73
(4)	15	5	40	0.2	9.0	1.46
(5)	5	5	40	0.2	9.0	1.50
(6)	15	5	80	0.2	3.5	21.72
(7)	5	15	80	0.2	3.5	10.37
(8)	5	5	80	0.2	3.5	3.57

Trial number	Dextran mass content (% wt)	Sucrose mass content (% wt)	Air temperature (°C)	Air velocity (m s^{-1})	Air absolute humidity (g kg^{-1})	Peclet number
(9)	15	15	80	0.5	3.5	29.20
(10)	15	15	40	0.5	3.5	17.08
(11)	15	5	40	0.2	9.0	7.70
(12)	5	15	40	0.2	9.0	3.16
(13)	5	5	40	0.2	9.0	2.74
(14)	5	15	80	0.2	3.5	7.50
(15)	15	5	80	0.2	3.5	18.30
(16)	5	5	80	0.2	3.5	6.51

Table 3.4 – Experimental conditions at low Peclet number and based in the work developed in Chapter 4

Trial number	Lactose mass content (% wt)	WPI mass content (% wt)	Air temperature (°C)	Air velocity (m s^{-1})	Air absolute humidity (g kg^{-1})	Peclet number
(17)	5	5			6.13	0.11
(18)	15	15	19	0	4.7	0.38
(19)	20	5			4.7	0.13
(20)	5	20			4.7	0.52

Trial number	Dextran mass content (% wt)	Sucrose mass content (% wt)	Air temperature (°C)	Air velocity (m s^{-1})	Air absolute humidity (g kg^{-1})	Peclet number
(21)	5	5			2.4	0.35
(22)	15	15	19	0	3.5	0.87
(23)	25	5			4.7	1.16
(24)	5	25			2.4	0.45

3.4.1 Final moisture content evaluation

The first characterization method applied at the end of each experiment was the measure of the final moisture content of the generated solid particle. In order to do so, the sample was put into an oven functioning under vacuum at 30 °C for 48 h. The weight of the

sample was measured before and after the use of the oven with the help of a microbalance (Sartorius Ultra-micro balance SE2, Goettingen, Germany) with a precision of 0.1 µg.

3.4.2 Differential scanning calorimetry

Differential scanning calorimetry (DSC) is a thermal analysis technique in which the heat flow into or out of a sample is measured as a function of temperature or time, while the sample is exposed to a controlled temperature program. DSC analysis can exhibit some limitations to detect the thermal transitions due to weak signals or overlapping events (e.g. water evaporation occurring at the same time). Temperature modulated DSC (TM-DSC) is then applied to overcome these limitations . Also, this method has a high sensitivity in measuring heat capacity [68, 88]. TM-DSC heats the samples with a combined sinusoidal temperature control and a constant rate temperature control. The sample temperature is raised, on average, at a constant rate, by repeated heating and cooling of the temperature in a short time period.

In this work, TM-DSC (DSC MDSC Q200, TA Instruments, France) analysis was used to evaluate the solid state (crystalline or amorphous) of the final particles generated from the suspended drying droplets. A RCS900 cooling system was set-up in order to control precisely the cooling rate. Nitrogen was used as the purging gas at $50\,\mathrm{mL\,min^{-1}}$. The analysis was carried out in a non-hermetic aluminum pans. The temperature and enthalpy calibrations were done with indium standards and an empty aluminum pan was used as a blank. Samples were scanned at a linear heating rate of $2\,^{\circ}\mathrm{C\,min^{-1}}$, from $-30\,^{\circ}\mathrm{C}$ and $150\,^{\circ}\mathrm{C}$ and with a superimposed harmonic signal of amplitude $1.2\,^{\circ}\mathrm{C}$ and period $60\,\mathrm{s}$.

3.4.3 Microscopy

The scanning electron microscope (SEM - ESEM FEG Philips, Holland) used for the particles produced from the glass-filament method is the same used in Chapter 2 for the analysis of the powder produced from the lab-scale spray dryer.

3.5 Set-up manipulation

This section is dedicated to give an overview on how the experiments are carried out. Also, it presents an important step regarding the treatment developed for ensuring the reliability of the initial and the final points in the drying kinetics data. Finally, this section presents the procedure used for extracting the droplet diameter from the images acquired with the camera.

3.5.1 Execution of the experiments

For each trial, the setpoint for the air velocity, temperature and absolute humidity, as well as the duration of the experiment, are written in the software specifically developed to collect the mass and the images out of the droplet-suspension set-up. The following parameter may also be modified if needed: the duration of the passage of the air flow in the wind tunnel before it is by-passed for the mass recording, the balance stabilization

time after the by-pass activation and the number of mass points measured before the air flow is redirected to the wind tunnel.

Before starting the experiments, the air at the droplet-suspension zone is set to the desired value. Once the desired air temperature is attained (the air velocity and absolute humidity can be modified more rapidly), the glass filament is attached under the balance. Next, the by-pass is activated and, with no flow in the wind tunnel, the balance is tared. The droplet is deposited at the tip of the glass filament with the micropipette. For facilitating the droplet transfer, the micropipette plastic tip is recovered with Teflon, a hydrophobic substance. Finally, the experiment is started. The time between the deposition of the droplet at the filament and the beginning of the experiments is approximately 30 s.

Two mass points are recorded by the balance in an interval of 1 s, while the droplet image is taken when the first mass point is recorded. The air starts to flow in the wind tunnel for 10 s. Then, the by-pass is activated and the weighing balance waits 8 s before recording two more mass points as well as another image. These cycles persists for the period specified at the beginning of the experiment (trials at 20 °C, 40 °C and 80 °C last 1 h 30 min, 50 min and 30 min, respectively).

At the end of the experiment, the solid particle is separated from the glass filament and transferred to the microbalance for beginning the analysis of the particle final moisture content (Section 3.4.1). This transfer is accomplished in less than 5 min. It should be noted that the measure of the mass of the dextran-sucrose particle is easily accomplished, since it can be effortlessly removed from the filament. On the other hand, the lactose-WPI particle adheres more to the glass filament, which makes its recovery harder and increases the probability of losing crust fragments.
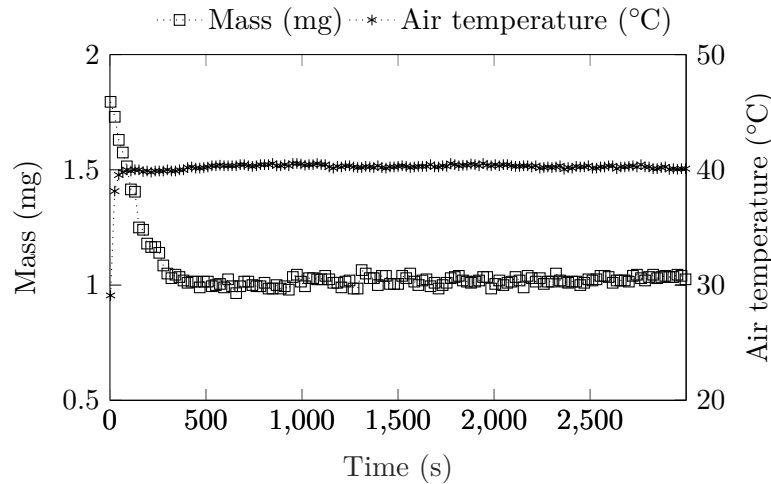
Figure 3.3 – Example of the drying kinetics data obtained with the droplet-suspension set-up. The air temperature is also represented in the plot. The setpoints were: $T_{ha} = 40$ °C, $Y_{ha} = 3.5$ g kg^{-1}, $u_{ha} = 0.5$ m s^{-1}. Liquid formulation: 15D-15S

The drying kinetics data plotted in Figure 3.3 serve to illustrate what is obtained in some of the experiments with the droplet-suspension set-up. It is possible to note

that the beginning of the drying process occurs under an increasing air temperature. When the droplet is transferred to the filament, the by-pass is activated, which in turn stops the heating element. As a result, the first mass point is recorded with an air temperature lower than the specified setpoint. The air temperature attains the setpoint a few moments later. Finally, it should be noted that the higher the air temperature before the deposition of the droplet, the bigger the difference between the first temperature point and the setpoint.

3.5.2 Correction of the initial drying point

The first treatment applied to the drying kinetics is related to the first mass measurement point. As mentioned previously, the first mass point is taken at approximately 30 s after the deposition of the droplet on the filament. In this period, the droplet can evaporate and the first mass measurement will be less than the real mass of the droplet produced with the micropipette. The correction applied here is related to the calculation of the real initial droplet mass, which can be used later for the calculation of the real mass of solutes in the droplet. Two elements should be considered: the air temperature around the droplet is inferior to the setpoint, as commented from Figure 3.3, and there is no forced air flow in the wind tunnel, thus a droplet evaporation through diffusion only can be considered.

Starting with Fick's law of diffusion [31], the evolution of the mass of the droplet with a diffusive evaporation flux can be written as follows,

$$m = \frac{4}{3}\pi\rho_{\text{drop}}\left[\left(\frac{3m_0}{4\pi\rho_{\text{drop}}}\right)^{2/3} - \frac{2D_{\text{v}}PMM_{\text{w}}}{RT\rho_{\text{drop}}}\ln\left(\frac{P-P_{\text{v}}}{P-P_{\text{v,d}}}\right)t\right]^{3/2} \tag{3.17}$$

Where m_0 is the initial droplet mass, ρ is the droplet density, D_{v} is the diffusion coefficient of water vapor in dry air, P is the total air pressure, R is the gas constant, MM_{w} is the molar mass of water, P_{v} is the vapor pressure in the air (calculated using the first absolute humidity point in the drying kinetics data), $P_{\text{v,d}}$ is the vapor pressure at the surface of the droplet (which is calculated considering a water activity at the droplet surface equal to unity). The temperature used in equation 3.17 corresponds to the first temperature point given in the drying kinetics data. As an example taken from the dextran-sucrose drying kinetics, a droplet dried at 20 °C, with an absolute humidity of 3.48 g kg^{-1} and an initial measured mass at 1.93 mg possesses a true mass of 1.97 mg. For a droplet trial with a temperature setpoint at 40 °C, the true droplet mass was calculated as equal to 1.72 mg, instead of 1.68 mg as given in the drying kinetics. As for the setpoint of 80 °C, in one of the trials, the real mass was 2.03 mg, instead of 1.91 mg.

3.5.3 Correction of the final drying point

The second treatment applied to the drying kinetics data is related to the validation of the final drying point. For that purpose, the particle produced at the end of a trial is weighted with another balance, as described in the Section 3.5.1, for the sake of comparison. It was observed, for all trials, that the last data point given in the kinetics curve is approximately two times bigger than the particle mass weighted *ex situ*. As mentioned previously, at least for the dextran-sucrose particle, all the solid material can

be recovered from the glass filament. In that way, the final drying point should coincide with the particle mass measured *ex situ*. Plus, the mass of dry particle obtained after placing it in the drying oven under vacuum for 48 h corresponds to the real mass of solute in the droplet (calculated after the correction of the initial drying point).

A trial was performed with the acquisition of the mass of only the filament over time and the result is plotted in Figure 3.4. As can be seen, the mass of the filament increases linearly over time. The same tendency of mass drifting can then be found in almost all droplet drying experiments and is responsible for increasing the mass given in the kinetics data with respect to the true sample mass.
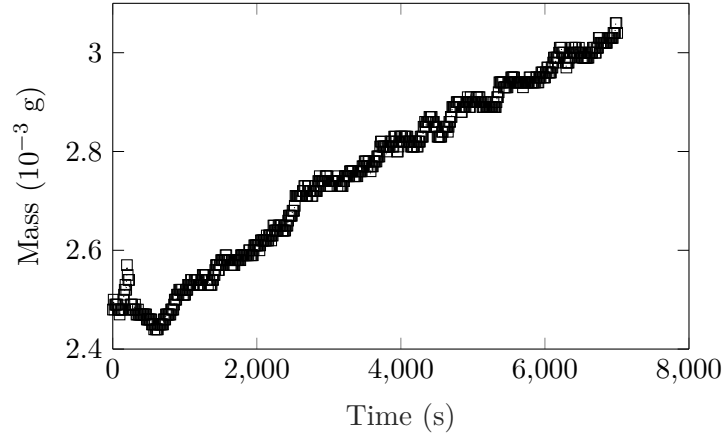
Figure 3.4 − Linear mass drift observed for a trial with the filament only

For calculating the mass drift, the sample moisture content is calculated based on the recorded mass points at each instant t and the real dissolved solids mass, as shown in Equation 3.18,

$$X = \frac{m_{\text{drop}} - m_{\text{ds}}}{m_{\text{ds}}} \tag{3.18}$$

With the final moisture content measured *ex situ*, the slope of the moisture content variation over time, or the mass drift, is calculated as follows,

$$\beta = \frac{X_{\text{f}}^{\text{exp}} - X^{\mu\text{B}}}{t_{\text{f}}} \tag{3.19}$$

Where β is the mass drift, $X_{\text{f}}^{\text{exp}}$ is the final moisture content calculated from the drying curve (an average of the last five points), $X^{\mu\text{B}}$ is the particle moisture content measured *ex situ* and t_{f} is the duration of the experiment. The mass drift coefficient β calculated for all the dextran-sucrose trials is presented in Table 3.5.

The correction of the drying curve is carried out by subtracting the mass drift over time from the raw drying data for both drying systems, as presented in Equation 3.20.

$$X^{\text{cor}} = X^{\text{exp}} - \beta t \tag{3.20}$$

Table 3.5 – The mass drift coefficient β is calculated for each trial based on the final moisture content calculated from the drying curve and the moisture content measured *ex situ*. Trials are organized in terms of solute concentration and air temperature

Air temperature (°C)	Dextran : Sucrose mass content (% wt)	Final moisture content (mg mg^{-1})	Moisture content *ex situ* (mg mg^{-1})	Mass drift (mg mg^{-1} s^{-1})	Corrected final moisture content (mg mg^{-1})
	05:05	1.49	0.10	2.58×10^{-4}	0.11
		1.19	0.14	1.95×10^{-4}	0.15
	05:25	0.83	0.23	7.10×10^{-5}	0.23
20	15:15	1.18	0.13	1.94×10^{-4}	0.14
		0.58	0.14	8.24×10^{-5}	0.14
	25:05	0.25	0.05	3.68×10^{-5}	0.05
		0.40	0.04	6.74×10^{-5}	0.04
	15:05	1.09	0.05	3.47×10^{-4}	0.07
		0.25	0.08	5.75×10^{-5}	0.08
	05:15	1.39	0.05	4.45×10^{-4}	0.08
40		0.37	0.08	1.60×10^{-4}	0.09
	05:05	3.71	0.06	1.20×10^{-3}	0.12
		1.17	0.05	4.56×10^{-4}	0.08
	15:15	1.11	0.07	3.49×10^{-4}	0.07
		0.85	0.03	2.73×10^{-4}	0.04
	05:15	0.87	0.002	4.81×10^{-4}	0.03
		1.07	0.004	5.95×10^{-4}	0.04
	15:05	1.00	0.06	5.52×10^{-4}	0.09
80		0.61	0.03	4.68×10^{-4}	0.05
	05:05	5.03	0.004	4.30×10^{-3}	0.23
		3.49	0.001	2.40×10^{-3}	0.13
	15:15	0.73	0.09	3.60×10^{-4}	0.11
		0.49	0.05	2.45×10^{-4}	0.06

Where X^{cor} stands for the corrected sample moisture content, X_i^{exp} is the sample moisture content at each instant t and β_i is the mass drift coefficient of each experiment.

3.5.4 Summary on the mass drift correction

In Figure 3.5, a summary of the treatment applied to the drying curve is represented. It shows the correction of the first drying point using the equation of diffusive evaporation flux, the linear mass drift from the trials with a filament only and the correction applied to the final drying point, where the mass drift slope is calculated based on the moisture content values and is applied to correct the drying curve.

3.5.5 Diameter assessment through image analysis

Along with the mass data obtained from the weighing balance, it is also important to have quantitative information from the images taken from the hanging droplet/wet particle for helping illustrating the drying behavior of the sample, as will be shown later in Section 3.7.2 on the drying kinetics. Using Matlab software, it is possible to extract
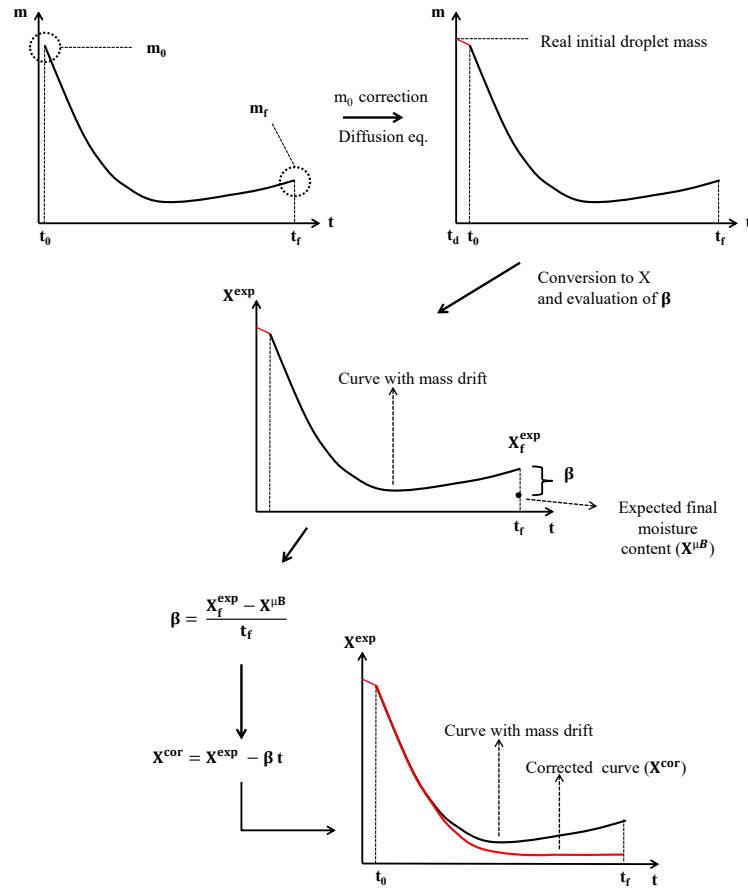
Figure 3.5 – Schematic representation of the treatment applied to the drying kinetics curve. The initial droplet mass m_0 is corrected considering a diffusive evaporation flux. The final mass m_f is converted into moisture content and corrected using the particle moisture content measured *ex situ* ($X^{\mu B}$). The tendency of a constant mass drift slope observed in previous test trials is used in the correction of the drying kinetics data

the droplet/wet particle diameter for every point in the drying curve. The diameter measured here corresponds to the number of pixels representing the largest diameter parallel to the air flow. In order to do so, the droplet image, as presented in Figure 3.6-1, is firstly read with Matlab. The software creates a matrix with the numbers of rows and columns representing the size of the image. To each matrix location, a value from zero to one is assigned. A one dimensional matrix is created due to fact that the image is in a gray scale, otherwise a matrix would be created for every basic color (red, blue and green) composing a colored image. Next, a threshold is applied to the pixel intensities (Figure 3.6-2). This is the simplest technique used to create binary images. An intensity constant was manually defined here and the pixels, whose values are inferior to that constant, become a black pixel (with a value equal to 0), otherwise they become white (with a value equal to 1). Next, a black to white conversion is applied to the image (Figure 3.6-3). With this technique, the pixels representing the droplet/wet particle have the value equal to unity and the rest of the pixels are equal

to zero. This step can be avoided, but it allows a better visualization of the sample using a plot of the sum of the pixel values in each column of the image-matrix versus the columns of the image-matrix. Indeed, the sum of the pixel values is equal to zero in the columns composed of only black pixels and the sum is superior to unity in the columns with the white pixels representing the droplet/wet particle.
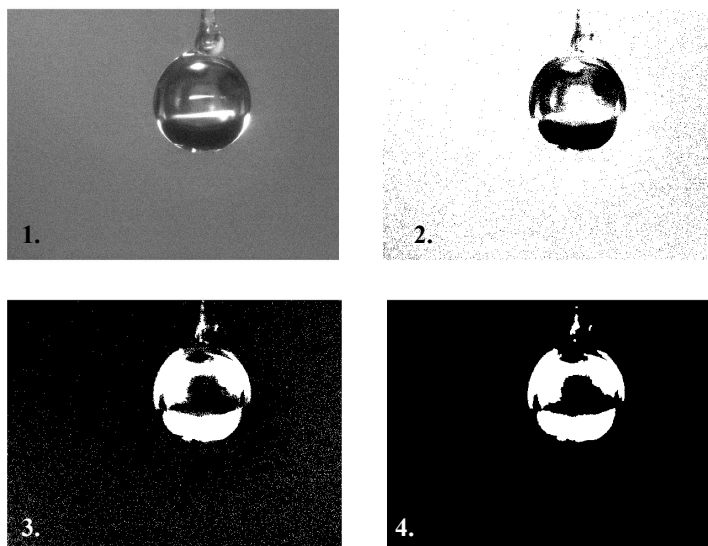
Figure 3.6 – The images represents the result of each step in the treatment of the droplet images. At the end, the number of pixels corresponding to the droplet diameter (parallel to the air flow) can be assessed. The images are: 1 the original image; 2 the result from the threshold technique; 3 the result from the black to white conversion; 4 the final image noise-free

Finally, a noise extraction is applied to the binary image for eliminating the small white pixels that can be seen distributed throughout the image (Figure 3.6-4). A constant value is used for this extraction. The higher the constant value the more the pixels will be erased from the image (this should be used with caution as important pixels representing the droplet can be erased). This Matlab function (strel) is applied with the intensity of 2 and the form "disk". In order to assess the droplet diameter, the first and the last non-zero elements (white pixels) are sought from left to right, which is why the noise extraction is important here. These elements correspond to the extremities of the droplet/wet particle. The difference in the column number containing these elements is related to the number of pixels composing the droplet diameter. The conversion from pixel to micrometer is achieved with the pixel size ($3.75\,\mu\text{m} \times 3.75\,\mu\text{m}$) from the camera specifications.

3.6 Particle design

This section is dedicated to the presentation of the particle morphologies obtained with the droplet-suspension set-up. They are organized according to the Peclet number. These morphologies are compared to those obtained from the spray scale experiments

(from Chapter 2). Next, the results from thermal analysis are presented in order to investigate the solid-state form (crystalline or amorphous) of the particles.

3.6.1 Peclet number inferior to unity

As presented in the experimental strategy section, the particles produced here at a low Peclet number correspond to the experiments carried out at 20 °C under stagnant air. At this temperature, the time scale at which the droplet morphology evolves is low, in that way the camera placed in front of the suspension zone can record small variations in the droplet surface aspect through time. For example, in Figure 3.7, a series of images are presented for the drying of a droplet containing 15D-15S. In this figure, it is possible to observe a reduction in the droplet diameter (from 0 s to 360 s), the appearance of the first solids at the droplet surface near the glass filament (at around 423 s), the complete covering of the droplet surface by the solid layer (at approximately 633 s) and finally the production of an entirely solid particle (at 1788 s).
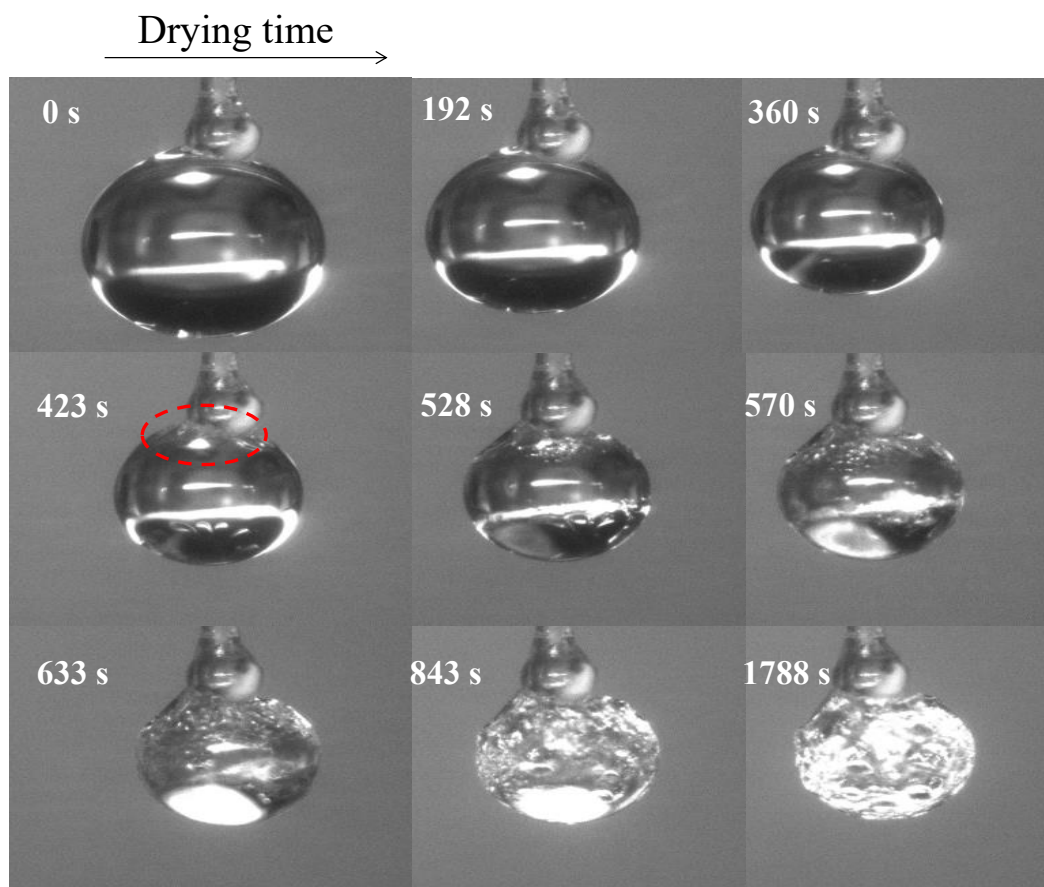
Figure 3.7 – Images taken from the drying of a droplet containing 15D-15S at 20 °C (trial 22 in Table 3.4)

It is interesting to note the small contact area between the droplet and the glass filament, as can be seen from Figure 3.7. Since the glass filament is covered with Teflon, its hydrophobic character maintains the dextran-sucrose droplet at the tip of the filament

and prevents it from going upward by capillarity. As a result, the solid particle obtained at the end of the experiment can be easily taken out from the glass filament. However, regarding the lactose-WPI system, it was not possible to produce such spherical solid particles with the glass filament in trials at 20 °C, apart from the experiment with 5L-20WPI. The reason is related to the amphiphilic character of the protein. In that way, the glass filament covered in Teflon would not keep the droplet at its tip, as was seen for the dextran-sucrose droplet. Instead, the lactose-WPI droplet would cover the whole filament knob throughout the entire drying process. At the end of drying, the solutes present in the droplet would form a solid layer on the filament knob (Figure 3.8). Thus, no solid particle could be recovered from the filament. On the other hand, with an elevated protein content in the droplet, such as 20 % wt, the external droplet/wet particle diameter was locked sooner, this in turn prevented the droplet/wet particle from forming a solid layer covering the filament knob and, as a result, the hollow core particle could be taken out from the filament.
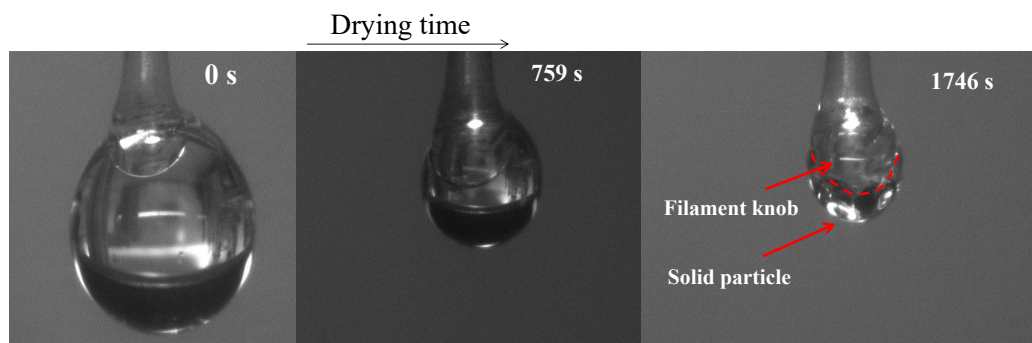
Figure 3.8 – Images taken from the drying of a droplet containing 5L-5WPI at 20 °C (trial 17 in Table 3.4). The droplet/wet particle covers the filament knob as the drying progresses

The dextran-sucrose particles obtained at the end of the trials at 20 °C are presented in Figure 3.9 with their respective Peclet number and the micrograph obtained with the scanning electron microscope. The first image (top-left) comes from the particle produced at the lowest Peclet number from the experimental matrix with the droplet containing 5D-5S. The particle surface is relatively smooth and the core is dense. The second image (top-right), with a particle produced with a high sucrose content (25 % wt), represents the surface aspect of the particle at only 35 % of the total drying time (3790 s out of 10 800 s). For this trial, in order to turn the solid particle into a relatively hard solid, the reduction in the moisture content had to be accomplished with a longer drying time. Otherwise, the particle would be sticky and could not be removed from the filament. Only one particle could be recovered from the filament in this way and it was used for the DSC analysis (which is why no SEM micrograph is coupled to the image of this particle). The third image (bottom-left) was taken from a particle containing 15D-15S. The particle surface is relatively smooth and the core is dense (apart from the presence of a small air pocket). Finally, the fourth image (bottom-right) represents the particle obtained with the highest Peclet number. For this case with the Peclet number near unity, the high dextran content (25 % wt) led to the formation of a hollow particle. The formation of such hollow core could be followed from the images acquired during the drying process, as represented in Figure 3.10.
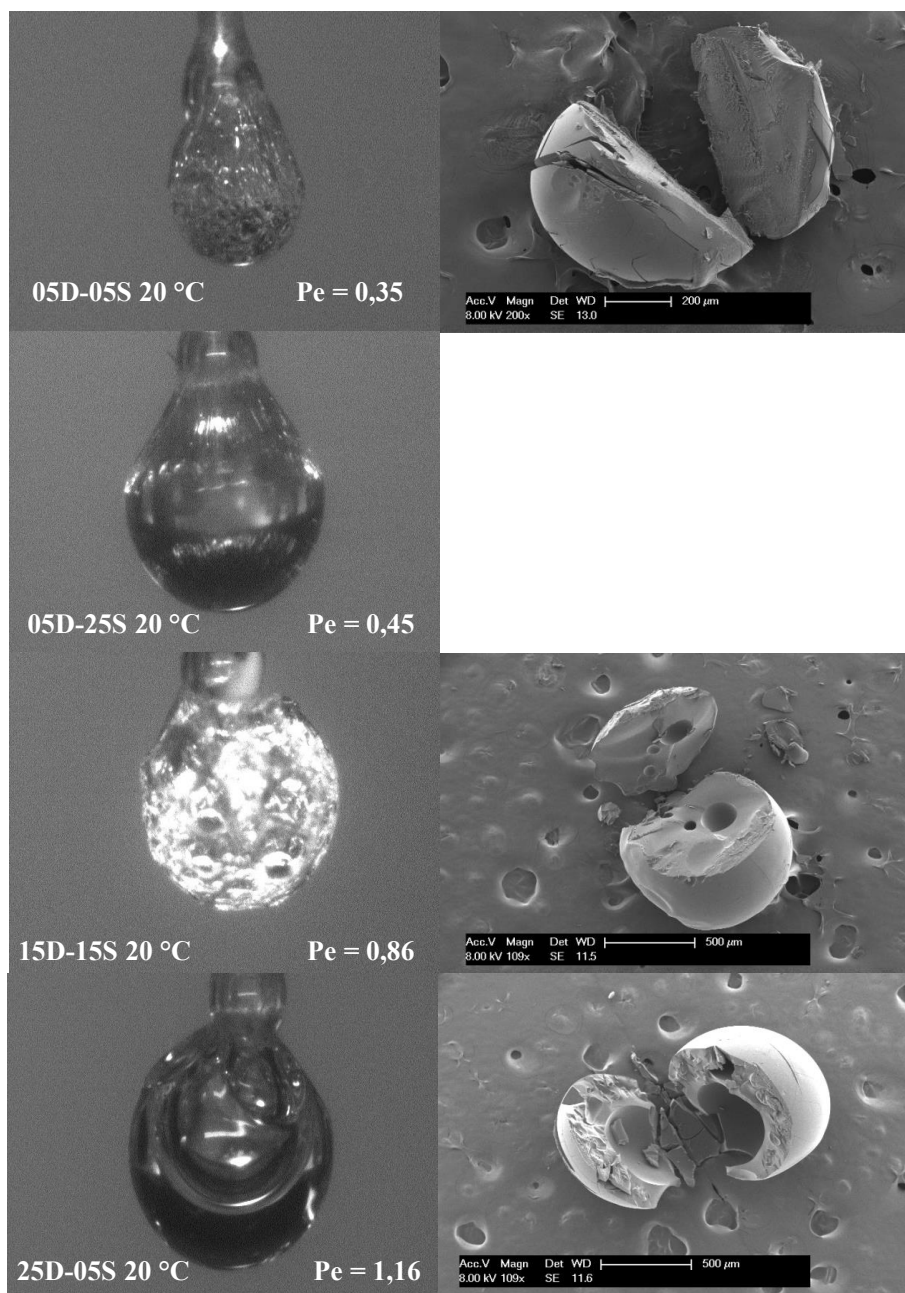
Figure 3.9 – Dextran-sucrose particles produced with the droplet-suspension set-up at a low Peclet number from the experiments at 20 °C under stagnant air. The image from the camera corresponds to the particles obtained at the end of the trials 21 to 24 in Table 3.4. The dextran and sucrose mass contents are indicated by xD-yS in each particle image

The formation of a hollow core presented in Figure 3.10 can be firstly seen at around 654 s of drying with the appearance of a bubble at the upper surface of the droplet (indicated by the red circle). This cavity appears moments after the start of the formation of a solid layer at the surface of the droplet (at 591 s). As the drying progresses, the hollow

core grows in diameter and can be followed with the help of the camera, thanks to the small evaporation rate at 20 °C.
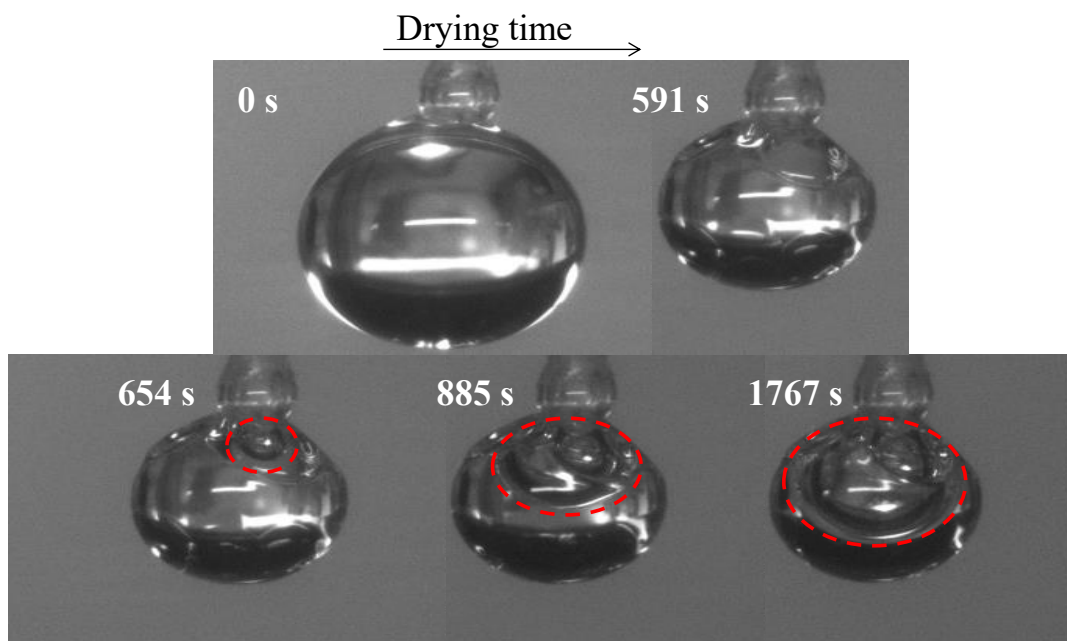
Figure 3.10 – Series of images representing the formation of a hollow core (indicated by the red circles) from the experiment 25D-5S (trial 23 in Table 3.4)

3.6.2 Peclet number superior to unity

The results presented here correspond to the trials (1), (2), (3) and (6) in Table 3.3 for the lactose-whey protein system and trials (9), (10), (11) and (14) for the dextran-sucrose system, which are trials performed with an air temperature at 40 °C and at 80 °C. For the experiments presented here, the rate at which the solid is formed is higher than the one seen in the previous section. As a result, important drying features, as the beginning of the crust formation and the time when the surface is completely covered by a solid layer, may not be precisely captured by the camera (this difficulty becomes more pronounced with the experiments at 80 °C).

In Figure 3.11, a series of images were taken from dextran-sucrose (series A) and lactose-WPI (series B) experiments (both with a solute proportion of 50:50, on dry basis) at 40 °C, for the sake of comparison. The time of the first solid appearance (at around 129 s) and the time of a surface covered by the solid (at approximately 171 s) are not very distant, as expected from the higher drying rate. It should be noted that for the lactose-WPI drying images, all the filament knob is immersed into the droplet at the beginning of the drying process. But, after the solid appearance at the droplet surface, the wet particle stays in suspension at only a fraction of the filament knob (the particle is oriented in the direction opposite to where the camera is placed). As a result, the particle could be taken out of the filament without much loss of solid matter, but not as easy as with the dextran-sucrose particles.
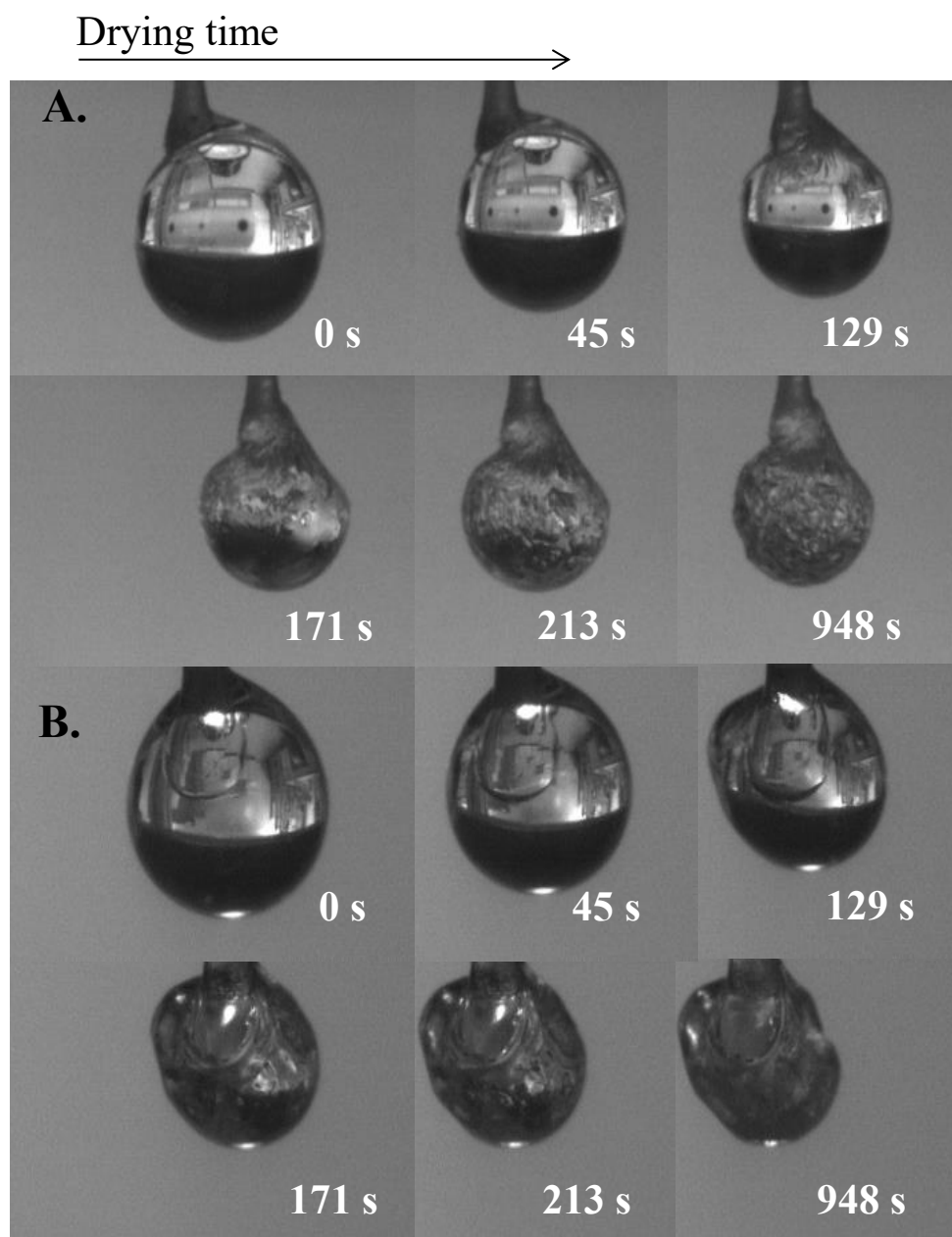
Figure 3.11 − Series of images taken from the experiments at 40 °C with a droplet containing (A) 15D-15S and (B) 15L-15WPI. Trials 10 (A) and 2 (B) in Table 3.3

In Figure 3.12, the images were taken from trials performed at 80 °C for the dextran-sucrose (series A) and lactose-WPI (series B) particles (both with a solute proportion of 50:50, on dry basis). Here, the image taken for representing the moment of appearance of a solid at the droplet surface (at 45 s) shows a surface layer covering almost the totality of the surface. For the dextran-sucrose particle, the droplet/wet particle loses its sphericity once a solid layer covers the droplet surface. Due to the high drying rate, the wet particle diameter is rapidly locked, which prevents the droplet from keeping its spherical shape through surface tension.

Drying time
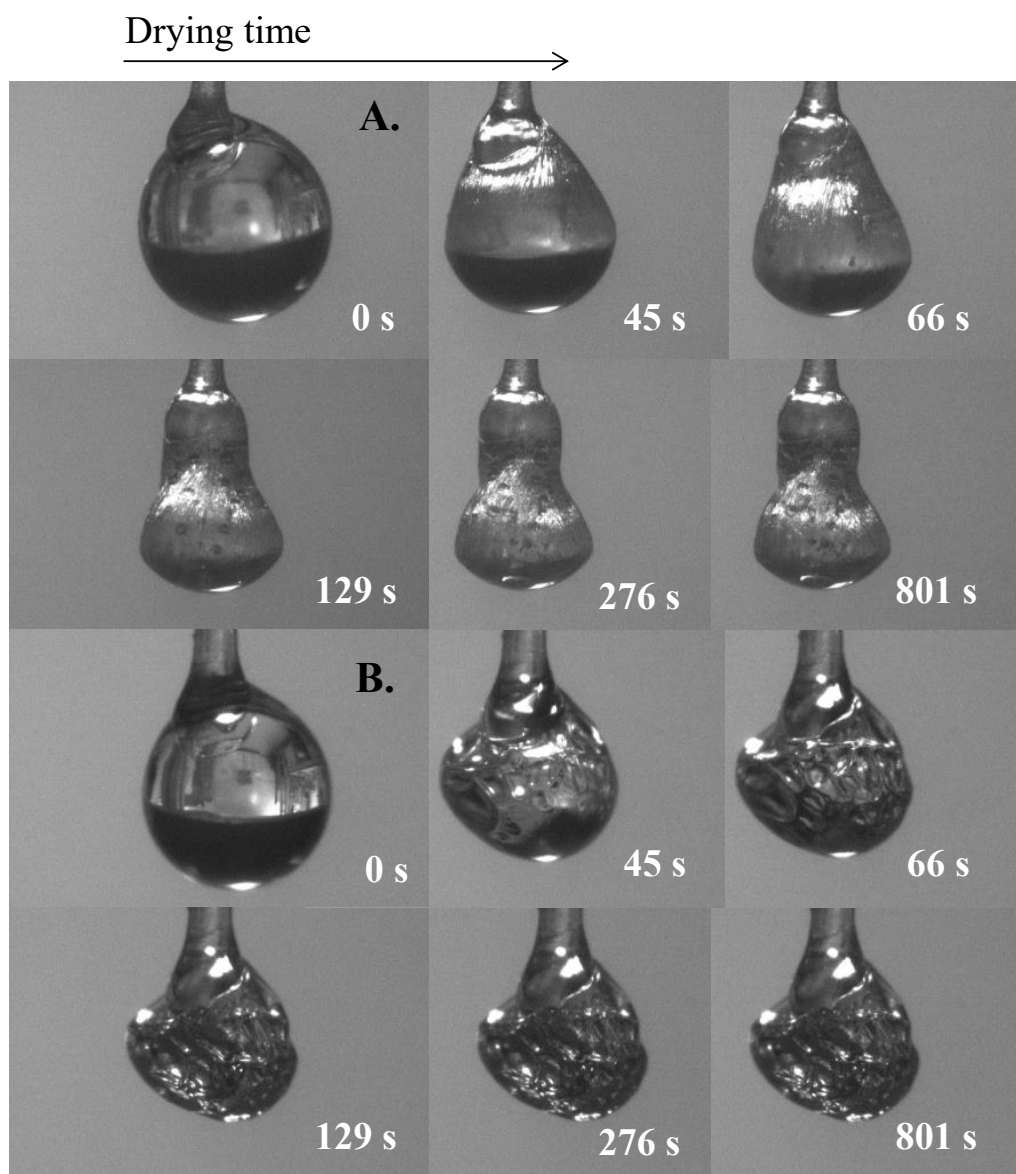
Figure 3.12 − Series of images taken from the experiments at 80 °C with a droplet containing (A) 15D-15S and (B) 15L-15WPI. Trials 9 (A) and 1 (B) in Table 3.3

The dextran-sucrose particles obtained with a high Peclet number are presented in Figure 3.13 with their respective SEM micrographs. The first image presents a dense core particle obtained from 15D-15S at 40 °C. It presents a dense core and a fairly smooth surface. The second and third images presented in this figure are produced from different experimental conditions leading to the same Peclet number. The second image represents a dextran-rich particle (15D-5S), which the external aspect presents big dimples. The third image represents a sucrose-rich particle (5D-15S) produced at 80 °C. It presents a fairly smooth surface and a dense core. The fourth image represents the particle obtained at the highest Peclet number from the experimental matrix. It

was produced with dextran-sucrose mass contents 15D-15S, at 80 °C. From the SEM micrograph, this particle seems to possess a dense core.
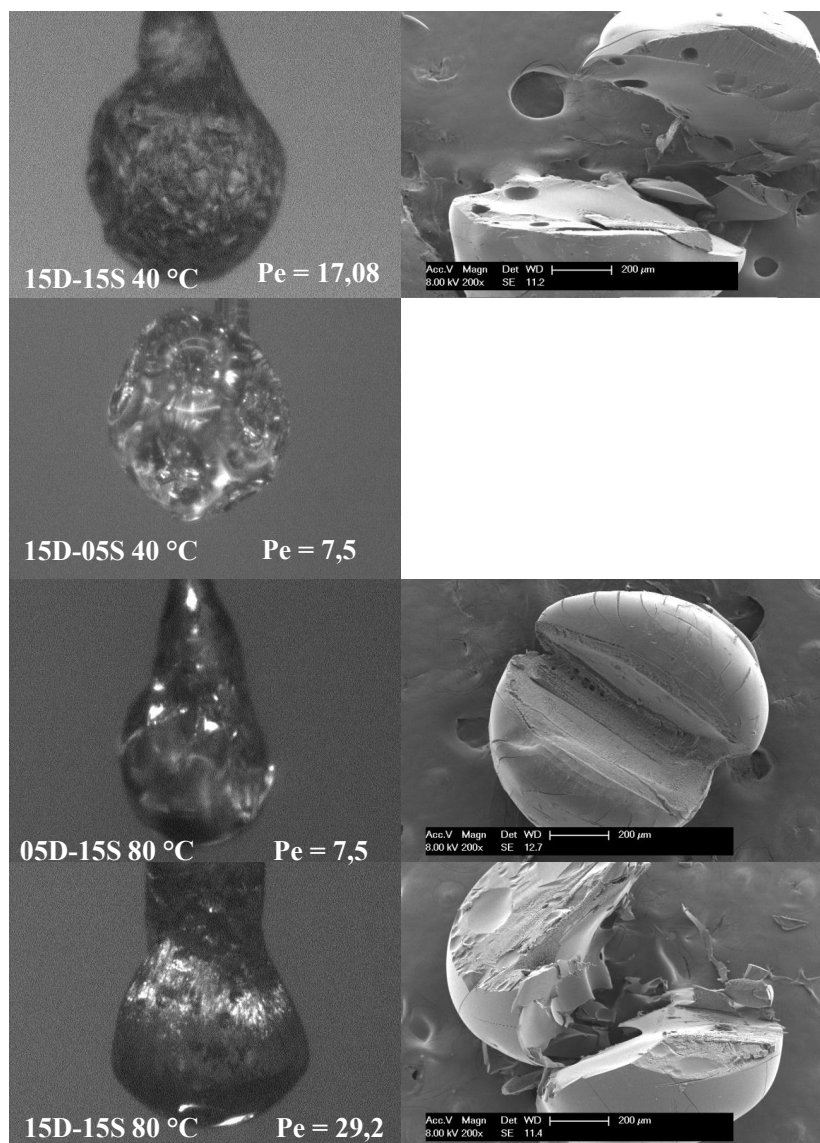
Figure 3.13 – Dextran-sucrose particles produced with the droplet-suspension set-up at a high Peclet number. Trials 10, 11, 14 and 9 from Table 3.3. The dextran and sucrose mass contents are indicated by xD-yS in each particle image

In Figure 3.14, the particles produced from the lactose-WPI system are presented with their respective SEM micrographs. The first image represents a particle produced at 40 °C with solute proportion at 50:50, on dry basis (15L-15WPI). Even though the droplet surface aspect cannot be well distinguished from the SEM micrograph, the camera image shows a rather wrinkled surface. From the micrograph, the particle seems to possess a hollow core. The second and third images represent experiments carried out with the same Peclet number. The second image represents the protein-rich particle (5L-15WPI) produced at 40 °C. In this trial, a hollow core particle with a smooth

surface was produced. Such a fragile crust makes the handling difficult, which is why the SEM micrograph only presents one small portion of the solid crust.
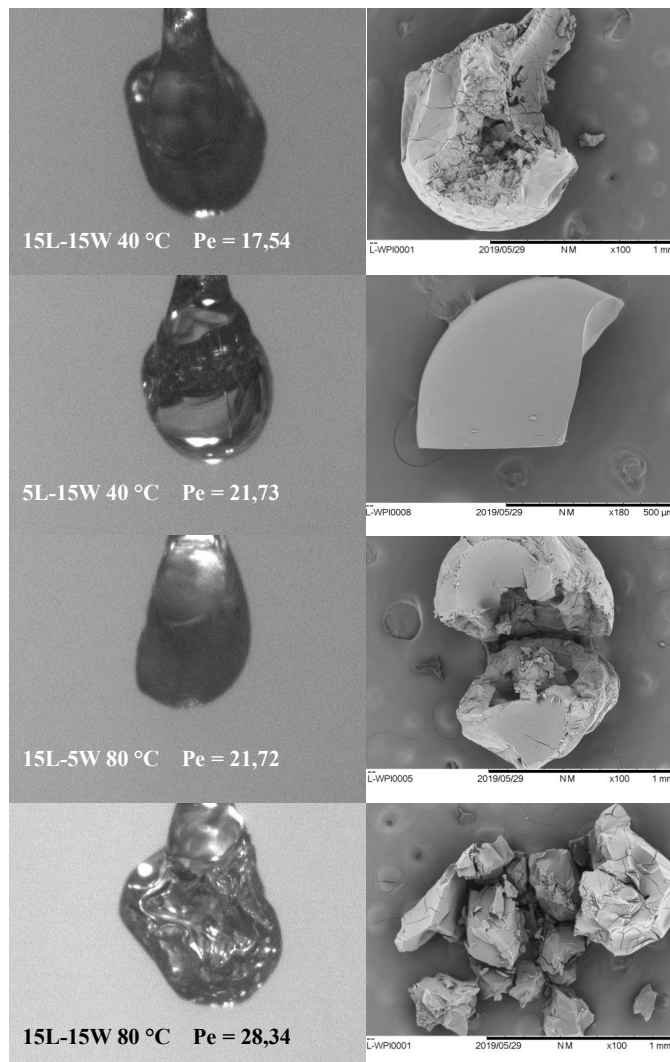
Figure 3.14 − Lactose-Whey protein isolate particles produced with the droplet-suspension set-up at a high Peclet number. The images obtained from the set-up are coupled with the corresponding particles SEM micrographs. Trial 2, 3, 6 and 1 in Table 3.3. The lactose and whey protein isolate mass contents are indicated by xL-yW in each particle image

The third image represents a lactose-rich particle (15L-5WPI) produced at 80 °C, where the particle is suspended at the opposite side of the filament facing the camera. The resulting particle morphology is a hollow core particle with a wrinkled surface. Likewise, the particle presented in the fourth image possesses a wrinkled surface as shown from the camera image. But, as for the SEM micrograph, no information regarding the particle morphology can be extracted (due to the brittle aspect of this particle crust, the particle shattered into pieces when cut with the scalpel).

3.6.3 Morphology comparison with the spray-scale experiments

Now that the particle morphologies have been presented from trials at the droplet scale in the two previous sections, it is possible to compare them with the morphologies generated at a higher drying rate at the spray scale in Chapter 2.

For the dextran-sucrose system:

- 5D-5S: particles with a smooth surface at both spray (Figure 2.10-B) and droplet scales. The dense core was observed at the droplet scale and inferred from the volume of occluded air at the spray scale;

- 5D-15S: particles with fairly smooth surface and a dense core at both spray (Figure 2.9-F) and droplet scales;

- 15D-5S: particles with big dimples at both spray (Figure 2.9-C) and droplet scales;

- 15D-15S: particles with a smooth surface at both spray (Figure 2.10-D) and droplet scales. The dense core was observed at the droplet scale and inferred from the volume of occluded air at the spray scale;

- 5D-25S: particles presenting a smooth surface at both spray (Figure 2.9-E) and droplet scales;

- 25D-5S: particle with a smooth surface and hollow core at the droplet scale. Particle with big dimples at the spray scales (Figure 2.9-B).

For the lactose-WPI system:

- 5L-15WPI: hollow core particles with a smooth surface obtained at both spray (Figure 2.7-F) and droplet scales;

- 15L-5WPI: hollow core particles with a wrinkled surface at both spray (Figure 2.7-C) and droplet scales;

- 15L-15WPI: particles with a wrinkled surface at the droplet and the spray scales. Hollow core at the spray scale (Figure 2.8-C), but harder to identify at the droplet scale.

The particle morphologies presented here clearly show a reproduction at the droplet scale of the morphologies obtained at the spray scale. The lactose-WPI droplets give way to hollow core particles, while the dextran-sucrose system generates dense core particles. Since the particle morphology could be scaled down, it indicates the importance of the liquid formulation in the definition of the final particle morphology. Moreover, the air temperature at the spray scale was much higher (at 103 °C) than that used in the droplet-suspension set-up, but the visual aspect of the solid crust was led by the proportion of the components used in the liquid formulation. Thus, following the results obtained here, it is possible to presume that in order to design a solid particle, the first parameter to be studied should be the proportion of the components present in the liquid droplet.

3.6.4 Characterization of the solid-state form

This section is dedicated to the results obtained from the use of a modulated differential scanning calorimetry (TM-DSC) for characterization of the solid-state of the final dried particles (i.e. crystalline, amorphous or a mixture of both).

The total signal of heat flow may be separated into reversing and non-reversing heat flows, as a result of the temperature modulation employed. Thermal transitions in the reversing signal arise from thermodynamic phenomena, such as glass transition temperature (T_g) and melting. The non-reversing signal exhibits kinetic phenomena, including evaporation and recrystallization. By plotting the reversing flow versus the temperature (as shown in Figure 3.15), the effect of solvent release is eliminated. This reveals a clear glass transition temperature resulting in a jump in the specific heat of the sample.
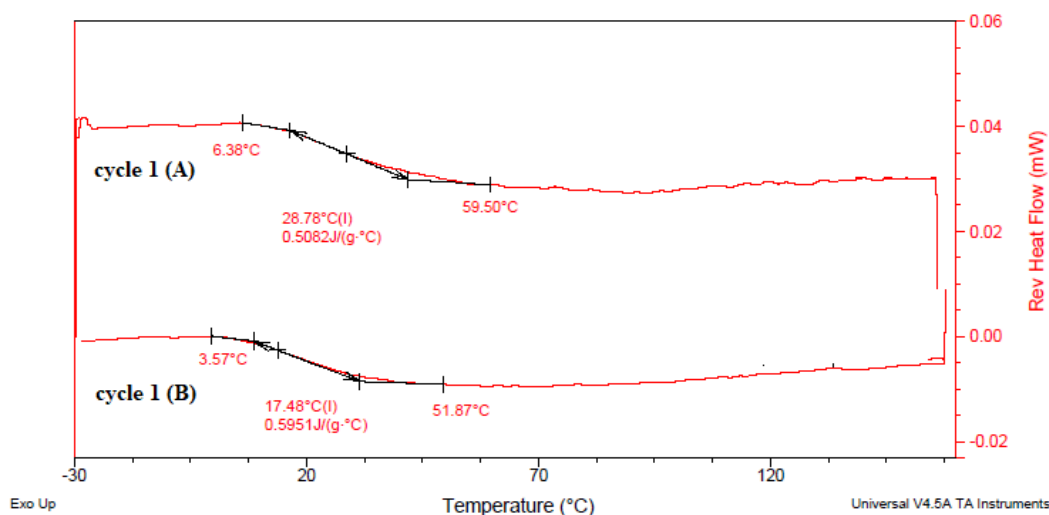
Figure 3.15 − DSC curves (heat flow against temperature) regarding the particles at 15D-15S and 40 °C (cycle 1 A) and 20 °C (cycle 1 B). The glass transition temperature (28.78 °C and 17.48 °C) in each trial is calculated as an integration between the onset temperature (here, 6.36 °C and 3.57 °C) and the offset temperature (here, 59.50 °C and 51.87 °C)

In Figure 3.15, the plot of reversing heat flow versus temperature is given for two particles obtained from initial mass contents 15D-15S (with the air temperatures at 20 °C and 40 °C). The T_g value was determined using the midpoint-by-half-height method. The results indicate the presence of only one T_g in each sample and, consequently, a single homogeneous amorphous phase of dextran-sucrose in the dried particle. The glass transition temperature obtained from the TM-DSC (the first cycle, as it corresponds to the thermal history of the sample) are presented in Table 3.6 for other dextran-sucrose particles and plotted in Figure 3.16.

It is interesting to note in Figure 3.16 an evolution of the T_g values given by the TM-DSC with an increasing dextran content in the solid particle. Such modification might arise from molecular interactions between the solutes contained in the sample, as stated in Starzak et al. [162]. Indeed, Imamura et al. [69] stated that in a sucrose-dextran

Table 3.6 – Glass transition temperatures obtained from the dextran-sucrose system from the first cycle performed with the TM-DSC. The trials are arranged according to the air temperature used in the drying experiment. Due to the small sample masses, the mass of sample and the residual water evaporated after the first cycle are presented

T_{ha} (°C)	Dextran : Sucrose mass content (% wt)	Dextran : Sucrose mass content, dry basis (% wt)	Sample mass in the TM-DSC (mg)	T_g (°C) (Cycle 1)	Residual water (%)
20	5:25	16:83	0.6440	6.52	7.8
	15:15	50:50	0.619	17.48	9.7
	25:5	83:16	0.5780	75.94	8.7
	15:15	50:50	0.5530	28.78	7.2
	15:5	75:25	0.4060	59.39	9.9
40					
80	5:15	25:75	0.4130	14.16	7.2
	15:15	50:50	0.6740	22.74	7.4

mixture, the intermolecular interactions are related to sucrose-sucrose, dextran-dextran and dextran-sucrose interactions. Furthermore, the strength of these interactions depend on the dextran and sucrose proportions in the sample. From low dextran contents up to 50 % wt (on dry basis), the dominant interaction in the solid comes from sucrose-sucrose. For dextran contents above 50 % wt (on dry basis), the dextran-dextran interactions become predominant. The variation in the T_g is much more pronounced at high dextran contents (above 50 % wt, on dry basis).
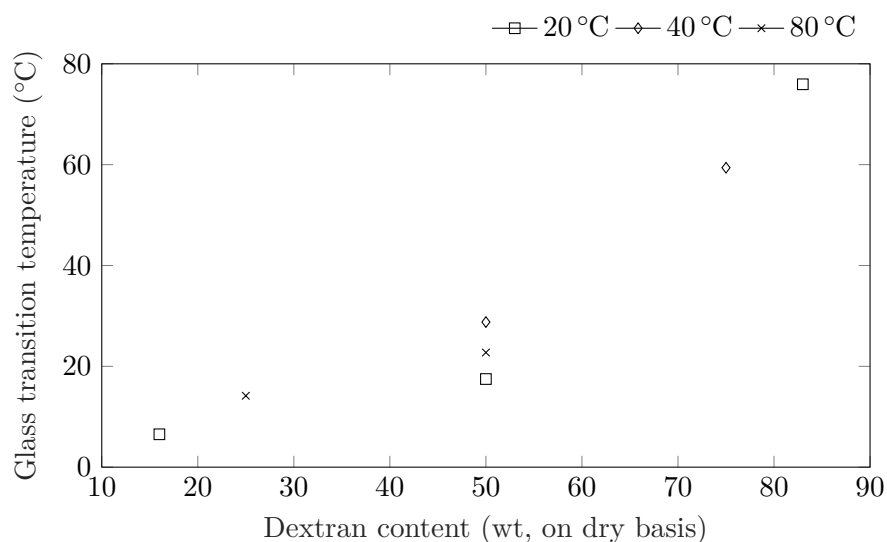
Figure 3.16 – Evolution of the glass transition temperature (from the first cycle in the TM-DSC) with increasing dextran content in the sample, on dry basis

Regarding the lactose-WPI system, the analysis of the heat flow curve presented two zones where a glass transition may take place. However, the intensity of such phenomena was very weak, which made it difficult for assessing precise T_g values. Such glass transition temperatures are shown in Figure 3.17 for the particle with initial mass contents 15L-15WPI (air temperature at 40 °C). For illustrative purposes only, the T_g evaluated for other lactose-WPI particles are presented in Table 3.7. These measurements can indicate the amorphous structure obtained from the lactose-WPI drying system. It can also indicate that the mixture of these components in the solid is not as homogeneous as in the dextran-sucrose system, due to the difference in the number of measured T_g. It should be interesting to deepen the analysis on the matter.
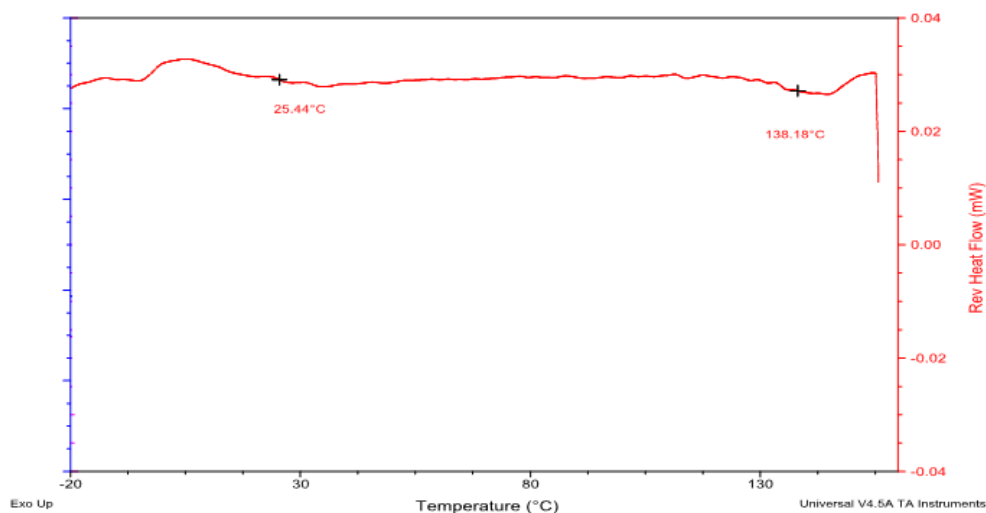
Figure 3.17 – DSC curve (heat flow against temperature) regarding the particle at 15L-15WPI wt and 40 °C. The glass transition temperatures are 25.44 °C and 138.18 °C

Table 3.7 – Glass transition temperatures obtained from the lactose-WPI system from the first cycle performed with the TM-DSC

$\mathbf{T}_{ha}$ (°C)	Lactose : WPI mass content (% wt)	$T_{g,1}$ (°C)	$T_{g,2}$ (°C)
40	15:15	25.44	138.18
80	15:5	42.59	124.31
	15:15	23.6	136.92

3.7 Drying behavior

This section is focused on the presentation of the shrinkage kinetics and the drying kinetics of the droplets considering the different experimental conditions proposed in the experimental matrix from Section 3.3. Regarding the shrinkage kinetics, the results are first shown for trials carried out at different air temperatures for the dextran-sucrose

system, but keeping the solute proportion constant. Such analysis is then used in the subsequent section for the presentation of the effect of the air temperature on the drying behavior of a dextran-sucrose droplet (from the same initial solute proportion), which covers the evolution of the mean moisture content over time and the drying flux. Next, the drying behavior is presented for a dextran-sucrose droplet under a convective and a diffusive drying. Finally, the analysis of the drying kinetics data is focused on the effect of the liquid formulation. The results shown here are displayed in Table 3.9. This table presents the experimental conditions employed in each trial (air properties and liquid formulation composition) and the corresponding Peclet number, along with the corrected initial mass of the droplet from the treatment presented in Section 3.5.2, the respective corrected initial mass of solutes and corrected initial moisture content ($X_{\mathrm{o}}^{\mathrm{cor}}$). Also, the Table 3.9 shows the normalized moisture content corresponding to the first appearance of a solid at the surface of the droplet ($X_{1\ \mathrm{sd}}^{\mathrm{n}}$) and the time as assessed from the camera ($t_{1\ \mathrm{sd}}$). Furthermore, the normalized moisture content when the crust is completely formed at the droplet surface ($X_{\mathrm{tc}}^{\mathrm{n}}$) and the corresponding time (t_{tc}) are also presented. The average and the respective standard deviation (σ) are also calculated for each trial performed in *duplicata*.

3.7.1 Shrinkage kinetics

The first aspect that should be considered regarding a drying droplet is its shrinkage behavior. Starting with a liquid droplet, its volume decreases over time due to moisture removal and, naturally, there is a reduction in the surface area available for mass transfer. However, as a solid phase is formed at the droplet surface, the reduction in the droplet volume is hindered. In Figure 3.18, the evolution of the droplet diameter (calculated following the description in Section 3.5.5) is presented from the trials 15D-15S, at the air temperatures of 20 °C, 40 °C and 80 °C and with an air velocity of 0.5 m s^{-1}. The trial at 20 °C under a convective air flow was not previously planned in the experimental matrix.

From the plot in Figure 3.18, it is possible to observe two tendencies in the droplet diameter reduction: a sharp decrease in the first moments of drying, followed by a slight reduction throughout the rest of the experiment. In order to differentiate these two tendencies, the data acquired from the camera was used for evaluating the time of appearance of the first solid at the surface of the droplet ($t_{1\ \mathrm{sd}}$) and the time where the solid crust completely covers the droplet surface (t_{tc}). These points are presented in Table 3.8 and represented as colored circles in Figure 3.18, where a different color is used for each air temperature.

Table 3.8 – The couple ($t_{1\ \mathrm{sd}}$, t_{tc}) for the the dextran-sucrose trials (15D-15S, $u_{\mathrm{ha}} = 0.5$ m s^{-1} and $Y_{\mathrm{ha}} = 3.5$ g kg^{-1}) and the corresponding droplet/wet particle diameters

Trial temperature	$t_{1\ \mathrm{sd}}$ (s)	$d(t_{1\ \mathrm{sd}})$ (mm)	t_{tc} (s)	$d(t_{1\ \mathrm{sd}})$ (mm)
20 °C	339	1.02	444	1.02
40 °C	87	1.16	150	1.13
80 °C	45	1.31	66	1.21
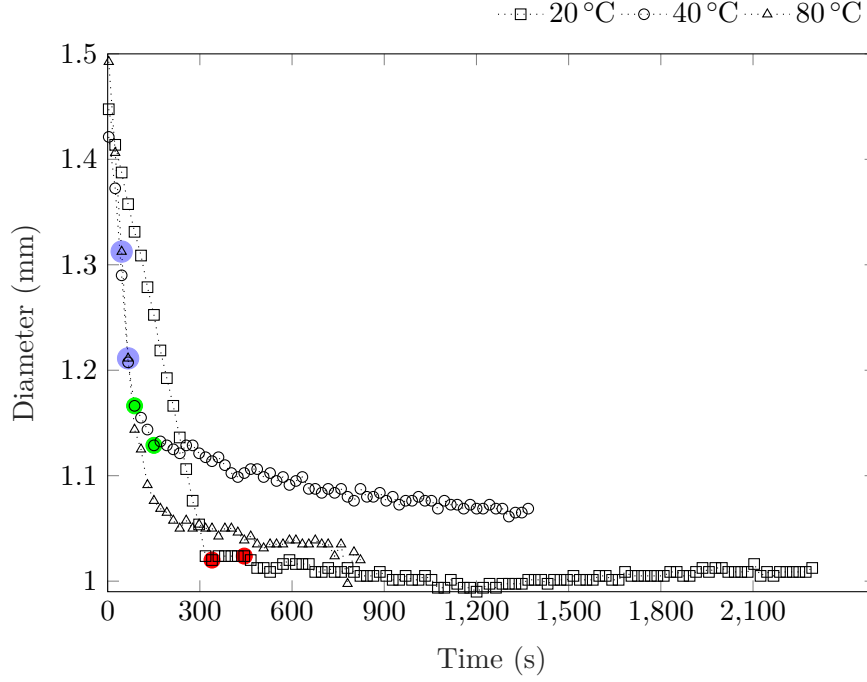
Figure 3.18 – Evolution of the droplet diameter from the trials with 15D-15S, at the air temperatures of 20 °C, 40 °C and 80 °C. The appearance of the first solid at the droplet surface and the covering of the surface by the crust are represented in the plot as colored circles (green, red and blue)

From the curve at 20 °C, a clear change in the curve slope is found for the time of first appearance of solid (first red dot). The second point, t_{tc}, is already associated to the slow-shrinking rate. The same tendency can be found from the experiment at 40 °C. For the trial at 80 °C, the droplet losses its sphericity due to the fast drying rate (as already highlighted in Figure 3.12). As a result, the diameter calculated from the image analysis is different from the droplet diameter that could have been obtained without the presence of the filament. Furthermore, the points $t_{1\ sd}$ (the time of appearance of the first solid at the surface of the droplet) and t_{tc} (the time where the solid crust completely covers the droplet surface) appear to belong to the same straight line, the high shrinking-rate curve. Finally, the first slope in the diameter-evolution curve represents a liquid droplet, while the second one represents a wet particle. It is interesting to note that even after the formation of a crust, the wet particle continues to contract slightly.

In order to evaluate if the shrinkage experienced by the droplet is ideal or not, which means that there is a proportionality between the volume reduction of the sample with the mass of water evaporated in the ideal case, the droplet volume was plotted against the normalized moisture content [90]. The droplet volume was calculated based on the volume of a sphere with the diameter presented in Figure 3.18. The resulting plot is shown in Figure 3.19 for the three temperatures. $t_{1\ sd}$ and t_{tc} were used for evaluating the corresponding sample moisture content (X) for the three curves. $X_{1\ sd}$ (when the first solid appears) and X_{tc} (when the crust covers the droplet surface) are represented as colored dots in Figure 3.19.
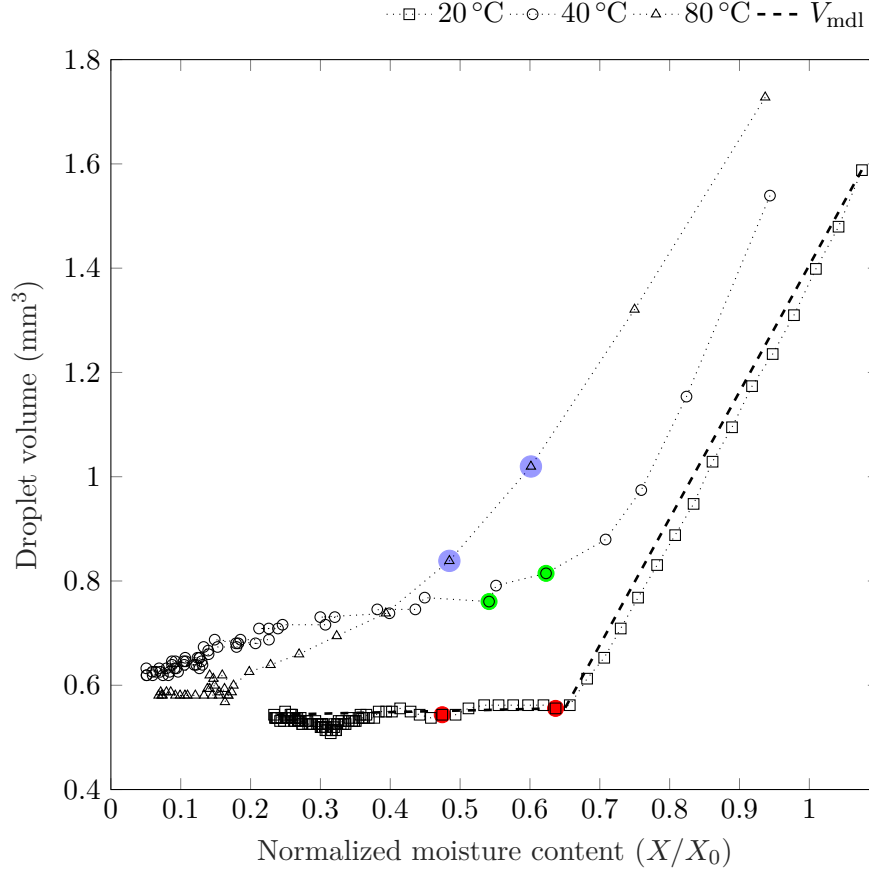
Figure 3.19 – Evolution of the droplet volume with the normalized moisture content from the trials with 15D-15S, at the air temperatures of 20 °C, 40 °C and 80 °C. The colored circles represent, from right to left, the appearance of a first solid at the surface and the covering of the surface by the crust. The dashed line represents the ideal shrinkage before and after the point of appearance of a solid

Using the point of first appearance of a solid at the droplet surface for differentiating the two slopes in the shrinkage curve, the volume of the droplet for a moisture content superior to $X_{1 \text{ sd}}$ can be represented as follows,

$$V = V_0 + \gamma \left(\frac{X - X_0}{X_0} \right) \tag{3.21}$$

Where V_0 is the initial volume, γ is a volumetric shrinkage coefficient and X_0 is the initial moisture content. Now, for a moisture content inferior to the point $X_{1 \text{ sd}}$, the volume reduction can be expressed as follows,

$$V = V_{\text{f}} + \alpha \left(\frac{X - X_{\text{f}}}{X_0} \right) \tag{3.22}$$

Where V_{f} is the final particle volume, α is the volumetric shrinkage rate from the slow drying rate and X_{f} is the final moisture content attained at the end of drying. The

result of equations 3.21 and 3.22 is plotted as a dashed line (V_{mdl}) in Figure 3.19 for the trial at 20 °C.

For a droplet drying at a low drying rate, as observed in the trial at 20 °C, it is indeed possible to observe the ideal shrinkage behavior of the droplet. The time scale for the droplet morphological evolution can be accurately captured by the camera, which helps in the precise definition of the moment of the appearance of the solid crust and its further development. Thus, the change in the shrinkage slope, as presented in Figure 3.19 is well defined by the appearance of the first solid. Also, two thirds of the droplet volume is lost before attaining the low-shrinking rate. After the appearance of the first solid at the droplet surface, the wet particle volume is reduced by only 1.8 %. In the trial at 40 °C, the droplet morphological changes occur more rapidly and the precision in the definition of the time of appearance of the crust is reduced. After the appearance of the first solid at the droplet surface, the volume of the wet particle is reduced by 24 %. For the trial at 80 °C, the definition of a change in the shrinkage rate with the appearance of the first solid at the droplet surface is less discernible for this trial. An important reduction in the wet particle volume (i.e. 46 %) was observed in the low-shrinking rate period.

3.7.2 Drying kinetics

After the presentation of the droplet shrinkage kinetics in the previous section, the present section is dedicated to the discussion of the droplet drying kinetics (here, the evolution of the sample moisture content through time). The effects of the air temperature on the drying of the droplet are first emphasized. Then, the drying behavior is presented for a dextran-sucrose droplet dried under an air flow (convective drying) and stagnant air (diffusive drying). Finally, the results displayed in Table 3.9 are compared between droplets dried under the same air properties but different liquid formulations, with a focus on the period of formation of the solid crust.

Influence of the air temperature

For evaluating the influence of the air temperature on the drying process, the trials should start from the same solute mass contents and be dried under the same air absolute humidity and velocity. The trials with mass contents 15D-15S are presented here. The normalized moisture content curve is presented in Figure 3.20. The colored points on the plots are the same points $t_{1\ sd}$ and t_{tc} as presented in the previous section.

From this figure, it is possible to visually divide the reduction in the moisture content into two distinct zones. A first zone with a steep decrease in the sample moisture content in the first moments of drying (before 500 s for the trial at 20 °C, for example) and a second zone where the sample moisture content varies slowly through most of the drying time. As the air temperature is increased, the transition between these two zones occurs sooner in the drying process and the slope of the normalized moisture content plot is modified. Indeed, rising the air temperature favors the moisture removal by an increase in the temperature difference between the air temperature and the droplet wet bulb temperature. Consequently, the moisture content varies more rapidly for the trial at 80 °C, compared to the one at 20 °C.

Taking into account the colored dots shown in Figure 3.20 (the first appearance of a solid and the crust complete formation), it is possible to see that the transition between
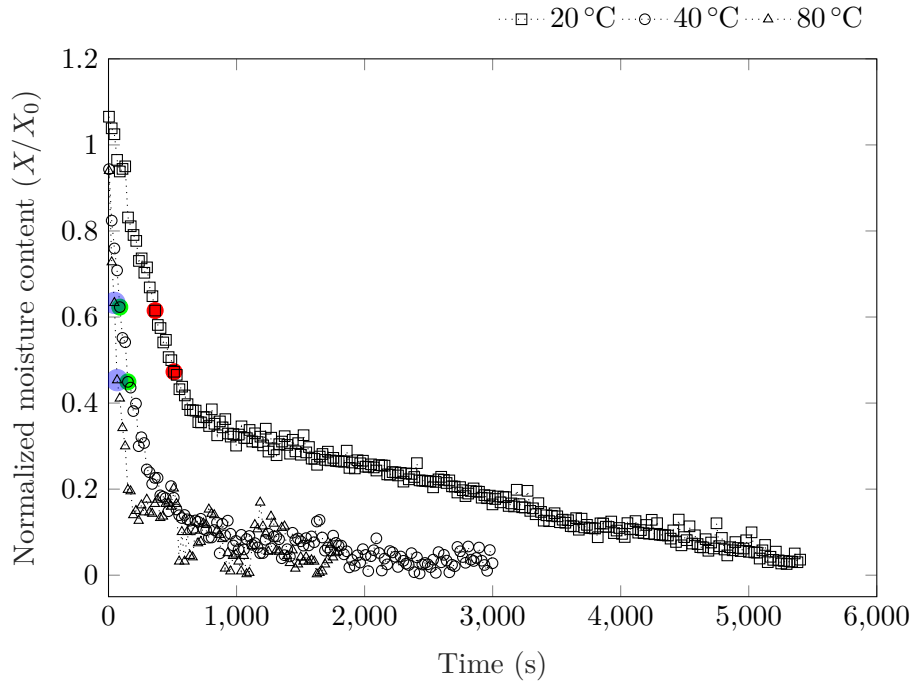
Figure 3.20 − Dextran-sucrose drying kinetics for the solution with mass contents at 15D-15S from 20 °C to 80 °C (air velocity at 0.5 m s^{-1} and air absolute humidity at 3.5 g kg^{-1}). The moisture contents related to the appearance of a first solid and the covering of the droplet surface by a crust are presented as colored circles

the liquid droplet and the wet particle takes place during the steep reduction in the moisture content. After the first solid appears, the sample moisture reduction still follows a quick pace, before the slope in the drying curve is changed. In order to help to better illustrate the drying behavior of the droplet/wet particle, the analysis can be carried out with the plot of the evaporation flux against the moisture content. The drying flux can be calculated as follows,

$$N_{\mathrm{v}} = -\frac{m_{\mathrm{ds}}}{S}\frac{\mathrm{d}X}{\mathrm{d}t} \tag{3.23}$$

Where N_{v} represents the drying flux, $\mathrm{d}X/\mathrm{d}t$ the drying rate (kg s^{-1} kg^{-1}), m_{ds} the mass of solutes (kg) and S is the surface area of a sphere representing the droplet/wet particle (m^2). In order to calculate the drying rate from the moisture plot, the data should first be fitted to a function capable of representing the drying process. The data fitting is necessary because any noise presented in the data is intensified in the values of the derivative function. Many methods are described in the literature for creating the best fit to represent the original drying data [73]. For example, the use of a second order polynomial function or, instead, two functions for representing the whole moisture content curve have been proposed. However, these cases cannot be applied to all drying processes. Here, the best fit was found through the use of a fourth or fifth polynomial order for representing the drying of the dextran-sucrose and lactose-WPI systems. The order of the polynomial function also depended here on the noise found

towards the end of each experiment. For the fitting function, a Savitzky-Golay filter is applied to the drying curves using Matlab software. With this smoothing function, a polynomial function is used to describe the "raw" data and the fluctuations are smoothed out by calculating a moving average with a predefined number of points. The higher the number of points used for the moving average, the smoother the result. Thus, the drying flux presented in Figure 3.21 was obtained using an average of 51 points for the creation of a smoother function. In this plot, the points of first appearance of a solid and the moment of surface covering by the crust are presented as colored points. For the sake of visualization, the drying flux was normalized to the values corresponding to the first drying stage (N_v'), which corresponds to the zone where the drying flux is nearly constant. The value of N_v' for the trials at 20 °C, 40 °C and 80 °C is equal to 1.6684×10^{-4} mg s^{-1} m^{-2}, 4.2197×10^{-4} mg s^{-1} m^{-2} and 7.4934×10^{-4} mg s^{-1} m^{-2}, respectively.
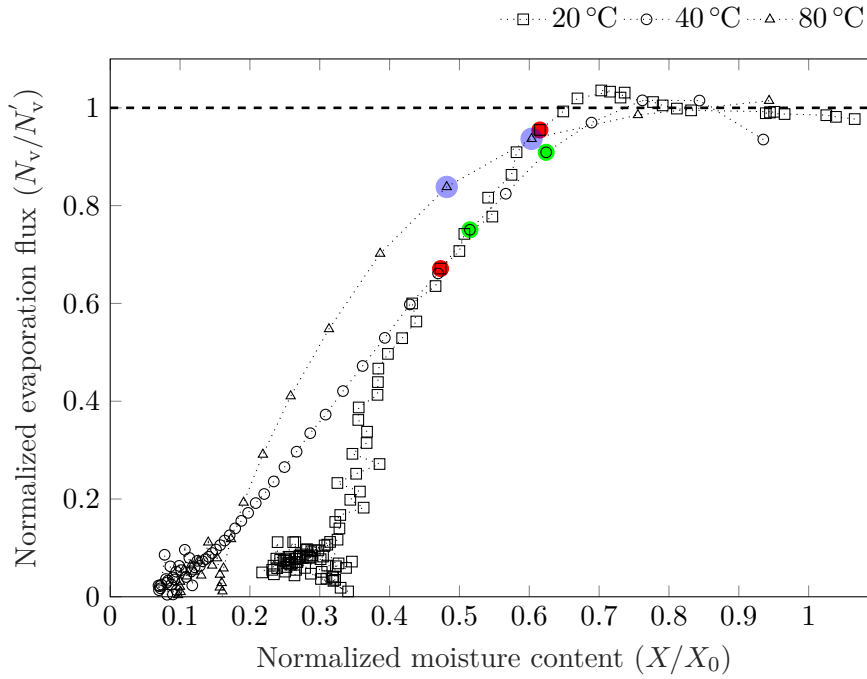
Figure 3.21 − Normalized drying flux (related to the first drying stage) for the trials with mass contents at 15D-15S from 20 °C to 80 °C (air velocity at 0.5 m s^{-1} and air absolute humidity at 3.5 g kg^{-1}). The moisture contents related to the appearance of a first solid and the covering of the droplet surface by a crust are presented as colored circles. The dashed line corresponds to the normalized drying flux at the first drying stage

With the drying behavior represented in the form shown in Figure 3.21, it is possible to clearly identify different drying phases, namely the first drying stage with the constant drying flux and the second drying stage, with the decrease in the drying flux. The heating up (or cooling down) period is too fast to be assessed by the weighing balance (with the predefined experimental settings). At the first drying stage, the heat and mass transfers are limited by the external conditions (at the boundary layer around the droplet), while enough unbound moisture is being supplied to the droplet surface

to keep the water activity at unity. The end of the first drying stage happens at some critical mean moisture content, where the water activity becomes inferior to unity at the droplet surface. The definition of such critical period was assessed through the use of the independent results from the camera and the weighing balance. As a matter of fact, it can be observed that the end of the first drying stage happens just before the first solid appears at the surface of the droplet, as the colored points presented in Figure 3.21 are placed at a normalized drying flux inferior to unity. This means that, before the visual perception of the solid appearance (by a modification in the light reflected from the sample surface), the water activity at the droplet surface becomes inferior to unity. The normalized moisture content of the points placed just before the colored circles in Figure 3.21 are 0.64, 0.68 and 0.75, for the trials at 20 °C, 40 °C and 80 °C, respectively. Even though the liquid formulation is the same (same initial solute mass contents), the onset of the falling-rate period happens at a higher normalized moisture content for higher drying air temperatures [152].

After the appearance of the solid crust, the water activity will continue to decrease towards an equilibrium value (which depends on the air temperature and absolute humidity) and the heat and mass transfers become limited inside the newly formed wet particle. As a result, the drying rate decreases. It is interesting to see that a part of the falling-rate period is placed in the zone of steep reduction of moisture content in Figure 3.20, for X/X_0 between 0.6 and 0.4 for the trial at 20 °C and between 0.6 and 0.2 for the other two trials. The change from both moisture transport rate in the falling-rate period may be related to a modification in the mechanism of moisture transport. It is possible to find in the literature [56] a division of the falling-rate period into two stages: one where the moisture is transported to the surface of the wet particle through diffusion (the first falling-rate period), and another where an evaporation front appears at the wet particle crust and the water is transported in vapor state through the solid crust and towards the surrounding drying air. However, by taking into account the BET surface area analysis presented in Chapter 2 and the fact that no clear porous structure could be observed from the SEM micrographs shown in the present chapter (which would explain a transport of vapor through the crust), it is more likely to presume that the adsorbed water is transported through other mechanisms towards the particle surface.

Regarding the end of the drying curves presented in Figure 3.21, the trials are performed in order to lead the solid particles to an equilibrium condition with the surrounding air at the end of the experiment. At equilibrium, the relative drying flux N_v/N_v' is equal to zero. The trial closer to equilibrium conditions is observed at 80 °C, with $N_v/N_v' = 0.003$. For the trials at 40 °C and 20 °C, $N_v/N_v' = 0.01$ and $N_v/N_v' = 0.05$. For the same air absolute humidity, an increase in the air temperature leads to a reduction in the air relative humidity. At equilibrium conditions, the solid particle water activity is equal to the relative humidity of the surrounding drying air. Since the particle water activity is related to the moisture content present in the solid structure, increasing the air temperature leads to a reduction in the equilibrium moisture content in the solid particle [169]. Such tendency could not be well distinguished between the trials at 80 °C and 40 °C, where the final normalized moisture content was equal to 0.09 and 0.08, respectively. For the trial at 20 °C, the normalized moisture content tends to a higher value.

Influence of the air velocity: diffusive and convective drying

For this section, the influence of the air velocity is presented for two trials carried out with the same liquid formulation (15D-15S), air temperature (at $20\,°C$) and air absolute humidity (at $3.5\,g\,kg^{-1}$), but with different conditions for the air flow. For one of these trials, no forced air flow is applied around the droplet, while for the other, an air velocity of $0.5\,m\,s^{-1}$ is used. The goal is to obtain drying kinetics data for a droplet drying under diffusive or convective regimes. The results are presented in Figure 3.22 with the moisture content being shown as colored circles when the first solid appears at the droplet surface and when the solid crust covers the droplet surface.
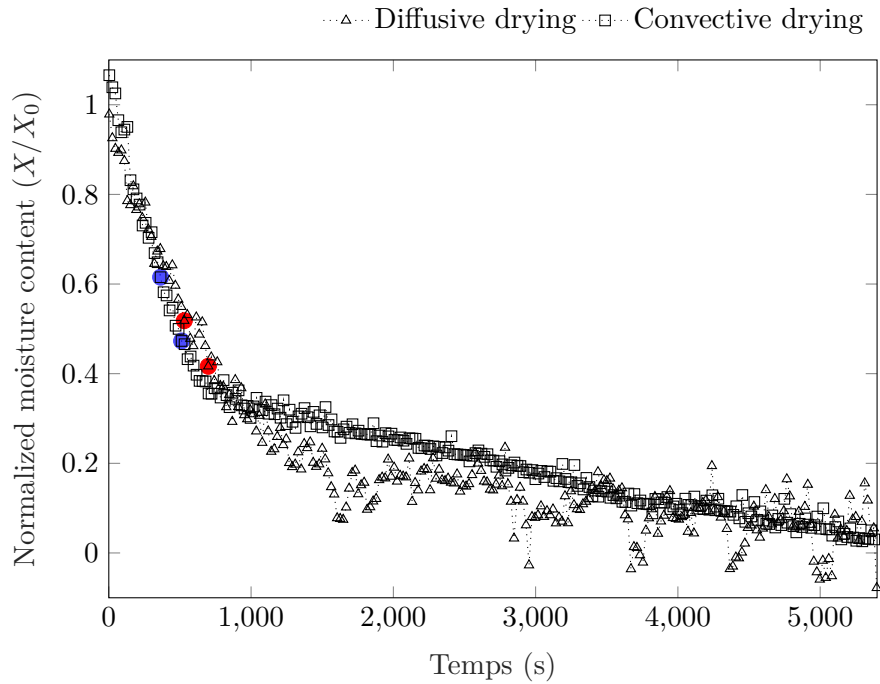
Figure 3.22 − Dextran-sucrose drying kinetics for a solution containing 15D-15S under diffusive (stagnant drying air) and convective (air velocity at $0.5\,m\,s^{-1}$) drying. The moisture content related to the appearance of a first solid and the covering of the droplet surface by a crust are presented as colored circles

From a first look at the results in Figure 3.22, the global aspect of the drying kinetics data (without considering the colored dots) seems unchanged by modifying the air flow around the droplet. However, from a closer inspection, it is possible to observe a small modification in the slope (drying rate) between the drying curves, which is higher for the trial under the convective drying. Indeed, for the first stage of drying, the role of the air velocity around the droplet is observed on the magnitude of the mass and heat transfers between the droplet surface and the air, where a higher air velocity enhances the drying rate during the first drying stage. Thus, the end of the first drying stage arrives sooner for the droplet under the convective air flow. In Figure 3.22, the first drying stage, which corresponds to the straight lines from the initial normalized moisture content until the first colored circle in each curve, the trial under a convective drying presents a shorter first drying phase (appearance of the solid at the droplet surface at $t_{1\,sd} = 375$ s), compared to the trial under stagnant air ($t_{1\,sd} = 522$ s). Accordingly, the

normalized moisture content related to these times are $X^n_{1\,sd} = 0.62$ and $X^n_{1\,sd} = 0.54$ for the convective drying and diffusive drying, respectively.

Regarding the falling rate period, where the mass and heat transfers around the droplet are no longer limiting with respect to the transport of adsorbed water in the wet particle, a modification in the air velocity should have a minor effect on the drying flux. In Figure 3.22, after the appearance of the crust at the solid surface, the modification in the pace of moisture removal from the wet particle happens at approximately $t = 638$ s (with a corresponding normalized moisture content at $X^n = 0.38$) for the trial under an air flow, against $t = 1000$ s and $X^n = 0.31$ for the trial under stagnant air (such difference in time comes from the different duration of the first stage of drying). Between the point of first appearance of a solid and the point of change of moisture removal rate, the normalized moisture content is decreased by 0.24 $(0.62 - 0.38)$ in 263 s for the trial under an air flow, while for the trial under stagnant air the normalized moisture content is also reduced by 0.24 $(0.54 - 0.31)$, but in 478 s. After the point of modification of the moisture rate, the normalized moisture content is reduced by approximately 0.30 in 4500 s for both trials. So, it would seem that the air flow still has an influence in the rate by which the moisture is removed from the wet particle during the period of steep reduction in the moisture content. Such influence cannot be observed after the point of modification of the moisture rate in the falling-rate period.

Influence of the liquid formulation

The analysis of the drying kinetics here is focused on the period of the crust formation (with the normalized moisture content and the time for the appearance of the first solid and the complete crust formation on the droplet surface) from the different trials shown in Table 3.9.

The trials presented in the set (I) in Table 3.9 correspond to trials presented previously in Table 3.4 with a Peclet number inferior to unity. The dextran-sucrose mass contents presented in Table 3.4 were 5D-5S, 5D-25S, 15D-15S and 25D-5S. It should be noted that two more liquid formulations (20D-10S and 30D) were carried out in order to help displaying a relation between the normalized moisture content at which the first solid is formed and the initial dextran mass content in the solution.

The trials presented in the set (I) were performed under an air absolute humidity ranging from $2.4\,\mathrm{g\,kg^{-1}}$ to $4.7\,\mathrm{g\,kg^{-1}}$, which at $20\,°C$ represent a relative humidity between $17\,\%$ and $32\,\%$, respectively. However, as can be seen in Figure 3.23, the influence of such small absolute humidity range over the drying rate is not very distinguishable between these trials. Consequently, the comparison of drying behavior here can be regarded as only an effect of the solutes present in the liquid phase.

Considering the trials presented in Figure 3.23, the total solute mass content is equal to $30\,\%$ wt and only the proportion of the solutes is changed. The trial with a higher mass content of dextran ($25\,\%$ wt) formed the first solid with a higher mean moisture content (the normalized value here is equal to 0.62). For these three trials, as the initial dextran concentration decreases, from $25\,\%$ wt to $5\,\%$ wt, the moisture content at which a first solid is formed decreases as well, from 0.62 to 0.42, which means that the first drying period is longer. These normalized moisture content values were plotted in Figure 3.24, along with the corresponding values from the other trials in set (I) with a total solute content at $30\,\%$ wt.
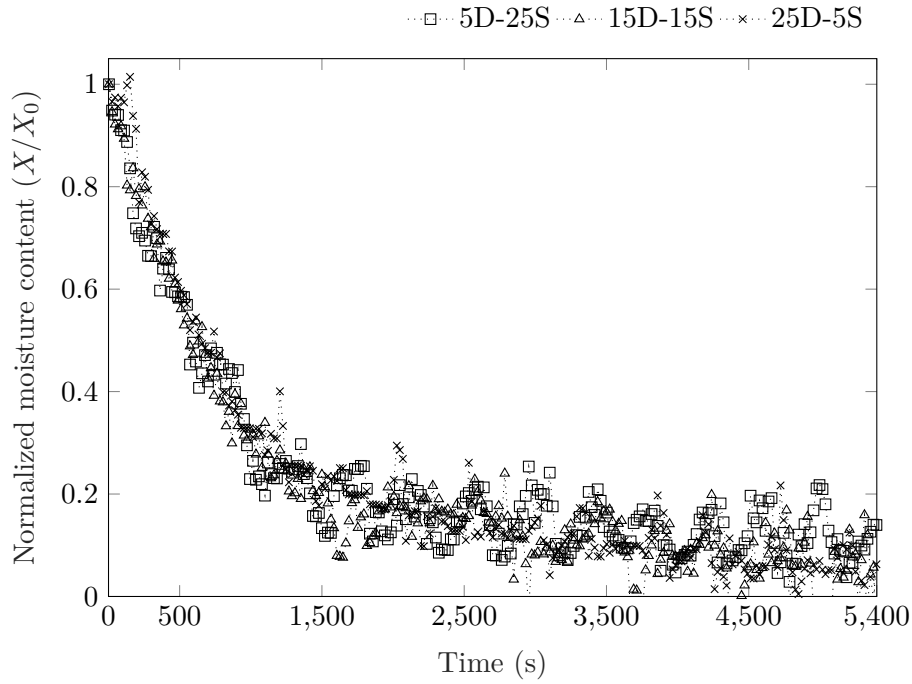
Figure 3.23 – Dextran-sucrose trials performed at $20\,°C$ with three different solute proportion. The absolute humidity employed here varies slightly from $2.4\,\mathrm{g\,kg^{-1}}$ to $4.7\,\mathrm{g\,kg^{-1}}$, however, the effect of such difference on the drying kinetics may be disregarded

From Figure 3.24, a linear relation between the values $\bar{X}^{\mathrm{n}}_{1\,\mathrm{sd}}$ and the dextran initial mass content in the dextran-sucrose mixture becomes evident, for a total solute content at $30\,\%$. Since these trials were performed under the same air properties, such relation can be regarded as only an effect of the liquid formulation, particularly the composition at the droplet surface, as both solutes present different solubilities (dextran is less soluble in water than sucrose as presented in Chapter 2 and a dextran-rich formulation attains more quickly a saturation value for the formation of the solid crust)

Regarding the normalized moisture content when the crust is completely formed, also for the trials presented in Figure 3.23, no value could be obtained for the trial with $25\,\%$ wt of sucrose. The formation of the solid layer at the surface of the droplet can be readily seen with the camera by a visual modification in the light reflected by the droplet. For the trial rich in sucrose, the moment of first appearance of a solid can be easily seen, but after this point no modification can be observed at the surface of the droplet (the camera is also limited to a certain number of pictures that did not correspond to the duration of this trial). Thus, a dried crust could have been formed at a time after the end of the image recording. The last image captured by the camera for this trial was presented in Figure 3.9, where the solid crust can be seen on the upper portion of the droplet. For the other two compositions, 15D-15S and 25D-5S, the crust covers the droplet surface at a higher moisture content for the trial at $25\,\%$ wt dextran ($\bar{X}^{\mathrm{n}}_{\mathrm{tc}} = 0.51$) than the trial at $15\,\%$ wt ($\bar{X}^{\mathrm{n}}_{\mathrm{tc}} = 0.42$). This tendency is similar to the one presented for the values of $\bar{X}^{\mathrm{n}}_{1\,\mathrm{sd}}$, with the crust being formed sooner with a higher dextran content in the initial solution.
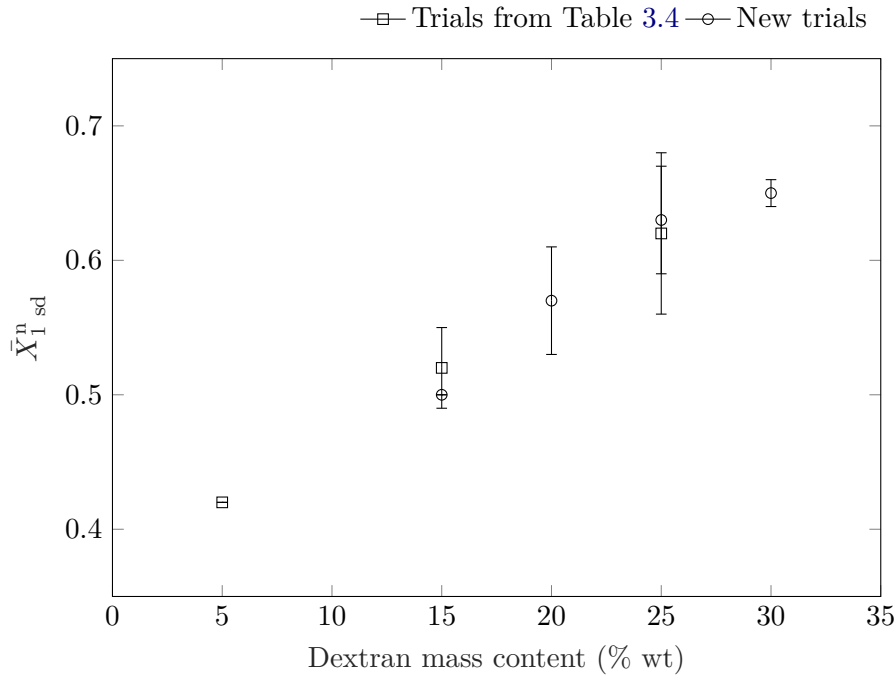
Figure 3.24 – Relation between the mean normalized moisture content at which the first solid appears and the initial dextran mass content in the dextran-sucrose solution. The trials represented here were carried out at 20 °C and the total solute content was equal to 30 % wt

Also at 20 °C, it is interesting to examine the effect of the total solute content from trials containing the same solute proportion (the trials 5D-5S and 15D-15S). As expected, the first drying stage lasts longer for the droplet with a smaller total solutes content (832 s, instead of 525 s for the trial 15D-15S), where more time is needed for attaining the solute saturation for the crust formation. Regarding the time for the crust to completely cover the droplet surface ($\bar{t}_{tc} - \bar{t}_{1\ sd}$), an important difference is observed between these two formulations, with 32 s for the more diluted droplet and 231 s for the trial 15D-15S (a duration six times larger than the former). Such difference in duration may arise firstly from the difference in the droplet size, and secondly from a difference in the composition at the droplet surface. From image analysis, the droplet with composition 5D-5S has a diameter of 0.71 mm when a first solid appears, while for the trial at 15D-15S the droplet diameter is approximately 1.1 mm. So, with a smaller surface, the crust would cover it more rapidly. As for the composition, if the droplet surface possesses a higher dextran content, the solid crust could be formed more rapidly.

Now, for the sets (II), (III) and (IV) in Table 3.9, the dextran-sucrose system is dried under different air temperatures, but with the same initial solute mass contents, 15D-15S (and the same air velocity and air absolute humidity). The values of $X_{1\ sd}^{n}$ are essentially the same for the three air temperatures in Table 3.9, with $\bar{X}_{1\ sd}^{n} = 0.6$, but the time for attaining such normalized moisture value for the trial at 20 °C is 8 times longer than the trial at 80 °C. Additionally, the time required for the crust to cover the droplet surface ($\bar{t}_{tc} - \bar{t}_{1\ sd}$) is 6 times longer for the trial at 20 °C than the time required at the

highest temperature, even though the difference $\bar{X}_{1\text{ sd}}^{\text{n}} - \bar{X}_{\text{tc}}^{\text{n}}$ is approximately the same ($\Delta\bar{X}^{\text{n}} = 0.12$) for the three temperatures.

In the sets (III) and (IV), the droplet containing lactose-WPI was also dried with an initial solute fraction at 15L-15WPI wt and under two different air temperatures (40 °C and 80 °C), with the same air velocity and air absolute humidity. The normalized moisture at which the first solid was visualized in the camera is very similar for both sets ($\bar{X}_{1\text{ sd}}^{\text{n}} = 0.82$ and $\bar{X}_{1\text{ sd}}^{\text{n}} = 0.79$), but the crust is formed sooner for the trials at the highest temperature. Also, the time for the crust to cover the droplet surface is 4 longer for the trial at 40 °C than the trial at 80 °C, in accordance to what was presented previously for the dextran-sucrose mixture. The sole disparity is related to the difference in the normalized moisture content between the points $\bar{X}_{1\text{ sd}}^{\text{n}}$ and $\bar{X}_{\text{tc}}^{\text{n}}$. For the system lactose-WPI, the value $\Delta\bar{X}^{\text{n}}$ at 80 °C is half of the value calculated for the trial at 40 °C, as if the effect of the solid crust on hindering the drying rate becomes more evident at the highest air temperature.

It is also possible to compare the drying behavior between the two drying systems in the sets (III) and (IV). Regarding the time for the crust appearance and covering of the droplet surface, a difference between both drying systems could only be observed at 40 °C. Furthermore, the normalized moisture content at which these steps take place is indeed higher for the lactose-WPI than for the dextran-sucrose system. For example, at 40 °C, $\bar{X}_{1\text{ sd}}^{\text{n}} = 0.82$ for the lactose-WPI system and $\bar{X}_{1\text{ sd}}^{\text{n}} = 0.61$ for the dextran-sucrose system, which gives a difference of approximately 34 % in the normalized moisture content. With the same time $\bar{t}_{1\text{ sd}}$, it is possible to say that the lactose-WPI system is drying faster.

For the sets (V) and (VI) in Table 3.9, the results will be discussed hereafter based on the effect of changing the solutes proportion (15:5 % wt and 5:15 % wt) for the same total solute content (20 % wt), on the drying behavior between the two drying systems, and finally the effect of the air temperature. As a matter of fact, even though the air relative humidity is 20 % for the conditions in set (V) ($T = 40$ °C and $Y = 9$ g kg^{-1}) and 2 % for the conditions in set (VI) ($T = 80$ °C and $Y = 3.5$ g kg^{-1}), the small influence of this parameter on the drying kinetics allows the comparison of the results between the sets (V) and (VI) without much error.

Starting with the effect of the solute proportion, the normalized moisture content at the first solid formation (for the dextran-sucrose mixture) in set (V) increases slightly with a higher content of dextran in the solution. Indeed, $\bar{X}_{1\text{ sd}}^{\text{n}}$ is changed from 0.58 to 0.62 when the dextran content is increased from 5 % wt to 15 % wt. In set (VI), the modification in the value $\bar{X}_{1\text{ sd}}^{\text{n}}$ is more noticeable, with an increase from 0.41 to 0.65 by increasing the dextran content in the solution. Such modification in the normalized moisture value would follow the trend presented previously with the trials at 20 °C in the set (I), even though the increase in the air temperature and consequently the drying rate may decrease the precision in evaluating such differences in the drying kinetics data. In the trials presented in Figure 3.24, more time was needed for the crust appearance in the solution containing less dextran. Such tendency is respected in the trials in the set (VI), but is reversed in the set (V). Such difference corresponds to an interval of one or two points in the drying kinetics curve. For the lactose-WPI system, no modification in the mean value $\bar{X}_{1\text{ sd}}^{\text{n}}$ could be observed in the set (V) with increasing whey protein content. However, in the set (VI), an increase in the whey protein content from 5 % wt to 15 % changed the value $\bar{X}_{1\text{ sd}}^{\text{n}}$ from 0.56 to 0.73. Here, the crust is formed sooner

for the solution with higher protein contents (for the trial at 80 °C). Again, the time interval is related to a two-point difference in the drying curve. Based on the solubility (at 20 °C) of both lactose and WPI, it would not be possible to explain the difference in time of appearance of the crust, because both solutes present similar solubilities (as presented in Chapter 2). However, whey protein has a surface active character due to the presence of hydrophobic groups in its chemical structure. In turn, some percentage of the protein present in the solution may be adsorbed at the droplet surface [5]. If increasing the protein mass content of the droplet would lead to a higher percentage of protein covering at the droplet surface, the time difference observed previously could be explained (with the protein leading to an early formation of the solid crust).

Taking into consideration the effect of the air temperature between the trials at 40 °C and 80 °C in the sets (V) and (VI) with the same initial solute mass contents, the values $\bar{X}_{1\,\text{sd}}^{\text{n}}$ given in Table 3.9 are very similar, despite the modification of the air temperature. The biggest differences are found for the experiments with a dextran-sucrose mixture at 5:15 % wt ($\bar{X}_{1\,\text{sd}}^{\text{n}} = 0.58$ at 40 °C and $\bar{X}_{1\,\text{sd}}^{\text{n}} = 0.41$ at 80 °C) and the drying of a lactose-WPI mixture at 5L-5WPI wt ($\bar{X}_{1\,\text{sd}}^{\text{n}} = 0.47$ at 40 °C and $\bar{X}_{1\,\text{sd}}^{\text{n}} = 0.66$ at 80 °C). It should be noted that the standard deviation for the dextran-sucrose mixture at 80 °C and the lactose-WPI mixture at 40 °C are one of the highest in the whole set of experiments in Table 3.9. Consequently, the discrepancy found here should actually be much narrower, which would then give similar values of $\bar{X}_{1\,\text{sd}}^{\text{n}}$, thus in accordance with the reasoning presented previously: liquid formulations with the same solute mass contents behave in a similar way despite the modification in the air temperature.

Finally, comparing the value $\bar{X}_{1\,\text{sd}}^{\text{n}}$ between the dextran-sucrose and lactose-WPI systems, in the sets (V) and (VI), the lactose-WPI system tends to start the process of crust formation at a higher mean normalized moisture content $\bar{X}_{1\,\text{sd}}^{\text{n}}$ and sooner, compared to the dextran-sucrose system. For example, at 80 °C, with the trials at 5:5 % wt, the onset of crust formation for the lactose-WPI mixture is at $\bar{X}_{1\,\text{sd}}^{\text{n}} = 0.66$ and $\bar{t}_{1\,\text{sd}}^{\text{n}} = 56$ s, while for the mixture dextran-sucrose $\bar{X}_{1\,\text{sd}}^{\text{n}} = 0.49$ and $\bar{t}_{1\,\text{sd}}^{\text{n}} = 87$ s. Using a smaller air velocity here ($u = 0.2$ m s^{-1}), compared to the set (IV) with $u = 0.5$ m s^{-1}, allowed a reduction in the drying rate and, consequently, a better distinction between the drying behavior of both drying systems. As a matter of fact, the lactose-WPI system dries faster and the solid crust is formed at higher moisture contents.

Table 3.9 – Summary of the drying results

	T_{air} (°C)	u_{air} (m/s)	Y_{air} (g/kg)	Comp.	ω (% wt)	Pe	m_{ini}^{cor} (mg)	m_{sd}^{cor} (mg)	X_o^{cor}	$\bar{X}_o/\sigma$	$X_{1\,sd}^{n}$	$\bar{X}_{1\,sd}^{n}/\sigma$	$t_{1\,sd}$	$\bar{t}_{1\,sd}/\sigma$	X_{tc}^{n}	$\bar{X}_{tc}^{n}/\sigma$	t_{tc}	$\bar{t}_{tc}/\sigma$
I	20	0	2.4	D:S	5:5	0.108	1.80	0.18	9.00	8.70 / 0.42	0.46	0.46 / 0.01	801	832 / 45	0.46	0.44 / 0.03	822	864 / 59
							1.79	0.18	8.94		0.46		864		0.42		906	
			2.4	D:S	5:25	0.453	2.04	0.61	2.34		0.42		735		-		-	
			3.5	D:S	15:15	0.869	1.96	0.59	2.32	2.33 / 0.01	0.54	0.52 / 0.03	522	525 / 4.24	0.42	0.42 / 0	711	756 / 63.6
							2.03	0.61	2.33		0.50		528		0.42		801	
							1.94	0.58	2.32	2.32 / 0	0.50	0.50 / 0	948	856 / 130	0.39	0.41 / 0.02	1039	1013 / 37
							1.87	0.56	2.32		0.50		764		0.42		987	
			3.5	D:S	20:10	1.18	1.95	0.58	2.33	2.33 / 0	0.59	0.57 / 0.04	696	772 / 107	0.54	0.52 / 0.04	801	880 / 111
							1.92	0.58	2.33		0.54		848		0.49		958	
			4.7	D:S	25:5	1.16	1.75	0.53	2.30	2.31 / 0.01	0.66	0.62 / 0.06	402	444 / 59	0.50	0.51 / 0.01	612	602 / 15
							1.91	0.58	2.32		0.58		486		0.52		591	
			3.5	D:S	30:0	1.74	1.88	0.57	2.32	2.32 / 0	0.60	0.63 / 0.04	672	591 / 115	0.62	0.57 / 0.07	829	686 / 202
							1.69	0.51	2.32		0.65		509		0.52		543	
							1.69	0.51	2.33	2.33 / 0	0.65	0.65 / 0.01	690	609 / 115	0.60	0.59 / 0.01	777	705 / 102
							1.61	0.48	2.33		0.64		528		0.58		633	
II	20	0.5	3.5	D:S	15:15	9.74	2.09	0.57	2.68	2.68 / 0	0.62	0.6 / 0.03	375	357 / 25	0.48	0.46 / 0.03	504	478 / 37
							2.00	0.54	2.68		0.58		339		0.44		452	
III	40	0.5	3.5	D:S	15:15	17.08	2.09	0.63	2.32	2.33 / 0.01	0.62	0.61 / 0.01	87	108 / 30	0.47	0.49 / 0.03	150	161 / 15
							1.87	0.56	2.34		0.60		129		0.51		171	
				L:W	15:15	17.54	1.97	0.59	2.34	2.34 / 0	0.90	0.82 / 0.12	87	87 / 0	0.75	0.68 / 0.1	171	160 / 15
							1.97	0.59	2.34		0.73		87		0.61		150	
IV	80	0.5	3.5	D:S	15:15	29.20	2.19	0.66	2.32	2.33 / 0.01	0.60	0.59 / 0.01	45	45 / 0	0.48	0.48 / 0.01	66	66 / 0
							1.80	0.54	2.33		0.58		45		0.47		66	
				L:W	15:15	28.34	2.01	0.60	2.35	2.35 / 0.01	0.78	0.79 / 0.01	45	45 / 0	0.73	0.72 / 0.01	66	66 / 0
							1.97	0.59	2.34		0.79		45		0.71		66	

Table 3.9 : Continued

	T_{air} (°C)	u_{air} ($\frac{m}{s}$)	Y_{air} ($\frac{g}{kg}$)	Comp.	ω (% wt)	Pe	m_{ini}^{cor} (mg)	m_{sd}^{cor} (mg)	X_o^{cor} ($\frac{mg}{mg}$)	$\bar{X}_o/\sigma$	$X_{1\,sd}^n$	$\bar{X}_{1\,sd}^n/\sigma$	$t_{1\,sd}$ (s)	$\bar{t}_{1\,sd}/\sigma$	X_{tc}^n	$\bar{X}_{tc}^n/\sigma$	t_{tc} (s)	$\bar{t}_{tc}/\sigma$
V	40	0.2	9	D:S	15:5	7.50	1.72	0.35	3.91	3.94	0.58	0.62	171	182	0.46	0.52	213	224
							1.74	0.35	3.97	/ 0.04	0.65	/ 0.05	192	/ 15	0.57	/ 0.08	234	/ 15
					5:15	3.16	1.85	0.37	3.99	3.99	0.56	0.58	171	161	0.51	0.52	192	180
							1.81	0.36	3.99	/ 0	0.59	/ 0.02	150	/ 15	0.53	/ 0.01	168	/ 17
					5:5	2.74	1.82	0.18	8.97	8.97	0.59	0.54	192	203	0.47	0.43	219	239
							1.89	0.19	8.97	/ 0	0.48	/ 0.08	213	/ 15	0.38	/ 0.06	258	/ 28
				L:W	5:15	21.73	1.77	0.35	4.06	4.02	0.63	0.69	150	150	0.55	0.58	192	203
							1.79	0.36	3.97	/ 0.06	0.74	/ 0.08	150	/ 0	0.60	/ 0.04	213	/ 15
					15:5	1.46	1.72	0.34	4.00	4.00	0.68	0.68	108	108	0.60	0.61	129	129
							1.58	0.32	4.00	/ 0	0.68	/ 0	108	/ 0	0.61	/ 0.01	129	/ 0
					5:5	1.51	1.81	0.18	8.95	8.96	0.37	0.47	192	171	0.31	0.41	213	192
							1.60	0.16	8.96	/ 0.01	0.57	/ 0.14	150	/ 30	0.50	/ 0.13	171	/ 30
VI	80	0.2	3.5	D:S	5:15	7.50	2.03	0.41	3.95	3.95	0.31	0.41	150	108	0.17	0.25	192	150
							2.03	0.41	3.95	/ 0	0.51	/ 0.14	66	/ 59	0.32	/ 0.11	108	/ 59
					15:5	18.30	1.91	0.38	4.00	4.00	0.68	0.65	66	66	0.58	0.55	87	87
							2.12	0.42	4.00	/ 0	0.62	/ 0.04	66	/ 0	0.52	/ 0.04	87	/ 0
					5:5	6.51	1.90	0.19	10.0	9.5	0.46	0.49	87	87	0.39	0.41	108	108
							1.83	0.18	8.97	/ 0.75	0.51	/ 0.04	87	/ 0	0.42	/ 0.02	108	/ 0
				L:W	15:5	21.72	1.97	0.39	4.05	4.03	0.61	0.56	66	77	0.52	0.44	87	108
							2.10	0.42	4.00	/ 0.04	0.50	/ 0.08	87	/ 15	0.35	/ 0.12	129	/ 30
					5:5	10.37	1.50	0.30	4.00	4.00	0.62	0.73	45	35	0.47	0.59	66	56
							1.88	0.38	4.00	/ 0	0.84	/ 0.16	24	/ 15	0.70	/ 0.16	45	/ 15
					5:5	3.57	1.97	0.20	8.96	8.96	0.69	0.66	45	56	0.57	0.52	66	77
							1.80	0.18	8.96	/ 0	0.63	/ 0.04	66	/ 15	0.47	/ 0.07	87	/ 15

3.8 Summary of the main findings of the chapter

In this chapter, the experimental work is carried out at the droplet scale with a droplet suspended at the tip of a thin filament. In order to help evaluating the influence of the liquid formulation and the air properties on the droplet drying behavior, a set-up was specifically designed during this thesis. With this set-up, the drying kinetics could be assessed under well controlled air conditions, while a camera placed in front of the droplet provided information about the diameter evolution and modifications in the surface aspect (i.e. the appearance of the first solid and the covering of this solid crust at the surface of the droplet and the production of an entirely solid particle).

The experimental conditions employed here were chosen with the help of the Peclet number, as a guide to modify the generated solid particles morphology, primarily between dense and hollow core particles. It was possible to observe a modification in the particle morphologies from the different experimental conditions. Also, it was possible to state a resemblance between the morphologies obtained at the droplet scale and at the spray scale, even though at higher drying rates (at $80\,°C$) at the droplet scale, the droplet tended to lose the spherical shape while the solid crust was being formed. Furthermore, despite the higher drying times observed at the droplet scale, it was possible to identify by differential scanning calorimetry that the generated solid particles presented an amorphous structure. Additionally, by analyzing an important property of amorphous materials, the glass transition temperature, an important modification in this property was observed with an increase in the dextran content in the dextran-sucrose solid particles.

Regarding the drying behavior, it was possible to present that the reduction in the droplet diameter follows an ideal behavior from the image analysis (a better definition of the shrinkage kinetics could be obtained at lower drying rates, at $20\,°C$). For the drying kinetics, a treatment was applied to the drying data in order to ensure their validity. The analysis of the evaporation flux and the moisture content over time helped identifying interesting aspects regarding the different drying phases of the droplet: the initial heat-up (or cool down) period was too brief to be obtained here; the first drying stage could last until a mean critical moisture content was obtained, which corresponded to the appearance of the first solid at the droplet surface; the falling-rate period could be composed of two mechanisms for the moisture transport, but different from what is usually reported in the literature, due to a non-porous solid structure produced here. Finally, with an analysis on the moisture content when the first solid appears, it was possible to observe (with a better definition at $20\,°C$) the impact of the nature of the liquid formulation on the solid formation. The lactose-WPI system dried faster than the dextran-sucrose system, with the solid being formed at a higher moisture content. The addition of dextran or WPI to their respective liquid formulations also leads to an early formation of the solid. Finally, despite the modification in the trials temperature, liquid formulations with the same composition could be dried in similar ways.

Regarding the drying behavior, the results in Chapter 3 were developed using mean moisture content values. From this analysis, some important aspects related to the solid formation from the drying droplet could be observed. However, it could be interesting to present a description of the spatial distribution of the solutes within the droplet, as it has a major impact on the particle properties, such as the surface chemistry. Aiming to access this type of information, Chapter 4 presents the study carried out with the

help of an *in situ* Raman technique to monitor the evolution of the solute mass content profiles in an acoustically levitated droplet during drying.

CHAPTER **4**

In situ Raman composition profiling in acoustically levitated drying droplets

In this chapter, an *in situ* Raman technique is employed on an acoustically levitated droplet. Such technique is applied in a novel way to assess spatially and temporally the distribution of the droplet components during drying. This techniques represents then a useful tool to assess the droplet characteristics without interfering in the drying process.

This experimental study was carried out at the Institute of Thermal, Environmental- and Resources' Process Engineering (ITUN), Technische Universität Bergakademie Freiberg (TUBAF) in collaboration with Prof. Andreas S. BRAEUER, who provided access to the Raman measurement facilities in his laboratory.

4.1 Motivation

In order to engineer solid particles, a first approach in the comprehension of the mechanisms of particle formation consists in the assessment of the droplet lumped characteristics, such as the mass or the external surface aspect, which represent the droplet as a whole, as accomplished in the previous chapter. However, such approach needs to be complemented by a finer experimental evaluation technique that indicates what is taking place inside of the droplet in a distributed fashion, i.e. at discrete points, such as the concentration of the droplet components or the temperature profiles. This type of experimental evaluation still presents a challenge in the spray drying process. Regarding the concentration profile, some techniques were presented in the literature to obtain the solutes concentration profile or the moisture profile, e.g. the rainbow refractometry, the magnetic nuclear resonance and Raman spectroscopy. For the former, the assessment of the solutes concentration profile in the droplet may become a complex task depending on the liquid formulation and such technique may not be adapted to the drying with a wet particle. For the magnetic nuclear resonance, the use of such technique is not widespread due to capital expenditure costs, despite its potential in giving water

107

distribution profiles. For the Raman spectroscopy, the use of this technique was focused on the concentration profile of one volatile substance inside a liquid droplet. Now, this technique is applied in a novel way to assess the evolution of the temporal and spatial distribution of the solutes in the drying systems. The mass content profiles resulting from this *in situ* technique are obtained from the liquid droplet, but also throughout the formation and development of the solid crust until the complete formation of a solid particle.

The content presented hereafter has been accepted for publication in *Powder Technology*. "R. de Souza Lima, A. Braeuer, P. Arlabosse, M.-I. Ré, *In situ* Raman composition profiling in drying droplets, Powder Technology (2020)".

4.2 The acoustic levitator

The acoustic levitator used in the present work consisted of two concave surfaces containing 32 transducers each [96]. The surfaces were separated by 15 cm. A droplet could then be placed in the pressure nodes of the acoustic field produced by the transducers and be levitated, with no vertical displacement. The most stable droplet position was achieved by placing the droplet in the center of the device, as represented in Figure 4.1. The frequency of the acoustic field was 40 kHz.
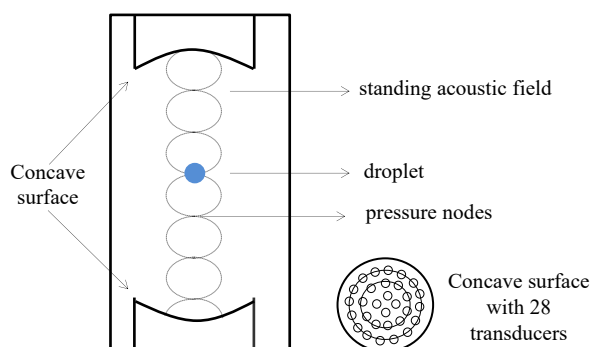
Figure 4.1 – Representation of the acoustic levitator used in the present work. A droplet can be held in place in the pressure nodes originated from the acoustic field

In order to influence the degree to which the droplet is imprisoned in the acoustic field, in relation to a possible horizontal displacement, the amplitude of the acoustic field could be varied with the help of a voltage regulator. The regulator operated from 5.38 V to 12 V. The lowest used voltage (5.38 V) gives the minimum force required to suspend the droplet, in that way a spherical shape could still be obtained. However, the levitation would be very sensitive to exterior disturbances. An increase in the voltage leads to a deformation of the droplet to an ellipsoidal shape, until the point where the droplet becomes a thin disk at the highest voltage (12 V) and disintegrates. All the experiments were carried out at a voltage of 5.38 V and the droplet horizontal displacement was minimized by avoiding any ventilation or movement in the laboratory during the experiments.

4.3 The *in situ* Raman technique

A continuous wave Nd:YVO$_4$ laser was used as excitation source. It operated at 532 nm with an output power of 1 W. A set of lenses was used in order to redirect the laser trajectory and to alter its diameter before launching the laser beam through the droplet, as it can be seen in Figure 4.2. The laser power could be attenuated using a polarization analyzer in combination with a half-wave plate (power deviator in Figure 4.2). In order to avoid non-linear light-matter interactions inside the levitated drops and the vaporization of the sample, the laser excitation power was reduced to 200 mW.

After passing through a concave and a convex lens, the laser beam had its diameter expanded. A third lens then focused the laser into the levitated droplet. Around the focal point, the laser beam forms a "focal beam waist", which has the shape of a thin horizontal cylinder, with a diameter of approximately 0.1 mm. Along this line-shaped one-dimensional measurement volume, Raman light was scattered by the matter present in the droplet and was captured spatially resolved by an imaging spectrometer. A similar configuration has been used for the analysis of heat and mass transfer processes in vaporizing droplets without solidification [14].

The captured Raman signals were spectrally dispersed inside the spectrometer and were detected spatially and spectrally resolved by a charge coupled device (CCD)-chip. The horizontal axis of the chip is used for the spectral information on 1600 pixels. It covers the wavelength range from 550 nm to 680 nm, which corresponds to Raman shifts of 615 cm^{-1} to 4091 cm^{-1}. The vertical axis is dedicated to the spatial information coming from the sample. It possesses 400 pixels and covers 3.2 mm along the beam waist (each pixel represents then 3.2 mm/400 = 8 μm). In order to enhance the signal-to-noise ratio, the pixels were binned together, forming superpixels. We used a combination of 10 pixels for the spatial axis (which give 40 points in space and a resulting spatial resolution of 80 μm) and a combination of 2 pixels for the spectral axis (giving then 800 spectral points). The acquisition time for one measurement (40x800 points) was set to 1 s, while the interval between two consecutive acquisitions was set as 2 s. The final result was then a set of points in time, space and for every wavelength captured by the sensor.

4.4 Drying conditions

The acoustic levitator employed in the present work provided no control over the air properties affecting the drying of the droplet (namely temperature, absolute humidity and flow). The air temperature was measured with the help of a thermocouple placed near the droplet and the absolute humidity in the laboratory was evaluated with a digital hygrometer (TP50, ThermoPro, U.S.A.). The acoustically levitated droplet dried under no forced convection and at room temperature and absolute humidity conditions (Table 4.1).

Different liquid formulations were used in order to modify the droplet drying behavior. The total solute content (dextran and sucrose or lactose and whey protein isolate) was varied between 10 % wt and 30 % wt, while the dextran-to-sucrose mass proportion or lactose-to-WPI changed between 1:1, 1:5 and 5:1, for the former and 1:1, 1:4; 4:1 for the latter (due to solubility limits at 20 °C), as shown in Table 4.1. The initial droplet volume was kept constant and equal to 2 μL throughout the experiments, using a micropipette model 0.5 ± 0.02 μL/10 ± 0.05 μL (Ergonomic High-Performance Pipettor,
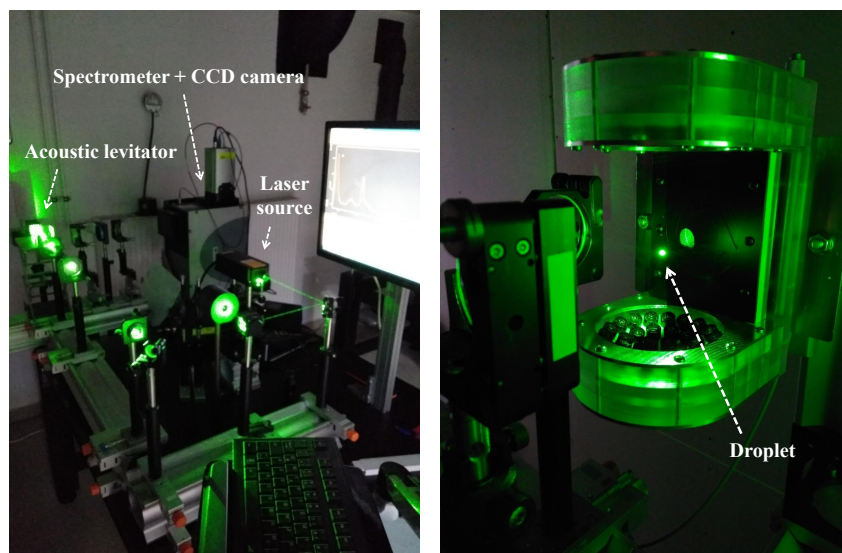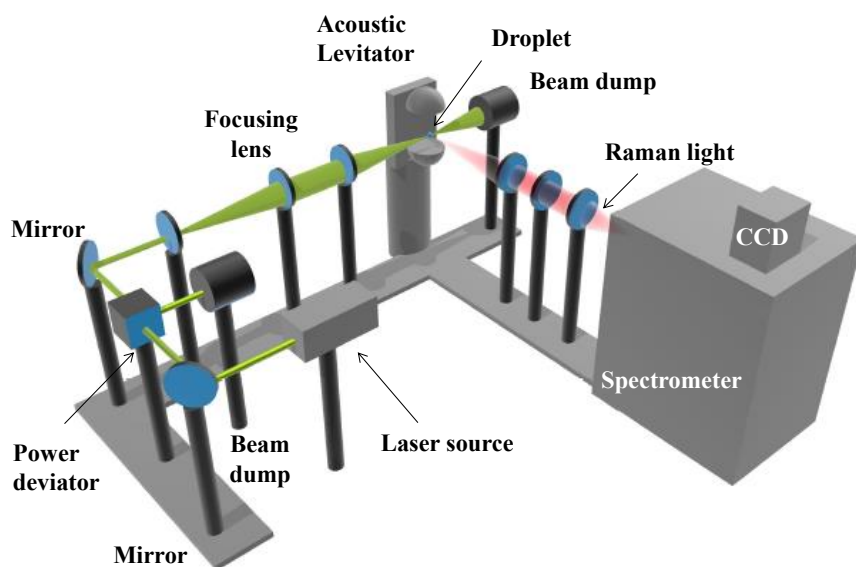
Figure 4.2 – Sketch of the in-house engineered Raman set-up along with the pictures of the set-up and the droplet levitation zone. The trajectory and diameter of the laser light is adjusted through a series of lenses in order to obtain a laser in the form of a thin cylinder inside the droplet

VWR International, USA). Consequently, the initial droplet diameter used in the trials is around 1.56 mm.

In order to ensure the validity of the results presented hereafter, experiments were performed with 5-mL solutions (binary or ternary) in a vial. The objective was to perfect the coupled spectrometer-CCD settings under which the Raman light was acquired and also the Raman spectra treatment. Regarding the Raman spectra treatment, the following points were used for its development: the precise evaluation of total solute mass fraction profiles from solutions in the vials with known composition and the precise

prediction of the solute proportion (results not shown here). Afterwards, trials with a levitating droplet were carried out for ensuring that the initial total solute mass fraction profiles and solute proportion in the droplet corresponded to the respective values in the stock solution. One trial with each composition shown in Table 1 could be performed with the appropriate spectrometer-CCD settings after the finalization of the Raman spectra treatment.

Table 4.1 – The experimental conditions employed in the drying of the acoustically levitated droplet. All the experiments were carried out at the same air temperature and with no convective air flow

Exp. number	Liquid composition (% wt)			Drying air conditions		
	water	dextran	sucrose	Temperature (°C)	Absolute humidity ($g\,kg^{-1}$)	Velocity ($m\,s^{-1}$)
(1).	90	5	5		2.4	
(2).	70	15	15	19	3.5	0
(3).	70	25	5		2.4	
(4).	70	5	25		4.7	
	water	lactose	WPI	Temperature (°C)	Absolute humidity ($g\,kg^{-1}$)	Velocity ($m\,s^{-1}$)
(5).	90	5	5		6.13	
(6).	70	15	15	19	4.7	0
(7).	75	5	20		4.7	
(8).	75	20	5		4.7	

4.5 The droplet Raman spectra through time

This section gives a first perspective of the results obtained from the Raman imaging technique. Firstly, the identification of the droplet interface with the distinction between the Raman light that actually comes from the droplet and the noise surrounding the droplet interface. Secondly, the spectra obtained from the drying droplet is presented in relation to the position in the droplet and through the drying time, thus the spectra from the center or the surface of the droplet coming from the substances in liquid or solid state.

4.5.1 Droplet interface identification

As commented previously, as the laser light enters in the levitating droplet, Raman light is emitted by the components in the droplet and is captured by the couple spectrometer+CCD camera, where the signal is spatially resolved. However, the identification of the measured points to their corresponding position in the sample is not straightforward. In the ideal case, as represented in Figure 4.3, with the laser power used during the trials, the Raman signal should be equal to a certain signal intensity throughout the droplet, while being equal to zero at the gas phase. Instead, in the real case, Raman

light is emitted by the droplet, with a higher intensity towards the droplet surface, but the Raman light is also captured from the region neighboring the droplet interface. The presence of the intensity maxima in the real case in Figure 4.3 may be derived from the droplet glare points [67]. In this phenomenon, a first glare point is formed by the light that is directly reflected at the droplet interface. In the case presented in Figure 4.3, this would correspond to the left side of the droplet, which is the location from where the laser arrives. The second glare point on the right side of the droplet is the result of the light that has refracted, thus entering in the droplet, and has accumulated at the droplet interface [40]. Regarding the noise detected around the droplet, it can come from small fluctuations in the droplet position due to exterior disturbances and it may arise from Raman light coming from the components in the droplet but attaining the CCD camera sensor from a different trajectory, thus inducing the appearance of data from a point that is not actually in the droplet. As a result, in the treatment of the acquired Raman spectra using the Matlab software, the glare points are identified for each time instant and for each trial and the Raman light detected at the exterior of the glare points are set to zero. This first treatment can be verified by considering the number of points representing the droplet at the initial drying time t_0 (in the order of 18 points) multiplied by the distance between the measurement points ($80\,\mu m$). The result is a droplet diameter of approximately $1.44\,mm$, which corresponds to a 2-µL droplet, considering the volume of a sphere.
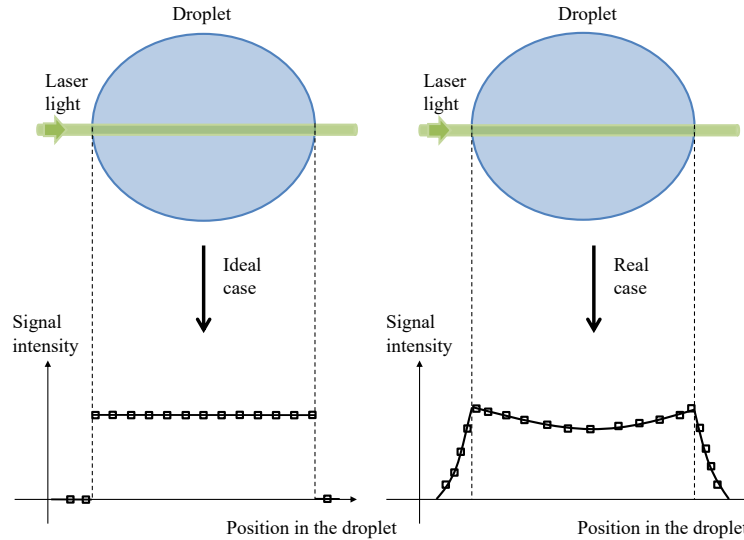
Figure 4.3 – Representation of the Raman signal acquired from the couple spectrometer+CCD camera at two cases: in the real case, the Raman light is only measured from the levitating sample; in the real case, the Raman light is measured with a varying intensity throughout the droplet, but it is also emitted from the region around the droplet interface

4.5.2 From liquid droplet to solid particle

Figure 4.4 illustrates the correlation of the Raman spectra acquired from the levitated droplet, using the water/dextran/sucrose system as an example for the spectra displayed.

From top to bottom, the figure illustrates the laser beam passing into the droplet/wet particle, the spectral and spatial distribution of the recorded signals and examples of spectra from the droplet/wet particle. It is possible to see in the figure that the spectra can be assigned to the droplet compounds, here water and solutes. From left to right, the figure shows how the spectra look like according to the position in the droplet over time.

At the beginning of the drying process, the solutes present in the liquid droplet are homogeneously distributed. As a result, the spectra obtained at the droplet surface (Figure 4.4, spectrum b) and at its center (Figure 4.4, spectrum c) look similar (this can be seen by the similar intensities of the water or the solutes peaks between these two positions in the droplet). For the sake of comparison, the spectrum a in Figure 4.4 is the spectrum recorded from air outside the droplet. Due to the low density of air compared to the droplet, no Raman intensity is captured from this region at the laser power employed during the experiments (considering a point in the gas phase that did not need the treatment presented in the previous section, a point away from the noisy region around the droplet interface). Next, as a result of the water molecules leaving the droplet in the first moments of drying, the region inside the droplet but in the vicinity of the surface becomes more concentrated in solutes, which means that the solutes' radial concentration profile decreases inwardly. After attaining a certain critical concentration [58], a solid crust is formed at the surface of the droplet. Then the solid phase grows towards the center of the droplet as the drying progresses. From this moment on, the droplet is considered a wet particle, with a liquid core. The appearance of the crust is represented in Figure 4.4 (spectrum d). By comparing with the spectrum obtained from the wet particle liquid core (Figure 4.4, spectrum e), a higher solute concentration is found at the wet particle surface due to a higher solute-to-water peaks intensity ratio. Finally, the drying process ends when the solid particle generated is in equilibrium with the surrounding air absolute humidity. At this moment, the residual water concentration profile is flat, which means that the spectra coming from the mixture of the solutes, now in solid state, are very similar throughout the particle solid structure (Figure 4.4-f).

The discussion presented hereafter is focused on extracting, from the spectra, quantitative information about the composition throughout the droplet. This is carried out by correlating the different peaks intensities (areas) in the spectrum to ratios of amounts of substances.

4.6 Treatment of the acquired spectra

After delimiting the zone in the CCD-camera sensor associated with the Raman light coming from the droplet in the previous section, the present section shows the steps employed in the treatment of the spectra, so that an information regarding the mass content inside of the droplet can be obtained. Thus, this section covers the creation of a baseline and subsequent correction of the spectra, the assessment of the area (or intensity) of the peaks corresponding to the water or the solutes in the droplet, the evaluation of the individual solutes intensities from the spectra of the mixture[1] and finally the conversion of the Raman intensity into mass content.

---

[1]Here, the Raman spectrum is not obtained from one single component at a time. It comes either from a binary mixture or a ternary mixture, which is why the term spectrum of the mixture is employed here
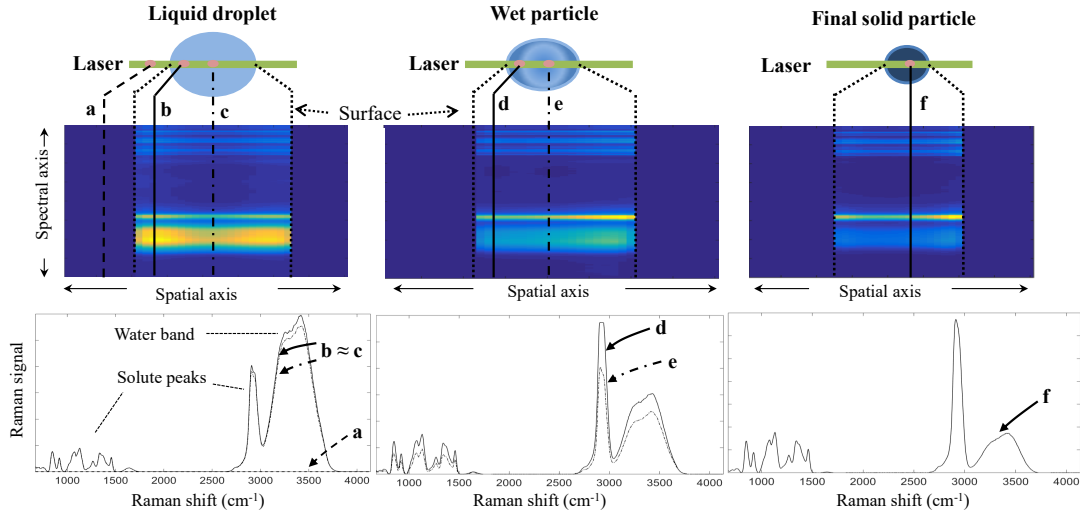
Figure 4.4 – Representation of the acquired spectra at different positions in the droplet through the drying time. From left to right, (a) represents the spectrum obtained from the gaseous environment; (b) and (c) are the spectra obtained at the beginning of the drying process; (d) stands for the solid crust spectrum while the wet particle core is still liquid (e); (f) shows the spectrum obtained throughout the particle solid structure

4.6.1 Baseline correction

The first step regarding the treatment of the measured spectra is the correction of the spectra with a baseline. With the baseline, it is possible to keep only features, or portions of the spectra, that are necessary for subsequent applications. For example, in Figure 4.5, the raw spectrum along with the corrected spectrum obtained from the mixture water/dextran/sucrose are presented for a certain position in the droplet and at a certain time t. In the raw spectrum, it is possible to see that the Raman signal is not equal to zero at some zones with no visible peaks. The objective of the baseline is then to bring all of the spectrum, except for the peaks of interest, to zero. This facilitates the measure of the areas corresponding to the peaks on the next steps.

The creation of the baseline is achieved using Matlab software. Firstly, a set of points should be given to the algorithm, where the value of the Raman signal at the corrected spectrum will be equal to zero. For the water/dextran/sucrose mixture, these points correspond to $\mathbf{S}_p = [805; 965 : 975; 1511 : 1540; 1840 : 2650; 3846 : 4120]$ cm^{-1} (where $\mathbf{S}$ is the spectrum). Next, the raw spectrum is smoothed with the Savitzky-Golay filter, with a third order polynomial and a moving average performed with 9 points. The smoothed spectrum helps the creation of the baseline. The creation of the baseline is achieved using a linear interpolation over the intervals not specified in the $\mathbf{S}_p$ points. Finally, the baseline is subtracted from the raw spectrum, which gives the corrected spectrum presented in Figure 4.5.

Regarding the spectra obtained from the mixture water/lactose/WPI, as can be seen in Figure 4.6, the peaks in the raw spectrum are not as defined as in the spectrum from the
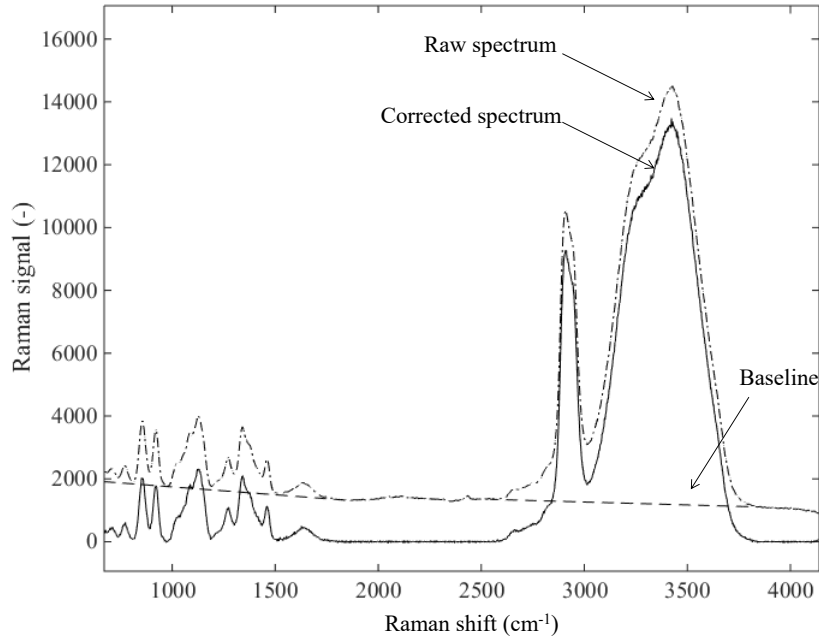
Figure 4.5 – Representation of a baseline applied to a raw spectrum obtained from the mixture water/dextran/sucrose at a certain drying time and position in the droplet. The result is then a spectrum where only the peaks of interest are different from zero

mixture water/dextran/sucrose and the spectrum has a general aspect of an arch. As a matter of fact, for the laser wavelength used in the present work, the peaks in the raw spectrum from the mixture water/lactose/WPI were masked due to the phenomenon of fluorescence, as a result of the presence of the protein. Such phenomenon, whose signal is much stronger than the Raman signal, is a result of the light absorbed by the molecule, but released with a different, longer wavelength than the originally absorbed light, which is seen as an amplification in the spectrum wavelengths. Such phenomenon is specific to certain excitation source wavelengths and may be avoided with the use of different laser wavelengths, such as in the near-infrared region (785 nm) [141]. However, in the present work, only the laser at 532 nm was used. For the creation of the baseline, the following points were used: $\mathbf{S}_\mathrm{p} = [672 : 730; 972 : 977; 1190 : 1198; 1506 : 1516; 1846 : 2650; 3799 : 4130]$ cm^{-1}. After subtracting the baseline from the raw spectrum, the corrected spectrum possesses a Raman signal at least four times weaker than the signal obtained for the mixture water/dextran/sucrose.

4.6.2 Calculation of Raman intensity

The Raman intensity related to a certain component in the droplet is calculated from the area of the peak corresponding to this component in the spectrum of the mixture. Before proceeding to the estimation of the peaks area, a more detailed view of the spectrum obtained from the drying systems is given. For the ternary mixture water/dextran/sucrose, the baseline corrected spectra obtained from a given point inside
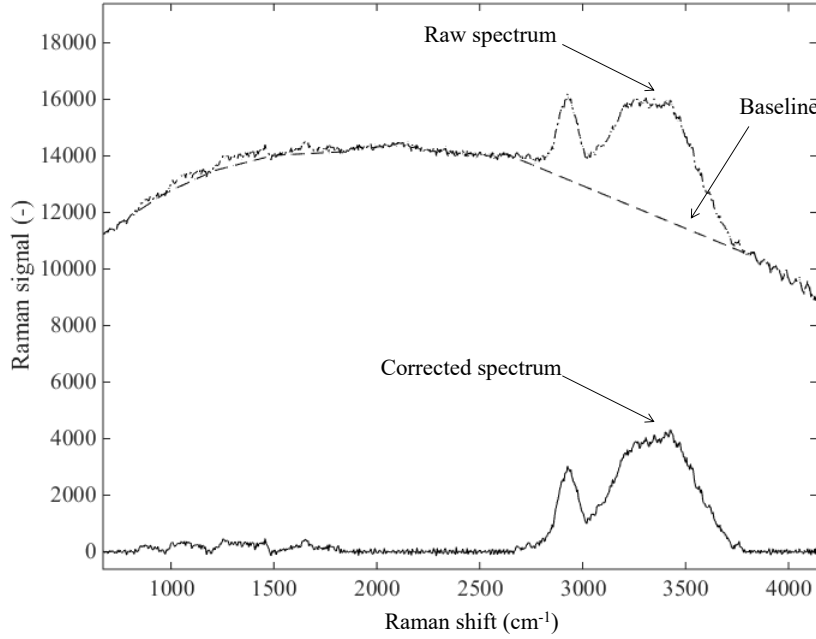
Figure 4.6 – Representation of a baseline applied to a raw spectrum obtained from the mixture water/lactose/WPI at a certain drying time and position in the droplet. The peaks are less visible in the raw spectrum because of the protein fluorescence. The Raman signal of the corrected spectrum is much smaller than the one obtained in the mixture water/dextran/sucrose

the droplet at an instant t for the ternary mixture but also for the binary mixtures water/dextran and water/sucrose are presented in Figure 4.7.

In Figure 4.7, the region between $805\,\text{cm}^{-1}$ and $1500\,\text{cm}^{-1}$ is called the fingerprint region and is used to individually characterize each solute present in the ternary mixture. For example, sucrose has a characteristic peak around $1060\,\text{cm}^{-1}$, while dextran may be differentiated by the peak around $920\,\text{cm}^{-1}$. At $2780\,\text{cm}^{-1}$, a peak representing the C-H bonding (emitted by both solutes) is intertwined with a region coming from the water symmetric stretching vibration H-O-H that goes up to $3800\,\text{cm}^{-1}$. In order to calculate the area beneath the peaks related to the water or the -CH bond, Gaussian functions are used to dissociate those peaks. For example, five Gaussian functions are used to represent the water band [66], as can be seen in Figure 4.7. The Gaussian function can be described as presented in Equation 4.1,

$$\mathbf{S}_{\text{G}}^{\text{n}}(\nu) = \frac{H_i}{\sqrt{(2\pi s_i^2)}} \exp\left(\frac{-(\nu - \lambda_{\text{c}_i})^2}{2s_i^2}\right) \tag{4.1}$$

where $\mathbf{S}_{\text{G}}$ represents the spectrum obtained with the Gaussian function, H_i is a parameter related to the height of the peak i, s_i is a parameter related to the width of the peak i, ν is the Raman shift in the spectrum and λ_{c_i} is a parameter related to the central Raman shift of the peak i. The parameters $[H, s, \lambda_{\text{c}}]$ are specified for each Gaussian function i and their values are optimized with the Matlab software with the function
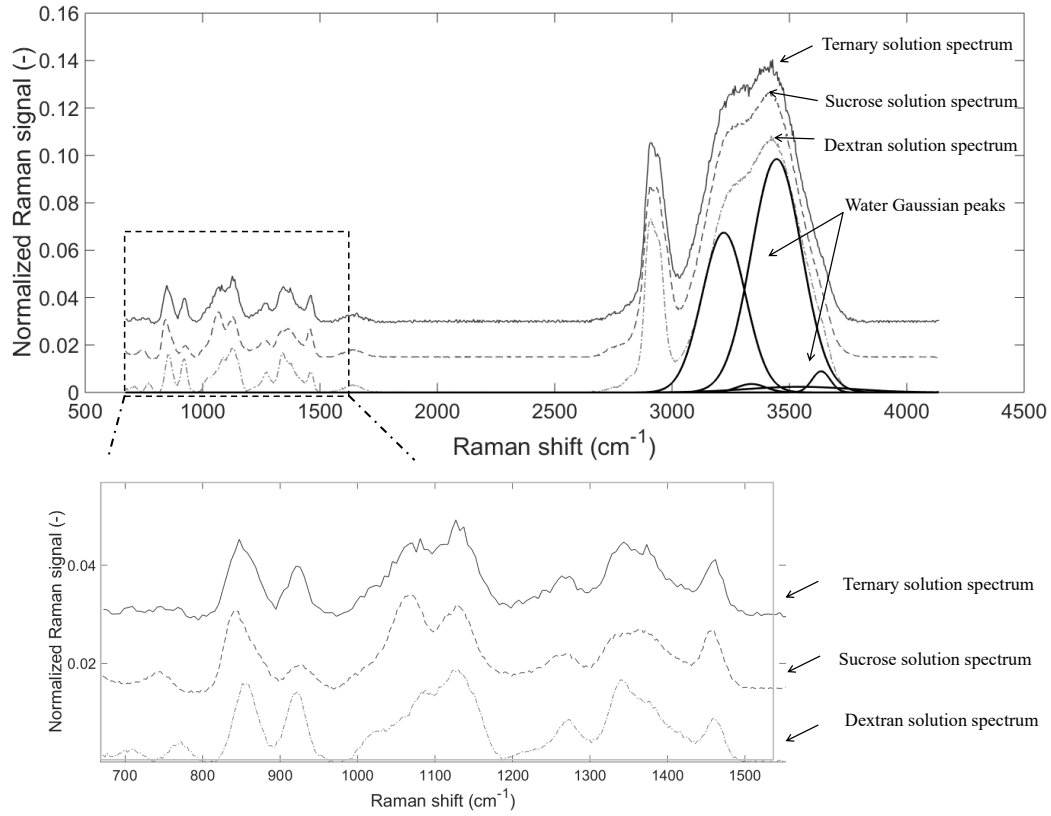
Figure 4.7 – Raman spectra obtained from dextran and sucrose binary solutions and multi-component solutions (dextran and sucrose). The set of Gaussian functions representing the water band is also depicted. The spectrum is normalized to the area of the peaks of the solutes comprised between $805\,\mathrm{cm}^{-1}$ and $1510\,\mathrm{cm}^{-1}$

lsqcurvefit, which is based on a non-linear curve fitting algorithm using the least-square method[2].

It should be noted that the Gaussian functions are fitted to the normalized Raman signal. As a matter of fact, the baseline corrected spectrum is normalized to the area of the fingerprint region, as shown in Equation 4.2, where $\mathbf{S}(\nu)$ stands for the spectrum and $\mathbf{S}^{\mathrm{n}}(\nu)$ stands for the normalized one. Such normalization step comes from the procedure developed for assessing the individual solute Raman intensities, as presented in the next section.

$$\mathbf{S}^{\mathrm{n}}(\nu) = \frac{\mathbf{S}(\nu)}{\int_{805\,\mathrm{cm}^{-1}}^{1500\,\mathrm{cm}^{-1}} \mathbf{S}(\nu)\mathrm{d}\nu} \tag{4.2}$$

---

[2]This methods is used to find a solution that minimizes the sum of the squared residuals, which are the difference between the observed value and the fitted value provided by a model.

As a result of the normalization step, the integral over the fingerprint region (which corresponds then to the intensity of the solutes) is equal to unity, as shown in Equation 4.3,

$$\int_{805\,\mathrm{cm}^{-1}}^{1500\,\mathrm{cm}^{-1}} \mathbf{S}_{\mathrm{fp}}^{\mathrm{n}}(\nu)\mathrm{d}\nu = 1 \tag{4.3}$$

The subscript fp stands for fingerprint. In order to assess the intensity I of the water band or the intensity of the -CH group, the integration is performed on the area of their respective fitted Gaussian functions, as shown in Equation 4.4

$$I_{\mathrm{CH}} = \sum_i \int \mathbf{S}_{\mathrm{G_{CH}}}^{\mathrm{n}}(\nu)\mathrm{d}\nu$$
$$I_w = \sum_i \int \mathbf{S}_{\mathrm{G_w}}^{\mathrm{n}}(\nu)\mathrm{d}\nu \tag{4.4}$$

Regarding the system water/lactose/WPI, the spectra from the ternary mixture and from the binary mixtures (water/lactose and water/WPI) are presented in Figure 4.8. Starting with the spectrum from the mixture water/lactose, the fingerprint region of this spectrum resembles the one obtained from the mixture water/sucrose, as lactose and sucrose posses a similar chemical structure. As a result, the well defined region between $805\,\mathrm{cm}^{-1}$ and $1500\,\mathrm{cm}^{-1}$ can be used for the normalization of the spectrum. For the mixture water/WPI, due to the fluorescence phenomenon, the peaks are not well defined in the raw spectrum. Thus, the points used for the construction of the baseline for the mixture water/lactose are also used for the mixture water/WPI in order to promote the appearance of some characteristic peaks in the fingerprint region. The peaks presented in Figure 4.8 corresponding to this mixture may be the result of the use of the baseline from the system water/lactose. When looking at the spectrum from the ternary mixture, it is possible to see that the water band peak or the -CH bond peak can be well distinguished. On the contrary, the peaks from the fingerprint region are noisier than the ones from the system water/dextran/sucrose. Furthermore, when the spectra of the ternary or binary mixtures involving lactose and WPI are normalized, the Raman signal is approximately three times weaker than the signal from Figure 4.7. As a result, for the next steps, computing Raman intensities and translating it to mass contents become more difficult.

4.6.3 Assessment of individual solute Raman intensities

The steps presented previously regarding the baseline correction, the normalization of the spectra and the calculation of the Raman intensities of the water or the -CH regions are employed for both binary and ternary mixtures. However, for a ternary mixture, as the fingerprint region is composed of the Raman light from both solutes, the challenge in the treatment of the spectrum is related to finding the contribution of each solute to the ternary mixture spectrum, based on the characteristic peaks from each solute.

In order to assess the individual solute Raman intensities from the mixture spectrum, a reference spectrum is firstly measured for each solute in solution. A better definition of
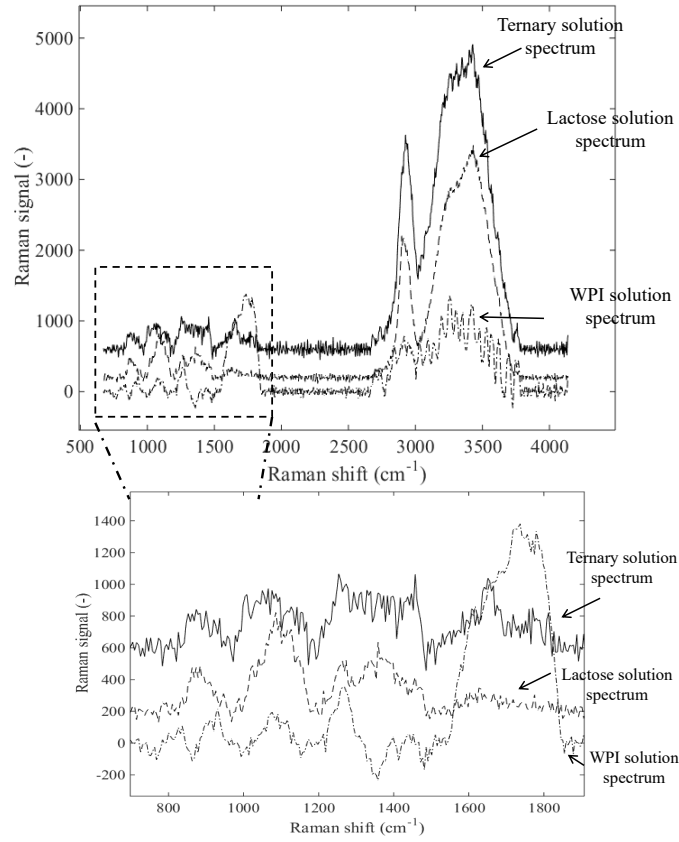
Figure 4.8 – Raman spectra obtained from lactose and WPI binary solutions and multi-component solutions (lactose and WPI)

the peaks in the fingerprint region is obtained with more concentrated solutions, as a result the reference spectra were taken from the binary solutions at 30 % wt for dextran and sucrose, and 20 % wt for lactose and WPI (due to solubility limits at 20 °C). Next, a linear combination of the reference spectra is performed with Matlab software, as shown in Equation 4.5, which solution is found using the least-square method.

$$\mathbf{S}_{fp}^{\mathrm{n}}(\nu) = \alpha \mathbf{S}_{\text{solute i}}^{\mathrm{n,ref}}(\nu) + \beta \mathbf{S}_{\text{solute j}}^{\mathrm{n,ref}}(\nu) \tag{4.5}$$

where the coefficients α and β represent the contribution of each solute to the ternary mixture spectrum. As a result of the normalization step, the area of each spectrum shown in Equation 4.5 is equal to unity, thus the coefficients α and β can be constrained as shown in Equation 4.6

$$\alpha + \beta = 1 \tag{4.6}$$

With Equation 4.6, it is also possible to bound the values of the coefficients α and β between zero and one for the least-square method. Additionally, a starting value should

be given for these coefficients in Matlab software. Finally, the Raman intensities related to each solute are presented in Equation 4.7.

$$
\begin{aligned}
I_{\text{solute i}} &= \alpha \\
I_{\text{solute j}} &= \beta
\end{aligned}
\tag{4.7}
$$

4.6.4 Conversion of Raman intensity into mass content

The final step regarding the treatment of the measured spectra is the conversion of the Raman intensities to mass content values. In order to do so, a calibration curve relating the Raman intensity to mass content for each solute in the liquid formulation is necessary. Firstly, a set of binary solutions with well-defined solute contents were prepared gravimetrically and the corresponding Raman spectra were measured. For sucrose, mass content ranges from 5% wt to 50% wt, while for dextran the mass contents were limited up to 30% wt. For lactose and WPI, both ranges were varied between 5% wt and 20% wt.

Next, the ratio between the area (i.e. intensity) of the fingerprint region to the water peak area is linearly correlated to the solution solute-to-water mass ratio $(R_{\text{s/w}})$, as presented in Equation 4.8. Since the correlation is done on a binary mixture, only one solute forms the fingerprint region and the Raman intensity is equal to one. For the case of a ternary mixture, as presented previously, the coefficients α or β appear in Equation 4.8. As a result, a calibration line as shown in Figure 4.9 can be created for each binary solution (measurements performed in *duplicata*). These calibration curves are used for the prediction of the evolving fractions of individual components once the drying droplet is a ternary solution.

$$
R_{\text{s/w}} = k \frac{I_{\text{solute}}}{I_{\text{water}}} = \frac{k}{I_{\text{water}}}
\tag{4.8}
$$

For the conversion into mass content, the mass ratios can be written as follows,

$$
\omega_{solute\ i} = \frac{R_{\text{s/w i}}}{R_{\text{s/w i}} + R_{\text{s/w j}} + 1}
\tag{4.9}
$$

where $R_{\text{s/w i}}$ and $R_{\text{s/w j}}$ stands for the mass ratios of the components i and j, respectively.

It should be noted that due to no visible difference between the solute spectra in solution or in the solid state, the calibration straight line can be used for the droplet composition estimation for the liquid droplet, but also once the solid particle is formed at higher mass contents.

4.7 Particle morphology

As mentioned previously, the droplet drying process starts at the surface of the droplet with the water molecules leaving it and the volume of the droplet reducing consequently. The concentration of the solutes near the droplet surface increases until a solid phase is
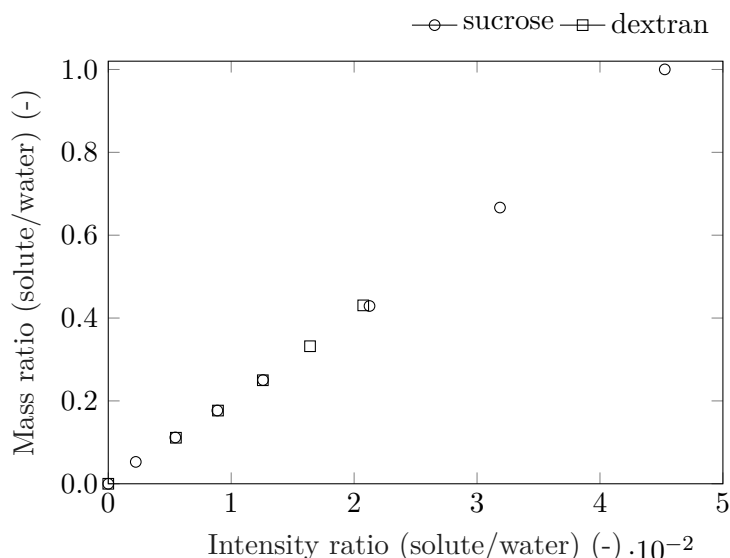
Figure 4.9 – Calibration curve created by relating the solution mass ratio (solute-to-water ratio) to the corresponding Raman peaks ratio. The intensity ratio corresponds to the solute's peak area (region from $805\,\mathrm{cm}^{-1}$ to $1510\,\mathrm{cm}^{-1}$) to the water peak area (obtained from Gaussian deconvolution). Trials performed in *duplicata*

formed [108]. It should be noted that this can happen only if the mass transfer inside the droplet is smaller than the mass transfer from the droplet surface to the bulk air. With the appearance of the solid crust and its development towards the center of the wet particle, the distribution of the components present in the droplet/wet particle evolve very slowly.

Regarding the model liquid formulations used in the present work, for instance, dextran and sucrose present distinct molecular diffusion coefficients as a result of their considerable difference in molecular size. An estimation using the Stokes-Einstein diffusion equation gives a dextran diffusion coefficient 10 times lower than that of the sucrose (at $20\,°\mathrm{C}$) [99, 140]. As for the liquid formulation with lactose and WPI, the Stokes-Einstein diffusion equation gives a protein diffusion coefficient around 6 times lower than the diffusion coefficient of lactose. As a consequence, a modification in the dextran-to-sucrose or lactose-to-WPI mass ratios or a modification in the total solute content could change the final component distribution in the solid particle and alter the crust properties, given that diffusion is the main mechanism controlling the transport of the solutes. The consequence could thus be a modification in the particle morphology.

Figure 4.10 shows two particle morphologies obtained from the water/dextran/sucrose mixture (the dark blue color in the droplet representations correspond to the solid phase and the laser beam is represented in green). The droplet in the experiments (1), (2) and (4) became a spherical transparent particle with a dense core, while the droplet in the experiment (3) generated a bowl-like particle, which can be seen in Figure 4.11.

Figure 4.10 also presents the evolution of the droplet through time as observed from the Raman line imaging technique. This representation is obtained by plotting the Raman
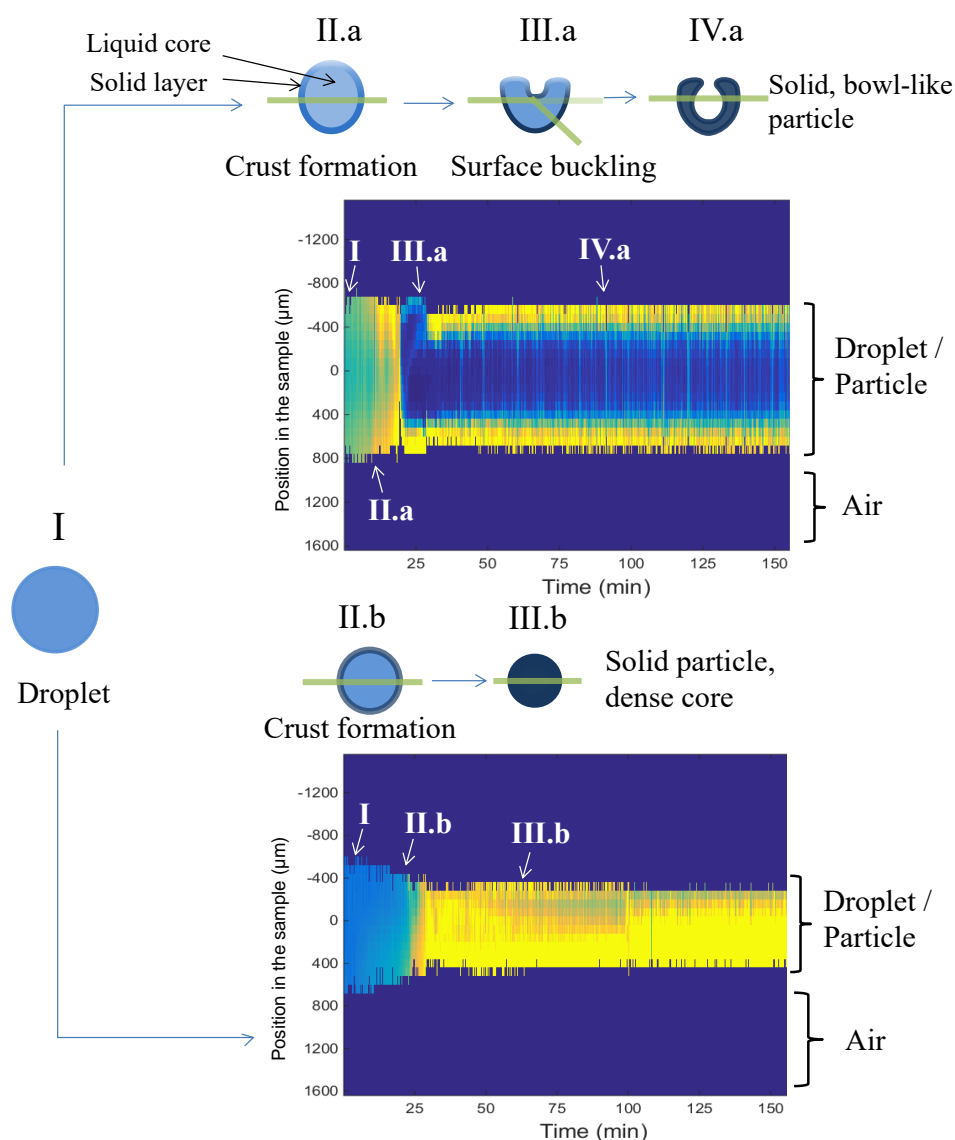
Figure 4.10 − Schematic representation of the particle morphologies obtained in the present work: a bowl-like particle and a particle with a dense core. Additionally, a qualitative view of the evolution of droplet through time is represented by plotting the Raman signal measured at the CH band ($2900\,\mathrm{cm^{-1}}$). The yellow color represents a higher Raman signal. The dark blue color in the droplet representations correspond to the solid phase. The laser beam is represented in green

signal obtained from the Raman shift corresponding to the -CH group (at $2900\,\mathrm{cm^{-1}}$). This gives a qualitative view of the increase in solute concentration in the droplet (where the yellow color represents a higher Raman signal) and also allows the distinction between droplet and surrounding air.

Regarding the bowl-like particle obtained by drying the solution with initial mass contents at $25\,\%$ wt of dextran and $5\,\%$ wt of sucrose (trial 3 in Table 4.1), a closer visual inspection of the process of the core formation showed that, after $20\,\mathrm{min}$ of drying,
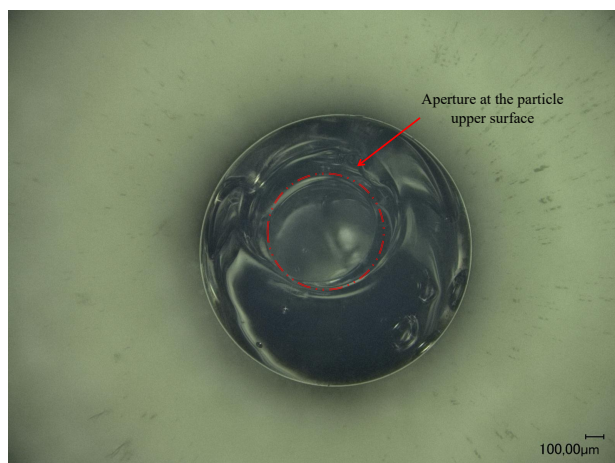
Figure 4.11 – Optical micrograph illustrating the hollow core particle produced from the mixture 25 % wt dextran and 5 % wt sucrose (trial 3 in Table 4.1). The small aperture at the upper surface of the solid particle is indicated by the arrow

the upper surface of the droplet starts to buckle and to move downward until the point where this bending surface reaches the laser light and starts to deviate its trajectory. As a result, the droplet side facing the laser is brighter than the opposite surface. This can be seen in Figure 4.10 from the change between the zones $II.a$ and $III.a$. The more the buckling process continues, the more the laser light is able to cross the droplet without disturbances in the trajectory. Once both exterior and interior surfaces of the present particle are solidified (at 30 min of drying), the laser light is able to cross the particle crust. From the results shown in Figure 4.10, the time interval between the moment the laser trajectory is deviated and the solidification of the entire particle is approximately 10 min.

The Raman intensities in Figure 4.10 are presented for the particle with 5 % wt dextran and 5 % wt sucrose (trial 1 in Table 4.1). From the plot, it is possible to observe a liquid phase at the beginning of the drying process, but also a solid structure after 50 min of drying, which would confirm the presence of a compact solid particle (dense core). The laser light is slightly darker at the particle side opposite to the one facing the laser around 100 min. This comes from the fact that the laser beam loses intensity after passing through the solid structure.

Regarding the experiments with the mixture water/lactose/WPI, the Raman signal corresponding to the Raman shift from the -CH group ($2900\,\text{cm}^{-1}$) is plotted over the drying time in Figure 4.12 for a case where a dense core particle have been possibly generated with the trial 6 in Table 4.1 (15 % wt lactose and 15 % wt whey protein isolate) and a case where a hollow core is formed in trial 7 in Table 4.1 (5 % wt lactose and 20 % wt whey protein isolate). For the trials with lactose and whey protein, the glare points were more difficult to find, which is why the Raman signal in Figure 4.12 is noisy and the droplet size appears to be much bigger than the droplet depicted in Figure 4.10. For the hollow core particle in Figure 4.12, the wet particle position in the levitator became unstable after approximately 22 min, which would make the wet particle fall from the entrapment zone.
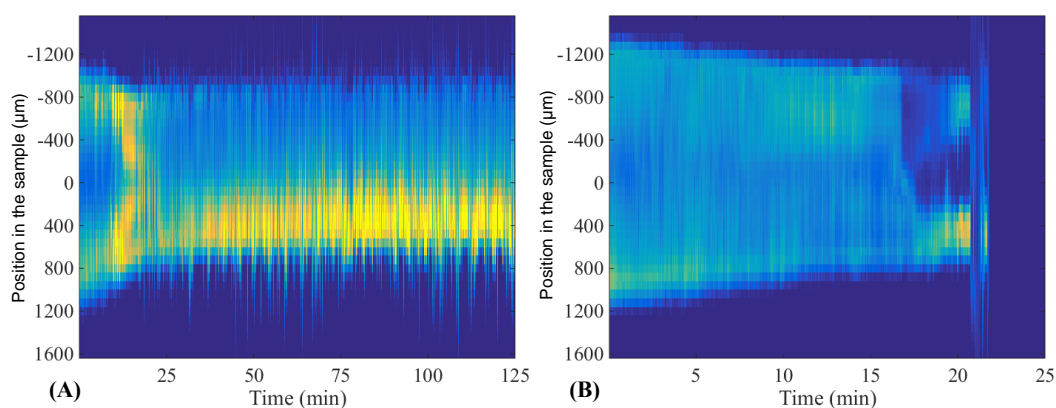
Figure 4.12 – Raman signal plotted for the Raman shift corresponding to the -CH group ($2900\,\mathrm{cm}^{-1}$) from trials with water/lactose/WPI. Two cases of particle morphology are presented: (A) a dense core particle formation with 15 % wt lactose and 15 % wt whey protein isolate (trial 6 in Table 4.1); (B) a hollow core particle formation with 5 % wt lactose and 20 % wt whey protein isolate (trial 7 in Table 4.1)

An image of the particles obtained from the experiments depicted in Figure 4.12 is presented in Figure 4.13. The particle from the trial 15:15 % wt (trial 6 in Table 4.1) presented a yellowish solid crust with a wrinkled aspect. Also, according to the Raman signal 4.12, the core of this particle may be dense. With this same liquid formulation, the particles shown in Chapters 2 and 3 also possessed a wrinkled surface, but presented a hollow core instead. As for the particle with initial mass content at 5:20 % wt lactose-WPI (trial 7 in Table 4.1), the surface presented a smooth surface and the core is hollow. Such morphology was also reproduced with faster drying kinetics as presented in Chapters 2 and 3. The particles from the other lactose/WPI trials also presented a wrinkled aspect with a dense core.
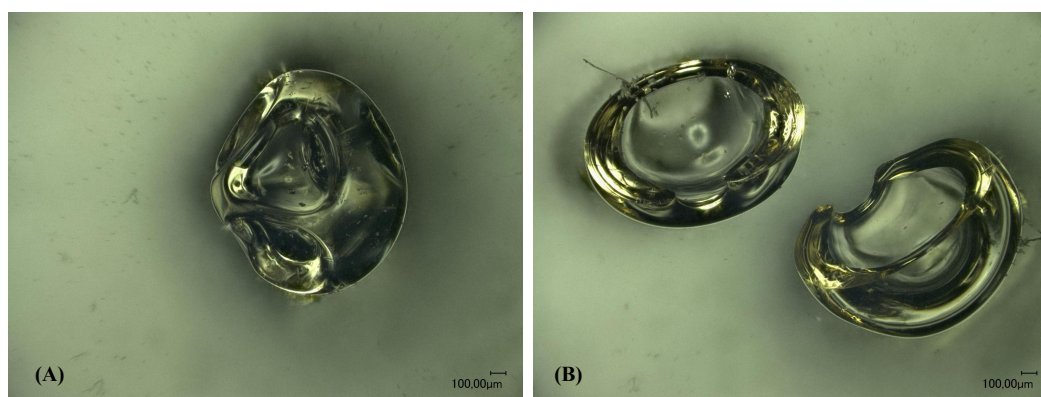
Figure 4.13 – Lactose/WPI particle morphologies obtained from the trials: (A) 15 % wt lactose and 15 % wt whey protein isolate (trial 6 in Table 4.1); (B) 5 % wt lactose and 20 % wt whey protein isolate (trial 7 in Table 4.1)

4.8 Drying behavior

4.8.1 Mass content profile evolution

In Figure 4.14, the total solute content profiles are presented for the formation of the dense core particle from trial 2 in Table 4.1 (with 15 % wt dextran and 15 % wt sucrose). In this figure, the mass content profiles are aligned at the center of the droplet. It is possible to observe the spatial evolution of the total solute content from the liquid droplet up to a dense solid state. It is noteworthy that the duration of the drying experiments was set in order to obtain, at the end of the experiment, a solid particle that tended to be in equilibrium with the surrounding air.
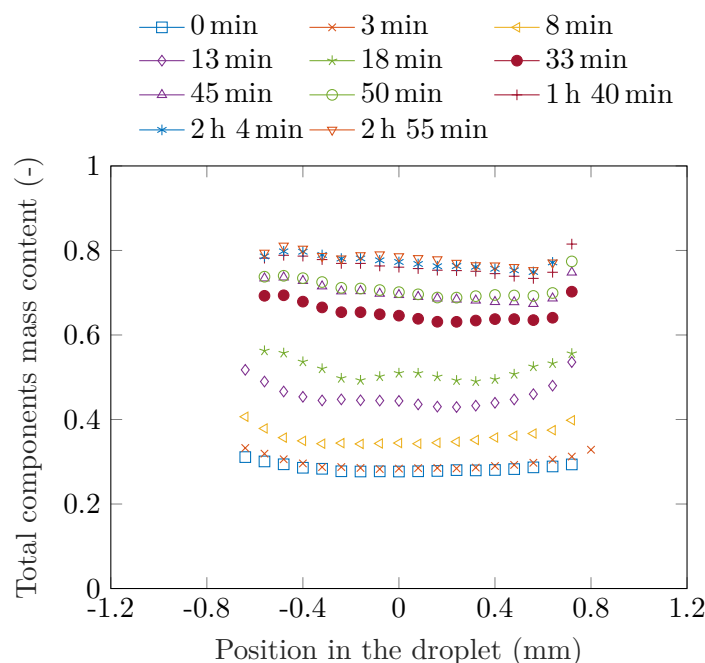
Figure 4.14 − Total solute content profiles during the drying of the droplet with the formation of a dense core particle. The initial composition is 15 % wt dextran and 15 % wt sucrose (trial 2 in Table 4.1)

As can be observed in Figure 4.14, the initial mass content profile is a flat, horizontal line, as expected when the composition inside the droplet is homogeneous. As the water is removed from the surface, there is a solute enrichment near the droplet surface (Figure 4.14 from 3 on). As to counteract the creation of such concentration gradient, the dissolved solutes will tend to diffuse towards the center of the droplet. In the present work, even though the employed drying conditions are mild, which would make the solutes inward diffusing process as important as the drying rate, the solute enrichment of the surface can be observed (Figure 4.14 at 3 and 8 min).

However, as the crust is formed at the liquid-air interface (Figure 4.14 at 13 min), a new barrier for the drying process is created, which will reduce the surface water activity. After the crust formation, the drying rate will decrease progressively. Consequently, the diffusion of the solutes towards the droplet center becomes prominent in definition of

the subsequent mass fraction profiles, which is observed as a reduction in the solute mass fraction difference between the center to the surface of the wet particle (Figure 4.14 at 18 min). At the end of the drying process, the mass content profile, on dry basis, will be a flat profile, similarly to the beginning of the experiment (Figure 4.14 at 2 h4 min and 2 h55 min).

In Figure 4.15 the total solute content profiles are presented for the formation of bowl-like particle from trial 3 in Table 4.1 (with 25 % wt dextran and 5 % wt sucrose). The initial profiles resemble the ones presented for the dense core particle formation, where the surface becomes rich in solute as the drying process progresses (Figure 4.15 at 8 min and 11 min). However, as visualized previously in the image acquired with the spectrometer, the upper wet particle surface will start to buckle and move inward (the beginning of such motion cannot be seen in the present work, since the laser only passes through the center of the droplet). This process alters the laser trajectory at the center of the sample and thus, affect the evaluation of the mass content points. That explains why in Figure 4.15, the plotted points at 20 min of drying correspond to the droplet surface facing the laser. The subsequent compositions were too noisy and thus were kept out the present figure. Only after the solidification of the interior surface (at 36 min), the mass content points in the solid structure could be calculated.
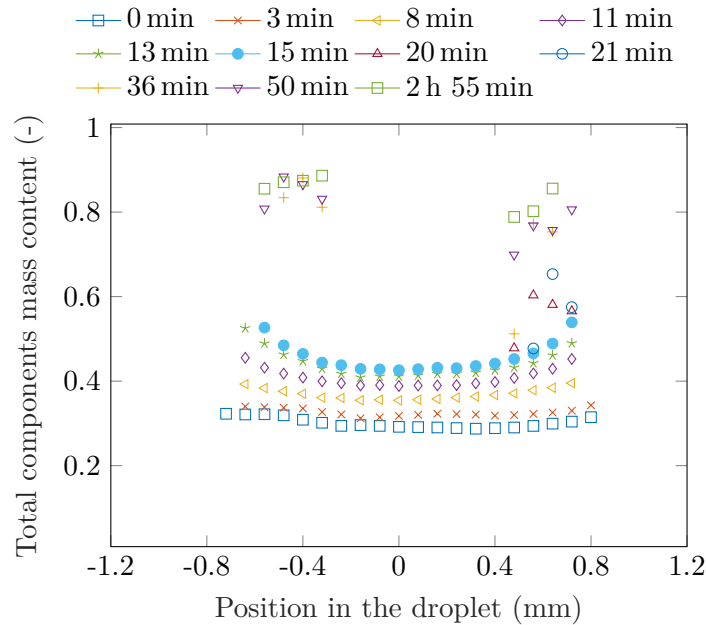
Figure 4.15 − Total solutes content profiles during the drying of the droplet with the formation of a bowl-like particle. The initial composition is 25 % wt dextran and 5 % wt sucrose (trial 3 in Table 4.1)

Regarding the trials with the water/lactose/WPI system, due to the weaker Raman signal after the baseline correction and a poorer peak definition, the mass content profiles are noisier than the profiles obtained from the water/dextran/sucrose mixture. As an example, some mass content profiles were plotted in Figure 4.16 from the trial 15L-15WPI (trial 6 in Table 4.1). As mentioned previously, due to a difficulty in finding the glare points, the droplet surface cannot be well identified in the mass content profiles

(although some mass content points have already been removed from Figure 4.16 due to a mass content value equal to zero or superior to one). It is possible to see in Figure 4.16 that even the initial mass content profile at 0 min is not a flat profile, as the points vary considerably throughout the droplet. As a result, neither the mass content profiles nor the individual solute mass contents were not further developed for the trials with lactose and whey protein isolate.
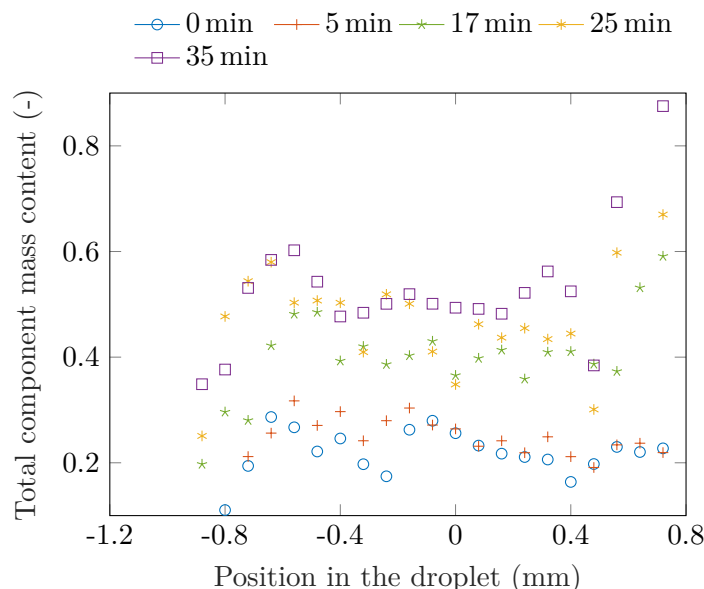
Figure 4.16 − Total solutes content profiles during the drying of the droplet with the formation of a dense core particle. The initial composition is 15 % wt lactose and 15 % wt whey protein isolate (trial 6 in Table 4.1)

4.8.2 Evaluation of component segregation

In this section, two distinct cases are presented, the first one where both solutes dry as one single constituent (trial 2 in Table 4.1 - 15 % wt dextran and 15 % wt sucrose) and the second with the component segregation (trial 1 in Table 4.1 - 5 % wt dextran and 5 % wt sucrose). As a reminder, the evaluation of the individual components mass content is achieved through a least-square method as described previously and the total solutes Raman intensity is a result of a linear combination of the individual solutes.

In Figure 4.17, it is possible to observe the evolution of the mass content of dextran and sucrose in the center (central point in the mass fraction profile) and at the surface (outermost point in the mass fraction profile) of the droplet from the initial liquid formulation composed of 15 % wt dextran and 15 % wt sucrose (trial 2 in Table 4.1). In order to detect an eventual separation between the components, the difference between the mass contents at the surface and at the center of the droplet for each solute was also plotted against the drying time. This plot was created only for the first 50 min of drying, as the solid particle is surely formed after that time and the solutes are fixed in the solid structure. As can be observed from Figure 4.17, both dextran and sucrose become slightly more concentrated at the surface in the first 15 min, as a result of drying process (the formation of a concentration gradient from both solutes was highlighted

in Figure 4.14 as well). However, both solutes seem to be following the same rate for increasing the difference between the mass content at the surface and at the center of the liquid phase, and thus a clear separation between the solutes can not be stated. They appear then to be drying as one single solute in the droplet. The slight decrease in dextran mass content difference from 25 min to 50 min can be due to the uncertainty in the measured data.
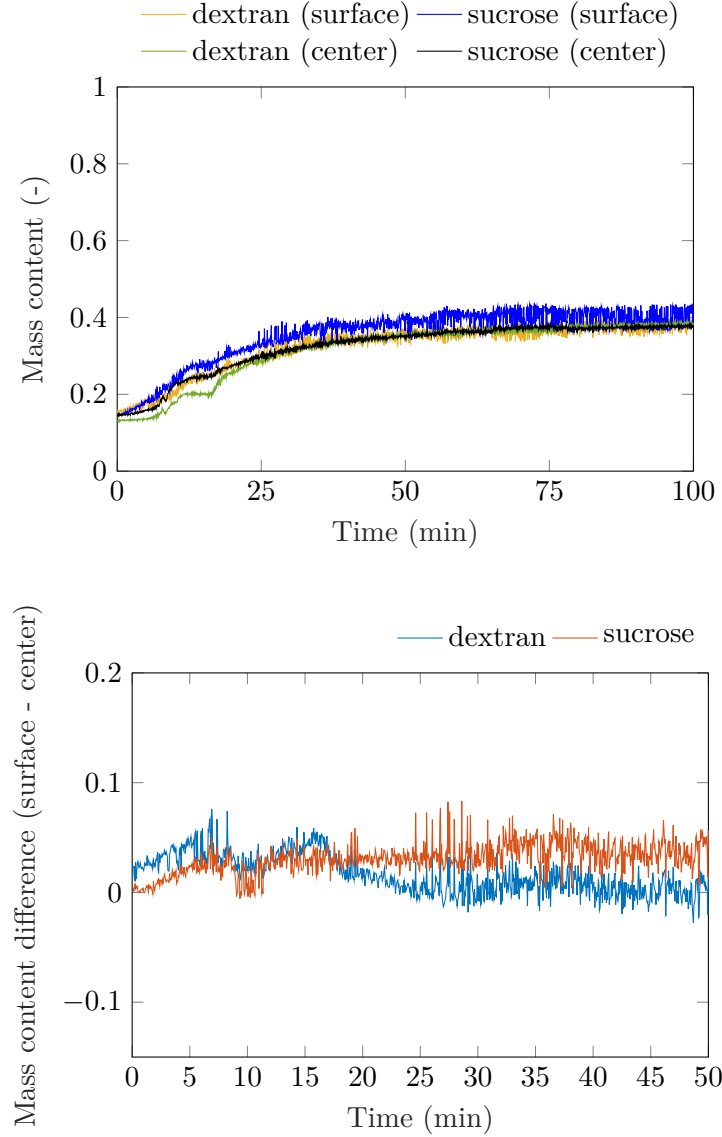
Figure 4.17 − Evolution of the individual component mass content at the surface and center of the droplet for the experiment with 15 % wt dextran and 15 % wt sucrose (trial 2 in Table 4.1). The plotted component segregation is represented as a difference between the mass content at the surface and at the center of the droplet

In the Figure 4.18, however, a much stronger difference between the mass contents at the surface and at the center of the droplet can be observed in the experiment with 5 % wt dextran and 5 % wt sucrose (trial 1 in Table 4.1). As the results are presented in

the form of mass contents, the creation of zones with higher values of mass contents would then represent a component segregation. The difference observed between these experiments can be explained by the initial solute concentration (and consequently, the diffusion coefficient of the solutes in the solution) and the time for the formation of a wet particle. The droplet from trial 1 contains a lower total solute content ($10\,\%$ wt) than the droplet from trial 2 ($30\,\%$ wt). Furthermore, the initially less concentrated droplet takes a longer drying time before attaining the supersaturated concentration necessary for the formation of the solid particle. This contributes for a higher time in the diffusive process of the solutes inside the droplet. The parameter here leading to a separation between the components was the total solute content. For the other experiments developed in the present work, no solute segregation was observed.

With the aim of demonstrating the creation of a region richer in one of the solutes present in the droplet, mass content profiles for the total solids, dextran and sucrose were represented in Figure 4.19 by choosing a random drying time in the trial 1 (Table 4.1). These profiles correspond to 28 min of drying. At this point, sucrose is homogeneously distributed in the liquid phase, while dextran already presents a higher concentration at the droplet surface. As mentioned previously, sucrose has a smaller diffusion coefficient than dextran, which allows this molecule to diffuse more easily in the liquid phase while being carried towards the surface of the droplet by the water molecules.

Regarding the component segregation in the droplet and the influence of the acoustic levitator, the acoustic levitators employed in the literature generate a strong droplet rotation about both vertical and horizontal axis [149, 150]. Because the spatial distribution of the droplet components is dependent on the flowfield inside the liquid phase, the presence of a centrifugal force could have an impact on the distribution of the solutes [149, 160, 179]. In those cases, the frequency employed in the acoustic levitator was in the order of 100 kHz. However, in the present work the frequency employed is less than half of this value. As a result, no rotation was observed within the liquid droplet at the beginning of the drying process. The rotating motion could be detected only after the solid particle was formed. Thus, the acoustic field in the present work did not influence the component segregation by centrifugal force, as the rotating motion only appeared when the solutes were already fixed in the particle solid structure.

4.9 Summary of the main findings of the chapter

The present chapter focused on a new *in situ* Raman technique to assess the mass content of the droplet components in a distributed fashion throughout the drying time, i.e. with a liquid droplet, with the presence of a solid crust at the surface of the droplet and with a completely solid particle. An *in situ* Raman technique was combined with an acoustic levitator to provide such insight into the solutes spatial distribution without much interference in the drying process.

The experimental conditions tested with the set-up presented in this chapter were limited to a modification in the liquid formulation, i.e. drying system, total solute content and solutes initial ratio. The idea was based on the acquisition of mass content profiles in different cases related to the particle morphology (dense or hollow core particles) and related to the presence of solute-rich zones. In order to compute these mass content profiles, the Raman light captured by the CCD-chip had to be treated (identification of the droplet interface, correction of the baseline, computation of peak intensity for each
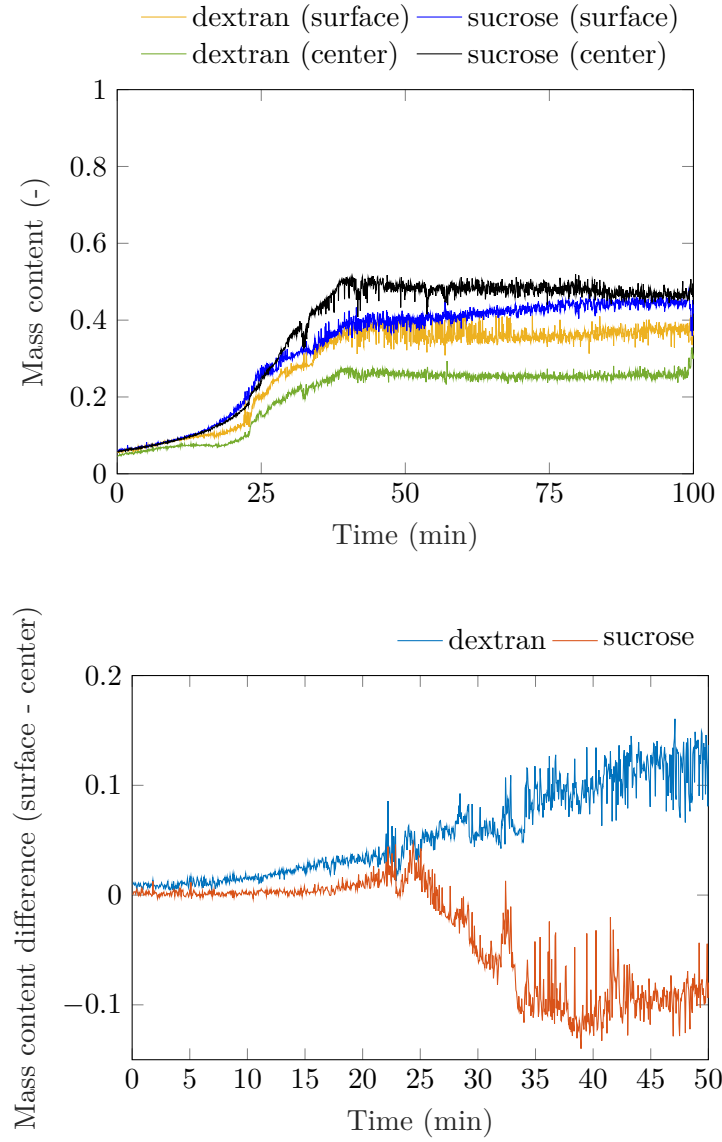
Figure 4.18 – Evolution of the individual component mass content at the surface and center of the droplet for the experiment with 5 % wt dextran and 5 % wt sucrose (trial 1 in Table 4.1). The plotted component segregation is represented as a difference between the mass content at the surface and at the center of the droplet

solute) and combined with calibration curves for each solute. As a matter of fact, an important challenge was related to the evaluation of the peak intensity from each solute based on the Raman spectrum of the ternary mixture. For the dextran-sucrose system, for example, only one peak would clearly identify one of these solutes in solution. For the lactose-WPI system, the fingerprint region presented an important noise, which made it difficult for the identification of each solute in the ternary mixture.

From a droplet containing a higher dextran-to-sucrose ratio, a bowl-like particle was obtained. As could be observed in this trial, the buckling process was visualized at the upper portion of the droplet and progressed towards its lower portion. Meanwhile,
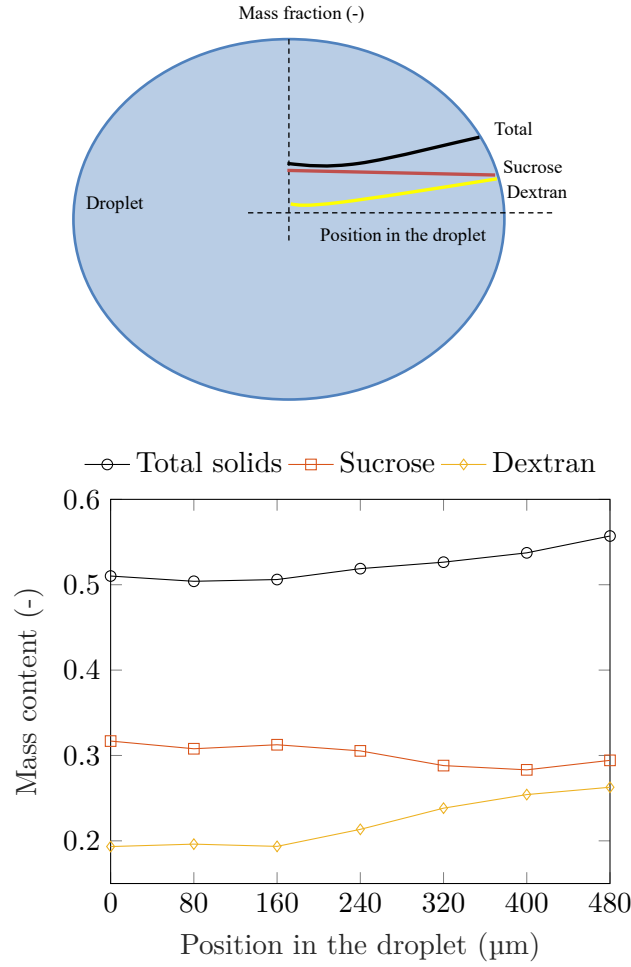
Figure 4.19 – Mass content profiles taken at 28 min for the experiment with 5 % wt dextran and 5 % wt sucrose (trial 1 in Table 4.1). At this stage, the droplet surface is starting to have a higher dextran concentration while sucrose is homogeneously dispersed in the liquid medium

the diameter of this buckling surface increased in this process. Consequently, the mass content profiles generated from this trial were continuous through the droplet until the point where the buckling surface attained the laser light. After this moment, the mass content profiles would present a discontinuity, which corresponded to the particle core. For the other trials with the dextran-sucrose system, dense core particles were generated. The mass content profiles were flat in the beginning and at the end of the drying process. The difference between the mass content at the droplet surface and at the droplet center increased until the formation of the solid crust. Such difference decreased afterwards. For the lactose-WPI system, a hollow core particle was obtained from a mixture containing a higher percentage of protein. Once the hollow core was formed, the particle could not be entrapped in the acoustic field. For the other lactose-protein trials, wrinkled dense core particles were obtained. However, for this system, the generated mass content profiles were too noisy to be exploited. This comes from the fact that the laser wavelength employed here induced a fluorescence phenomenon in the droplet

solutes and a proper measurement of the Raman light was not possible. A modification in the laser wavelength would be necessary for the work with the whey protein.

Regarding the mass content profiles for each solute in the dextran-sucrose trials, a dextran-rich surface and a sucrose-rich core could be observed at the dense core particle generated from a low total solute content (10 % wt) and the same initial solute ratio. For the other trials, the solutes dried as one single component. No clear separation could be observed. Such results presented the effect of the formulation viscosity (due to a lower solute content) on the component segregation by a diffusive mechanism. As dextran possesses a lower diffusion coefficient than sucrose, it would have the tendency to accumulate at the droplet surface during the drying process.

The technique developed in this chapter presents an important progress in the study of the drying process of multi-component droplets. The technique may be adapted to other liquid formulations by taking into account its compatibility with the employed laser wavelength, so that fluorescence phenomena may be avoided. Also, the mass content profiles obtained here are useful for supporting the development of droplet drying models, as these profiles finally give insight into the droplet components distribution through time. Naturally, the drying model can present solute mass content profiles from droplets dried at harsher conditions. The validation of these results would require a modification in the set-up presented here for the work with higher air temperatures and air velocities, for example. Such modification could be a combination of this set-up with the one presented in Chapter 3 to give simultaneous mass loss and mass content profiles results under different air properties.

Single droplet drying modeling

From the knowledge acquired from the previous chapters, a mathematical model is developed to physically represent the drying behavior of a single droplet. After the presentation of the retained set of equations and the implementation on the software, the results given by the model are compared to those obtained experimentally from Chapters 3 and 4. The results are focused on the drying kinetics and solutes distribution during the crust formation. A sensibility analysis is carried out on the input experimental conditions (i.e. air properties and liquid formulation mass contents) in order to observe their influence on the drying kinetics and solute distribution.

5.1 Motivation

The experimental work employed in the previous chapters allowed the design of different solid structures through distinct air properties and liquid formulations. Also, the developed set-ups provided quantitative information regarding the droplet shrinkage kinetics, as well as the drying kinetics, with an emphasis on the evolution of the sample moisture content, the duration of the first drying stage and the formation of the solid crust. Likewise, the individual solute mass content profiles of droplets dried at mild conditions were obtained through the use of a Raman technique. However, a multitude of other variables regarding the drying of droplet could not be experimentally obtained, such as the droplet temperature profiles, the solutes mass content profiles when harsher drying conditions are employed or the representation of the evaporation flux over the droplet surface. A solution for accessing such variables is through the use of a numerical model finely defining the coupled physics taking place inside the droplet during the drying process. The development of such model should, naturally, be based on experimental evidence.

5.2 Physical model and modeling hypothesis

The description given here of the phenomena related to the drying droplet is dedicated to the presentation of the coupled mass, momentum and energy transfers taking place

until the appearance of the solid crust at the droplet surface. Firstly, when a droplet is place under an air flow (or stagnant air), the droplet temperature and drying rate are strictly unsteady and evolve to attain the conditions related to the first drying stage.

In the first drying stage, the moisture removal occurs at the surface of the droplet. The water molecules leaving the droplet are transported to the gas phase through a coupled convective and diffusive processes. Also, the droplet surface remains saturated with water (with a water activity at unity) and only unbound moisture is evaporated.

Even though the drying process is limited by the air properties in the first drying phase, a special attention should be given to the transport of moisture and solutes inside the droplet during this phase. As a matter of fact, Wei et al. [179] stated that the presence of a convective air flow around the droplet promotes the appearance of two toroidal circulating paths inside the liquid droplet. Such convective movement was experimentally observed during this thesis.

The convection in the droplet has an important role regarding the homogenization of the solutes and the temperature. However, in the literature, the drying of droplet is commonly described without the presence of convection and only depending on the diffusion of the components present in the liquid phase [59, 109, 181]. Without liquid circulation, the moisture profile established in the droplet decreases from the center to the surface of the droplet and the solutes diffusion occur radially inward. By considering the effect of the air flow around the droplet, a different moisture profile is obtained in the liquid phase [160, 179]. Following the toroidal paths, the moisture content is low at the droplet surface but also towards the center and a maximum value is placed at point where the liquid velocity is stagnant [179], thus the solutes transport are determined by a combined effect of the convection and diffusion processes.

Regarding the energy transfer, the water removal from the droplet is an endothermic process, which has a cooling effect upon the former. Thanks to the energy supplied by the air stream, the droplet temperature can be stabilized at the wet bulb temperature in the first drying stage. The presence of the convective movement inside the liquid droplet would also help to homogenize the temperature throughout the droplet. However, it should be noted that, depending on the air flow, a temperature gradient may be established along the droplet surface [26]. Such temperature gradient generates a surface tension gradient. The surface tension decreases with increasing temperature, thus a surface element placed at a lower surface tension region will be pulled towards the region with high surface tension. Consequently, the surface tension gradient promotes a steady flow pattern in the liquid referred to as the Marangoni effect. As a result, such effect may increase the order of magnitude of the velocity of the liquid toroidal flow.

Throughout the first drying stage, the moisture is removed from the surface of the droplet, which causes consequently a local increase in the solutes concentration. Such increase in the solutes concentration is accompanied by an increase in the droplet viscosity. A higher droplet viscosity hinders the transport of the solutes towards the center of the droplet. Eventually, saturated conditions are attained at the droplet surface, which promotes the formation of a solid crust. The appearance of this solid layer represents the end of the first drying stage, as observed in Chapter 3. Also from the observations in this chapter, the solidification process started at the contact line between the droplet and the glass filament (by heterogeneous nucleation) and then spread through the rest of the droplet surface. In the literature, the droplets are

modeled without the presence of a physical support to hold the droplet in place, thus the crust formation is considered to form uniformly at the droplet surface [59, 102, 106]. Consequently, the local dependence between the crust formation and the evaporation flux is often neglected. Finally, with the end of the first drying stage, the water activity becomes inferior to unity and bound moisture is evaporated.

The model developed in this chapter considers a spherical droplet freely suspended in the drying air stream (the presence of the glass filament is not added to the model). Also, an axisymmetric droplet is considered, with an axis of symmetry parallel to the air flow. Only water evaporates from the droplet and vapor is transported by a combined convective and diffusive processes in the drying air. If the drying air is stagnant (to represent the results from Chapter 4), only a diffusive transport is considered in the gas phase. In the liquid droplet, the appearance of the toroidal circulating path as a consequence of the air flow is taken into account. As a result, the solutes present in the droplet are transported by combined diffusive and convective mechanisms. Also, the presence of a multi-component mixture is considered for the evaluation of the transport fluxes in the droplet. Regarding the energy transfer, the droplet temperature profile is calculated through time and, along the droplet surface, the surface tension gradient is taken into account (which leads to the Marangoni effect).

It should be noted that the drying time simulated in this chapter follows the results observed in Chapter 3: it considers a first 30-second diffusive drying, as in the correction applied for each trial in Chapter 3 (once the by-pass is activated for the suspension of the droplet); secondly, the simulation ends at t_{tc} (Chapter 3), when the crust completely covers the droplet surface . However, no equations representing the solid formation and growth are considered here. Only the local dependence of the evaporation flux with the increase in solutes viscosity is considered for hindering the transport of the solutes. Additionally, at the time when the crust covers the droplet surface, the first drying rate has ended. Consequently, the water activity of the droplet is evaluated through the use of empirical models in order to represent a reduction in the evaporation flux. Finally, only the dextran-sucrose system is simulated in this chapter. The work with the lactose-WPI system would require the addition of adsorption kinetics of the protein at the droplet interface during drying and the eventual formation of a hollow core particle (to represent the morphology obtained in the previous chapters).

5.3 Mathematical model

In order to represent the drying of the droplet, a set of equations are written for the droplet and for the drying air to described the transfer of mass, momentum and energy. Boundary conditions are used to link the equations between both phases. The section ends with the presentation of the correlations chosen for estimating important physicochemical properties of the modeled mixture.

5.3.1 Mass transfer

In order to account for the mass transfer between the droplet and the drying air, a set of equations is written for the conservation of mass for each phase, as well as for the individual species present in these phases, i.e. the water vapor in the gas phase and the solutes in the liquid phase. In the gas phase, two independent mass balance equations

can be written (considering the water vapor and the dry air as two components). For the droplet, three independent mass balances can be written, since the droplet is composed of three species.

The microscopic formulation for the conservation of the water vapor mass in the drying air can be derived from Equation 5.1, where the left-hand side of the equation represents the summation of an infinitesimal mass of water vapor in the control volume V' of the fluid for an instant t and its variation through time. The right-hand side of the equation represents the flux of mass of water vapor leaving (or entering) the surface S' enclosing the control volume. Using the divergence theorem from vector calculus, it is possible to convert the integral on the surface by the integral on the control volume of the flux leaving (or entering) it.

$$\frac{\mathrm{d}}{\mathrm{d}t} \iiint_{V'} \rho_v \mathrm{d}V' = -\iint_{S'} \left[(\vec{j}_v \cdot \vec{n}) + \rho_v(\vec{U}_{ha} \cdot \vec{n}) \right] \mathrm{d}S'$$
$$= -\iiint_{V'} \vec{\nabla} \cdot \left(\vec{j}_v + \vec{U}_{ha}\rho_v \right) \mathrm{d}V' \tag{5.1}$$

ρ_v is the density of the water vapor in the drying air, $\vec{j}_v$ is the diffusive mass flux of water vapor and $\vec{U}_{ha}$ represents the velocity field in the drying air. The Equation 5.1 can be rewritten as presented below,

$$\frac{\mathrm{d}\rho_v}{\mathrm{d}t} + \vec{\nabla} \cdot \left(\vec{j}_v + \vec{U}_{ha}\rho_v \right) = 0 \tag{5.2}$$

For the sake of simplicity, the formulation presented in Equation 5.2 uses the velocity of the drying air for the estimation of fluxes, instead of the velocity of the individual water molecules in the gas phase. Also, the mass flux of water vapor is written as a contribution of the convective ($\vec{\nabla} \cdot \vec{U}_{ha}\rho_v$) and diffusive fluxes ($\vec{\nabla} \cdot \vec{j}_v$). Using Fick's law of diffusion, the flux $\vec{j}_v$ can be written as shown in Equation 5.3, where D_v represents the diffusion coefficient of water vapor in the drying air.

$$\vec{j}_v = D_v \nabla \rho_v \tag{5.3}$$

The second independent mass balance equation is written for the drying air, as presented in Equation 5.4.

$$\frac{\mathrm{d}\rho_{ha}}{\mathrm{d}t} + \vec{\nabla} \left(\rho_{ha}\vec{U}_{ha} \right) = 0 \tag{5.4}$$

Thus, the first term to the left represents the mass variation with time and the second term is the mass flux.

Regarding now the droplet, a mass balance is written for each solute i, as presented in Equation 5.5. For this equation, the notation adopted is related to the solute mass content.

$$\rho_{\mathrm{drop}}\frac{\mathrm{d}\omega_i}{\mathrm{d}t} + \vec{\nabla} \cdot \vec{j}_i + \rho_{\mathrm{drop}} \left(\vec{U}_{\mathrm{drop}} \cdot \vec{\nabla} \right) \omega_i = 0 \tag{5.5}$$

In Equation 5.5, ρ_{drop} is the density in the droplet, ω_i is the mass content of the solute i, $\vec{j}_i$ is the diffusive mass flux of the solute i and $\vec{U}_{\text{drop}}$ is the velocity field vector inside the droplet. The mass content of a solute i may be calculated for a certain point inside the droplet as a ratio between the solute density ρ_i and the solution density ρ_{drop}. Using the mass contents as a notation for the conservation of mass equation, the summation of the mass contents of all species in the droplet should be equal to unity throughout time and at every point in the droplet (Equation 5.6).

$$\sum_i \omega_i = 1 \tag{5.6}$$

Regarding the diffusive mass flux of a species i in the droplet, the presence of other substances is accounted during the evaluation of the variable $\vec{j}_i$, as shown in Equation 5.7.

$$\vec{j}_i = -\left(\rho_{\text{drop}} D_i \vec{\nabla} \omega_i + \rho_{\text{drop}} \omega_i D_i \frac{\vec{\nabla} M_{\text{n}}}{M_{\text{n}}}\right) \tag{5.7}$$

with,

$$M_{\text{n}} = \left(\sum_i \frac{\omega_i}{MM_{\text{i}}}\right)^{-1} \tag{5.8}$$

with MM_{i} the molar mass of the substance.

In order to link the mass transport equations between the droplet and the drying air, a boundary condition related to the water evaporation flux ($\vec{N}_{\text{v}}$) should be used. At the droplet-air interface, such boundary condition may be written as follows,

$$\vec{N}_{\text{v}} = \rho_w \left(\vec{U}_w \cdot \vec{n}\right) = \rho_{\text{v}} \left(\vec{U}_{\text{v}} \cdot \vec{n}\right) \tag{5.9}$$

Where the subscript w is related to the water in liquid state, while v represents the water in the gas phase. Thus, the Equation 5.9 represents the transport of water molecules at the interface at the droplet and at the air sides. Instead of using the velocity of the water molecules, it is better to use the velocity of the fluid, in particular the air, which is more easily measurable at the experimental scale. Thus, the evaporative flux may be written considering the mass transfer on the gas side of the droplet-air interface as follows,

$$\vec{N}_{\text{v}} = \rho_{\text{v,d}} \left(\vec{U}_{\text{ha}} \cdot \vec{n}\right) + D_{\text{v}} \left(\vec{\nabla} \rho_{\text{v}} \cdot \vec{n}\right) \tag{5.10}$$

Where $\rho_{\text{v,d}}$ is the vapor density above the droplet interface, which depends on the water density on the liquid side of the interface. The Equation 5.10 uses the air velocity for the convective contribution of the evaporative flux and Fick's law of diffusion for the diffusive contribution $D_{\text{v}} \vec{\nabla} \rho_{\text{v}}$. Such representation of the evaporation flux is valid for every point over the droplet surface.

As the droplet loses water by evaporation, its volume is reduced over time. So, it is possible to link the evaporation rate to the reduction in the droplet radius over time, which corresponds to the droplet interface receding velocity. By considering the droplet as a sphere, the evaporation rate $\mathrm{d}m/\mathrm{d}t$ from the whole droplet surface can be written as,

$$\vec{J}_{\mathrm{tot}} = \frac{\mathrm{d}m}{\mathrm{d}t} = \left(\rho_{\mathrm{drop}} 4\pi r^2 \frac{\mathrm{d}r}{\mathrm{d}t} \right) + \left(\frac{4\pi r^3}{3} \frac{\mathrm{d}\rho_{\mathrm{drop}}}{\mathrm{d}t} \right) \tag{5.11}$$

$\overrightarrow{J_{\mathrm{tot}}}$ is the evaporation rate over the droplet surface (i.e. an integration of the evaporation flux $\vec{N}_{\mathrm{v}}$) and r is the droplet radius. However, due to a convergence problem regarding the evaluation of the derivative $\mathrm{d}\rho_{\mathrm{drop}}/\mathrm{d}t$, Equation 5.11 is simplified to the form presented in Equation 5.12

$$\vec{J}_{\mathrm{tot}} = \frac{\mathrm{d}m}{\mathrm{d}t} = \rho_{\mathrm{drop}} \left(4\pi r^2 \frac{\mathrm{d}r}{\mathrm{d}t} \right) \tag{5.12}$$

With the definition of the evaporation flux, the receding interface velocity $\overrightarrow{v_{\mathrm{int}}}$ is then,

$$\vec{v}_{\mathrm{int}} = \frac{\mathrm{d}r}{\mathrm{d}t} = \frac{\vec{J}_{\mathrm{tot}}}{\rho_{\mathrm{drop}} 4\pi r^2} \tag{5.13}$$

The use of this simplified version of the receding interface velocity from Equation 5.13 causes a difference of only 6 % in relation to the value given by Equation 5.11. This percentage was calculated for the trials at 15D-15S wt (air temperature at 40 °C, air velocity at $0.5\,\mathrm{m\,s^{-1}}$ and air absolute humidity at $3.5\,\mathrm{g\,kg^{-1}}$) at the time of the crust appearance.

5.3.2 Momentum transfert

The momentum of a fixed mass of fluid in movement can change as a function of the forces acting upon the fluid. The velocity and pressure fields of this moving fluid can be described by the Navier-Stokes Equation (for a Newtonian fluid). Here, one equation is written for each domain, as presented in Equation 5.14,

$$\rho_k \frac{\mathrm{d}\vec{U}_k}{\mathrm{d}t} + \rho_k (\vec{U}_k \cdot \vec{\nabla}) \vec{U}_k = \vec{\nabla} \cdot \left[-\vec{P}_k + \mu_k \left(\vec{\nabla}\vec{U}_k + (\vec{\nabla}\vec{U}_k)^{\mathrm{T}} \right) - \frac{2}{3} \mu_k \left(\vec{\nabla} \cdot \vec{U}_k \right) I \right] \tag{5.14}$$

The subscript k represents the liquid or the gaseous phase, ρ is the density of the fluid, $\vec{U}$ the velocity vector, P the pressure and μ the fluid viscosity. In the left-hand side of the equation, the first term represents the change on the fluid momentum with time, while the second term represents the momentum transfer through convection. For the right-hand side of the equation, the first term represents the pressure acting on the fluid and the other two terms describe the viscous "diffusion".

As mentioned previously, the presence of a convective air flow around the liquid droplet induces a convective movement inside the latter. In order to describe such momentum

transfer at the droplet-air interface, it is important to firstly describe the local velocity field of both phases. At this interface, the velocity field may be described in terms of its normal and tangential components (Figure 5.1). The normal component of the velocity field across both sides of the droplet-air interface is equal to the velocity of the interface $\overrightarrow{v_{\text{int}}}$ (Equation 5.15). This velocity was presented in Equation 5.13 as a consequence of the droplet evaporation and reduction in volume.
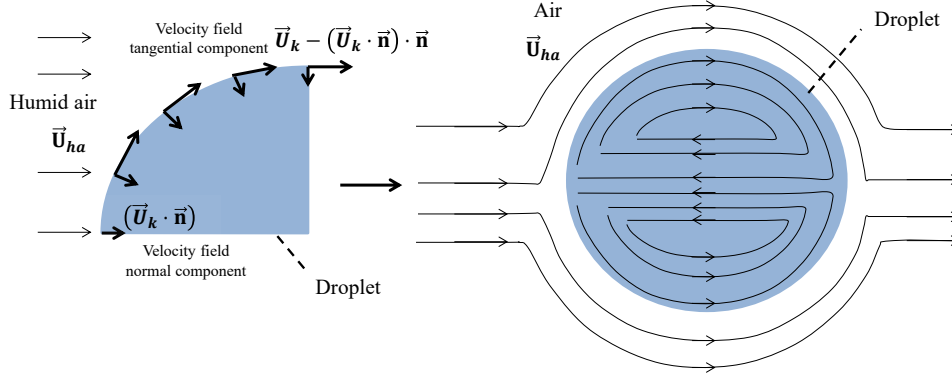
Figure 5.1 – Schematic representation of the velocity field at the liquid droplet-air interface and the resulting two toroidal circulating paths inside the liquid droplet. Subscripts k and ha correspond to the phase (humid air or liquid droplet) and humid air, respectively

$$\left(\vec{U}_{\text{ha}} \cdot \vec{n}\right) = \left(\vec{U}_{\text{drop}} \cdot \vec{n}\right) = \vec{v}_{\text{int}} \tag{5.15}$$

Now, in order to describe the tangential component of the velocity field across the droplet-air interface, a condition linking the tangential stress in each fluid at the interface becomes necessary. As a matter of fact, the tangential shear τ stress must be equal on both fluids for the conservation of momentum. Such shear stress may be calculated as shown in Equation 5.16.

$$\tau = \mu_{\text{drop}}\frac{\mathrm{d}U_{\text{drop}}}{\mathrm{d}r} = \mu_{\text{ha}}\frac{\mathrm{d}U_{\text{ha}}}{\mathrm{d}r} \tag{5.16}$$

With this equation, it is expected that an important difference in velocity should be found between the droplet and the air as a result of the difference in the fluid viscosities. Indeed, the viscosity of the liquid phase, as it contains water, is at least one thousand times higher than the viscosity of the humid air. Also, with an increase in the droplet concentration, and consequently in viscosity, during drying, the order of magnitude of the velocity field in the droplet is decreased.

Regarding the initial values, both droplet and humid air are stagnant during the 30-second diffusive drying. After this period, the inlet air velocity is equal to the velocity setpoint (corresponding to the simulated trial).

5.3.3 Heat transfer

In order to account for the variations in temperature in the air and in the droplet, the equation for the conservation of energy is written for each domain, as can be seen in Equation 5.17, with a term representing the variation of energy with time and also the convective and conductive energy fluxes in the domain.

$$\rho_k C_{p_k} \frac{dT}{dt} + \rho_k C_{p_k} \left(\vec{U}_k \cdot \vec{\nabla} T \right) + \vec{\nabla} \cdot (-\kappa_k \nabla T) = 0 \tag{5.17}$$

The subscript k represents the liquid or the gaseous phase. In Equation 5.17, C_{p_k} is the heat capacity of the fluid, T is the temperature and κ_k is the thermal conductivity.

The boundary condition used to link the transport of energy in each domain is related to the heat of vaporization of water, which is related to the quantity of water evaporated from the droplet. Even though the temperature is continuous through the droplet-air interface, the heat flux is not due to the latent heat of vaporization and such discontinuity is represented by

$$\left(-\kappa_{drop} \vec{\nabla} T \right)_{drop} + \left(\kappa_{ha} \vec{\nabla} T \right)_{ha} = \vec{N}_v h^{l \to g}(T) \tag{5.18}$$

where $h^{l \to g}$ is the latent heat of vaporization of water, calculated at the temperature of the droplet interface.

The last variable added to the model regarding the heat transport equation is the Marangoni effect on the droplet interface, where the shear stress depends on the tangential temperature gradient and can be written as

$$\left[\mu_{drop} \left(\vec{\nabla} \vec{U}_{drop} + (\vec{\nabla} \vec{U}_{drop})^T \right) \right] \cdot \vec{n} = \gamma \vec{\nabla}_t T \tag{5.19}$$

where γ is the temperature derivative of the surface tension σ.

Regarding the initial values, the droplet initial temperature is homogeneous throughout the liquid phase and equal to 293.15 K. For the drying air, the temperature during the 30-second diffusive drying corresponds to the first temperature measurement from a trial in Chapter 3 (as a reminder, this temperature is much inferior than the setpoint). After this period, the air temperature is equal to the setpoint.

5.3.4 Solute physical properties

This section is dedicated to the presentation of the correlations chosen for the estimation of some physicochemical properties of the mixture water-sucrose-dextran, i.e. the water activity, the viscosity, the diffusion coefficient and the density. These properties have a strong impact on the drying kinetics and the distribution of the solutes in the droplet. Even though some data may be found in the literature regarding the estimation of those properties for binary mixtures, i.e. water-sucrose and water-dextran, the data for the ternary system are rare or non-existent. For this reason, the correlations used here consider a combination of the experimental data of the binary systems for the estimation of the properties for the ternary mixture.

Regarding the water activity of the sucrose solution, a four-suffix Margules equation was used in [161] to represent the water activity of sucrose solutions from dilute to highly concentrated solutions (over $96\,\%$ wt of sucrose). The coefficients of the correlation were obtained by regression of different experimental data (sucrose solubility, enthalpy of dilution and vapor-liquid equilibrium data). These thermodynamic properties of the sucrose-water solution were specifically chosen as they allow for the calculation of the water activity coefficient $\Gamma_{\mathrm{w_{suc}}}$ in the solution.

$$\ln(\Gamma_{\mathrm{w_{suc}}}) = \alpha(\theta) \left(x_{\mathrm{suc}}^2 - 1.9831 x_{\mathrm{suc}}^3 + 0.92730 x_{\mathrm{suc}}^3\right) \tag{5.20}$$

The influence of the temperature on the water activity coefficient is accounted with the following parameter,

$$\alpha(\theta) = \left(\frac{-268.59}{\theta}\right) - 861.42 - 1102\log(\theta) + 1399.9\theta - 277.88\theta^2 \tag{5.21}$$

where $\theta = T/T_{\mathrm{ref}}$ (T stands for the air temperature). For the reference temperature T_{ref}, Starzak et al. [161] used $298\,\mathrm{K}$ for the fitting.

From Equation 5.20, the water activity can be calculated as a function of the molar fraction of sucrose x_{suc},

$$a_{\mathrm{w_{suc}}} = (1 - x_{\mathrm{suc}})\Gamma_{\mathrm{w_{suc}}} \tag{5.22}$$

Regarding the dextran solution, experimental data are less common than for the sucrose solution. Furthermore, dextran properties (i.e. diffusion, viscosity, etc.) are different with regard to the multitude of dextran fractions, which makes it difficult for finding experimental data for certain dextran fractions in the literature, specially for highly concentrated solutions. For the dextran fraction used in the present thesis (T40), Gaube et al. [45] proposed the empirical relation in Equation 5.23 from vapor-liquid equilibrium data for a dextran mass content up to $35\,\%$ wt.

$$a_{\mathrm{w_{dex}}} = \exp\left[-V_w MM_{\mathrm{w}} \left(\frac{\mathbf{c}}{23600} + 0.00131\mathbf{c}^2 + 0.0081\mathbf{c}^3\right)\right] \tag{5.23}$$

where V_{w} is the specific volume of water, MM_{w} is the water molar mass and $\mathbf{c}$ stands for the dextran concentration in the solution (in $\mathrm{g\,cm^{-3}}$ for the correlation). The evolution of the water activity with solute mass content for both sucrose (at $298\,\mathrm{K}$) and dextran solutions is presented in Figure 5.2. The water activity is extrapolated for dextran mass contents superior to $35\,\%$ wt. It should be noted that the results given by the correlation were tested during this thesis against experimental data (provided in [45]) for a dextran fraction T500 up to $75\,\%$ wt dextran mass content. The difference between the experimental data and the results given by the model is inferior to $5\,\%$.

In order to estimate the influence of a ternary mixture on the water activity, the correlation employed in the present thesis was adapted from the one used in [36] for the estimation of the water activity of fruit juices, which were considered by the authors as a mixture of three different sugars (i.e. fructose, glucose and sucrose) in different proportions. The developed expression (Equation 5.24) multiplies the water activity
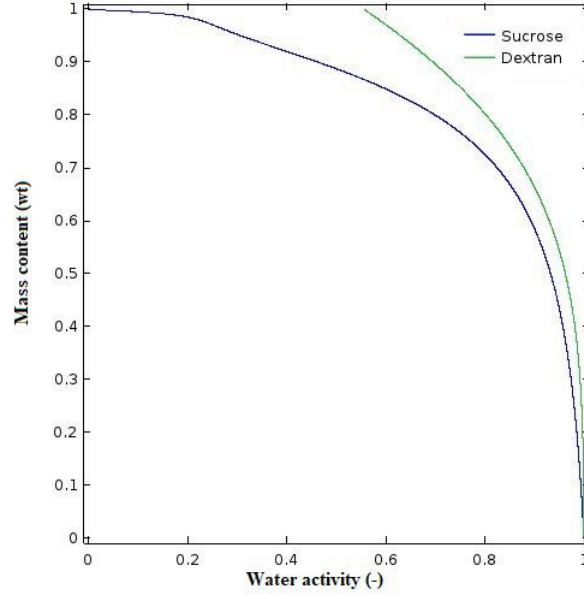
Figure 5.2 – Evolution of the water activity with the solute mass content for the sucrose and dextran binary solutions

given by each binary correlation, $a_{w_{suc}}$ and $a_{w_{dex}}$. These values are evaluated with the total solute content of the droplet, ω_{mix}, instead of using only the sucrose (ω_{suc}) or dextran mass contents (ω_{dex}).

$$a_{w_{mix}} = [a_{w_{suc}}(\omega_{mix})]^{(\omega_{suc}/\omega_{mix})} [a_{w_{dex}}(\omega_{mix})]^{(\omega_{dex}/\omega_{mix})} \quad (5.24)$$

Now, for the viscosity estimation, it could be seen in the literature that, for a binary solution, a set of two empirical correlations were needed for describing the evolution of the solution viscosity with the solute mass content. In other words, a correlation would be developed for the viscosity with solute mass contents below the solute saturation point (generally at $20\,°C$) and another correlation would be used for supersaturated solutions. As a result, a smoothing function should be needed for linking the set of two expressions.

For the sucrose solution viscosity, an Arrhenius model is used in [137] for representing the viscosity from experimental data up to a sucrose mass content of $70.86\,\%$ wt. The effect of the temperature was also added to the model presented in Equation 5.25.

$$\mu_{Arr_{suc}} = \frac{1}{A_{Arr} + B_{Arr}/\omega_{suc}} \exp\left[C_{Arr} \exp(D_{Arr}\omega_{suc}) \left(\frac{1}{T} - \frac{1}{313.15}\right)\right] \quad (5.25)$$

where $\mu_{Arr_{suc}}$ is the viscosity of the solution given by the Arrhenius equation. The temperature T in Equation 5.25 is in K. The coefficients used in this Equation are presented in Table 5.1. In the same work, for the supersaturated solution, creep measurements under small stresses were performed in order to avoid sucrose crystallization. The results were fitted with a WLF (Williams, Landel and Ferry) model. The development of this model is normally related to the glass transition temperature as a reference

temperature. However, the authors found a better fit to the experimental data with a reference temperature of 273.15 K and the resulting expression is shown in Equation 5.26.

$$\log(\mu_{\text{wlf}_{\text{suc}}}) = \left[A_{\text{wlf}} \exp(B_{\text{wlf}} \omega_{\text{suc}}) + \frac{C_{\text{wlf}} \exp(D_{\text{wlf}} \omega_{\text{suc}}(T - 273.15))}{C_2 + (T - 273.15)} \right] \quad (5.26)$$

where $\mu_{\text{wlf}_{\text{suc}}}$ is the viscosity of the supersaturated solution given by the WLF Equation. The temperature T in Equation 5.26 is in K. The coefficients used in this equation are presented in Table 5.1. The viscosity values given by these two models are presented in Figure 5.3, where the dashed curves indicate the tendency of the models if they were used to cover individually the mass content range from 0 % wt to 100 % wt of sucrose. From Figure 5.3, the combination of the Arrhenius and WLF model does give a better representation of the sucrose solution viscosity, compared to the use of only one of these models. However, an inflection point appears at the point where the models intersect. Consequently, in the sucrose mass content range 0.6-0.8 wt, the viscosity values found here may not be as representative of the actual system than the viscosity values calculated for other sucrose mass contents.
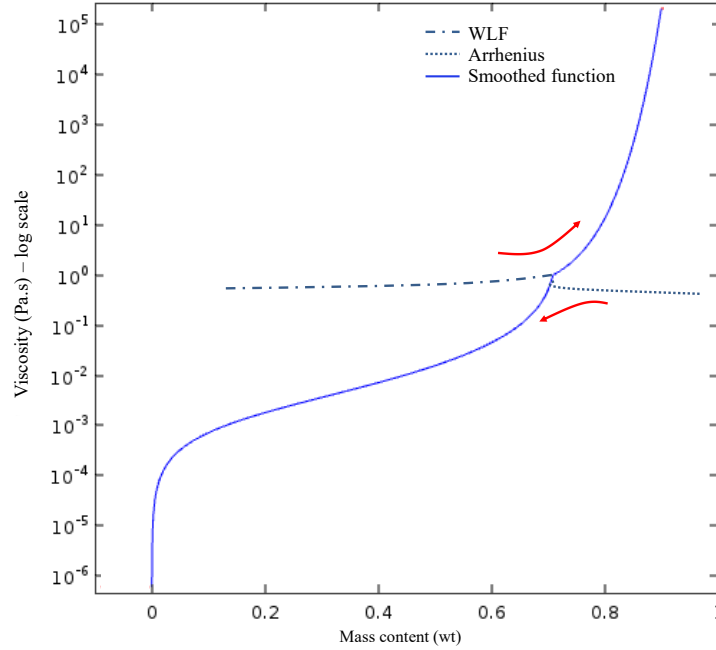
Figure 5.3 – Evolution of the sucrose solution viscosity as a function of the sucrose mass content. Two empirical models (Arrhenius and WLF) are linked together at the mass content 0.7086 wt for a better representation of the solution viscosity

For the dextran, the viscosity below the saturation point (around 50 % wt at 20 °C) is calculated with the Huggins relation (Equation 5.27),

$$\mu_{\text{hug}_{\text{dex}}} = \mu_w \left(\mathbf{c}[\mu] + k_{\text{h}}[\mu]^2 \mathbf{c}^2 \right) \quad (5.27)$$

Table 5.1 – Coefficients employed in Equations 5.25 and 5.26 for estimating the sucrose solution viscosity

Parameters	Arrhenius model	WLF model
A	-2.52×10^2	5.76×10^{-4}
B	1.81×10^4	1.06×10^{-1}
C	4.49×10^2	-1.23×10^{-1}
D	4.02×10^{-2}	4.90×10^{-2}
C_2	-	69.16

where $\mu_{\text{hug}_{\text{dex}}}$ is the viscosity of the dextran solution given by the Huggins model, μ_w is the viscosity of pure water, $[\mu]$ is the dextran intrinsic viscosity ($0.25\,\text{cm}^3\,\text{g}^{-1}$), which is obtained by measuring the viscosity of the diluted solution of the polymer and then linearly correlating it to the polymer molecular mass [12], k_h is Huggins' constant (0.607) and c is the dextran concentration (in $\text{g}\,\text{cm}^{-3}$) [98]. The values of the dextran intrinsic viscosity and the Huggins's constant used here are valid for the dextran fraction T40.

Due to the lack of experimental data of dextran viscosity for supersaturated solutions, in this thesis, the WLF model is used for the dextran mass contents between 50 % wt and 100 % wt (Equation 5.28).

$$\log\left(\frac{\mu_{\text{wlf}_{\text{dex}}}}{\mu_{\text{gl}}}\right) = -\frac{l_1(T - T_\text{g})}{l_2 + T - T_\text{g}} \tag{5.28}$$

where μ_{gl} is a universal viscosity at the glass transition ($10^{11}\,\text{Pa s}$), l_1 and l_2 are "universal" parameters in the WLF model (17.4 and 51.6 K, respectively) [12]. In order to smooth the passage between the Huggins and the WLF models, the value is slightly changed to 16.4 without changing the aspect of the curve. As described in [30], the values of the "universal" WLF parameters may vary slightly between different polymers, for example the l_1 parameter may vary between 16 and 17, while the l_2 parameter may stand between 24 K and 104 K.

The glass transition temperature T_g in Equation 5.28 is calculated with Gordon-Taylor equation, as shown in Equation 5.29.

$$T_\text{g} = \frac{\omega_w \Delta C_{\text{p}_\text{w}} T_{\text{g}_\text{w}} + \omega_{\text{dex}} \Delta C_{\text{p}_{\text{dex}}} T_{\text{g}_{\text{dex}}}}{\omega_w \Delta C_{\text{p}_\text{w}} + \omega_{\text{dex}} \Delta C_{\text{p}_{\text{dex}}}} \tag{5.29}$$

where the subscripts w and dex refer to water and dextran, respectively, ω is the mass content (wt), T_{g_w} is the glass transition temperature of water, $T_{\text{g}_{\text{dex}}}$ is the glass transition temperature of dextran and ΔC_p is the change in heat capacity at the glass transition of water or dextran. These values are presented in Table 5.2. For the glass transition of dextran and its change in heat capacity, a calorimetry analysis was performed with a pure dextran powder with the conditions presented in Chapter 2.

At the present, the viscosity of the binary solutions water-sucrose and water-dextran can be evaluated for the whole range of mass content of the solutes. In order to link

Table 5.2 – Glass transition temperature and change in heat capacity at the glass transition for water and dextran

Substance	T_g (K)	ΔC_p ($\mathrm{J\,g^{-1}\,K^{-1}}$)
Water	134	1.92
Dextran (T40)	222.35	0.3836

the viscosity of these binary solutions to the desired ternary solution, the correlation suggested by [25] is used (Equation 5.30).

$$\mu_\mathrm{mix} = \phi_\mathrm{suc}^2 \ln \mu_\mathrm{suc} + \phi_\mathrm{dex}^2 \ln \mu_\mathrm{dex} + 2\phi_\mathrm{suc}\phi_\mathrm{dex} \left(\frac{2\mu_\mathrm{suc}\mu_\mathrm{dex}}{\mu_\mathrm{suc} + \mu_\mathrm{dex}} \right) \tag{5.30}$$

where ϕ stands for the volume fraction of the solute.

Regarding the diffusion coefficient of the solutes, the Stokes-Einstein equation was adopted, as shown in Equation 5.31. With this correlation, the number of required parameters for evaluating the diffusion coefficient is very small, i.e. only two (the Stokes radius of the molecule and the temperature). Experimental assessment of multi-component diffusion coefficients is complicated, as each component diffuses in each other, and theoretical evaluation of such coefficient often involves more complex theories and a wider number of required parameters [103].

$$D_i = \frac{K_\mathrm{b}T}{6\pi r_{st_i}\mu_\mathrm{drop}} \tag{5.31}$$

where K_b is the Boltzmann constant (1.38×10^{-23} $\mathrm{kg\,m^2\,s^{-2}\,K^{-1}}$), r_{sti} is the Stokes radius of the substance and T and μ_drop are the temperature and viscosity of the liquid mixture. Even though the Stokes-Einstein equation is employed here, the calculation of the diffusive flux takes into account the presence of other solutes in solution (as presented previously in Equation 5.7).

Regarding the density of the droplet, it is calculated as a contribution of all individual densities and mass contents of the components present in the droplet,

$$\frac{1}{\rho_\mathrm{mix}} = \frac{\omega_\mathrm{suc}}{\rho_\mathrm{suc}} + \frac{\omega_\mathrm{dex}}{\rho_\mathrm{dex}} + \frac{\omega_w}{\rho_w} \tag{5.32}$$

5.4 Numerical model (implemented in COMSOL Multiphysics)

The implementation of the droplet drying model is carried out on COMSOL Multiphysics software. With this interactive software, it is possible to study a variety of processes related to different physics, such as electromagnetics, heating, fluid mechanics, chemical reactions and acoustics. It is possible to couple different partial differential equations (PDE), ordinary differential equations (ODE) and algebraic equations coming from different physics in order to give a multiphysics solution to the problem.

After applying the necessary representative equations, initial and boundary conditions to represent the studied system, the software transforms them into their weak form. The equations described previously to represent the drying of the droplet are partial differential equations that should be valid at every point inside the droplet and the drying air. The retained functions and its derivatives should remain smooth in every point of the domain. However, the resolution of such strict equation is not always straightforward as the physicochemical properties of the materials being simulated, for example, may not follow smooth variations depending on the simulated physics. Thus, the weak formulation is applied to give solutions to the underlying physics in a less-strict way, where the terms are not necessarily well-defined at every point, but rather its integral is. For example, in Equation 5.33, with the strong formulation, the solution u should respect the shown relation for the whole domain Ω,

$$R(u) = f \quad , \ (\Omega) \tag{5.33}$$

While in the weak form, the solution u is found by considering the integral of the condition R on the domain Ω. The variable ν is called a test function and helps finding the desired solution. More information on the weak formulation may be found in [120].

$$\int_\Omega R(u)\nu = \int_\Omega f\nu \tag{5.34}$$

5.4.1 Geometry definition

The first step regarding the implementation of a given model on COMSOL is the definition of the geometry representing the studied case. Here, the model is defined on two dimensions with an axis of symmetry for reducing the computational time when evaluating the equations. So, a rectangle is used to represent the wind tunnel and a circle is used for the droplet. The representation of such geometry is shown in Figure 5.4. The axis of symmetry is predefined as a vertical axis on COMSOL. In order to represent the actual horizontal drying tunnel, all the vector directions should be considered accordingly. Also, the air is set to flow upward. Finally, the center of the droplet is set at the origin of the axis (r, z). The droplet-air boundary may be defined in two different ways in COMSOL: it can either be a *Union*, where both domains share the same boundary and the continuity of the fields and fluxes are maintained by default, or the geometry can form an *Assembly*, where the contact boundary between the domains is separately defined for each one of them, with no overlapping and the continuity of fields should be explicitly defined. The option *Union* is used for the droplet model here.

5.4.2 Coupled physics implementation

Modeling the drying of the droplet with COMSOL does not consist of only writing the right set of equations. Instead, a couple of options should be changed within the software standard settings in order to better represent the physics being simulated.

For dealing with the fluid flow, a weakly compressible flow option is used for calculating the density of the fluid. With the Navier-Stokes equation, the fluid may be handled as an incompressible fluid, as a weakly compressible fluid or a compressible one. The difference
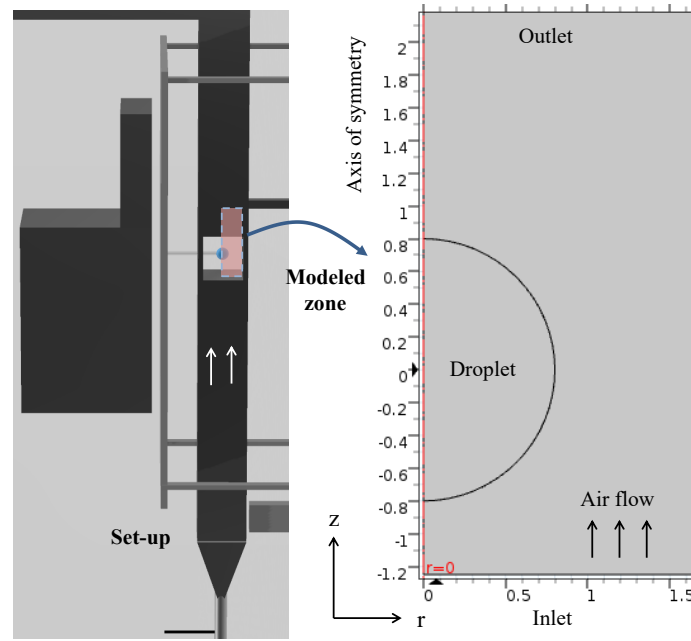
Figure 5.4 – Schematic representation of the modeled zone in the set-up designed in Chapter 3 and the geometry defined in COMSOL (with dimensions in millimeters). A 2-D axisymmetric model is defined with a vertical axis of symmetry. The flow of air is computed upwards.

between these settings is related to the dependence of the fluid properties with the temperature and the pressure. For the incompressible fluid, the Navier-Stokes equation can be separated from the temperature field evaluation. For the weakly compressible flow, the effect of the pressure on the fluid density can be disregarded. The use of the weakly compressible fluid formulation requires appropriate stabilization techniques, for example the use of pseudo time step, as used in [47]. The temperature field coming from the heat transport equation is used for calculating the fluid properties. Also, a step function varying slowly from zero to one in one second is multiplied by the inlet flow of air, thus the value given by the inlet condition slowly increases from zero to the set value and a proper initialization of the model can be performed. Furthermore, for improving the model accuracy, the velocity field is discretized to a quadratic basis, while the pressure field is discretized to a linear basis.

For the transport of moisture in the gas phase, the conservative form is used to handle the weakly compressible fluid. The velocity field comes from the Navier-Stokes equation and the temperature comes from the heat transport equation. For the boundary conditions at the droplet interface, the option "reaction terms" is applied only for the moisture transport module. This ensures that no additional flux term will be added in the calculation of solute transport inside the droplet.

Regarding the transport of solutes inside the droplet, the water evaporation flux is also multiplied by the step function used with the air inlet flow condition. The fluid velocity and pressure comes from the Navier-Stokes equation, while the droplet temperature is obtained with the heat transport equation. In order to minimize numerical errors, the

water mass content is solved from the sucrose and dextran mass contents, as the former presents the higher mass content.

Finally, for the heat transport equation, velocity and pressure are used from the Navier-Stokes equation, while the solutes concentrations in the droplet and the vapor concentration in the air come from their respective transport equations. It is also important to specify the "source" for the latent heat of vaporization evaluation. Here, the option "upside" is selected, as it refers to the droplet.

5.4.3 Meshing

The meshing technique, which consists of dividing the geometry of the model in a finite number of elements with which the functions are evaluated, is a critical step in the development of the model. Indeed, the convergence of the model and the accuracy of the results strongly depends on the mesh applied to the geometry. A coarse mesh may give fast results with a relatively low precision, while a fine mesh gives finer results but with an important computational cost. For a 2-D model, triangular of quadrilateral elements may be used to discretize the geometry. In the present model, triangular elements were used for the air and the droplet domains. Also, a finer mesh distribution at the droplet-air interface is selected so that the boundary fluxes can be properly computed, as presented in Figure 5.5.
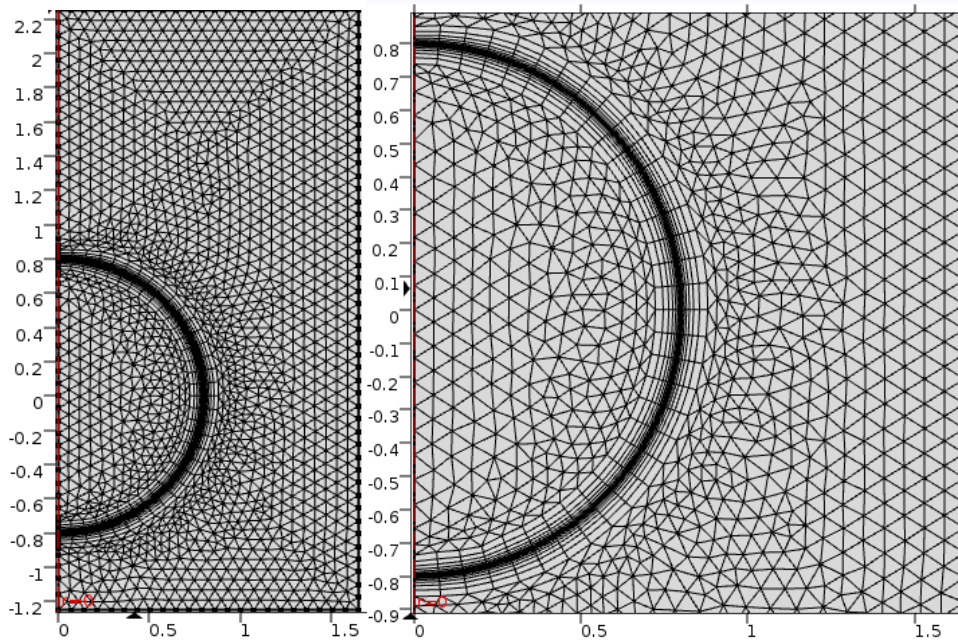
Figure 5.5 – Representation of the mesh elements used to discretize the liquid and gas domains. A finer mesh resolution is chosen at the droplet-air boundary for better computing the transport fluxes. The number of mesh elements used for the whole geometry is equal to 3493 elements

The size of the mesh elements can be easily chosen with COMSOL (i.e. normal, coarse, fine, etc), where predefined size parameters are already selected, such as the maximum element size, the minimum element size, the size of the mesh along curved boundaries

(curvature factor), the element growth rate (to determine the rate at which elements can grow from a region with small elements to a region with larger elements) and the resolution of narrow regions. A coarse mesh, with 1716 elements (given the geometry size of $3.3\,\text{mm} \times 3.5\,\text{mm}$), was firstly chosen for testing the convergence of the model. However, the precision required for the fluxes estimation could not be satisfied by this mesh and the model would not converge. The convergence could be attained with a normal mesh (3493 elements) and a fine mesh (5492 elements). A finer mesh (with more than 8200 elements) could not be used due to a limitation in the computer available memory. The selection of the mesh size was accomplished by comparing the drying kinetics and the solute distribution results. As no difference could be seen between the results from the normal and the fine meshes, the former was used as mesh size in the present model. The maximum and minimum element sizes were $0.0743\,\text{mm}$ and $0.0033\,\text{mm}$, respectively. The maximum element growth rate was 1.15, the curvature factor was set at 0.3 and the resolution of narrow regions was equal to 1. With the parameters presented above, every simulation was accomplished in 40 min with 2 GB of memory.

5.4.4 Moving mesh definition

The final section regarding the implementation of the droplet drying model is related to the use of a module of moving mesh, in order to represent the reduction in droplet diameter resulting from the moisture removal. In COMSOL, three methods can be employed for tracking boundaries such as the droplet-air interface: the level set, the phase field and the Arbitrary Lagragian-Eulerian moving mesh (ALE) method. The first two of these methods use a function denoted ϕ, which varies between zero and one, for indicating two different phases. For example, the value of one may be attributed to the gas phase, while the value of zero may be attributed to the droplet. The value of 0.5 is then attributed to the droplet-air interface. The fluid properties are calculated according to the value of the function ϕ. However, such methods could not be employed in the present model because the center of the droplet is fixed in space. These methods can track an interface, but both fluids should be in movement.

The ALE method can be used to accurately track the interface. The mesh nodes are smoothly displaced with such method and the Navier-Stokes equations are fully coupled to the mesh equations and are solved on a moving frame. The Arbitrary Lagragian-Eulerian method combines two common fluid descriptions: the Lagragian description and the Eulerian description. In the former, each individual node of the computational mesh follows the fluid material and can be used to easily track free surfaces. As for the Eulerian description, which is a common technique used in the computational fluid dynamics, the mesh nodes are fixed in space and the fluid moves from one mesh node to another. For the drying droplet model, a normal velocity v_{int} is set to the droplet interface and the rest of the geometry moves accordingly. In the ALE method, neither the material nor the spatial frames are used as a reference for the mesh nodes, instead a third frame, the reference frame, is added to identify the mesh nodes. More information on the underlying mathematical formulation of the Arbitrary Lagragian-Eulerian method can be found in [28].

5.5 Drying behavior

This section is dedicated to the results given by the model regarding the drying kinetics and the component distribution inside the droplet. The results are given until the time when the crust completely covers the droplet surface, which correspond to the time t_{tc} obtained experimentally in Chapter 3 for every trial. Consequently, for the drying kinetics, the analysis is focused on the accordance between the experimental and modeled moisture content for the period of appearance of a solid at the surface of the droplet and the complete formation of a crust at the droplet surface. The time $t_{1\ sd}$ and t_{tc} from Chapter 3 are used for the comparison. For the component distribution, the modeling results are firstly compared to the mass content profiles presented in Chapter 4. Secondly, the component distribution is presented for trials at higher drying air temperatures. Finally, a 30-second diffusive drying was added to every simulation in order to mimic the correction done at the drying kinetics in Chapter 3. Unless explicitly stated, the drying time presented hereafter considers the end of this diffusive drying period as the initial time 0.

Before starting the analysis on the drying kinetics, it is interesting to present some general tendencies observed with the drying of the droplet, for example, the evaporation flux profile at the droplet surface and the temperature differences across the surface or between the droplet center and surface. The Figure 5.6 presents the evaporation flux calculated at approximately 40 s for a dextran-sucrose droplet (with mass contents 15D-15S wt) dried at 40 °C (air velocity at $0.5\,\mathrm{m\,s^{-1}}$ and absolute humidity at $3.5\,\mathrm{g\,kg^{-1}}$). For a better visualization, the mass flux is presented as a function of the droplet surface arc length and the value of zero corresponds to the droplet side facing the air flow.
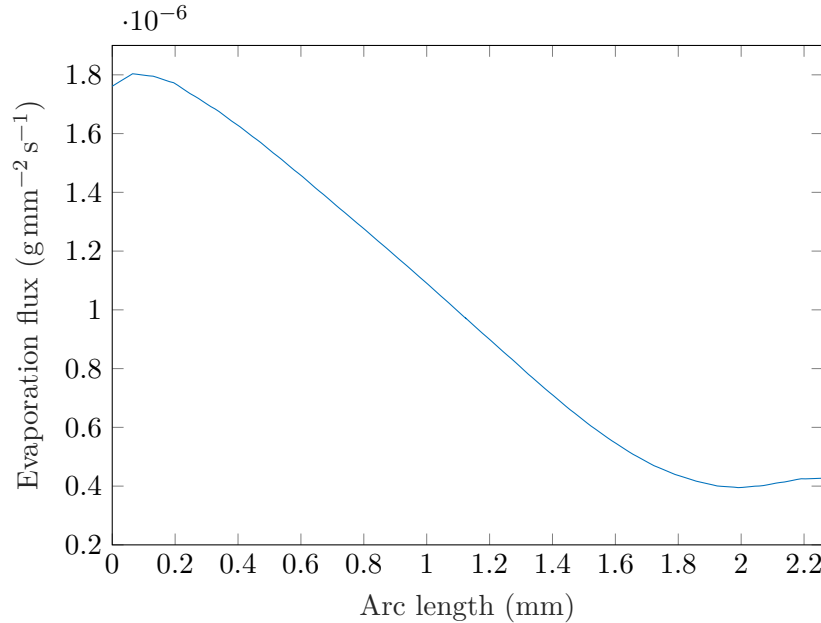
Figure 5.6 – Evaporation flux as a function of the droplet surface arc length for a dextran-sucrose droplet with mass contents 15D-15S wt and dried at 40 °C. The inlet air velocity is $0.5\,\mathrm{m\,s^{-1}}$ and the inlet air absolute humidity is $3.5\,\mathrm{g\,kg^{-1}}$. The value of zero for the arc length corresponds to the droplet side facing the air flow

The evaporation flux is four times bigger at the droplet side facing the air flow compared to the opposite side, for the given example. This difference can be explained by the distribution of water vapor around the droplet and, consequently, the driving force for mass transfer. A schematic representation of the water vapor concentration (in $kg\,m^{-3}$) and the drying air velocity field (red arrows, scaled according to the velocity field intensity) are shown in Figure 5.7 for the conditions stated above for the evaporation flux. As can be seen, the global transport of water vapor in the drying gas follows the trajectory of the air flow. The water molecules leaving the droplet side facing the air flow will be transported around the droplet before leaving the drying tunnel. A higher accumulation of water vapor at the rear side of the droplet is linked to the local velocity profile. As a matter of fact, a small vortex is formed at the rear side of the droplet. In order to explain the appearance of such vortex, the Reynolds number of the air flow around the droplet was calculated and it stands at approximately $Re = 50$. If the Reynolds number were much inferior to 1, the air flow streamlines would be symmetrical on both sides of the droplet. But, as the Reynolds number is inferior to 100, a small steady vortex is formed at the rear side of the droplet. The air velocity at this zone is as small as 10^{-6} $m\,s^{-1}$. As a result, the water vapor concentration is higher at the rear side of the droplet and in turn the concentration gradient is smaller. Since the evaporation flux depends on the vapor concentration distribution in the gas phase, its value is superior at the droplet side facing the air flow.
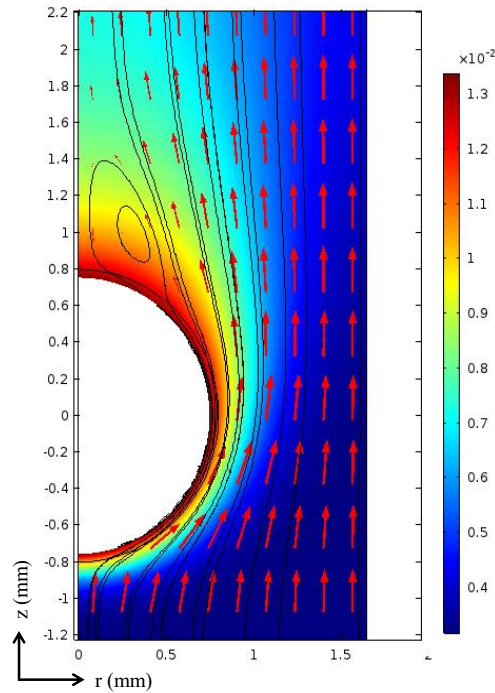
Figure 5.7 – Representation of the water vapor concentration profile (in $kg\,m^{-3}$) around the dextran-sucrose droplet (15D-15S wt) at 40 s. The velocity field is indicated by the red arrows (these are scaled according to the magnitude of the velocity vector). The inlet air velocity is $0.5\,m\,s^{-1}$, the inlet air absolute humidity is $3.5\,g\,kg^{-1}$ and the inlet air temperature is $40\,°C$. The geometry dimensions are presented in mm

The difference in the evaporation flux across the droplet surface also affects the droplet temperature. Due to the evaporative cooling effect, the droplet side with greater evaporation flux will experience the lowest temperature. The difference in temperature across the surface was found to be approximately $0.2\,\mathrm{K}$. Naturally, with a macroscopic point of view of the drying process, such small difference could be disregarded, but thanks to the subtlety in the results obtained with the microscopic modeling, such difference becomes evident. As for the temperature difference between the droplet center and surface, it stands at $0.1\,\mathrm{K}$ in the first seconds of drying, but is reduced afterwards to approximately $0.05\,\mathrm{K}$, as shown in Figure 5.8. The hypothesis used in the literature of an isothermal first drying stage is reasonable. If the simulation continued through the falling-rate period, the difference in temperature between the wet particle center and surface would be more pronounced, as a result of a lower evaporative cooling effect coming from the lower evaporation flux. According to [106], the temperature difference can attain considerable values (superior to $10\,\mathrm{K}$) depending on the drying air temperature.

5.5.1 Droplet moisture loss

In order to compare the drying kinetics obtained from the droplet drying model, the moisture content is presented during the time of first appearance of a solid ($t_{1\,\mathrm{sd}}$) and the time when the crust covers the droplet surface (t_{tc}), the same parameters shown in Chapter 3. For all the experimental conditions performed with the dextran-sucrose droplet, the modeling results are displayed in Table 5.3. The superscript *exp* refers to the moisture content obtained in Chapter 3, while the superscript mdl refers to the modeling results. A relative difference Δ was calculated between each modeled and experimental moisture content (the experimental value was used as reference). The moisture content given by the model is calculated from the solutes mass content as shown in Equation 5.35 and is normalized to the first moisture content in the simulation.

$$X^{\mathrm{mdl}} = \frac{1 - \omega_{\mathrm{ds}}}{\omega_{\mathrm{ds}}} \tag{5.35}$$

From the results presented in Table 5.3, it is possible to observe two tendencies in the results given by the model: the accordance between the modeling results and the experimental data for the trials under stagnant air and for the trials under a convective air stream.

Firstly, for the trials carried out at $20\,^{\circ}\mathrm{C}$ (under stagnant air), the relative difference between the modeled and experimental normalized moisture content is inferior to $10\,\%$ at the time $t_{1\,\mathrm{sd}}$. The exception is found for the trial 15D-15S wt. For this trial, the model underestimated the drying rate and, consequently, the normalized moisture content at the time $t_{1\,\mathrm{sd}}$ is higher in the model ($X_{1\,\mathrm{sd}}^{\mathrm{n,mdl}} = 0.59$ and $X_{1\,\mathrm{sd}}^{\mathrm{n,exp}} = 0.52$). Considering X_{o}, $X_{1\,\mathrm{sd}}$ and $t_{1\,\mathrm{sd}}$, the experimental drying rate is $0.002\,\mathrm{kg\,s^{-1}\,kg^{-1}}$ and the modeled drying rate is $0.0018\,\mathrm{kg\,s^{-1}\,kg^{-1}}$. Despite these small differences, it is possible to say that the model corresponds well to the experimental data. For the time when the crust covers the droplet surface t_{tc}, the difference between the experimental and modeling results is also near $10\,\%$.

Now, regarding the simulations performed with a convective air flow, an important difference between the modeling and experimental results can be found. Such difference
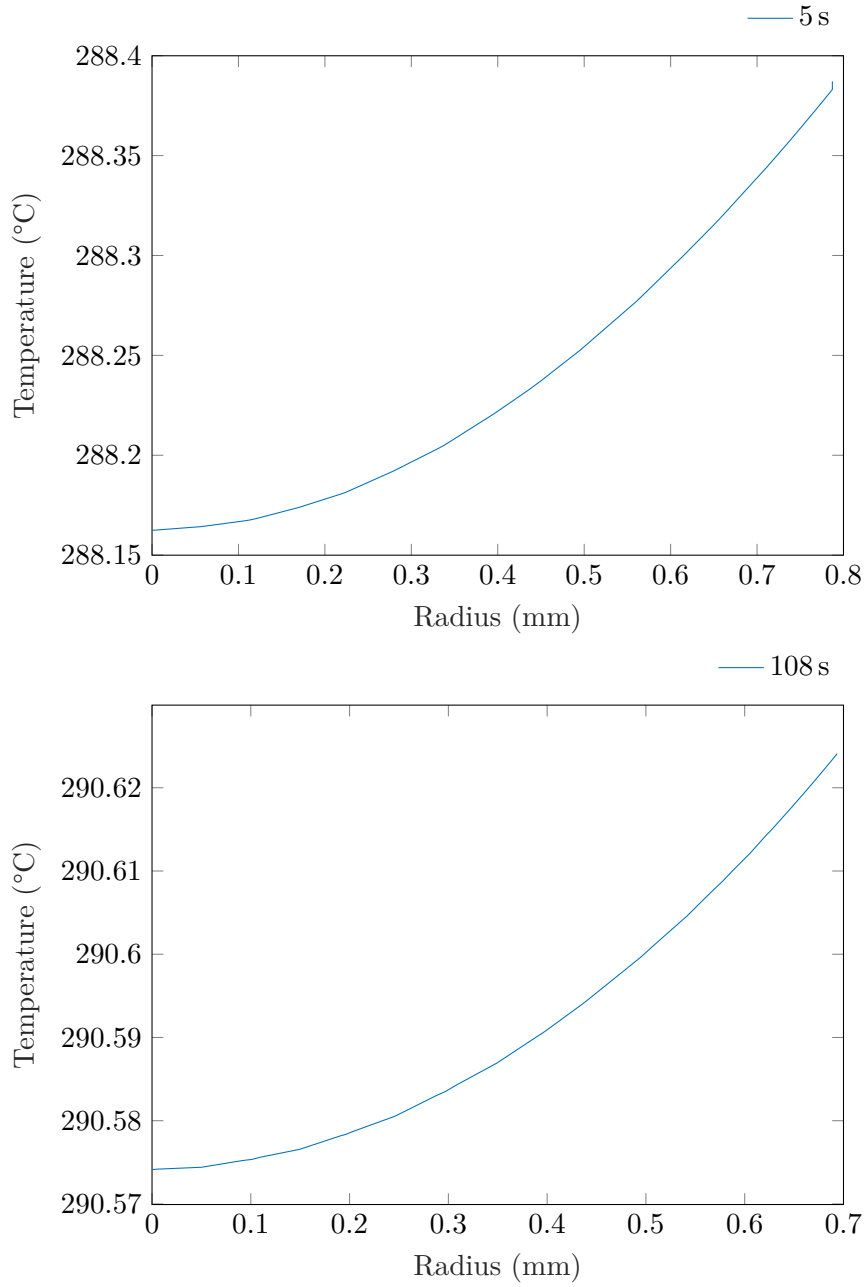
Figure 5.8 − Radial temperature profiles across the droplet. The profiles were taken at the beginning of the convective drying (5 s) and at the time $t_{1\text{ sd}}$ (108 s). Trial at 40 °C, with air velocity at $0.5\,\text{m}\,\text{s}^{-1}$ and absolute humidity at $3.5\,\text{g}\,\text{kg}^{-1}$. Initial mass content: 15D-15S wt

can be as high as 30 % for the time $t_{1\text{ sd}}$. For the time t_{tc}, the relative difference also presents similar values. In these cases, the evaporation rate calculated by the model is superior to the experimental evaporation rate. For example, in the case where $\Delta = 0.3$ ($T_{\text{ha}} = 40$ °C, $u_{\text{ha}} = 0.2\,\text{m}\,\text{s}^{-1}$, $Y_{\text{ha}} = 9\,\text{g}\,\text{kg}^{-1}$, 5D-15S wt) the evaporation rate from the model can be estimated at $0.015\,\text{kg}\,\text{s}^{-1}\,\text{kg}^{-1}$, while the experimental one

is $0.010 \, \mathrm{kg \, s^{-1} \, kg^{-1}}$. Such difference arises from the way at which the experiments and the simulations are carried out. In the model, the inlet flow of air is constant through the drying time. In the experiments, the droplet dries in cycles with convective and stagnant drying air. Consequently, the constant flow of air favors the evaporation and, at a given time, the modeled normalized moisture content is indeed inferior to the experimental one. Despite these differences, the model can still be used to illustrate the evolution of the dextran-sucrose droplet properties during drying.

5.5.2 Influence of internal convection on mass content profile

This section is dedicated to the analysis of the influence of the convection inside the droplet on the resulting total solute content profiles. The analysis is performed on the simulation with an air temperature at $40 \, °\mathrm{C}$ (inlet air velocity at $0.5 \, \mathrm{m \, s^{-1}}$ and inlet air absolute humidity at $3.5 \, \mathrm{g \, kg^{-1}}$) and mass content of 15D-15S wt. As commented previously, the flow of air around the droplet promotes the appearance of a convective movement in the droplet. Such motion is presented in Figure 5.9 with the help of the velocity vectos (red arrows). Also, with the help of the streamlines (dark lines), it is possible to see that the center of the vortex inside of the droplet is located at approximately $0.5 \, \mathrm{mm}$ from the droplet center. With the airflow at $0.5 \, \mathrm{m \, s^{-1}}$, the velocity magnitude in the droplet is around $2 \times 10^{-6} \, \mathrm{m \, s^{-1}}$ at the droplet center and at its surface, while in the vortex the velocity is decreased to approximately $3 \times 10^{-7} \, \mathrm{m \, s^{-1}}$. Such small velocity arises from the higher dextran-sucrose droplet viscosity (approximately $0.7 \, \mathrm{Pa \, s}$), in relation to the viscosity of the drying air ($1.5 \times 10^{-5} \, \mathrm{Pa \, s}$).
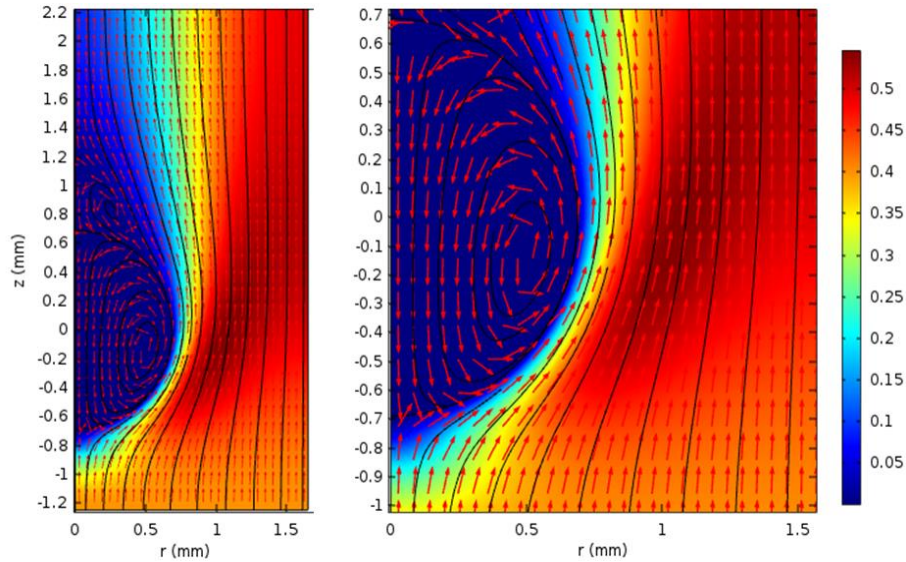
Figure 5.9 − Representation of the fluid flow for both the drying air and the droplet. The sense of the motion is indicated by the red arrows. The streamlines are represented by the dark lines and the velocity magnitude (in $\mathrm{m \, s^{-1}}$) is indicated by the colored pattern. The geometry dimensions are presented in mm. The inlet air velocity is $0.5 \, \mathrm{m \, s^{-1}}$, the inlet air absolute humidity is $3.5 \, \mathrm{g \, kg^{-1}}$ and the inlet air temperature is $40 \, °\mathrm{C}$. The droplet initial composition is 15D-15S wt

Regarding now the total solute content profile, an overview of such profile is presented in Figure 5.10 for the time of first appearance of a solid ($t_{1\,sd} = 108$ s). The colored pattern is used to represent the zones of higher and lower total solutes contents. At a first view, the results shown in Figure 5.10 display an external layer with higher mass content (at approximately $\omega = 0.70$ wt), while the core of the droplet is relatively at the initial total solute content of $\omega = 0.30$ wt. Also, the solute mass content at the surface of the droplet seems to increase from the droplet side facing the air flow to the rear side. Following the direction of the vector field in the droplet, the solute mass content goes from $\omega = 0.60$ to $\omega = 0.71$ across the droplet surface.
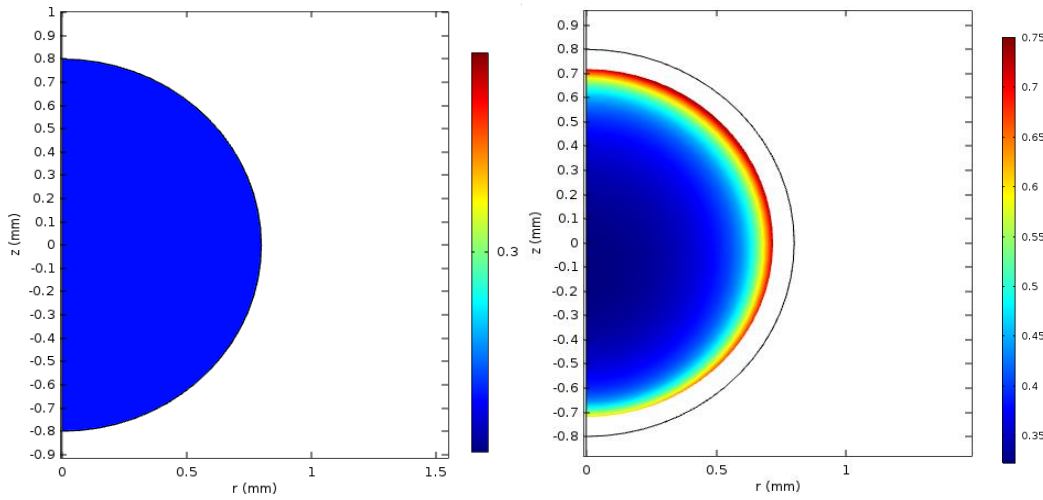
Figure 5.10 − Representation of the total solutes content at the beginning of the simulation at $40\,^{\circ}$C (the inlet air velocity is $0.5\,\mathrm{m\,s^{-1}}$ and the inlet air absolute humidity is $3.5\,\mathrm{g\,kg^{-1}}$) and at the time of first appearance of the solid (at $108\,$s). The droplet initial composition is 15D-15S wt. From blue to red, the colored pattern helps visualize the zone with higher mass contents

In order to better see the total solutes content profiles, the mass contents are plotted in Figure 5.11 for the droplet coordinates $(r, z = 0)$ from the time $0\,$s until the time of first appearance of a solid. Although the velocity profile inside the droplet presented a vortex, the effect of the radial component of the velocity field is not much visible in the radial mass content profiles, as they seem to increase radially outward. In order to see if such profile is the result of the higher dextran-sucrose droplet viscosity, a test was performed with the droplet viscosity set at the viscosity of pure water. For this case, the total solute content profiles also presented a vortex at $r = 0.5$ mm. Thus, it can be said that the profiles shown in Figure 5.11 are much more linked to the diffusive transport of the solutes, than to the convective transport. It is also interesting to see that, while the mass contents at the center of the droplet slowly increase from the beginning of the simulation until the time $t_{1\,sd}$ (from $\omega = 0.3$ wt to approximately $\omega = 0.33$ wt), the calculated mass contents at the surface of the droplet increase much faster. This would indicate a much faster evaporation flux, compared to the homogenization of the components inside the droplet.

The time $t_{1\,sd}$ obtained in Chapter 3 was used as a reference in the simulation to indicate the onset of solid formation. In the literature, regarding the droplet drying simulations,
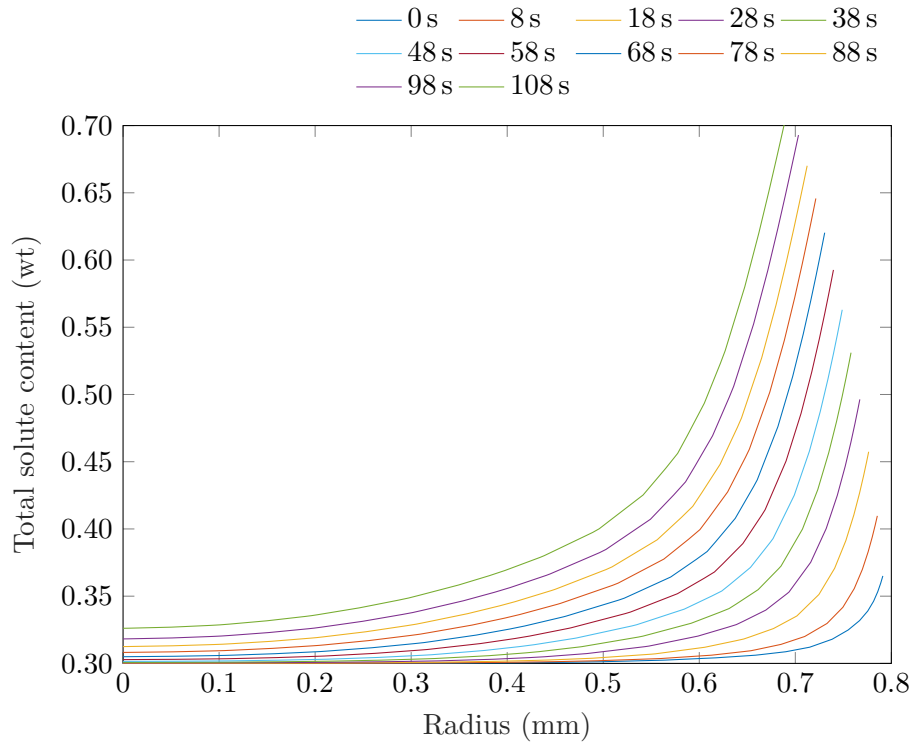
Figure 5.11 − Total solute content profile from the time $0\,\mathrm{s}$ until the time of the first appearance of a solid ($87\,\mathrm{s}$) for the trial at $40\,^\circ\mathrm{C}$ (the inlet air velocity is $0.5\,\mathrm{m\,s^{-1}}$ and the inlet air absolute humidity is $3.5\,\mathrm{g\,kg^{-1}}$) and mass contents at 15D-15S wt

the volume fraction is used as an indicator of the formation of the solid crust [109]. The value of $\phi = 0.6$ should be attained for the formation of a crust (this value is derived from the maximum packing fraction of equal-sized spheres). For the profiles shown in Figure 5.11, the volume fraction at the droplet surface is equal to 0.65 at $108\,\mathrm{s}$, while it is equal to 0.60 and 0.55 at $98\,\mathrm{s}$ and $88\,\mathrm{s}$, respectively. The use of such criterion may be reasonable for indicating the formation of the solid crust at the droplet surface.

5.5.3 Analysis on the component distribution

For this section, the presentation of the mass content profiles of dextran and sucrose on the droplet coordinate $(r, z = 0)$ is firstly carried out with the trials at $20\,^\circ\mathrm{C}$ and mass contents 5D-5S wt and 15D-15S wt, under stagnant air, as shown in Chapter 4. Next, the mass content profiles are presented for simulations with higher air temperatures (with the dextran-sucrose mass contents 15D-15S wt), under convective air flow.

As a reminder, from the Raman technique, it was possible to observe with the trial 5D-5S wt a dextran-rich zone at the droplet surface and a sucrose-rich zone at the droplet core, with such difference becoming more evident towards the end of the experiment (higher Raman intensity from the solutes). Also, a mass content profile at $28\,\mathrm{min}$ of drying was presented for this trial, where the sucrose mass content was relatively the same along the droplet radius and the dextran presented a higher mass content at the droplet

surface. For the models presented here, the simulations did not last as long as the trials performed in the acoustic levitator. So, the analysis of the component distribution was carried out using the time of first solid appearance from Chapter 3. In Figure 5.12, the dextran and mass content profiles are plotted at 832 s. The droplet radius values displayed in the axis x almost coincide with the spacing between the measurement points in the Raman technique (0.08 mm).
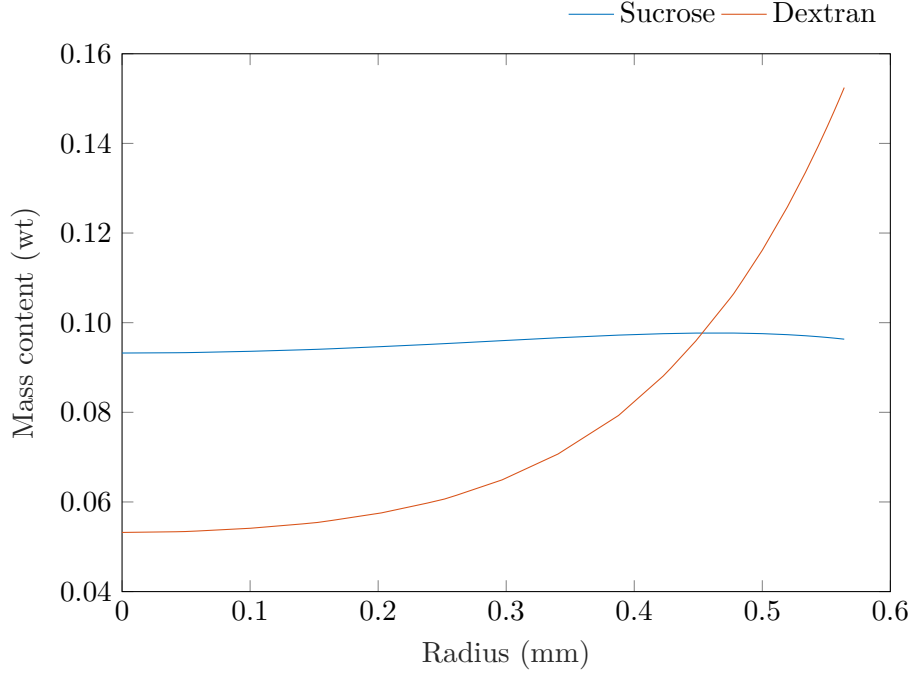
Figure 5.12 – Dextran and sucrose mass content profiles for the trial at 20 °C (stagnant air and $Y_{ha} = 2.4$ g kg^{-1}) and mass contents 5D-5S wt. The profile presented here corresponds to the time of a first solid appearance (832 s)

From the modeling results at the time $t_{1\,sd}$ in Figure 5.12, it is possible to observe that the dextran mass content profile increases radially outward, while the sucrose mass content is virtually linear along the droplet radius. Even though the simulation started with both solutes at $\omega = 0.05$ wt, the dextran mass content at the surface is almost three times higher than the mass content at the droplet center. The slow-diffusing dextran accumulates at the droplet surface as the droplet shrinks, while the sucrose diffuses towards the droplet center. The mass content profiles from the Raman technique did not indicate a richer dextran region at the drying time presented in Figure 5.12, but only indicated such difference (of approximately 0.1 wt between the droplet surface and center) a few minutes later. It can be that the Raman signal from the solutes was not high enough for the data treatment algorithm to identify such segregation (the solutes' signal would increase as the solid particle was being formed and higher solutes contents were measured).

For the 15D-15S wt, the mass content profiles taken at the time of the first solid appearance also presented a higher dextran mass content at the droplet surface, as can be seen in Figure 5.13. However, for the sucrose, it can be seen that the mass content increases slightly from the droplet surface to the position $r = 0.5$ mm (from

$\omega = 0.19$ to $\omega = 0.21$, respectively). Apart from this small curvature in the sucrose mass content profile, the tendencies in Figure 5.13 and 5.12 are very similar. With the Raman technique, the formation of a dextran- or a sucrose-rich zones could not be clearly identified. As the biggest increase in the dextran mass content is found in the 0.1-mm external layer, the Raman technique could have presented a certain difficulty in measuring the mass content at the wet particle surface due to light distortion. Alternatively, such dextran profile might have risen from an overprediction of the dextran diffusion coefficient, which would lead to a higher accumulation at the droplet surface, or else the droplet viscosity is not well represented as to avoid the solutes' diffusion inside of the liquid droplet.
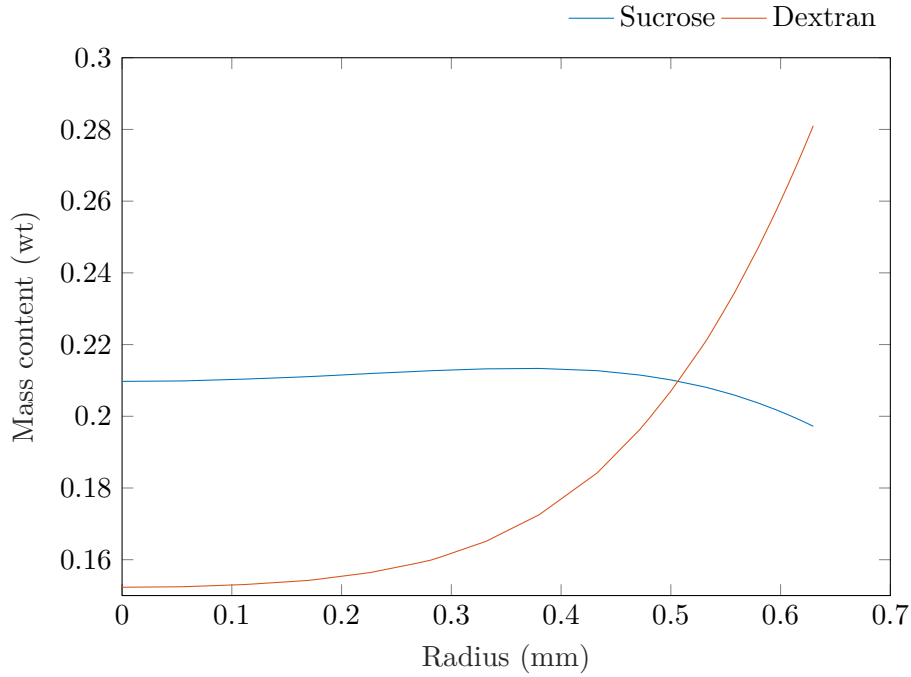
Figure 5.13 – Dextran and sucrose mass content profiles for the trial at $20\,°\text{C}$ (stagnant air and $Y_{\text{ha}} = 2.4\ \text{g kg}^{-1}$) and mass contents 15D-15S wt. The profile presented here corresponds to the time of a first solid appearance ($525\,\text{s}$)

Now, regarding the simulations at higher air temperatures, the dextran and sucrose profiles are presented in Figure 5.14 from the droplet coordinate ($r, z = 0$) at the time of the first solid appearance. The initial solutes contents corresponded to 15D-15S wt. As a reminder, for the trial at $40\,°\text{C}$ ($u_{\text{ha}} = 0.5$ m/s, $Y_{\text{ha}} = 35\,\text{g kg}^{-1}$), the time $t_{1\ \text{sd}}$ was said to be $108\,\text{s}$, while for the trial at $80\,°\text{C}$ ($u_{\text{ha}} = 0.5$ m/s, $Y_{\text{ha}} = 35\,\text{g kg}^{-1}$) the $t_{1\ \text{sd}}$ is equal to $45\,\text{s}$.

In Figure 5.14, the increase in the dextran mass content profile is essentially found in the 0.1-mm external layer, where the mass content increases from $\omega = 0.15$ wt to approximately $\omega = 0.64$ wt in the simulation at $80\,°\text{C}$. As a matter of fact, such steep increase in the mass content is indeed related to the higher evaporation flux found at this trial temperature. The evaporation flux at the droplet side facing the air flow is equal to $3.8 \times 10^{-6}\ \text{g mm}^{-2}\,\text{s}^{-1}$ at the air temperature $80\,°\text{C}$, while the evaporation flux is reduced at $1.8 \times 10^{-6}\ \text{g mm}^{-2}\,\text{s}^{-1}$ and $2.4 \times 10^{-7}\ \text{g mm}^{-2}\,\text{s}^{-1}$ for the air temperatures at $40\,°\text{C}$
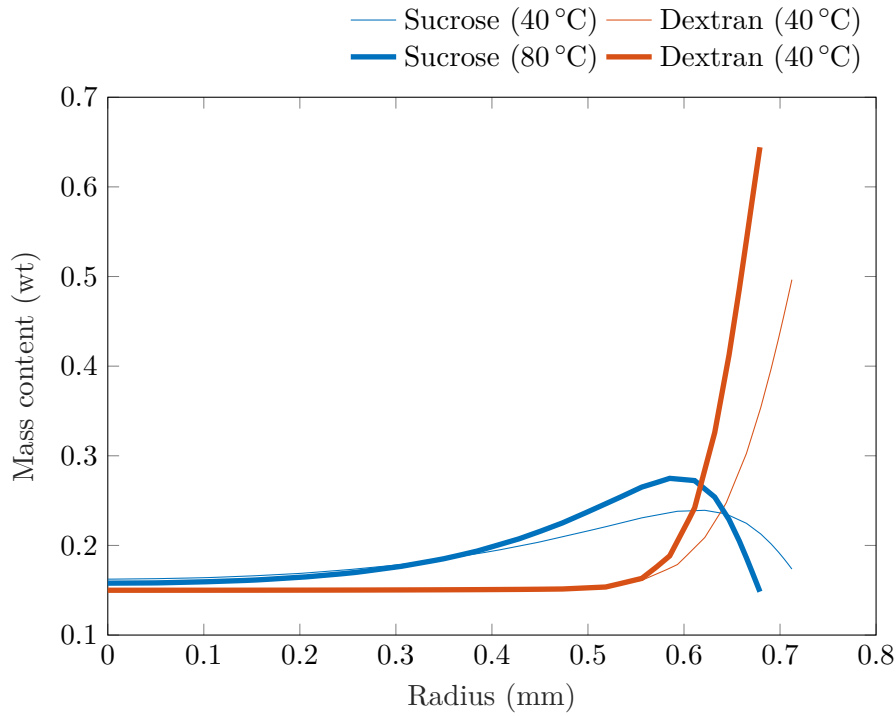
Figure 5.14 − Dextran and sucrose mass content profiles for the trials at $40\,°C$ and $80\,°C$. The inlet air velocity is $0.5\,m\,s^{-1}$ and the inlet air absolute humidity is $3.5\,g\,kg^{-1}$. The initial solutes mass content was set at 15D-15S wt and the profiles were taken at the time of the first appearance of a solid, which correspond to $108\,s$ and $45\,s$, respectively

and $20\,°C$, respectively. Thus, the fast water removal from the droplet interface promotes a higher dextran accumulation at the interface. Such increase is naturally higher for the simulation at $80\,°C$ than at $40\,°C$. For the sucrose profiles, the increase in mass content is not as steep as for the dextran. Instead, the mass content attains a maximum value at the end of the 0.1-mm external layer and then slowly decreases towards the center of the droplet. Such profile can be better visualized form the simulation at $80\,°C$. Since the profiles presented in Figure 5.14 correspond to the time of first appearance of a solid, it is possible to imagine that the final solid particle produced under such conditions would present a fine external layer composed mainly of dextran, while the sucrose would be protected at the droplet core.

5.6 Sensitivity analysis

The previous section showed the accordance between the modeling and the experimental results relative to the moisture content during the period of crust formation and presented the mass content profiles of dextran and sucrose resulting from the drying of the droplet. Here, the objective of this section is to present how the change of input parameters, i.e. the air properties and the liquid formulation mass contents, would affect the change in the resulting drying kinetics and the dextran and sucrose distributions. The sensitivity analysis is performed with the simulation at $40\,°C$ ($u_{ha} = 0.5$ m/s, $Y_{ha} = 3\,5\,g\,kg^{-1}$) and

initial mass contents at 15D-15S wt. Also, the input parameters are varied by 10 % and 20 % regarding the original setpoint.

5.6.1 Air temperature

The first parameter upon which the setpoint is varied by 10 % and 20 % is the drying air inlet temperature. The results presented in Figure 5.15 are related to the drying air temperatures of 44 °C and 36 °C for the 10 % interval, and 48 °C and 32 °C for the 20 % interval. The drying kinetics curve is plotted until the time $t_{1 \text{ sd}} = 138$ s (considering the initial 30-second diffusive drying) and the mass content profile are presented at that time $t_{1 \text{ sd}}$.

The effect of varying the temperature setpoint becomes visually more pronounced towards the final points in the drying kinetics from Figure 5.15. At the time $t_{1 \text{ sd}}$, the moisture content from the normal curve is equal to 1.176. For the 10 % interval, the moisture content stands at 1.092 and 1.237 for the air temperatures of 44 °C and 36 °C, respectively. The difference between these values is slightly inferior for -10 % (0.061) than for the increase in temperature (0.084). For the 20 % interval, the moisture content values were 1.009 and 1.332 for the air temperatures of 48 °C and 32 °C, respectively. Also, the difference between these moisture content values to the value of the normal curve is 0.167 for $+20$ % and 0.156 for -20 %. The standard deviations for the 10 % and 20 % are 0.07 and 0.16, respectively.

For the mass content profiles, it is possible to observe that the droplet radius is changed due to the a modification in the evaporation flux with the air temperature. For example, the droplet diameter from the normal curve is equal to 0.693 mm, while it is changed to 0.684 mm at 44 °C and to 0.675 mm at 48 °C. The increase in 20 % at the air temperature caused a decrease of 3 % in the droplet radius. Regarding the effect on the mass content increase, for the dextran profile for example, the mass content rose from $\omega = 0.544$ wt at 40 °C to $\omega = 0.0.572$ wt at 44 °C and to $\omega = 0.600$ wt at 48 °C. Thus, the increase in 20 % at the air temperature caused an increase of approximately 10.3 % of the dextran mass content at the droplet surface.

5.6.2 Air velocity

The results of the sensitivity analysis performed on the drying air velocity are displayed in Figure 5.16. The normal curve was obtained here with the air velocity set at 0.5 m s^{-1}. A first inspection of the drying kinetics from Figure 5.16 shows that the drying kinetics obtained with the increment of 10 % and 20 % are closer to the "original" drying curve than the results from Figure 5.15 with a varying air temperature. Indeed, a decrease of 20 % in the air velocity contributed to an increase of 5 % in the moisture content (from $X = 1.176$ to $X = 1.120$) at 138 s (instead of the increase of 10 % found when the air temperature was decreased of 20 %).

In the mass content profile plots, the effect of varying the drying air velocity on the droplet radius is also smaller than that found in Figure 5.15 with the temperature. Indeed, a increase in 20 % at the air velocity only contributed to a reduction of approximately 0.7 % in the droplet radius. As for the mass content variations, the increase in the air velocity of 20 % induced an increase in the dextran mass content at the droplet surface of 5 %.

5.6.3 Air absolute humidity

For the drying air absolute humidity, the results displayed in Figure 5.17 show that this air property has the lowest effect on the drying kinetics and on the mass content profiles. The modification of 20 % in the setpoint value ($3.5\,\mathrm{g\,kg^{-1}}$) only caused a change of 2 % in the moisture content at 138 s. This confirms the assumption taken in Chapter 3 where the effect of a small modification in the air absolute humidity for the trial at 20 °C was negligible.

In the mass content profile plot, varying by 20 % the air absolute humidity only caused a modification of 0.4 % in the droplet radius and an increase of 3 % for the dextran mass content at the droplet surface.

5.6.4 Sucrose content

The results of the sensitivity analysis performed on the initial sucrose mass content are presented in Figure 5.18. For the tests, the initial dextran mass content was kept constant and equal to 15 % wt. Thus, the total content in the droplet changes when varying the sucrose mass content by 10 % and 20 %, while for the sensitivity analysis on the air properties the droplet initial total content was the same (30 % wt). From the drying kinetics in Figure 5.18, it is possible to see that although the drying kinetics do not start at the same moisture content (due to a change in the total content), the curves seem to follow the same tendency of decreasing moisture content with time. As a matter of fact, the results presented in Figure 5.18 correspond to the first drying stage, thus the controlling mechanism for the moisture removal is at the gas phase.

The drying curves were presented at the time $t_{1\,\mathrm{sd}} = 138$ s in Figure 5.18, however with a modification in the sucrose initial mass content, it is expected that the such modification may alter the time of the crust formation. Through the use of the volume fraction value of $\phi = 0.6$ at the droplet surface as an indicator of the crust formation, the volume fraction at 138 s for the normal curve is 0.67. In this case, the value of $\phi = 0.6$ was attained at 108 s. For the curve -10 % (first dashed plot below the normal curve in Figure 5.18), the volume fraction is equal to 0.66, while for the curve -20 % (the second dashed curve below the normal curve in Figure 5.18) the volume fraction at the droplet surface is 0.65. The value of $\phi = 0.6$ was obtained at 111 s and 114 s, for the -10 % and -20 % curves, respectively. Regarding the curve $+10$ % (first dashed plot above the normal curve in Figure 5.18), the volume fraction of $\phi = 0.6$ was attained at 105 s, while for the curve -20 %, the formation of the crust is predicted to happen at 102 s. The addition of sucrose in the liquid formulation helps inducing the formation of the crust, as a result of the addition of more solute to the liquid phase.

Regarding the mass content profiles presented in Figure 5.18, a higher sucrose mass content is found at the position $r = 0.6$ mm when its initial mass content is incremented by 20 %, as expected. A decrease in the initial sucrose mass content also generates a reduction in the value found at $r = 0.6$ mm. The external 0.1-mm layer rich in dextran seem to not have underwent a modification by the varying initial sucrose mass content.

5.6.5 Dextran content

Regarding the sensitivity analysis on the initial dextran mass content the results are plotted in Figure 5.19. As observed with the drying kinetics from Figure 5.18, the

drying kinetics with varying initial dextran mass content also do not start at the same moisture content due to a different initial total solute content. The volume fraction $\phi = 0.6$ is also used to indicate the formation of the solid crust, as performed in the sensitivity analysis with the sucrose content. The drying kinetics in the normal curve gives a volume fraction of 0.67 at 138 s, as presented previously. For the curve -10 %, the volume fraction is equal to 0.64, while for the curve -20 % the volume fraction at the droplet surface is 0.61. The value of $\phi = 0.6$ was obtained at 123 s and 135 s, for the -10 % and -20 % curves, respectively. Looking now at increasing initial dextran mass fractions, the curve $+10$ % attained the volume fraction of $\phi = 0.6$ at 97 s, while for the $+20$ %, the formation of the crust started at 87 s. For this last result, the crust was formed much earlier than with the drying kinetics at $+20$ % of the initial sucrose mass content. Thus, varying the dextran content in the liquid formulation has an effect much more pronounced on the solid crust formation than the effect obtained by varying the sucrose content. Regarding the mass content profiles, an increase of 20 % in the initial dextran mass content generated a droplet with a dextran mass content 14 % higher than the setpoint mass content.

5.7 Summary of the main findings of the chapter

In this chapter, a microscopic model was developed to simulate the coupled transfers taking place with a multi-component drying droplet. The drying of the spherical, freely suspended droplet was simulated according to the time of crust formation observed from each trial in Chapter 3. Also, only a droplet containing dextran and sucrose was considered here. An important aspect related to the conception of the model was the definition of a convective movement inside the droplet, due to the external air flow. In that way, the transport of dextran and sucrose in the liquid phase could be described by a convective and a diffusive transport. For the latter, the Stokes-Einstein equation was employed for the diffusion coefficients, but the diffusive flux considered the effect of more than one solute in the liquid phase.

The results obtained here showed that, despite the momentum transfer between the drying air and the droplet, the velocity profile inside the droplet did not have a strong influence in the components radial distribution. The mass content profiles generated by the model increased radially outward from the center of the droplet, as found when diffusion is the predominant mechanism of transport of solutes in the evaporating droplet. Additionally, a droplet with a lower viscosity could present a stronger convective movement. Considering the simulations performed with the experimental conditions from Chapter 4, a dextran-rich surface could be observed and the sucrose mass content profile was relatively homogeneous in the liquid phase. While in accordance with one of the results presented in the previous chapter, a better evaluation of the physicochemical data of the solutes would help to define more accurately the mass contents found under these drying conditions. For the trials performed under higher air temperatures, a first layer composed mainly of dextran could be found in the droplet, followed by a portion of the liquid phase where the sucrose mass content was the highest. It was possible to presume that such spatial distribution could well indicate what would be found in solid particles at the end of the drying process.

The results obtained here also showed that the evaporation flux was not uniform across the droplet surface, which can promote the formation of an inhomogeneous crust around

the droplet. Also, the model could have been simplified by considering an isothermal droplet during the first drying stage. Regarding the drying kinetics, the simulated moisture contents at a given time were often inferior to the ones obtained in Chapter 3. This indicated higher evaporation rates from the simulations. The simulations used a constant air temperature and flow during the drying time, while in the experiments the flow of air was intermittent and the temperature was not as strictly constant as in the model.

From the sensitivity analysis, it was possible to observe that the air temperature has a major impact on the droplet drying behavior, in comparison with the air velocity and the air absolute humidity. In the liquid formulation, based on a volume fraction criterion, it was possible to observe a reduction in the time of the crust appearance by adding solutes to the liquid phase. Furthermore, the addition of dextran to the droplet had a much stronger effect on the time of crust appearance than sucrose, as expected from the observations in the past chapters.

Table 5.3 – Comparison of the moisture content values obtained experimentally and numerically at the time of first appearance of a solid ($t_{1\,sd}$) and the time when the crust covers the droplet surface (t_{tc}). The superscript mdl refers to the modeling results. The relative difference Δ between experimental and modeling results is also presented the superscript exp refers to the results from Chapter 3, while

T_{air} (°C)	u_{air} ($\frac{m}{s}$)	Y_{air} ($\frac{g}{kg}$)	ω (% wt)	Pe	X_o^{exp}	X_o^{mdl}	$t_{1\,sd}$	$X_{1\,sd}^{n,exp}$	$X_{1\,sd}^{n,mdl}$	$\Delta_{1\,sd}$	t_{tc}	$X_{tc}^{n,exp}$	$X_{tc}^{n,mdl}$	Δ_{tc}
20	0	2.4	5:5	0.108	8.70	8.99	832	0.46	0.46	0	864	0.44	0.44	0
		2.4	5:25	0.453	2.34	2.33	735	0.42	0.44	0.05	-	-	-	-
		3.5	15:15	0.869	2.33	2.33	525	0.52	0.59	0.13	756	0.42	0.47	0.12
		4.7	25:5	1.160	2.31	2.33	444	0.62	0.67	0.08	602	0.51	0.57	0.12
40	0.5	3.5	15:15	17.08	2.33	2.33	108	0.61	0.50	0.18	161	0.49	0.33	0.33
80	0.5	3.5	15:15	29.20	2.33	2.33	45	0.59	0.52	0.12	66	0.48	0.36	0.25
40	0.2	9	15:5	7.50	3.94	3.99	182	0.62	0.52	0.16	224	0.52	0.44	0.15
			5:15	3.16	3.99	4.00	161	0.58	0.40	0.31	180	0.52	0.34	0.35
			5:5	2.74	8.97	8.99	203	0.54	0.39	0.28	239	0.43	0.31	0.28
80	0.2	3.5	5:15	7.50	3.95	3.99	108	0.41	0.32	0.22	150	0.25	0.16	0.36
			15:5	18.30	4.00	4.00	66	0.65	0.52	0.20	87	0.55	0.41	0.25
			5:5	6.51	10.0	9.20	87	0.49	0.45	0.08	108	0.41	0.35	0.15
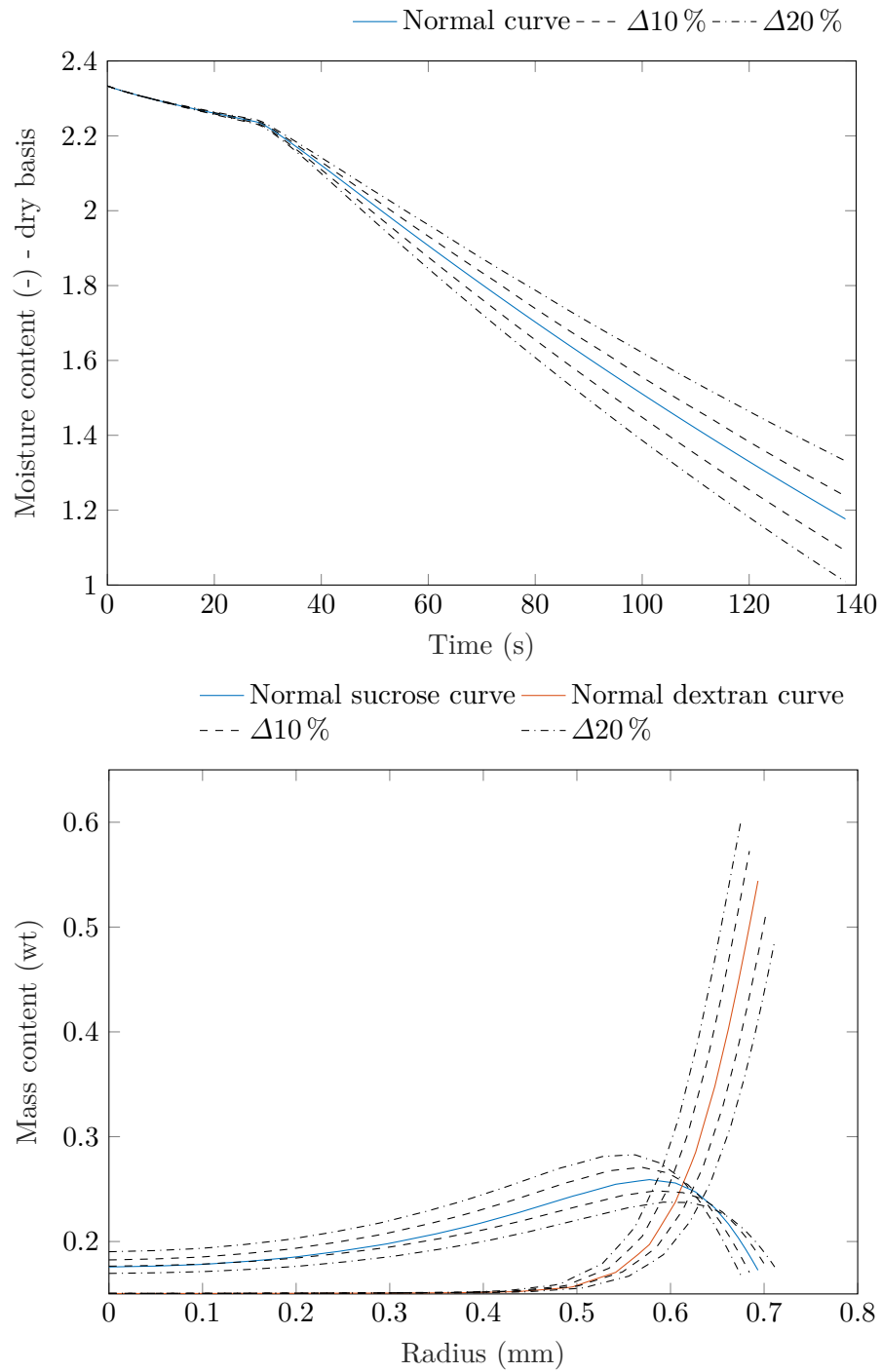
Figure 5.15 − Sensitivity analysis performed on the drying air inlet temperature (setpoint at 40 °C) with the intervals of 10 % (dashed line) and 20 % (dash and dotted line) from the setpoint of 40 °C. The initial mass contents were 15D-15S wt
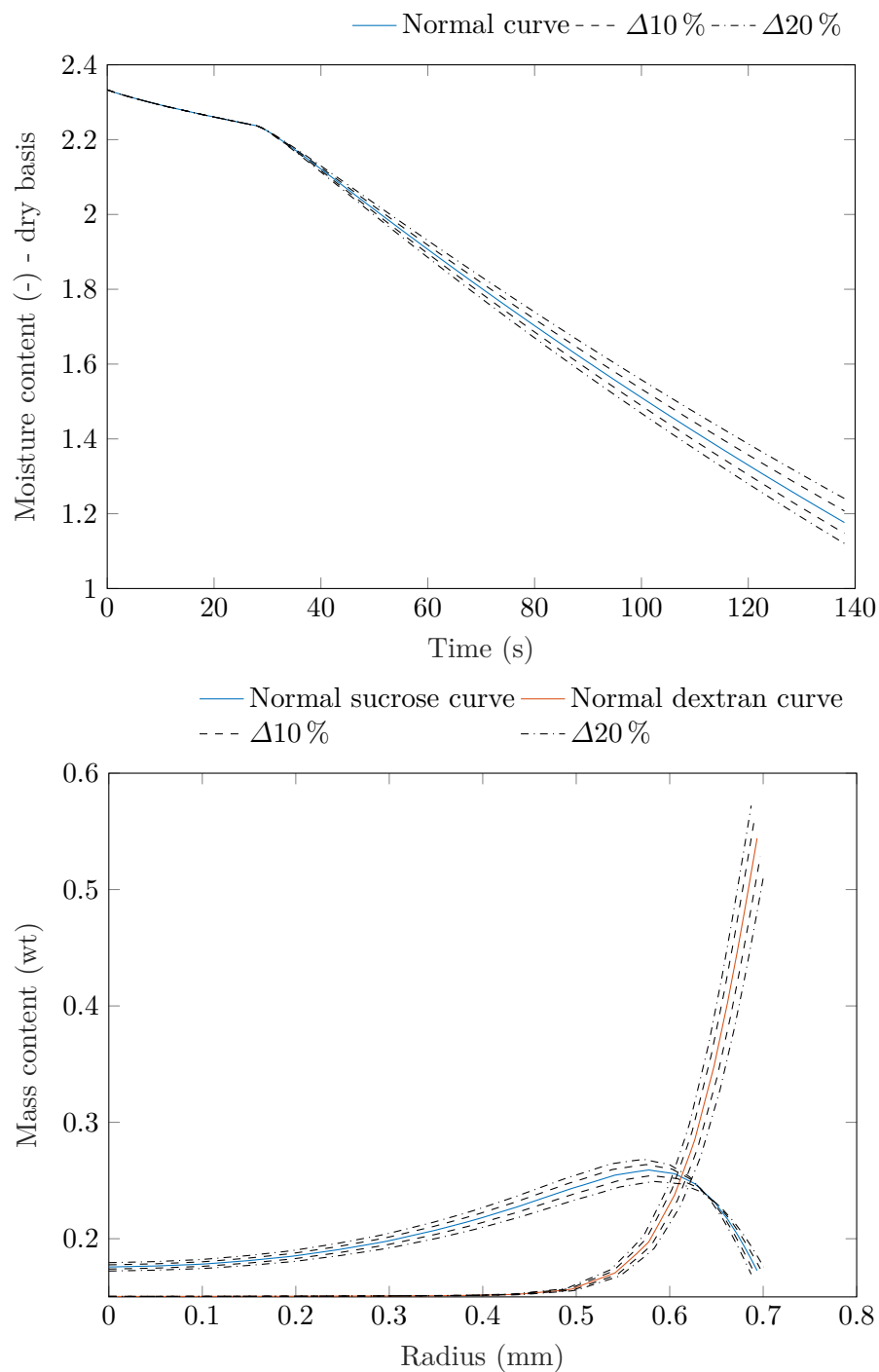
Figure 5.16 – Sensitivity analysis performed on the drying air inlet velocity (setpoint at $0.5\,\mathrm{m\,s^{-1}}$) with the intervals of $10\,\%$ (dashed line) and $20\,\%$ (dash and dotted line) from the setpoint of $40\,^{\circ}\mathrm{C}$. The initial mass contents were 15D-15S wt
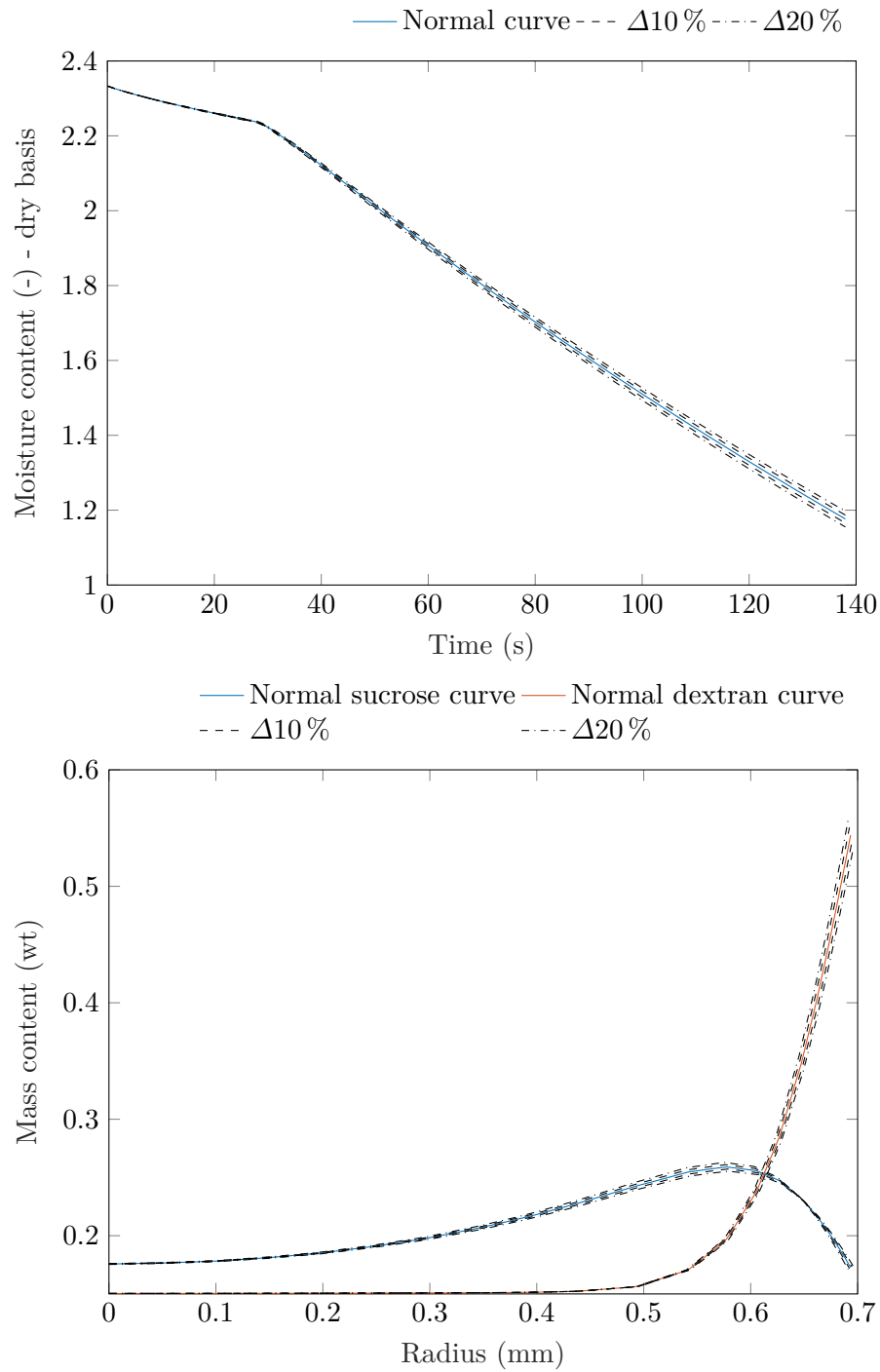
Figure 5.17 – Sensitivity analysis performed on the drying air absolute humidity (setpoint at $3.5\,\mathrm{g\,kg^{-1}}$) with the intervals of 10 % (dashed line) and 20 % (dash and dotted line) from the setpoint of $40\,^{\circ}\mathrm{C}$. The initial mass contents were 15D-15S wt
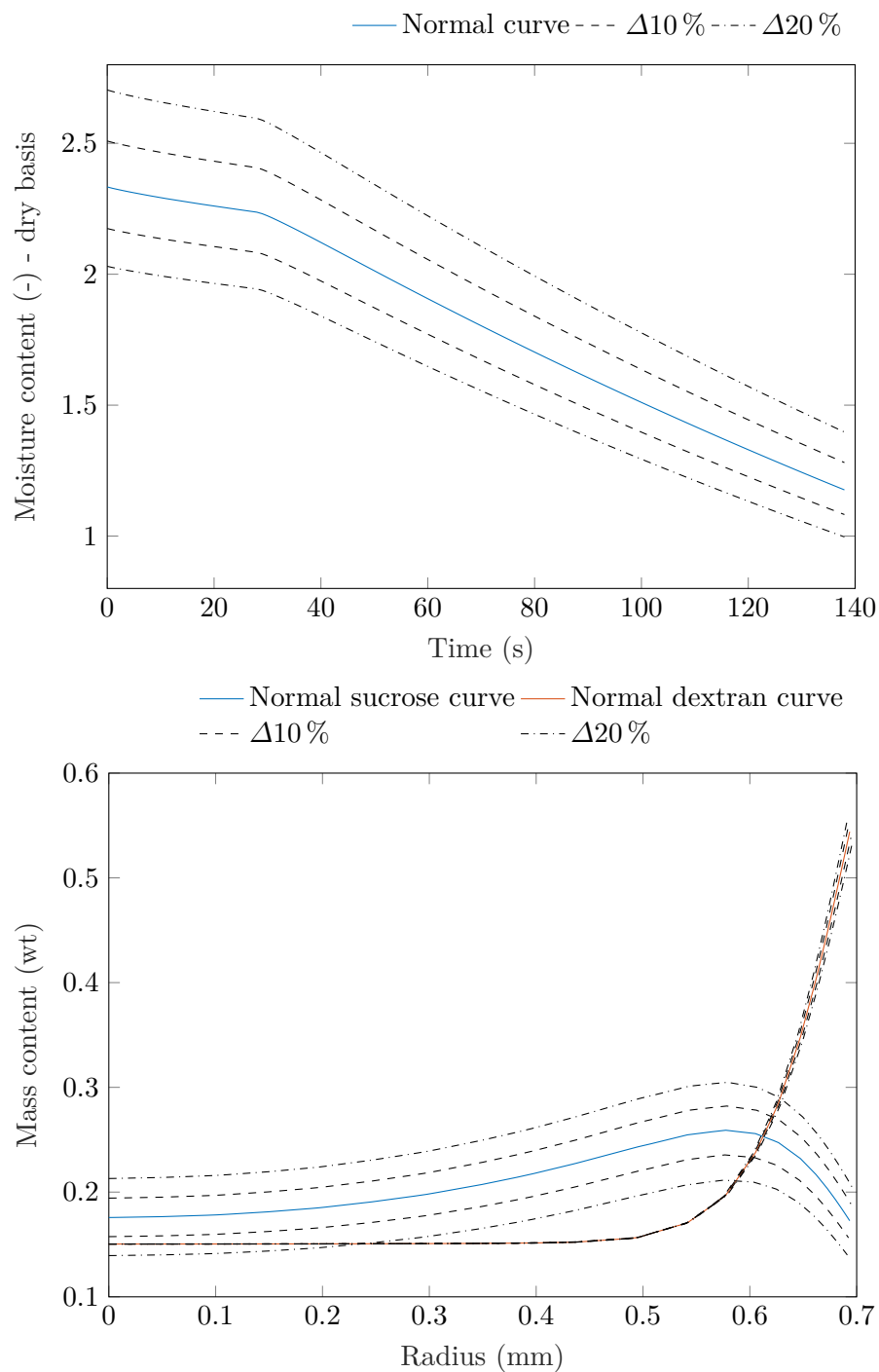
Figure 5.18 − Sensitivity analysis performed on the initial sucrose mass content (setpoint at 15 % wt) with the intervals of 10 % (dashed line) and 20 % (dash and dotted line) from the setpoint of 40 °C. The dextran initial mass contents was 15 % wt
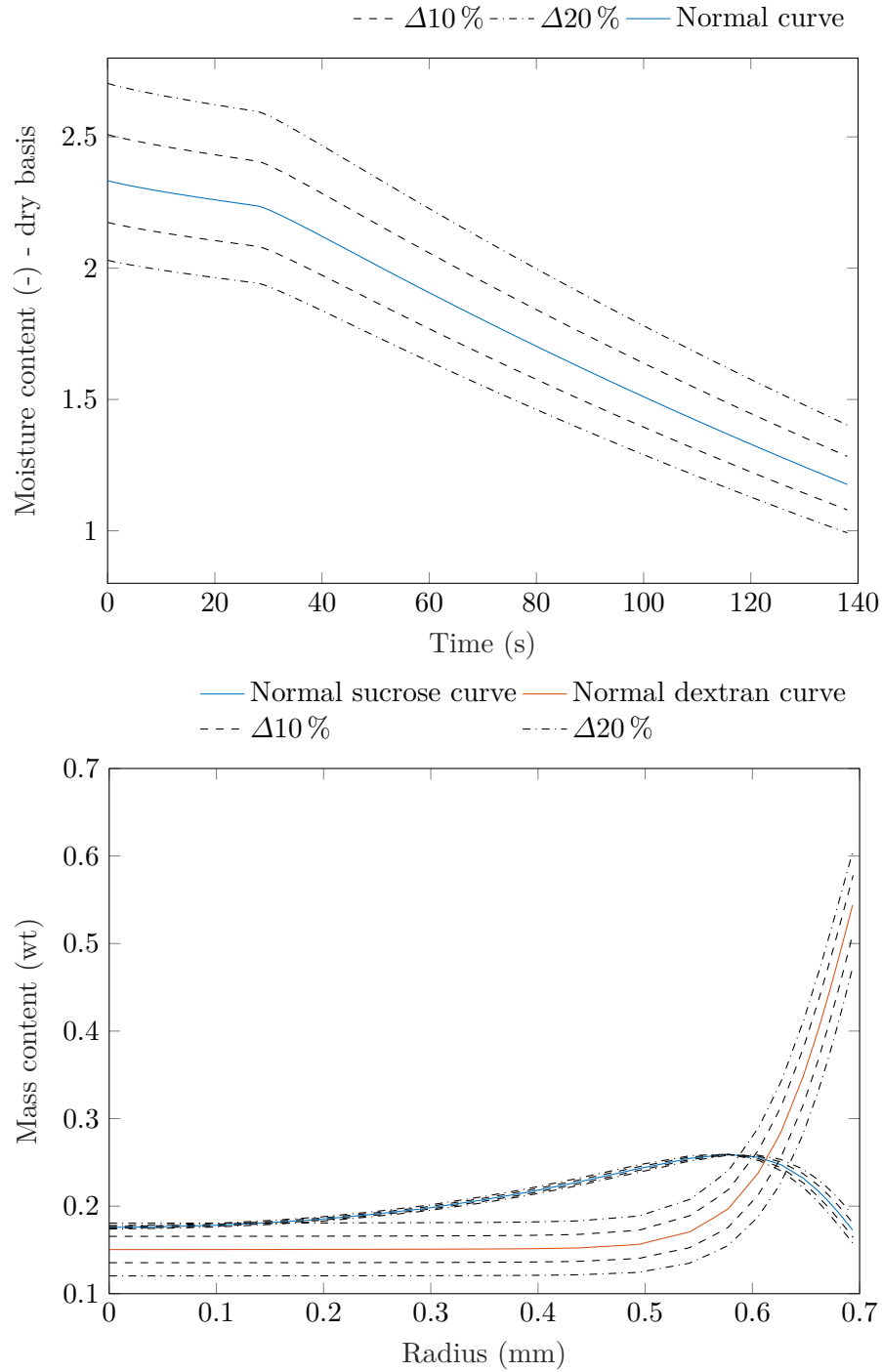
Figure 5.19 − Sensitivity analysis performed on the initial dextran mass content (setpoint at 15 % wt) with the intervals of 10 % (dashed line) and 20 % (dash and dotted line) from the setpoint of 40 °C. The sucrose initial mass contents was 15 % wt

Conclusion and perspectives

The objective of the present thesis was to bring together the experimental and the modeling approaches at the droplet scale to contribute to the scientific understanding of the mechanisms involved in solid particles formation from multi-component drying droplets. From the literature review performed in the first chapter, scientific and technological challenges were identified. The difficulties needing to be addressed were the prediction of the spatial distribution of the components in the droplets during drying and, consequently, an evaluation of the droplet properties through time without much interference in the drying process. Considering the possible observation scales within this process, the spray scale and the droplet scale, the latter was the most suitable to help meeting the above challenges. Consequently, two different, but complementary set-ups were employed during this thesis for the work with a single droplet to provide insightful information about the drying process. Plus, a reference picture needed to be created at a lab-scale spray dryer to maintain the link between the particles generated at the spray and at the droplet scales. A microscopic model using Computational Fluid Dynamics (CFD) was also developed for completing the results obtained experimentally until the period of crust formation and for accessing variables that had not been obtained with the experimental approach.

The mechanisms of particle formation from liquid droplets are often explored in the literature with droplets containing a dispersed phase. With solution droplets containing dissolved solids, the generated particles presented crystalline structures. Therefore, it was considered important for this thesis to broaden the studies on particle formation mechanisms by using aqueous solutions containing two solutes as a starting point and the generation of multi-component amorphous particles. The chosen drying systems were composed of dextran-sucrose or lactose-whey protein isolate (WPI). The analysis of the particle formation from these drying systems can be performed from a macroscopic point of view, regarding the particle morphologies, through a finer investigation with the drying kinetics and finally ending with a microscopic point of view from the distribution of the solutes across the drying droplet.

As a matter of fact, regarding the particle morphologies, it was possible to modulate the particle structure by altering the proportion of the solutes in the liquid droplet. With the dextran-sucrose system, wrinkled particles were obtained for droplets containing only dextran, while smooth particles were observed for droplets containing only sucrose. The mixture of both solutes could generate a wrinkled particle or a smooth one depending on the solute with the highest concentration in the droplet. For the lactose-WPI system, droplets containing only lactose or only whey protein generated smooth particles. The mixture of both solutes gave wrinkled particles, as long as the protein content was not superior to the lactose content in the initial droplet. Also, for the conditions tested here, dense core particles were obtained from the dextran-sucrose system, while hollow core particles were observed from the lactose-WPI system. These different morphologies

obtained by a modification in the liquid formulation were found both at the spray and the droplet scale. Consequently, it shows the validity of the droplet scale studies for producing representative solid particles from the drying system of interest. Furthermore, it is possible to observe the primordial role of the liquid formulation in defining the final aspect of the solid particles. Droplets dried with different air properties, but with similar composition, generated particles with resembling morphologies.

Apart from the observations on the particle morphologies as presented above, an experimental apparatus was designed during this thesis to help apprehend the drying behavior of the selected drying systems. From such set-up, it was possible to evaluate the drying and shrinkage kinetics from a droplet suspended by a filament and placed under an air flow with controlled properties. By combining the droplet weight data and the image acquisitions, for the trials performed with the dextran-sucrose system, the ideal behavior in the droplet shrinkage kinetics could be observed. Also, it was possible to detect a slight reduction in the solid particle diameter between the formation of the solid crust and the end of the trial. Such reduction in the wet particle diameter is often disregarded during the development of drying models in the literature. The first drying phase persisted until the appearance of the solid phase at the surface of the droplet. Naturally, the duration of such drying phase decreased when higher air temperatures were employed. Regarding the period of crust formation, in the dextran-sucrose system, using higher dextran mass contents in the liquid formulation could induce the crust formation at higher moisture content. Such effect could be found in relation to the lower solubility of dextran in water, compared to the solubility of sucrose in water. For the lactose-WPI system, the crust could be formed at higher moisture content when the whey protein-lactose proportion in the droplet was superior to one. This could be related to the surface active character of the protein. Furthermore, for the falling-rate period, considering the non-porous structure found in the solid particles here, it is possible to argue over the hypothesis regularly considered in the literature for the transport of moisture across the crust. Instead of a transport of water vapor, the analysis on the mechanisms of transport of adsorbed liquid water across the solid structure needs to be investigated.

Once the drying behavior of the drying systems was evaluated with the drying kinetics, it was important to deepen the analysis of the drying process by evaluating how the droplet components were distributed in the liquid phase through time (at experimental and modeling scales). A set-up was adapted by combining an *in situ* Raman technique with an acoustic levitator to provide quantitative information with mass content profiles from the drying droplet under mild drying conditions. Thus, the measured Raman spectra were corrected with a baseline, normalized to the intensity of fingerprint region (corresponding to the solutes) and intensity ratios were correlated to calibration curves with mass content ratios. The challenge was related to the dissociation of the fingerprint region into intensities of each solute. Distributed mass content profiles were obtained throughout the measurement volume in the droplet and through time. This work could only be developed with the dextran-sucrose system, as the lactose-WPI system required a different laser wavelength for the acquisition of the Raman spectra. From droplets containing the same solute proportion, it was possible to put in evidence the effect of the total solute content on the component distribution. From a more diluted droplet, a dextran-rich surface and a sucrose-rich core were identified. The CFD microscopic model could also give information about the distribution of dextran and sucrose across the droplet until the period of crust formation. The simulated results also revealed

a dextran-rich layer towards the surface of the droplet, followed by a portion of the droplet more concentrated in sucrose. Such spatial distribution can be justified by the lower diffusion coefficient of dextran, which hinders its diffusion towards the center of the droplet. In the presence of such component segregation, it is possible to say that the surface of a particle generated under these conditions will become more related to the properties of the component in major concentration at the surface.

From the observations of particle morphologies, drying kinetics and solutes spatial distribution from both drying systems, the influence of the liquid formulation on the final particle structure was highlighted. The use of molecules with different physicochemical properties, namely the chemical structure, the molecular size and the solubility, had an important role in defining the structure of the final solid. With the presence of a solute gradient, the solutes in the liquid phase could be separated based on their molecular size (which affects the molecule diffusion in a medium), even though the viscosity in the droplet could hinder such process. Also, based on the degree at which the solutes are segregated and their respective molecular size, the viscoelastic properties of the forming crust could be modified. By changing the crust properties, it may modify its ability to withstand the compressive pressure related to the drying process, thus different surface aspects may be obtained. Naturally, the time scale at which the characteristics of the liquid formulation evolves is limited by the drying air properties, specially the air temperature. With higher air temperatures, the time scale for the solutes to diffuse throughout the droplet is reduced, as the liquid droplet quickly becomes a solid particle. Also, an important relative velocity between the drying air and the droplet may help hinder the solute segregation by inducing a convective movement inside the droplet.

Perspectives for future work

There are numerous ways in which the present work may be extended and improved. These can be related to the set-ups employed here, the liquid formulations and their physicochemical properties and the droplet drying model.

Improvement of the set-ups

Regarding the set-up with a droplet suspended by a filament, a thermographic camera could be placed in front of the suspended droplet. In that way, temperature data could be obtained. In fact, an interesting development would be the acquisition of temperature profiles across the droplet, instead of only the droplet surface temperature. In that way, a better definition of temperature gradients could be observed between the droplet/wet particle center and surface. Indeed, such gradient would be better observed during the second drying stage, as stated in the literature. Thus, it would be possible to empirically correlate the temperature gradient across the solid structure with a mean particle composition, as the thermographic camera would not give access to concentration profiles. This correlation would give indications about the thermal properties of the solid, i.e. the thermal diffusivity. Such data is necessary in the modeling work.

Regarding the concentration profiles, combining the set-up with a droplet suspended by a filament and the Raman technique could give linked information between the mass loss and mass content profiles. Additionally, the Raman profiles could be obtained

under harsher drying conditions than the ones employed in Chapter 4. However, the combination of both techniques is not as straightforward, since the access to the suspension zone (for placing the droplet at the tip of the filament) may become more difficult. Also, the presence of the laser light may prevent the camera from acquiring images from the droplet/wet particle. In that way, two experiments would be necessary if the morphology and composition profile are obtained from a given liquid formulation. Finally, the Raman light emitted from the droplet is captured with an angle of 90° from the incident laser beam. Consequently, the incident laser should not be placed perpendicularly to the droplet suspension set-up (or else the Raman light is sent inside the wind tunnel).

Liquid formulation and physicochemical properties

A limiting factor related to the work with multi-component mixtures is the lack of physicochemical data in the literature, especially for concentrated solutions. The need for precise data related to both temperature and composition in the droplet becomes evident during the development of models of drying multi-component droplets. As described in Chapter 5, the properties of interest in the liquid mixture are the diffusion coefficient of each solute in the mixture, the density of the mixture and the viscosity of the mixture. Without taking into consideration the extensive time needed for acquiring a comprehensive set of experimental data, the most direct measurements is related to the density of the mixture. Indeed, a density meter can readily give a precise value (with a five- or six-digit accuracy) for a solution at a given temperature and composition. For the viscosity measurement, the difficulty is related to the use of low shear rates to avoid crystallization, if supersaturated solutions are being analyzed. The diffusion coefficient is the most difficult property to evaluate experimentally, for mixtures with three (or more) solutes. Also, the theoretical description of these variable often involves more complex thermodynamics equations. After the solid is formed from the droplet, the water activity becomes an important variable to describe the drying process. Gravimetric methods under controlled relative humidity conditions (with salt solutions or with the dynamic vapor sorption - DVS) have been proposed in the literature. However, special attention should be given to the temperature at the wet particle surface during the measurements, as it affects the wet particle water activity. The technique with salt solutions can provide water activity values for ambient temperatures, while the DVS technique can provide such information for temperatures up to 80 °C. Such temperatures may not be representative of the wet particle surface temperature during the spray drying process, consequently the measurement of precise values of water activity for representing the wet particle may become difficult.

Another aspect that should be taken into consideration is the intermolecular interaction of the multi-component mixture as the droplet approaches the conditions for the crust formation. This may, for example, have an impact on the elasticity of the solid crust. Thus, the focus is given on the chemical structure of the solutes and how the different functional groups of the molecules attract or repel each other. This kind of perspective may be found in the literature on studies related to the stabilization of the protein structure by sugars during drying [104]. The sugar would replace the water molecules in the water-protein hydrogen bonds as water is removed from the droplet. Consequently, the sugar-protein hydrogen bonds would have a role on maintaining the protein structure (thus protecting it) during drying.

Finally, regarding the liquid formulations employed during this thesis, the dextran-sucrose system can also replace lactose in the drying process of proteins. It would be interesting to see the addition of the protein to a system that generates mainly dense core particles.

Droplet drying model

A complete version of the droplet drying model is related to the simulation of a given morphology (dense, hollow, with smooth or wrinkled surface) based on a set of initial air properties (temperature, velocity, absolute humidity) and liquid formulation characteristics (type of solute, concentration). The model developed during this thesis lacked in the definition of the physics taking place during the formation of the solid crust and the subsequent falling-rate period.

A microscopic definition of the crust formation from a multi-component solution needs to be addressed. The model should be able to describe the physics taking place near the droplet surface, where a layer of solutes give place to a solid phase. Also, the kinetics of growth of the solid crust towards the wet particle center should be considered. It should also be mentioned that, while the crust becomes thicker, the external diameter of the wet particle reduces slightly, as observed in Chapter 3 and stated in [58] and [59]. Mechanical properties of the crust should be used for considering the moment when the crust becomes strong enough to sustain the compressive pressure related to the drying process. Such information requires experimental studies on the mechanical properties of the solids formed during spray drying. As stated in Chapter 3, the drying systems employed during this thesis did not generate a porous solid structure, which could indicate a mechanism of transport of water vapor through the pores of the solid structure during the falling-rate period. Consequently, the mechanism of moisture removal to be simulated are related to the transport of adsorbed water in liquid state through the solid structure. Regarding the energy transfer, thermal properties of the solid crust should be considered, for taking into account the increase in temperature of the wet particle and the heat conduction throughout the solid phase. The properties such as heat capacity and heat conductivity, which depends on the composition and moisture content of the solid crust, would also need experimental data.

The points presented here could be used for simulating the formation of a dense core particle, with a smooth surface. The simulation of a droplet becoming a wrinkled particle has not been presented yet in the literature. Such implementation would require more experimental data on mechanical properties of the solid crust.

Regarding the formation of a hollow core particle, the challenge with CFD is related to the creation of such hollow core in the model geometry. A pressure-based criterion should be used for indicating when the pressure drop inside the droplet is sufficient for promoting the appearance of the hollow core. Next, the model should also be able to simulate the mass transfers taking place at the inner surface of the expanding hollow core. Such model is consequently more complex than the one representing the formation of the dense core particle.

Résumé étendu en français

A.1 Introduction

Les gouttes liquides se sont avérées des vecteurs importants pour la production de particules solides à propriétés contrôlées, comme la morphologie, la composition de surface, la porosité ou la densité. Différents procédés industriels se servent de ces vecteurs pour former des particules solides, comme par exemple le procédé de séchage par atomisation. D'ailleurs, celui-ci est devenu dans les dernières années un outil pour la structuration de solides à partir d'alimentations liquides multi-constituants. Avec ce procédé, il est possible de modifier les propriétés de l'air et les formulations liquides pour en générer différentes particules solides pour des applications plus pointues, comme les profils de dissolution et de relargage contrôlé, la réactivité, le masquage de goût et la mouillabilité.

Cependant, des verrous scientifiques et technologiques sont encore présents lors de l'utilisation du procédé de séchage par atomisation pour la structuration, pour un contrôle plus fin de la structure solide des particules générées. Ces verrous concernent une description détaillée de la distribution des composants dans la goutte multi-constituants au cours du séchage et, par conséquent, un suivi des caractéristiques de la goutte dans le temps. Également, le développement d'un modèle capable de prédire différentes structures solides selon les conditions de séchage se fait nécessaire pour accélérer le développement de nouveaux produits solides.

De manière à lever les verrous mentionnés précédemment, des approches de modélisation et d'expérimentation ont été proposées dans la littérature pour appréhender les mécanismes de formation des particules solides à partir des goutte multi-constituants. Ces approches sont développées soit à l'échelle du nuage de gouttes soit à l'échelle de la goutte. Plus de détails sur ces différentes approches et échelles sont donnés dans la section suivante. Il est important de savoir que la présente thèse s'est déroulée avec une approche couplée modélisation/expérimentation à l'échelle de la goutte pour aider à lever les verrous cités précédemment.

En ce qui concerne l'approche expérimentale, deux dispositifs sont utilisés pour l'étude du séchage d'une goutte. Les particules produites avec ces dispositifs sont comparées avec celles obtenues à partir d'une étude à l'échelle du nuage de gouttes. Pour la modélisation, un modèle numérique est développé pour suivre les caractéristiques de la goutte multi-constituants jusqu'à la période d'apparition d'une phase solide sur la surface de la goutte.

A.2 Contexte

Le premier chapitre est consacré tout d'abord à l'introduction des étapes composant le procédé de séchage par atomisation, à savoir l'atomisation de l'alimentation liquide, le séchage des gouttes et la formation des particules et la récupération de la poudre produite (Figure 1.1).

En ce qui concerne l'étape d'atomisation, la production des gouttelettes peut se faire sous des mécanismes divers, en fonction des forces appliquées sur le jet liquide et la configuration du dispositif d'atomisation, les buses. La classification des buses utilisées est basée sur le nombre de courants (liquide ou gaz) passant à travers la buse, de cette manière les caractéristiques des buses comportant de un à quatre courants (Figures 1.2 jusqu'à 1.4) ont été présentées succinctement.

Pour la présentation de l'étape suivante, le séchage des gouttes et la formation des particules, la discussion est basée sur l'aspect de séchage (avec les Figures 1.5 et 1.6), sans se concentrer sur la structure du solide formé. Le procédé de séchage débute avec une phase de mise en température (durant un dixième de seconde dans des conditions de séchage industrielles), où la température et le flux de séchage de la goutte évoluent pour atteindre les conditions retrouvées dans la première phase de séchage. La première phase de séchage est caractérisée par un flux évaporatif constant et par l'activité de l'eau à la surface de la goutte égale à l'unité. Durant cette phase, un régime permanent est établi entre la chaleur cédée par l'air de séchage et celle utilisée par la goutte pour l'évaporation de l'eau. La température qui en résulte est la température de bulbe humide. La transition entre la première et la deuxième phase de séchage est caractérisée par la formation d'une phase solide à la surface de la goutte. A partir de ce point, l'activité de l'eau à la surface de la goutte ne va cesser de décroître pendant l'opération de séchage. Par conséquent, le flux évaporatif diminue et la température de la particule humide augmente au cours du temps.

Enfin, le solide généré est séparé du courant d'air de séchage et récupéré à l'aide de cyclones ou de sacs de filtrage.

Une fois les notions de séchage présentées, les différentes structures solides obtenues avec le procédé de séchage par atomisation sont montrées. En jouant sur les propriétés de l'air (température, débit et humidité absolue) et les formulations liquides (type de dispersion, nature des constituants et les concentrations), les particules générées exhibent diverses structures solides : les particules à cœur dense ou creux, avec des surfaces lisses ou rugueuses, les particules très poreuses, les particules présentant des formes variées, comme une "framboise" ou un "beignet" (Figure 1.8).

La production des particules à cœur dense ou creux va dépendre de l'accumulation des constituants sur la surface de la goutte et de leur transport au sein de la phase liquide. Lorsque le flux évaporatif et l'accumulation des constituants à la surface de la goutte est plus important que la redistribution de ces composant au sein de la goutte, la particule à cœur creux peut être produite. Au contraire, le transport des composants dans le liquide est plus important que leur accumulation à la surface de la goutte, la particule à cœur dense peut être formée. L'aspect lisse ou rugueux de la surface de la particule dépend des propriétés mécaniques de la croûte solide et, par conséquent, des constituants qui en font partie. Pour les autres structures solides, le type de dispersion (émulsion, suspension ou solution) a un rôle fondamental pour la définition de la structure finale. Par exemple,

la particule avec un aspect de framboise est produite lorsque une suspension avec des nanoparticules (dont la taille peut aller jusqu'à 650 nm) est utilisée.

La capacité à produire toutes ces particules solides a fait du procédé de séchage par atomisation un outil pour structurer des solides, comme mentionné précédemment. Avec cette vision du procédé, des verrous scientifiques et technologiques sont encore présents. Pour aider à les lever, les approches présentées ci-après ont été proposées dans la littérature.

Avec l'approche expérimentale, l'étude du procédé de séchage par atomisation peut se faire à l'échelle du nuage de gouttes ou à l'échelle de la goutte. A l'échelle du nuage de gouttes, les propriétés de l'air et les formulations liquides utilisées sont reliées aux propriétés de la poudre générée (composition de surface, porosité, morphologie, masse volumique apparente). Cela permet d'avoir un aperçu sur l'influence des conditions de séchage sur le solide formé. Cependant, à cette échelle, le suivi *in situ* du séchage de chaque goutte n'est pas possible. Comme solution, les études à l'échelle de la goutte ont été proposées. De cette manière, le suivi du séchage de la goutte est possible grâce à l'utilisation des gouttes plus grandes (donc un temps de séchage plus long) et à l'emploi d'appareils de laboratoire qui permettent de suivre les caractéristiques de la goutte au cours du temps. Pour le travail à l'échelle de la goutte, celle-ci peut être maintenue en place à l'aide de supports physiques (lesdites méthodes invasives, Figures 1.11-a et 1.11-b) ou à l'aide de forces physiques (les méthodes non-invasives, Figures 1.11-c et 1.11-d). La goutte peut aussi tomber librement le long d'une chambre de séchage (méthode non-invasive, Figure 1.11-e). Avec les méthodes invasives, la goutte peut être suspendue au bout d'un filament ou posée sur une surface hydrophobe. Pour les méthodes non-invasives, la goutte peut être lévitée à l'aide d'un champ acoustique ou d'un courant d'air ou bien tomber librement dans la chambre de séchage.

Avec chacune de ces méthodes, certaines informations sur la goutte peuvent être obtenues, mais aussi des limitations techniques se font présentes. Par exemple, avec la méthode de lévitation acoustique, il est possible de suivre l'évolution du diamètre de la goutte et la composition radiale des constituants dans la goutte. Cependant, cette méthode ne permet pas une mesure directe de la masse de la goutte et des difficultés à maintenir la goutte en place peuvent apparaître. Il est important de noter aussi que l'utilisation de ces méthodes de travail avec la goutte a poussé le développement de techniques qui ont pour but d'accéder de manière *in situ* à des profils de composition dans la goutte (Figure 1.12).

En ce qui concerne l'approche modélisation, des modèles ont aussi été développés en considérant le nuage de gouttes ou une seule goutte. Pour l'échelle du nuage de gouttes, l'écoulement des flux gazeux et liquide est couplé à la description du séchage de la goutte. Par conséquent, les modèles à l'échelle du nuage de gouttes ont aussi besoin d'utiliser la description du séchage de l'échelle d'une goutte. Cette description est réalisée à partir des approches empiriques ou déterministes. Les modèles basés sur une approche empirique donnent des résultats de manière plus rapide et les équations sont relativement simples à implémenter. Pour l'approche déterministe, le séchage est décrit de manière plus détaillée, avec des équations plus complexes et un temps de calcul plus long. L'avantage de cette dernière approche est la capacité à simuler la formation de particules avec un cœur dense ou creux. La validation expérimentale des modèles sur la première phase de séchage se fait de manière plus récurrente dans la littérature. Cependant, la validation de la période d'apparition et épaississement de la

croûte solide reste un challenge, dû au manque de données expérimentales plus fines sur cette période. Le développement des modèles dans la littérature est souvent basé sur les gouttes contenant des constituants du lait, sur des suspensions de nanoparticules ou bien avec des solutions contenant des solutés, dont la particule solide présente une structure cristalline.

A.3 L'étude à l'échelle du nuage de gouttes

Dans le Chapitre 2 de la thèse, le travail réalisé à l'échelle du nuage de gouttes est présenté. L'objectif de cette étude est la construction d'une cartographie représentant les morphologies de particules obtenues à partir de deux systèmes de séchage: l'eau-dextrane-saccharose et l'eau-lactose-lactosérum. L'aspect visuel de la surface et du cœur (lorsque cela était possible) de la poudre a été observé avec la microscopie électronique à balayage (MEB). Des analyses de pycnométrie ont été réalisées afin de donner des indices sur la morphologie des particules (cœur dense ou creux) à partir de l'analyse du volume d'air inclus. D'autres propriétés des particules (distribution de taille, teneur en eau finale et porosité) ont aussi été évaluées. Les structures solides obtenues dans ce chapitre ont servi de référence pour les résultats obtenus dans les chapitres suivants de la thèse.

Le choix des systèmes de séchage est basé sur les éléments suivants: l'utilisation de solutions aqueuses contenant deux solutés ; la production de particules amorphes à partir de ces solutions multi-constituants ; la mise en évidence dans la littérature de la production de différentes morphologies de particules ; l'utilisation de solutés présentant une différence de taille de molécule et de coefficient de diffusion ; la manipulation de solutés non dangereux. Les Figures 2.1 et 2.2 représentent les travaux dans la littérature qui ont guidé le choix des systèmes de séchage. Les structures chimiques et quelques propriétés physicochimiques sont montrées sur la Figure 2.3 et le Tableau 2.1.

En ce qui concerne la morphologie des particules, des structures différentes ont été observées entre les deux systèmes de séchage (en faisant varier la proportion massique des solutés dans la solution initiale). Pour le système lactose-lactosérum, les particules peuvent présenter des surfaces rugueuses ou lisses selon la proportion massique du lactose et du lactosérum (Figure 2.7). La production de particules à cœur creux avec ce système de séchage présentée sur les Figures 2.7 et 2.8. Pour le système dextrane-saccharose, l'aspect de la surface a aussi pu être modifié entre lisse ou rugueux en faisant varier la proportion de dextrane et saccharose dans le mélange initial (Figure 2.9). Cependant, il n'a pas été possible d'observer l'intérieur des particules produites avec ce système. La présence de particules à cœur dense avec le système dextrane-saccharose a pu être supposée à partir des résultats de volume d'air inclus. En effet, le volume d'air inclus mesuré pour le système dextrane-saccharose était dix fois inférieur à celui du système lactose-lactosérum (Figure 2.11).

Concernant les autres propriétés de poudre mesurées, il n'a pas été constaté des différences importantes de distribution de taille de particules entre les deux systèmes de séchage (Figure 2.12) et une modification de la teneur en solutés initiale dans la goutte (pour les deux systèmes) n'a pas engendré des modifications considérable sur la taille finale des particules. Le résultat obtenu avec l'analyse de la surface spécifique sert à corroborer avec les images MEB sur l'idée de la production de particules solides ne présentant pas une structure microporeuse. De cette manière les solides produits

sont très compacts. Enfin, en ce qui concerne la teneur en eau finale dans la poudre, l'utilisation de gouttes avec une teneur en eau initiale plus importante occasionne la production de particules solides présentant aussi une teneur en eau plus grande (Tableau 2.6). Malgré les résultats obtenus dans ce chapitre, il n'a pas été possible de suivre le séchage de la goutte au cours du temps. C'est pourquoi l'étude expérimentale réalisée dans les chapitres suivants porte sur l'utilisation de deux dispositifs expérimentaux pour suivre les caractéristiques de la goutte.

A.4 Séchage d'une goutte suspendue par un filament en verre

Dans le chapitre 3, l'étude expérimentale est réalisée avec une goutte suspendue par un filament en verre. Dans le but d'aider à évaluer l'influence de la formulation liquide et les propriétés de l'air sur le séchage de la goutte, un dispositif expérimental a été créé durant cette thèse. Avec un tel dispositif, la cinétique de séchage peut être mesurée sous un courant d'air à propriétés bien contrôlées, pendant qu'une caméra placée en face de la goutte donne des informations sur l'évolution du diamètre et des modifications sur l'aspect morphologique de la goutte. Sur la Figure 3.1, il est possible de voir les différentes parties du dispositif expérimental. Un courant d'air comprimé est tout d'abord envoyé à une colonne contenant du gel de silice pour enlever l'humidité absolue résiduelle contenu dans le courant d'air. La pression du courant d'air est contrôlée avec un régulateur de pression et ensuite l'air est divisé et envoyé vers deux débitmètres massiques en parallèle. Sur l'un des chemins, l'air est envoyé dans une colonne remplie d'eau pour saturer le courant d'air en vapeur d'eau, tandis que sur l'autre chemin, le courant d'air reste sec. Les deux courants d'air sont mélangés de manière à ce que l'humidité absolue du courant d'air qui en résulte corresponde à la consigne (le rôle des débitmètres massiques est aussi de respecter une consigne traduite en vitesse de passage dans la gaine de séchage). Après le mélange, l'air peut être envoyé soit vers la zone de chauffage soit vers l'extérieur avec deux vannes tout-ou-rien (ce système est mis en place pour la mesure de la masse de la goutte). Sur la zone de chauffage, le courant d'air passe autour d'une résistance électrique pour l'augmentation en température avant d'être envoyé vers un nid d'abeille pour atténuer des éventuelles turbulences dans le courant. Après le nid abeille, le courant d'air est envoyé vers la zone de suspension de la goutte.

En prenant en compte les variables présentant une influence sur le séchage de la goutte (la température de l'air, la vitesse et l'humidité absolue de l'air autour de la goutte et les teneurs en masse de chaque soluté), un plan factoriel fractionnaire à deux niveaux a été utilisé à l'aide du numéro de Peclet pour définir les conditions expérimentales à appliquer avec le dispositif expérimental. Pour rappel, le nombre de Peclet prend en compte le taux de rétrécissement de la goutte par rapport à la diffusion de solutés à l'intérieur de la goutte. De cette manière, avec les conditions expérimentales choisies, le numéro de Peclet peut être supérieur ou inférieur à l'unité (Tableaux 3.3 et 3.4).

Pour assurer la fiabilité des données de séchage obtenues avec le dispositif expérimental, deux traitements ont été systématiquement réalisés pour chaque cinétique de séchage. Le premier traitement concerne la correction de la masse initiale de la goutte en considérant une perte de masse en régime diffusif durant 30 s. Pour le traitement suivant, la teneur

en eau finale de la particule est mesurée *ex situ* et comparée avec celle donnée par la cinétique de séchage. La correction appliquée a pour but de rapprocher la valeur de teneur en eau donnée par la balance avec celle mesurée *ex situ* (Figure 3.5). A part les traitements réalisés sur la cinétique de séchage, un autre traitement sur les images capturées par la caméra a aussi été développé. Ainsi, le diamètre de la goutte/particule humide peut être évalué. Enfin, il faut aussi savoir que les particules obtenues avec le dispositif expérimental ont été caractérisées avec le MEB (pour l'aspect de la surface et du cœur de la particule) et la calorimétrie différentielle à balayage (DSC, pour la structure cristalline ou amorphe du solide).

Pour la présentation des résultats, les morphologies obtenues selon le nombre de Peclet sont montrées. Ensuite, la discussion est centrée sur la cinétique de rétrécissement de la goutte et sur la cinétique de séchage (avec l'influence de la température de l'air, de l'écoulement de l'air et enfin de la formulation liquide). En ce qui concerne les particules obtenues avec un Peclet inférieur à l'unité (avec l'air à 20 °C), l'évolution morphologique de la goutte est plus lente et de cette manière la caméra placée en face de la goutte peut enregistrer des petites variations sur l'aspect de surface de la goutte au cours du temps. Sur la Figure 3.7, il est possible de voir sur la goutte contenant du dextrane-saccharose une réduction dans le diamètre, l'apparition du premier solide en surface, le recouvrement de la surface de la goutte par une croûte solide et la formation d'une particule entièrement solide. Les particules obtenues avec le mélange dextrane-saccharose pour un Peclet inférieur à l'unité sont montrées sur la Figure 3.9. Les particules présentent un cœur dense, à part celle obtenue avec la formulation la plus riche en dextrane. Pour le système lactose-lactosérum, il n'a pas été possible de récupérer des particules solides. Pour les particules obtenues avec un nombre de Peclet supérieur à l'unité, les modifications morphologiques ont lieu plus rapidement, ce qui rendait difficile la capture du moment d'apparition du premier solide à la surface de la goutte, par exemple. Les particules obtenues pour les systèmes dextrane-saccharose et lactose-lactosérum sont montrées sur les Figures 3.13 et 3.14. Les particules présentées en Figure 3.13 ont un cœur dense, alors que les particules en Figure 3.14 ont un cœur creux. Il a aussi été possible de montrer une similitude entre les particules obtenues à l'échelle de la goutte et celles obtenues à l'échelle du nuage de gouttes, ce qui valide la réalisation des études à l'échelle de la goutte pour la production des particules solides représentatives pour les systèmes de séchage d'intérêt.

En ce qui concerne la caractérisation de l'état solide, des particules amorphes ont pu être produites à l'échelle de la goutte à partir des deux systèmes de séchage (Figures 3.15 et 3.17). Pour le système dextrane-saccharose, la température de transition vitreuse subit des variations plus importantes lorsque la proportion dextrane-saccharose est supérieur à l'unité (Tableau 3.6). Pour le système lactose-lactosérum, deux températures de transition vitreuse ont été mesurées par particule, cependant l'intensité du signal a rendu difficile une mesure précise de chaque valeur (à titre indicatif, les mesures ont été montrées dans le Tableau 3.7).

Lors de l'analyse de la cinétique de rétrécissement, l'évolution du diamètre de la goutte au cours du temps et le volume de la goutte en fonction de la teneur en eau sont présentées dans les Figures 3.18 et 3.19, respectivement. Il a été possible de voir deux tendances de réduction dans le diamètre de la goutte: une forte réduction pendant les premiers instants du séchage et une réduction légère pendant le reste de l'expérience. Aussi, il a été montré que la réduction dans le volume de la goutte suit un caractère

idéal (une proportionnalité entre la réduction du volume et le taux d'évaporation). Ce comportement a pu mieux être identifié pour l'essai à 20 °C, avec un faible taux évaporatif.

Par rapport à la cinétique de séchage, l'analyse de la densité de flux évaporatif (Figure 3.21) et de la teneur en eau au cours du temps (Figure 3.20) ont aidé à l'identification de certains aspects liés aux différentes phases de séchage: la période de mise en température était trop courte pour être évaluée expérimentalement ; la première phase de séchage durait jusqu'à ce qu'une teneur moyenne critique était obtenue, ce qui correspond à l'apparition du premier solide à la surface de la goutte ; la deuxième phase de séchage peut être composée de deux mécanismes de transport de l'eau adsorbée, mais différents de ce qui est souvent mentionnée dans la littérature, due à la production de particules solides non-poreuses produites dans le présent chapitre.

Enfin, avec l'analyse de la teneur en eau lorsque le premier solide apparaît sur la surface de la goutte, il est possible d'observer (avec une meilleure définition avec l'air à 20 °C) l'impact de la formulation liquide sur la formation du solide. Le système lactose-lactosérum sèche plus rapidement que le système dextrane-saccharose, avec l'apparition du solide à une teneur en eau plus grande. L'addition de dextrane au système dextrane-saccharose a conduit à la formation de la croûte solide à des teneurs en eau plus importantes. Cet effet est en relation avec une plus faible solubilité du dextrane dans l'eau, par rapport à celle du saccharose dans l'eau. Pour le système lactose-lactosérum, la croûté solide est formée à des teneur en eau plus grandes lorsque la proportion lactosérum-lactose est supérieur à l'unité. Ceci pourrait être lié à l'accumulation du lactosérum à la surface de la goutte (agent de surface).

Dans le présent chapitre, l'analyse du séchage de la goutte a été réalisée en considérant des teneurs en eau moyennes (une valeur pour la goutte/particule humide à chaque instant). Une analyse plus approfondie du séchage serait intéressante avec une description de la distribution spatiale des constituants dans la goutte. Dans le but d'acquérir ce type d'information, le chapitre suivant a été développé.

A.5 Mesure de profils de composition *in situ* dans des gouttes lévitées acoustiquement

Le chapitre 4 est consacré à la présentation d'une nouvelle application à la technique de Raman *in situ* pour l'acquisition de la teneur massique des solutés dans la goutte de façon discrète au cours du temps (avec une goutte liquide, en présence d'une croûte en surface et avec une particule entièrement solide). Cette technique est combinée avec un lévitateur acoustique (Figure 4.2) pour l'obtention de ce type d'information sans trop perturber le séchage de la goutte.

Les conditions expérimentales testées avec le dispositif expérimental présenté dans le chapitre 4 sont limitées à des modifications dans la formulation liquide (teneur en masse et la proportion des solutés). L'idée est basée sur l'acquisition des profils de teneur en masse avec des morphologies de particules différentes (à cœur dense ou creux) et aussi liée à la présence de zones riches en un soluté. Afin de calculer ces profils de teneur en masse, la lumière Raman capturée par la caméra CCD a dû être traitée. Les étapes consistent à : identifier l'interface des gouttes (Figure 4.3), corriger les

lignes de base (Figures 4.5 et 4.6), calculer l'intensité des pics pour chaque soluté et en déduire les teneurs en masse à partir de courbes d'étalonnage pour chaque soluté (Figure 4.9). Un défi important est lié à l'évaluation de l'intensité du pic de chaque soluté dans le spectre Raman du mélange ternaire. Pour le système dextrane-saccharose, par exemple, un seul pic identifie clairement l'un de ces solutés en solution. Pour le système lactose-lactosérum, la région d'identification des solutés présente un bruit important, ce qui rend difficile l'identification des pics correspondant à chaque soluté dans le mélange ternaire.

La goutte contentant une teneur en masse en dextrane égale à 25 % a générée une particule ressemblant à un bol (Figure 4.11). Avec cet essai, le processus de contraction a été d'abord observée à partir de la surface supérieure de la goutte. Avec le temps, le rétrécissement de la surface supérieure progresse vers la surface inférieure de la goutte. Par conséquent, les profils de teneur en masse obtenus avec cet essai étaient continus à travers la goutte jusqu'au point où la surface supérieure a atteint la lumière laser. A partir de ce moment-là, les profils de teneur en masse présentent une discontinuité (Figure 4.15). Pour les autres essais avec le système dextrane-saccharose, des particules à cœur dense ont été obtenues. Les profils étaient plats au début et à la fin du séchage. La différence des teneurs en solutés entre le centre et la surface de la goutte augmente jusqu'à la formation de la croûte. Cette différence diminue par la suite (Figure 4.14). Pour le système lactose-WPI, une particule à cœur creux a été obtenue à partir d'un mélange contenant un pourcentage plus élevé de lactosérum. Une fois le cœur creux formé, la particule ne reste plus piégée dans le champ acoustique (Figure 4.12). Pour les autres avec le système lactose-lactosérum, des particules à cœur dense ont été obtenues. Cependant, pour ce système, les profils de teneur en masse sont trop bruyants pour être exploités. Cela vient du fait que la longueur d'onde du laser utilisée dans les essais induit le phénomène de fluorescence dans la goutte pour ce système-là et par conséquent une mesure correcte de la lumière Raman n'est pas possible. Une modification de la longueur d'onde du laser serait donc nécessaire pour le travail avec le lactosérum.

En ce qui concerne les profils de teneur en masse pour chaque soluté, dans les essais avec le système dextrane-saccahrose, une surface riche en dextrane et un cœur riche en saccharose ont pu être observés avec une particule à cœur dense générée à partir d'une goutte à faible teneur totale en soluté (10 %). Dans cet essai, les solutés ont été initialement ajoutés à la même proportion massique. Pour les autres essais, une ségrégation des solutés n'a pas été observée. Ces résultats ont présenté l'effet du coefficient de diffusion des solutés de la formulation (en raison d'une teneur en soluté plus petite) sur la ségrégation des composants par un mécanisme diffusif. Comme le dextrane possède un coefficient de diffusion plus faible que celui du saccharose, il aurait tendance à s'accumuler à la surface des gouttes pendant le séchage.

La technique développé dans le chapitre 4 présente un progrès important dans l'étude du séchage des gouttes multi-constituants. La technique peut être adaptée à d'autres formulations liquides en tenant compte de sa compatibilité avec la longueur d'onde du laser employée, de manière à éviter les phénomènes de fluorescence. De plus, les profils de teneur en masse obtenus ici sont utiles pour soutenir le développement de modèles de séchage, car ces profils donnent enfin un aperçu de la distribution des composants des gouttes dans le temps. En plus, le modèle de séchage peut compléter les résultats obtenus dans ce chapitre avec des conditions de séchage plus dures.

A.6 Modélisation du séchage d'une goutte

Dans le chapitre 5, un modèle numérique a été développé pour simuler les transferts couplés ayant lieu pendant le séchage d'une goutte multi-constituants. Le séchage de la goutte sphérique en libre suspension a été simulé en fonction du temps de formation de la croûte observé lors de chaque essai du chapitre 3. De plus, seule une goutte contentant du dextrane et du saccharose a été considérée dans le présent chapitre. Un aspect important lié à la conception du modèle est la définition d'un mouvement convectif à l'intérieur de la goutte, dû au flux d'air. De cette manière, le transport du dextrane et du saccharose en phase liquide peut être décrit par un transport convectif et diffusif. Pour celui-ci, l'équation de Stokes-Einstein a été utilisée pour les coefficients de diffusion, la présence de plus d'un soluté en phase liquide a été prise en compte dans le calcul du flux diffusif.

Les résultats obtenus dans le chapitre 5 ont montré que, malgré le transfert de quantité de mouvement entre l'air de séchage et la goutte, le profil de vitesse à l'intérieur de la goutte n'a pas une forte influence sur la distribution radiale des composants (Figure 5.10). Les profils de teneur en masse générés par le modèle augmentent radialement du centre vers la surface de la goutte (Figure 5.11), ce qui peut être observé lorsque la diffusion est le mécanisme prédominant de transport des solutés dans la goutte pendant le séchage. De plus, une goutte avec une viscosité plus faible peut présenter un mouvement convectif plus fort. Compte tenu des simulations effectuées avec les conditions expérimentales du chapitre 4, une surface riche en dextrane a pu être observée et le profil de teneur en masse du saccharose est relativement homogène dans la phase liquide (Figure 5.12). Bien qu'en accord avec l'un des résultats présentés dans le chapitre 4, une meilleure évaluation des données physicochimiques des solutés permettrait de définir plus précisément les teneurs en masse trouvées dans ces conditions de séchage. Pour les essais effectués sous des températures de l'air plus élevées, une première couche composée principalement de dextrane a pu être observée dans la goutte, suivie d'une partie de la phase liquide où la teneur en masse du saccharose était la plus élevée (Figure 5.14). Il est possible de supposer qu'une telle distribution spatiale pourrait bien indiquer ce qui serait trouvé dans les particules solides à la fin du processus de séchage.

Les résultats obtenus ici ont également montré que le flux d'évaporation n'est pas uniforme sur la surface des gouttes, ce qui pourrait favoriser la formation d'une croûte non homogène autour de la goutte. De plus, le modèle aurait pu être simplifié en considérant une goutte isotherme lors de la première étape de séchage. En ce qui concerne la cinétique de séchage, les teneurs en eau simulées à un instant donné sont souvent inférieures à celles obtenues au chapitre 3 (Tableau 5.3). Cela indique des taux d'évaporation plus élevés à partir des simulations. Les simulations ont utilisé une température et un débit d'air constants pendant le temps de séchage, tandis que dans les expériences, le débit d'air est intermittent et la température n'est pas aussi strictement constante que dans le modèle.

À partir de l'analyse de sensibilité, il a été possible d'observer que la température de l'air a un impact majeur sur le séchage des gouttes (Figure 5.15), par rapport à la vitesse (Figure 5.16) et l'humidité absolue de l'air (Figure 5.17). Dans la formulation liquide, en utilisant un critère basé sur la fraction volumique pour indiquer la formation de la croûte, il a été possible d'observer une réduction du temps d'apparition de la croûte en ajoutant des solutés à la phase liquide. En outre, l'ajout de dextrane à la

gouttelette a eu un effet beaucoup plus fort sur le temps de l'apparition de la croûte que le saccharose, comme prévu d'après les observations des chapitres précédents.

A.7 Conclusion

À partir des observations de la morphologie des particules, de la cinétique de séchage et de la distribution spatiale des solutés des deux systèmes de séchage, l'influence de la formulation liquide sur la structure finale des particules a été mise en évidence. L'utilisation de molécules aux propriétés physico-chimiques différentes, à savoir la structure chimique, la taille de la molécule et la solubilité, a joué un rôle important dans la définition de la structure du solide final. En présence d'un gradient de soluté, les solutés en phase liquide pourraient être séparés en fonction de leur taille moléculaire (ce qui affecte la diffusion des molécules dans un milieu), même si la viscosité dans la goutte pourrait freiner un tel processus. En outre, en fonction du degré auquel les solutés sont séparés et de leur taille moléculaire, les propriétés viscoélastiques de la croûte pourraient être modifiées. En changeant les propriétés de la croûte, il est possible de modifier sa capacité à résister à la compression liée au procédé de séchage, ainsi différents aspects de surface pourraient être obtenus. Naturellement, l'échelle de temps à laquelle les caractéristiques de la formulation liquide évoluent est limitée par les propriétés de l'air de séchage, en particulier la température de l'air. Avec des températures de l'air plus élevées, l'échelle de temps pour que les solutés se diffusent à travers la goutte est réduite, car la goutte liquide devient rapidement une particule solide. De même, une vitesse relative importante entre l'air de séchage et la goutte pourrait aider à retarder la ségrégation des solutés en induisant un mouvement convectif à l'intérieur de la goutte.

List of Figures

189

List of Tables

List of symbols

Alphanumerics

A	m^2	Cross-sectional area of the wind tunnel	60
Y	$\mathrm{kg\,kg^{-1}}$	Air absolute humidity	9
A_c	m^2	Bubble column cross-sectional area	61
α_b	$\mathrm{m^2\,m^{-3}}$	Specific area of bubbles	61
a_w	-	Water activity	10
β	$\mathrm{mg\,mg^{-1}\,s^{-1}}$	Mass drift coefficient	73
c	$\mathrm{kmol\,m^{-3}}$	Molar concentration	136
$\mathbf{c}$	$\mathrm{kg\,m^{-3}}$	Mass concentration	141
C_p	$\mathrm{J\,kg^{-1}\,K^{-1}}$	Specific heat capacity	144
D	$\mathrm{m^2\,s^{-1}}$	Diffusion coefficient	136
d	m	Droplet diameter	66
d_h	m	Wind tunnel hydraulic diameter	68
h	$\mathrm{J\,kg^{-1}}$	Specific enthalpy	62
HR	-	Air relative humidity	10
h_t	$\mathrm{W\,m^{-2}\,K^{-1}}$	Heat transfer coefficient	67
$h^{\mathrm{l}\rightarrow\mathrm{g}}$	$\mathrm{kJ\,kg^{-1}}$	Enthalpy of vaporization of water	140
$[\mu]$	$\mathrm{m^3\,kg^{-1}}$	Intrinsic viscosity	143
I	-	Raman peak intensity	117
j	$\mathrm{kg\,m^{-2}\,s^{-1}}$	Diffusive mass flux vector	136
J_tot	$\mathrm{kg\,s^{-1}}$	Evaporation rate from the whole droplet surface	138
K_b	$\mathrm{kg\,m^2\,s^{-2}\,K^{-1}}$	Bolztmann constant	145
k_h	-	Intrinsic viscosity	143
m	kg	Mass	9
$\dot{m}$	$\mathrm{kg\,s^{-1}}$	Mass flow	60
MM	$\mathrm{kg\,kmol^{-1}}$	Molar mass	9
x	-	Molar fraction	141
μ_gl	$\mathrm{Pa\,s}$	Universal viscosity at the glass transition	144
n	-	Normal unit vector	136
Nu	-	Nusselt number	67
N_v	$\mathrm{kg\,s^{-1}\,m^{-2}}$	Evaporation flux	12
P	Pa	Pressure	9

Greek letters

Superscripts

Subscripts

Bibliography

[1] B. Adhikari, T. Howes, and B. R. Bhandari. "Use of solute fixed coordinate system and method of lines for prediction of drying kinetics and surface stickiness of single droplet during convective drying." In: *Chemical Engineering and Processing: Process Intensification* 46.5 (2007), pp. 405–419 (cit. on pp. 24, 30).

[2] B. Adhikari, T. Howes, B. R. Bhandari, and T. A. G. Langrish. "Effect of addition of proteins on the production of amorphous sucrose powder through spray drying." In: *Journal of Food Engineering* 94.2 (2009), pp. 144–153 (cit. on p. 40).

[3] B. Adhikari, T. Howes, B. R. Bhandari, and V. Truong. "Experimental studies and kinetics of single drop drying and their relevance in drying of sugar-rich foods: A review." In: *International Journal of Food Properties* 3.3 (2000), pp. 323–351 (cit. on pp. 21, 25).

[4] A. B. Al Zaitone and C. Tropea. "Evaporation of pure liquid droplets: Comparison of droplet evaporation in an acoustic field versus glass-filament." In: *Chemical Engineering Science* 66.17 (2011), pp. 3914–3921 (cit. on pp. 24, 25).

[5] I. M. Andersson, M. Glantz, M. Alexander, A. Millqvist-fureby, M. Paulsson, and B. Bergenståhl. "Impact of surface properties on morphology of spray-dried milk serum protein / lactose systems." In: *International Dairy Journal* 85 (2018), pp. 86–95 (cit. on p. 101).

[6] Anton PAAR. *How to Appropriately Characterize the BET area of a microporous material* (cit. on p. 55).

[7] J. Bahadur, D. Sen, S. Mazumder, B. Paul, H. Bhatt, and S. G. Singh. "Control of buckling in colloidal droplets during evaporation-induced assembly of nanoparticles." In: *Langmuir* 28.3 (2012), pp. 1914–1923 (cit. on pp. 16, 17, 20, 36).

[8] Al. Baldelli, M. A. Boraey, D. S. Nobes, and R. Vehring. "Analysis of the Particle Formation Process of Structured Microparticles." In: *Molecular Pharmaceutics* 12.8 (2015), pp. 2562–2573 (cit. on pp. 21, 25).

[9] J. Barbosa and P. Teixeira. "Development of probiotic fruit juice powders by spray-drying: A review." In: *Food Reviews International* 9129.April (2016), pp. 1–24 (cit. on p. 5).

[10] R. Bellinghausen. "Spray drying from yesterday to tomorrow: An industrial perspective." In: *Drying Technology* 37.5 (2019), pp. 612–622 (cit. on p. 65).

[11] E. M. Both, A. M. Karlina, R. M. Boom, and M. A. I. Schutyser. "Morphology development during sessile single droplet drying of mixed maltodextrin and whey protein solutions." In: *Food Hydrocolloids* 75 (2018), pp. 202–210 (cit. on p. 21).

[12] E. M. Both, I. Siemons, R. M. Boom, and M. A. I. Schutyser. "The role of viscosity in morphology development during single droplet drying." In: *Food Hydrocolloids* 94.March (2019), pp. 510–518 (cit. on p. 144).

[13] J. Bouman, P. Venema, R. J. de Vries, E. van der Linden, and Maarten A. I. Schutyser. "Hole and vacuole formation during drying of sessile whey protein droplets." In: *Food Research International* 84 (2016), p. 16 (cit. on p. 24).

[14] A. Braeuer, O. S. Knauer, J. Quiño, and A. Leipertz. "Quantification of the mass transport in a two phase binary system at elevated pressures applying Raman spectroscopy: Pendant liquid solvent drop in a supercritical carbon dioxide environment." In: *International Journal of Heat and Mass Transfer* 62.1 (2013), pp. 729–740 (cit. on pp. 28, 29, 109).

[15] K. Cal and K. Sollohub. "Spray Drying Technique . I : Hardware and Process Parameters." In: 99.2 (2010), pp. 575–586 (cit. on pp. 6, 14, 15).

[16] D. H. Charlesworth and W. R. Marshall. "Evaporation from drops containing dissolved solids." In: *AIChE Journal* 6.1 (1960), pp. 9–23 (cit. on p. 17).

[17] X. D. Chen and S. X. Q. Lin. "Air drying of milk droplet under constant and time-dependent conditions." In: *AIChE Journal* 51.6 (2005), pp. 1790–1799 (cit. on p. 31).

[18] X. D. Chen, H. Sidhu, and M. Nelson. "Theoretical probing of the phenomenon of the formation of the outermost surface layer of a multi-component particle, and the surface chemical composition after the rapid removal of water in spray drying." In: *Chemical Engineering Science* 66.24 (2011), pp. 6375–6384 (cit. on p. 40).

[19] X. D. Chen and G. Z. Xie. "Fingerprints of the Drying Behaviour of Particulate or Thin Layer Food Materials Established Using a Reaction Engineering Model." In: *Food and Bioproducts Processing* 75.4 (1997), pp. 213–222 (cit. on p. 31).

[20] X. Chen, V. Boyko, J. Rieger, F. Reinhold, B. Reck, J. Perlich, R. Gehrke, and Y. Men. "Buckling-induced structural transition during the drying of a polymeric latex droplet on a solid surface." In: *Soft Matter* 8.48 (2012), p. 12093 (cit. on pp. 17, 24).

[21] J. H. Chew, N. Fu, T. Gengenbach, X. D. Chen, and C. Selomulya. "The compositional effects of high solids model emulsions on drying behaviour and particle formation processes." In: *Journal of Food Engineering* 157 (2015), pp. 33–40 (cit. on pp. 24, 31).

[22] J. H. Chew, M. W. Woo, X. D. Chen, C. Selomulya, and J. H. Chew. "Mapping the Shrinkage Behavior of Skim Milk Droplets During Convective Drying Mapping the Shrinkage Behavior of Skim Milk Droplets During Convective Drying." In: *Drying Technology* 33.9 (2015), pp. 1101–1113 (cit. on p. 31).

[23] V. Cristiglio, I. Grillo, M. Fomina, F. Wien, E. Shalaev, A. Novikov, S. Brassamin, M. Réfrégiers, J. Pérez, and L. Hennet. "Combination of acoustic levitation with small angle scattering techniques and synchrotron radiation circular dichroism. Application to the study of protein solutions." In: *Biochimica et Biophysica Acta (BBA) - General Subjects* 1861.1 (2017), pp. 3693–3699 (cit. on p. 25).

[24] M. Damak, S. R. Mahmoudi, M. N. Hyder, and K. K. Varanasi. "Enhancing droplet deposition through in-situ precipitation." In: *Nature Communications* 7 (2016), p. 12560 (cit. on p. 24).

[25] R. Dey and P. Biswas. "A novel and effective approach for viscosity prediction of binary and multicomponent liquid mixtures." In: *Journal of Molecular Liquids* 265 (2018), pp. 356–360 (cit. on p. 145).

[26] C. Diddens, J. G. M. Kuerten, C. W. M. van der Geld, and H. M. A. Wijshoff. "Journal of Colloid and Interface Science Modeling the evaporation of sessile multi-component droplets." In: *Journal of Colloid And Interface Science* 487 (2017), pp. 426–436 (cit. on p. 134).

[27] M. Dissanayake. "Modulation of Functional Properties of Whey Proteins by Microparticulation." PhD thesis. Victoria University, 2011, p. 285 (cit. on p. 40).

[28] J. Donea, A. Huerta, J.-Ph. Ponthot, and A. Rodríguez-Ferran. *Arbitrary Lagrangian–Eulerian Methods.* Aug. 2004 (cit. on p. 149).

[29] Z. Duan, B. He, and Y. Duan. "Sphere Drag and Heat Transfer." In: *Scientific Reports* 5 (July 2015), p. 12304 (cit. on p. 67).

[30] J. Dudowicz, J. F. Douglas, and K. F. Freed. "The meaning of the "universal" WLF parameters of glass-forming polymer liquids." In: *The Journal of Chemical Physics* 142.1 (Jan. 2015), p. 14905 (cit. on p. 144).

[31] B. K. Dutta. "Principles of mass transfer and separation processes." In: *The Canadian Journal of Chemical Engineering* 87.5 (Oct. 2009), pp. 818–819 (cit. on p. 72).

[32] J. Elversson, K. Andersson, and A. Millqvist-Fureby. "An Atomic Force Microscopy Approach for Assessment of Particle Density Applied to Single Spray-Dried Carbohydrate Particles." In: *Journal of pharmaceutical sciences* 96.4 (2007), pp. 905–912 (cit. on pp. 16, 36, 37).

[33] J. Elversson and A. Millqvist-Fureby. "Particle size and density in spray drying - Effects of carbohydrate properties." In: *Journal of Pharmaceutical Sciences* 94.9 (2005), pp. 2049–2060 (cit. on pp. 16, 20, 38–40, 48, 50).

[34] J. Elversson, A. Millqvist-Fureby, G. Alderborn, and U. Elofsson. "Droplet and particle size relationship and shell thickness of inhalable lactose particles during spray drying." In: *Journal of Pharmaceutical Sciences* 92.4 (2003), pp. 900–910 (cit. on pp. 16, 21).

[35] M. Eslamian and N. Ashgriz. "Evaporation and Evolution of Suspended Solution Droplets at Atmospheric and Reduced Pressures." In: *Drying Technology* 25.6 (2007), pp. 999–1010 (cit. on p. 24).

[36] C. Ferro Fontan, J. CHirife, and R. Bouquet. "Water activity in multicomponent non-electrolyte solutions." In: *Journal of Food Technology* 18 (1981), pp. 553–559 (cit. on p. 141).

[37] M. Foerster, T. Gengenbach, M. W. Woo, and C. Selomulya. "The impact of atomization on the surface composition of spray-dried milk droplets." In: *Colloids and Surfaces B: Biointerfaces* 140 (2016), pp. 460–471 (cit. on pp. 21, 25).

[38] M. Foerster, T. Gengenbach, M. W. Woo, and C. Selomulya. "The influence of the chemical surface composition on the drying process of milk droplets." In: *Advanced Powder Technology* 27.6 (2016), pp. 2324–2334 (cit. on pp. 24, 30).

[39] G. A. Frank. "Measurement analysis of glass transition temperature for sucrose and trehalose aqueous solutions." In: *Journal of Physical and Chemical Reference Data* 36.4 (2007), pp. 1279–1285 (cit. on pp. 40, 48).

[40] A. Frohn and N. Roth. *Dynamics of Droplets*. Experimental Fluid Mechanics. Springer Berlin Heidelberg, 2013 (cit. on p. 112).

[41] N. Fu, M. W. Woo, and X. D. Chen. "Colloidal transport phenomena of milk components during convective droplet drying." In: *Colloids and Surfaces B: Biointerfaces* 87.2 (2011), pp. 255–266 (cit. on pp. 24, 65).

[42] N. Fu, M. W. Woo, and X. D. Chen. "Single Droplet Drying Technique to Study Drying Kinetics Measurement and Particle Functionality: A Review." In: *Drying Technology* 30.15 (2012), pp. 1771–1785 (cit. on pp. 21, 24).

[43] N. Fu, M. W. Woo, C. Selomulya, and X. D. Chen. "Shrinkage behaviour of skim milk droplets during air drying." In: *Journal of Food Engineering* 116.1 (2013), pp. 37–44 (cit. on pp. 24, 36).

[44] N. Fu, W. D. Wu, M. Yu, F. T. Moo, M. W. Woo, C. Selomulya, and X. D. Chen. "In situ observation on particle formation process via single droplet drying apparatus: Effects of precursor composition on particle morphology." In: *Drying Technology* 34.14 (2016), pp. 1700–1708 (cit. on pp. 24, 26).

[45] J. Gaube, A. Pfennig, and M. Stumpf. "Vapor-Liquid Equilibrium in Binary and Ternary Aqueous Solutions." In: *Journal of Chemical and Engineering Data* 38 (1993), pp. 163–166 (cit. on p. 141).

[46] Ol. A. George, X. D. Chen, J. Xiao, M. Woo, and L. Che. "Modeling and simulation of the polymeric nanocapsule formation process." In: *AIChE Journal* 61 (2015), pp. 4140–4151 (cit. on p. 31).

[47] Ol. A. George, J. Xiao, C. S. Rodrigo, R. Mercadé-Prieto, J. Sempere, and X. D. Chen. "Detailed numerical analysis of evaporation of a micrometer water droplet suspended on a glass filament." In: *Chemical Engineering Science* 165 (2017), pp. 33–47 (cit. on p. 147).

[48] I. Gouaou, M. S. Koutchoukali, and A. Kharaghani. "Experimental study of drying conditions on starch single droplet shrinkage and morphology during drying." In: *Third International Conference on Energy, Materials, Applied Energetics and Pollution*. 2016, pp. 326–332 (cit. on p. 24).

[49] N. Grasmeijer, H. W. Frijlink, and W. L. J. Hinrichs. "Model to predict inhomogeneous protein-sugar distribution in powders prepared by spray drying." In: *Journal of Aerosol Science* 101 (2016), pp. 22–33 (cit. on pp. 31, 32).

[50] M. Griesing, H. Grosshans, T Hellwig, R Sedelmayer, S. R. Gopireddy, W. Pauer, E. Gutheil, and H.-U. Moritz. "Influence of the Drying Air Humidity on the Particle Formation of Single Mannitol-Water Droplets." In: *Chemie-Ingenieur-Technik* submitted.7 (2015), pp. 1–9 (cit. on pp. 21, 25).

[51] J. D. Griffith, A. E. Bayly, and M. L. Johns. "Magnetic resonance studies of detergent drop drying." In: *Chemical Engineering Science* 63.13 (2008), pp. 3449–3456 (cit. on p. 30).

[52] C. Groenewold, C. Möser, H. Groenewold, and E. Tsotsas. "Determination of single-particle drying kinetics in an acoustic levitator." In: *Chemical Engineering Journal* 86.1-2 (2002), pp. 217–222 (cit. on pp. 21, 25).

[53] H. Grosshans, M. Griesing, M. Mönckedieck, T. Hellwig, B. Walther, S. R. Gopireddy, R. Sedelmayer, W. Pauer, H. U. Moritz, N. A. Urbanetz, and E. Gutheil. "Numerical and experimental study of the drying of bi-component droplets under various drying conditions." In: *International Journal of Heat and Mass Transfer* 96 (2016), pp. 97–109 (cit. on p. 25).

[54] M. A. Hampton, T. A. H. Nguyen, A. V. Nguyen, Z. P. Xu, L. Huang, and V. Rudolph. "Influence of surface orientation on the organization of nanoparticles in drying nanofluid droplets." In: *Journal of Colloid and Interface Science* 377.1 (2012), pp. 456–462 (cit. on p. 24).

[55] K. Han, G. Song, X. Ma, and B. Yang. "An experimental and theoretical study of the effect of suspended thermocouple on the single droplet evaporation." In: *Applied Thermal Engineering* 101 (2016), pp. 568–575 (cit. on p. 24).

[56] C. S. Handscomb. "Simulating droplet drying and particle formation in spray towers." PhD thesis. 2008 (cit. on p. 95).

[57] C. S. Handscomb and M. Kraft. "Simulating the structural evolution of droplets following shell formation." In: *Chemical Engineering Science* 65.2 (2010), pp. 713–725 (cit. on p. 31).

[58] C. S. Handscomb, M. Kraft, and A. E. Bayly. "A new model for the drying of droplets containing suspended solids." In: *Chemical Engineering Science* 64.4 (2009), pp. 628–637 (cit. on pp. 31, 113, 175).

[59] C. S. Handscomb, M. Kraft, and A. E. Bayly. "A new model for the drying of droplets containing suspended solids after shell formation." In: *Chemical Engineering Science* 64.4 (2009), pp. 628–637 (cit. on pp. 31–33, 134, 135, 175).

[60] M. A. Haque, B. Adhikari, and A. Putranto. "Predictions of drying kinetics of aqueous droplets containing WPI-lactose and WPI-trehalose by application of composite reaction engineering approach (REA)." In: *Journal of Food Engineering* 189 (2016), pp. 29–36 (cit. on p. 24).

[61] M. A. Haque, P. Aldred, J. Chen, C. J. Barrow, and B. Adhikari. "Comparative study of denaturation of whey protein isolate (WPI) in convective air drying and isothermal heat treatment processes." In: *Food Chemistry* 141.2 (2013), pp. 702–711 (cit. on p. 40).

[62] M. Amdadul Haque, Jie Chen, Peter Aldred, and Benu Adhikari. "Drying and denaturation characteristics of whey protein isolate in the presence of lactose and trehalose." In: *Food Chemistry* 177 (2015), pp. 8–16 (cit. on pp. 37, 38, 40).

[63] H. M. Hassan and C. J. Mumford. "Mechanisms Drying of Skin-Forming Materials. I.Droplets of Material Which Gelatinised at High Temperature." In: *Drying Technology* 11.7 (1993), pp. 1713–1750 (cit. on pp. 15, 24).

[64] D. Heng, S. H. Lee, W. K. Ng, and R. B. H. Tan. "The nano spray dryer B-90." In: (2011), pp. 965–972 (cit. on p. 21).

[65] L. Hennet, V. Cristiglio, J. Kozaily, I. Pozdnyakova, H. E. Fischer, A. Bytchkov, J. W. E. Drewitt, M. Leydier, D. Thiaudière, S. Gruner, S. Brassamin, D. Zanghi, G. J. Cuello, M. Koza, S. Magazù, G. N. Greaves, and D. L. Price. "Aerodynamic levitation and laser heating: Applications at synchritrin and neutron sources." In: *The European Physical Journal Special Topics* 196.1 (2011), pp. 151–165 (cit. on pp. 21, 25).

[66] C. Holzammer, A. Finckenstein, S. Will, and A. Braeuer. "How Sodium Chloride Salt Inhibits the Formation of CO2 Gas Hydrates." In: *The Journal of Physical Chemistry B* 120.9 (Mar. 2016), pp. 2452–2459 (cit. on p. 116).

[67] H. C. van de Hulst and R. T. Wang. "Glare points." In: *Applied Optics* 30.33 (1991), pp. 4755–4763 (cit. on p. 112).

[68] J. M. Hutchinson and S. Montserrat. "The application of temperature-modulated DSC to the glass transition region: II. Effect of a distribution of relaxation times." In: *Thermochimica Acta* 377.1 (2001), pp. 63–84 (cit. on p. 70).

[69] K. Imamura, A. Fukushima, K. Sakaura, T. Sugita, T. Sakiyama, and K. Nakanishi. "Water Sorption and Glass Transition Behaviors of Freeze-Dried Sucrose – Dextran Mixtures." In: 91.10 (2002), pp. 2175–2181 (cit. on p. 86).

[70] F. Iskandar. "Nanoparticle processing for optical applications – A review." In: *Advanced Powder Technology* 20 (2009), pp. 283–292 (cit. on p. 5).

[71] Y. Jin and X. D. Chen. "Numerical Study of the Drying Process of Different Sized Particles in an Industrial-Scale Spray Dryer." In: *Drying Technology* 27.3 (2009), pp. 371–381 (cit. on p. 31).

[72] R. B. Keey. *Drying of Loose and Particulate Materials.* Ed. by New York: Hemisphere Pub. 1991 (cit. on p. 12).

[73] I. C. Kemp, B. C. Fyhr, S. Laurent, M. A. Roques, C. E. Groenewold, E. Tsotsas, A. A. Sereno, C. B. Bonazzi, J.-J. Bimbenet, and M. Kind. "Methods for processing experimental drying kinetics data." In: *Drying Technology* 19.1 (Jan. 2001), pp. 15–34 (cit. on p. 93).

[74] A. Khoufech, M. Benali, and K. Saleh. "Influence of liquid formulation and impact conditions on the coating of hydrophobic surfaces." In: *Powder Technology* 270 (2015), pp. 599–611 (cit. on p. 24).

[75] A. Khoufech, M. Benali, and K. Saleh. "Influence of liquid formulation and impact conditions on the wetting of hydrophobic surfaces by aqueous polymeric solutions." In: *Chemical Engineering Research and Design* 110 (2016), pp. 233–244 (cit. on p. 24).

[76] K. Kondo, T. Niwa, and K. Danjo. "Preparation of sustained-release coated particles by novel microencapsulation method using three-fluid nozzle spray drying technique." In: *European Journal of Pharmaceutical Sciences* 51 (2014), pp. 11–19 (cit. on pp. 6, 8).

[77] M. Kreimer, I. Aigner, S. Sacher, M. Krumme, T. Mannschott, P. van der Wel, A. Kaptein, H. Schroettner, G. Brenn, and J. G. Khinast. "Mechanical strength of microspheres produced by drying of acoustically levitated suspension droplets." In: *Powder Technology* 325 (2018), pp. 247–260 (cit. on p. 25).

[78] T. A. G. Langrish and T. K. Kockel. "The assessment of a characteristic drying curve for milk powder for use in computational fluid dynamics modelling." In: 84 (2001), pp. 69–74 (cit. on p. 31).

[79] R. Leardi. "Experimental design in chemistry : A tutorial." In: *Analytica Chimica Acta* 652 (2009), pp. 161–172 (cit. on p. 64).

[80] D. A. LeClair, E. D. Cranston, Z. Xing, and M. R. Thompson. "Optimization of Spray Drying Conditions for Yield, Particle Size and Biological Activity of Thermally Stable Viral Vectors." In: *Pharmaceutical Research* 33.11 (2016), pp. 2763–2776 (cit. on p. 19).

[81] F. Lemoine and G. Castanet. "Temperature and chemical composition of droplets by optical measurement techniques: A state-of-the-art review." In: *Experiments in Fluids* 54.7 (2013) (cit. on pp. 29, 30).

[82] X. Li, N. Anton, T. M. C. Ta, M. Zhao, N. Messaddeq, and T. F. Vandamme. "Microencapsulation of nanoemulsions: novel Trojan particles for bioactive lipid molecule delivery." In: *International journal of nanomedicine* 6 (2011), pp. 1313–1325 (cit. on pp. 16, 20).

[83] J.-C. Lin and J. W. Gentry. "Spray Drying Drop Morphology: Experimental Study." In: *Aerosol Science and Technology* 37.1 (2003), pp. 15–32 (cit. on pp. 21, 24).

[84] S. X. Q. Lin and X. D. Chen. "Improving the Glass-Filament Method for Accurate Measurement of Drying Kinetics of Liquid Droplets." In: 80.May (2002) (cit. on pp. 21, 24).

[85] S. X. Q. Lin and X. D. Chen. "Changes in Milk Droplet Diameter During Drying Under Constant Drying Conditions Investigated Using The Glass-Filament Method." In: *Food and Bioproducts Processing* 82.3 (2004), pp. 213–218 (cit. on pp. 24, 36).

[86] H. Liu and M. H. Sharqawy. "Experimental performance of bubble column humidifier and dehumidifier under varying pressure." In: *International Journal of Heat and Mass Transfer* 93 (2016), pp. 934–944 (cit. on p. 61).

[87] W. Liu, X. D. Chen, and C. Selomulya. "On the spray drying of uniform functional microparticles." In: *Particuology* 22 (2015), pp. 1–12 (cit. on p. 21).

[88] X. H. Liu, X. Feng, R. O. Williams, and F. Zhang. "Characterization of amorphous solid dispersions." In: *Journal of pharmaceutical investigaton* 48 (2017), pp. 19–41 (cit. on p. 70).

[89] H. Lodish, A. Berk, S. L. Zipursky, P. Matsudaira, D. Baltimore, and J. Darnell. *Molecular Cell Biology*. Ed. by W. H. Freeman and Company. 4th Editio. 2000 (cit. on p. 40).

[90] J. Madiouli, J. Sghaier, J-J. Orteu, L. Robert, H. Sammouda, L. Robert, J. Madiouli, and J. Sghaier. "Non-contact Measurement of the Shrinkage and Calculation of Porosity During the Drying of Banana." In: 3937 (2011) (cit. on p. 90).

[91] L. Malafonte, L. Ahrné, E. Kaunisto, F. Innings, and A. Rasmuson. "Estimation of the effective diffusion coefficient of water in skim milk during single-drop drying." In: *Journal of Food Engineering* 147 (2015), pp. 111–119 (cit. on p. 32).

[92] S. Manukyan, H. M. Sauer, I. V. Roisman, K. A. Baldwin, D. J. Fairhurst, H. Liang, J. Venzmer, and C. Tropea. "Imaging internal flows in a drying sessile polymer dispersion drop using Spectral Radar Optical Coherence Tomography (SR-OCT)." In: *Journal of Colloid and Interface Science* 395.1 (2013), pp. 287–293 (cit. on pp. 24, 25, 30).

[93] A. G. Marín, H. Gelderblom, D. Lohse, and J. H. Snoeijer. "Order-to-disorder transition in ring-shaped colloidal stains." In: *Physical Review Letters* 107.8 (2011), pp. 1–4 (cit. on p. 24).

[94] A. G. Marín, H. Gelderblom, A. Susarrey-Arce, A. van Houselt, L. Lefferts, J. G. E. Gardeniers, D. Lohse, and J. H. Snoeijer. "Building microscopic soccer balls with evaporating colloidal fakir drops." In: *Proceedings of the National Academy of Sciences of the United States of America* 109.41 (2012), pp. 16455–8 (cit. on pp. 21, 24).

[95] G. Marty and N. Tsapis. "Monitoring the buckling threshold of drying colloidal droplets using water-ethanol mixtures." In: *European Physical Journal E* 27.2 (2008), pp. 213–219 (cit. on pp. 17, 22).

[96] A. Marzo, A. Barnes, and B. W. Drinkwater. "TinyLev: A multi-emitter single-axis acoustic levitator." In: *Review of Scientific Instruments* 88.8 (Aug. 2017), p. 85105 (cit. on p. 108).

[97] K. Masters. *Spray Drying Handbook.* 5th editio. Longman Scientific & Technical, 1991, p. 725 (cit. on pp. 6, 65).

[98] M. A. Masuelli. "Dextrans in Aqueous Solution . Experimental Review on Intrinsic Viscosity Measurements and Temperature Effect." In: 1.1 (2013), pp. 13–21 (cit. on p. 144).

[99] M. Mathlouthi and P. Reiser. *Sucrose: Properties and Applications.* 1st ed. 1995, p. 294 (cit. on pp. 38, 121).

[100] U. Maurice, M. Mezhericher, A. Levy, and I. Borde. "Drying of Droplet Containing Insoluble Nanoscale Particles: Numerical Simulations and Parametric Study." In: *Drying Technology* 31.15 (2013), pp. 1790–1807 (cit. on pp. 31–33).

[101] U. Maurice, M. Mezhericher, A. Levy, and I. Borde. "Drying of Droplets Containing Insoluble Nanoscale Particles: Second Drying Stage." In: *Drying Technology* 33.15-16 (2015), pp. 1837–1848 (cit. on pp. 31, 33, 36).

[102] U. Maurice, M. Mezhericher, A. Levy, and I. Borde. "Particle formation from droplet containing nanoparticles : Internal bubble growth." In: 3937.June (2017) (cit. on pp. 31, 33, 135).

[103] O.O. Medvedev and A. A. Shapiro. "Verifying reciprocal relations for experimental diffusion coefficients in multicomponent mixtures." In: *Fluid Phase Equilibria* 208.1 (2003), pp. 291–301 (cit. on p. 145).

[104] M. A. Mensink, H. W. Frijlink, K. van der Voort Maarschalk, and W. L. Hinrichs. "How sugars protect proteins in the solid state and during drying (review): Mechanisms of stabilization in relation to stress conditions." In: *European Journal of Pharmaceutics and Biopharmaceutics* 114 (2017), pp. 288–295 (cit. on p. 174).

[105] M. Mezhericher, A. Levy, and I. Borde. "Theoretical Drying Model of Single Droplets Containing Insoluble or Dissolved Solids." In: *Drying Technology* 25.6 (2007), pp. 1025–1032 (cit. on pp. 31–33).

[106] M. Mezhericher, A. Levy, and I. Borde. "Theoretical Models of Single Droplet Drying Kinetics: A Review." In: *Drying Technology* 28.2 (2010), pp. 278–293 (cit. on pp. 13, 36, 135, 152).

[107] M. Mezhericher, A. Levy, and I. Borde. "Modelling the morphological evolution of nanosuspension droplet in constant-rate drying stage." In: *Chemical Engineering Science* 66.5 (2011), pp. 884–896 (cit. on pp. 16, 31, 32).

[108] M. Mezhericher, A. Levy, and I. Borde. "Multi-Scale Multiphase Modeling of Transport Phenomena in Spray-Drying Processes." In: *Drying Technology* 33.1 (2014), pp. 2–23 (cit. on p. 121).

[109] M. Mezhericher, M. Naumann, M. Peglow, A. Levy, E. Tsotsas, and I. Borde. "Continuous species transport and population balance models for first drying stage of nanosuspension droplets." In: *Chemical Engineering Journal* 210 (2012), pp. 120–135 (cit. on pp. 31, 33, 36, 134, 156).

[110] R. Mondragon, L. Hernandez, J. Enrique Julia, J. Carlos Jarque, S. Chiva, B. Zaitone, and C. Tropea. "Study of the drying behavior of high load multiphase droplets in an acoustic levitator at high temperature conditions." In: *Chemical Engineering Science* 66.12 (2011), pp. 2734–2744 (cit. on p. 21).

[111] R. Mondragon, J. C. Jarque, J. E. Julia, L. Hernandez, and A. Barba. "Effect of slurry properties and operational conditions on the structure and properties of porcelain tile granules dried in an acoustic levitator." In: *Journal of the European Ceramic Society* 32.1 (2012), pp. 59–70 (cit. on pp. 25, 28, 36).

[112] R. Mondragon, J. E. Julia, A. Barba, and J. C. Jarque. "Microstructure and mechanical properties of grains of silica nanofluids dried in an acoustic levitator." In: *Journal of the European Ceramic Society* 32.16 (2012), pp. 4295–4304 (cit. on p. 27).

[113] A. Al-Mubarak, M. Belkharchouche, M. Al-Hayan, and A. Husain. "Mechanisms of single droplet drying." In: *Kuwait Journal of Science and Engineering* 37.1 B (2010), pp. 161–179 (cit. on p. 24).

[114] A. S. Mujumdar. *Handbook of Industrial Drying.* Ed. by CRC Press. Third Edit. 2007, p. 1312 (cit. on p. 9).

[115] M. Munoz-Ibanez, M. Nuzzo, C. Turchiuli, B. Bergenståhl, E. Dumoulin, and A. Millqvist-Fureby. "The microstructure and component distribution in spray-dried emulsion particles." In: *Food Structure* 8 (2016), pp. 16–24 (cit. on p. 19).

[116] A. B. D. Nandiyanto and K. Okuyama. "Progress in developing spray-drying methods for the production of controlled morphology particles: From the nanometer to submicrometer size ranges." In: *Advanced Powder Technology* 22.1 (2011), pp. 1–19 (cit. on pp. 9, 16, 17).

[117] S. Nešić and J. Vodnik. "Kinetics of droplet evaporation." In: *Chemical Engineering Science* 46.2 (1991), pp. 527–537 (cit. on p. 21).

[118] J. J. O'Sullivan, E.-A. Norwood, J. A. Mahony, and A. L. Kelly. "Atomisation technologies used in spray drying in the dairy industry : A review." In: *Journal of Food Engineering* 243.August 2018 (2019), pp. 57–69 (cit. on pp. 6–9, 11, 65).

[119] D. E. Oakley. "Spray Dryer Modeling in Theory and Practice." In: *Drying Technology* 22.6 (June 2004), pp. 1371–1402 (cit. on p. 12).

[120] O. Oluwole. "The Weak Formulation BT - Finite Element Modeling for Materials Engineers Using MATLAB®." In: ed. by Oluleke Oluwole. London: Springer London, 2011, pp. 3–12 (cit. on p. 146).

[121] A. Osman, L. Goehring, A. Patti, H. Stitt, and N. Shokri. "Fundamental Investigation of the Drying of Solid Suspensions." In: (2017) (cit. on pp. 26, 31, 36).

[122] M. Pal, L. Wan, Y. Zhu, Y. Liu, Y. Liu, W. Gao, Y. Li, and G. Zheng. "Scalable synthesis of mesoporous titania microspheres via spray-drying method." In: *Journal of Colloid And Interface Science* 479 (2016), pp. 150–159 (cit. on p. 5).

[123] P. Papadopoulos, X. Deng, L. Mammen, D. M. Drotlef, G. Battagliarin, C. Li, K. Müllen, K. Landfester, A. del Campo, H. J. Butt, and D. Vollmer. "Wetting on the microscale: Shape of a liquid drop on a microstructured surface at different length scales." In: *Langmuir* 28.22 (2012), pp. 8392–8398 (cit. on pp. 21, 24).

[124] K. C. Patel and X. D. Chen. "Prediction of spray-dryied product quality using two simple drying kinetics models." In: 28 (2005), pp. 567–594 (cit. on p. 31).

[125] K. C. Patel, X. D. Chen, and S. X. Qi Lin. "A Composite Reaction Engineering Approach to Drying of Aqueous Droplets Containing Sucrose, Maltodextrin (DE6) and Their Mixtures." In: *AIChE Journal* 55.1 (2009), pp. 217–231 (cit. on p. 31).

[126] B. Pathak and S. Basu. "Modulation of Buckling Dynamics in Nanoparticle Laden Droplets Using External Heating." In: *Langmuir* 32.11 (2016), pp. 2591–2600 (cit. on p. 25).

[127] L. Pauchard and Y. Couder. "Invagination during the collapse of an inhomogeneous spheroidal shell." In: *Europhysics Letters (EPL)* 66.5 (2004), pp. 667–673 (cit. on pp. 17, 24).

[128] A. Paudel, Z. A. Worku, J. Meeus, S. Guns, and G. van den Mooter. "Manufacturing of solid dispersions of poorly water soluble drugs by spray drying : Formulation and process considerations." In: *International Journal of Pharmaceutics* 453.1 (2013), pp. 253–284 (cit. on p. 5).

[129] D. L. Pearce. "A Novel Way to Measure the Concentration of a Spray in a Spray Dryer." In: *Drying Technology* 24.6 (2006), pp. 777–781 (cit. on p. 21).

[130] D. H. G. Pelegrine and C. A. Gasparetto. "Whey proteins solubility as function of temperature and pH." In: *LWT - Food Science and Technology* 38.1 (2005), pp. 77–80 (cit. on p. 40).

[131] J. Perdana, M. B. Fox, M. A.I. Schutyser, and R. M. Boom. "Mimicking Spray Drying by Drying of Single Droplets Deposited on a Flat Surface." In: *Food and Bioprocess Technology* 6.4 (2013), pp. 964–977 (cit. on pp. 21, 24, 25).

[132] S. Poozesh and E. Bilgili. "Scale-up of pharmaceutical spray drying using scale-up rules: A review." In: *International Journal of Pharmaceutics* 562 (2019), pp. 271–292 (cit. on p. 7).

[133] S. Poozesh, N. Stiawan, F. Arce, P. Sundararajan, J. D. Rocca, A. Rumondor, D. Wei, R. Wenslow, H. Xi, S. Zhang, J. Stellabott, Y. Su, J. Moser, and P. J. Marsac. "Understanding the process-product-performance interplay of spray dried drug-polymer systems through complete structural and chemical characterization of single spray dried particles." In: *Powder Technology* (2017), pp. 685–695 (cit. on p. 19).

[134]   A. Porowska, M. Dosta, L. Fries, A. Gianfrancesco, S. Heinrich, and S. Palzer. "Predicting the surface composition of a spray-dried particle by modelling component reorganization in a drying droplet." In: *Chemical Engineering Research and Design* 110 (2016), pp. 131–140 (cit. on p. 39).

[135]   J. Quiño, T. Hellwig, M. Griesing, W. Pauer, H. U. Moritz, S. Will, and A. Braeuer. "One-dimensional Raman spectroscopy and shadowgraphy for the analysis of the evaporation behavior of acetone/water drops." In: *International Journal of Heat and Mass Transfer* 89 (2015), pp. 406–413 (cit. on pp. 28, 29).

[136]   J. Quiño, M. Ruehl, T. Klima, F. Ruiz, S. Will, and A. Braeuer. "Supercritical drying of aerogel: In situ analysis of concentration profiles inside the gel and derivation of the effective binary diffusion coefficient using Raman spectroscopy." In: *Journal of Supercritical Fluids* 108 (2016), pp. 1–12 (cit. on p. 29).

[137]   M. Quintas, C. L. M. Silva, and R. L. Cunha. "Rheology of supersaturated sucrose solutions." In: *Food Hydrocolloids* 77 (2006), pp. 844–852 (cit. on p. 142).

[138]   S. Rogers, Y. Fang, S. X. Q. Lin, C. Selomulya, and X. D. Chen. "A monodisperse spray dryer for milk powder: Modelling the formation of insoluble material." In: *Chemical Engineering Science* 71 (2012), pp. 75–84 (cit. on pp. 25, 28).

[139]   S. Rogers, W. D. Wu, S. X. Q. Lin, and X. D. Chen. "Particle shrinkage and morphology of milk powder made with a monodisperse spray dryer." In: *Biochemical Engineering Journal* 62 (2012), pp. 92–100 (cit. on pp. 21, 25).

[140]   Y. Rong. "Probing the structure of dextran systems and their organization." PhD thesis. The State University of New Jersey, 2008 (cit. on pp. 39, 121).

[141]   A. Rygula, K. Majzner, K. M. Marzec, A. Kaczor, M. Pilarczyk, and M. Baranska. "Raman spectroscopy of proteins: a review." In: *Journal of Raman Spectroscopy* 44.8 (Aug. 2013), pp. 1061–1076 (cit. on p. 115).

[142]   M. H. Sadafi, I. Jahn, A. B. Stilgoe, and K. Hooman. "Theoretical and experimental studies on a solid containing water droplet." In: *International Journal of Heat and Mass Transfer* 78 (2014), pp. 25–33 (cit. on pp. 31, 32).

[143]   M. H. Sadafi, I. Jahn, A. B. Stilgoe, and K. Hooman. "A theoretical model with experimental verification for heat and mass transfer of saline water droplets." In: *International Journal of Heat and Mass Transfer* 81 (2015), pp. 1–9 (cit. on pp. 24, 31, 32).

[144]   C. Sadek, H. Li, P. Schuck, Y. Fallourd, N. Pradeau, C. Le Floch-Fouéré, and R. Jeantet. "To What Extent Do Whey and Casein Micelle Proteins Influence the Morphology and Properties of the Resulting Powder?" In: *Drying Technology* 32.13 (2014), pp. 1540–1551 (cit. on p. 21).

[145]   C. Sadek, L. Pauchard, P. Schuck, Y. Fallourd, N. Pradeau, C. Le Floch-Fouéré, and R. Jeantet. "Mechanical properties of milk protein skin layers after drying: Understanding the mechanisms of particle formation from whey protein isolate and native phosphocaseinate." In: *Food Hydrocolloids* 48 (2015), pp. 8–16 (cit. on pp. 22, 24, 27).

[146]   C. Sadek, P. Schuck, Y. Fallourd, N. Pradeau, R. Jeantet, and C. Le Floch-Fouéré. "Buckling and collapse during drying of a single aqueous dispersion of casein micelle droplet." In: *Food Hydrocolloids* 52 (2016), pp. 161–166 (cit. on pp. 17, 24).

[147]   C. Sadek, P. Schuck, Y. Fallourd, N. Pradeau, C. Le Floch-Fouéré, and R. Jeantet. "Drying of a single droplet to investigate process–structure–function relationships: a review." In: *Dairy Science and Technology* 95.6 (2015), pp. 771–794 (cit. on pp. 15, 17, 21).

[148]   C. Sadek, H. Tabuteau, P. Schuck, Y. Fallourd, N. Pradeau, C. Le Floch-Fouéré, and R. Jeantet. "Shape, shell, and vacuole formation during the drying of a single concentrated whey protein droplet." In: *Langmuir* 29.50 (2013), pp. 15606–15613 (cit. on p. 24).

[149]   A. Saha, S. Basu, and R. Kumar. "Particle image velocimetry and infrared thermography in a levitated droplet with nanosilica suspensions." In: *Experiments in Fluids* 52.3 (2012), pp. 795–807 (cit. on pp. 24, 129).

[150]   A. Saha, S. Basu, and R. Kumar. "Velocity and rotation measurements in acoustically levitated droplets." In: *Physics Letters, Section A: General, Atomic and Solid State Physics* 376.45 (2012), pp. 3185–3191 (cit. on pp. 25, 30, 129).

[151]   T. M. El-Sayed, D. A. Wallack, and C. J. King. "Changes in particle morphology during drying of drops of carbohydrate solutions and food liquids. 1. Effect of composition and drying conditions." In: *Industrial & Engineering Chemistry Research* 29.12 (1990), pp. 2346–2354 (cit. on pp. 21, 24).

[152]   E. U. Schlünder. *Handbook of heat-exchangers.* Ed. by Dryers. 1998 (cit. on p. 95).

[153]   P. Schuck, R. Jeantet, B. Bhandari, X. D. Chen, I. T. Perrone, A. F. de Carvalho, M. Fenelon, and P. Kelly. "Recent advances in spray drying relevant to the dairy industry: A comprehensive critical review." In: *Drying Technology* 34.15 (2016), pp. 1773–1790 (cit. on pp. 5, 19).

[154]   P. Seydel, J. Blömer, and J. Bertling. "Modeling Particle Formation at Spray Drying Using Population Balances." In: *Drying Technology* 24.2 (2006), pp. 137–146 (cit. on p. 31).

[155]   U. V. Shah, V Karde, C. Ghoroi, and J. Y. Y. Heng. "Influence of particle properties on powder bulk behaviour and processability." In: *International Journal of Pharmaceutics* 518 (2017), pp. 138–154 (cit. on p. 17).

[156]   S. Shakiba, S. Mansouri, C. Selomulya, and M. W. Woo. "In-situ crystallization of particles in a counter-current spray dryer." In: *Advanced Powder Technology* 27.6 (2016), pp. 2299–2307 (cit. on pp. 48, 50).

[157]   S. Shamaei, A. Kharaghani, S. S. Seiiedlou, M. Aghbashlo, F. Sondej, and E. Tsotsas. "Drying behavior and locking point of single droplets containing functional oil." In: *Advanced Powder Technology* 27.4 (2016), pp. 1750–1760 (cit. on pp. 16, 27).

[158]   S. Shamaei, S. S. Seiiedlou, M. Aghbashlo, and H. Valizadeh. "Mathematical modeling of drying behavior of single emulsion droplets containing functional oil." In: *Food and Bioproducts Processing* 101 (2017), pp. 100–109 (cit. on pp. 31, 32).

[159]   H. Al-Shehri, T. S. Horozov, and V. N. Paunov. "Preparation and attachment of liquid-infused porous supra-particles to liquid interfaces." In: *Soft Matter* 12.40 (2016), pp. 8375–8387 (cit. on p. 24).

[160] A. T. Shih and C. M. Megaridis. "Suspended droplet evaporation modeling in a laminar convective environment." In: *Combustion and Flame* 102.3 (1995), pp. 256–270 (cit. on pp. 129, 134).

[161] M. Starzak and M. Mathlouthi. "Temperature dependence of water activity in aqueous solutions of sucrose." In: *Food C* 96 (2006), pp. 346–370 (cit. on p. 141).

[162] M. Starzak, S. D. Peacock, and M. Mathlouthi. "Hydration Number and Water Activity Models for the Sucrose-Water System : A Critical Review." In: *Critical Reviews in Food Science and Nutrition* 4.February 2014 (2000), pp. 327–367 (cit. on p. 86).

[163] H. Steckel and H. G. Brandes. "A novel spray-drying technique to produce low density particles for pulmonary delivery." In: *International Journal of Pharmaceutics* 278.1 (2004), pp. 187–195 (cit. on pp. 16, 20).

[164] A. Stunda-Zujeva, Z. Irbe, and L. Berzina-Cimdina. "Controlling the morphology of ceramic and composite powders obtained via spray drying - A review." In: *Ceramics International* 43 (2017), pp. 11543–11551 (cit. on p. 5).

[165] Z. Sun, L. Zhou, C. Xiao, X. Du, and Y. Yang. "Nanoparticle motion and deposition near the triple line in evaporating sessile water droplet on a superhydrophilic substrate." In: *Experimental Thermal and Fluid Science* 76 (2016), pp. 67–74 (cit. on p. 24).

[166] O. Syll, S. Khalloufi, and P. Schuck. "Dispersibility and morphology of spray-dried soy powders depending on the spraying system." In: *Dairy Science & Technology* 93.4 (2013), pp. 431–442 (cit. on p. 52).

[167] S. M. Thaker, P. A. Mahanwar, V. V. Patil, and B. N. Thorat. "Synthesis and Spray Drying of Water-Redispersible Polymer Synthesis and Spray Drying of Water-Redispersible Polymer." In: 3937.May (2010) (cit. on p. 5).

[168] T. T. H. Tran, M. Jaskulski, J. G. Avila-Acevedo, and E. Tsotsas. "Model parameters for single-droplet drying of skim milk and its constituents at moderate and elevated temperatures." In: *Drying Technology* 35.4 (2017), pp. 444–464 (cit. on p. 37).

[169] J. Vasseur. "Séchage : principes et calcul d'appareils Séchage convectif par air chaud (partie 1)." fre. In: *Techniques de l'ingénieur Opérations unitaires : évaporation et séchage* base docum.ref. article : j2451 (Mar. 2009) (cit. on pp. 13, 95).

[170] R. Vehring. "Pharmaceutical particle engineering via spray drying." In: *Pharmaceutical Research* 25.5 (2008), pp. 999–1022 (cit. on pp. 5, 16, 17).

[171] R. Vehring, W. R. Foss, and D. Lechuga-Ballesteros. "Particle formation in spray drying." In: *Journal of Aerosol Science* 38.7 (2007), pp. 728–746 (cit. on p. 31).

[172] M. L. Vignolles, C. Lopez, M. N. Madec, J. J. Ehrhardt, S. Méjean, P. Schuck, and R. Jeantet. "Fat properties during homogenization, spray-drying, and storage affect the physical properties of dairy powders." In: *Journal of Dairy Science* 92.1 (2009), pp. 58–70 (cit. on p. 52).

[173] D. E. E Walton and C. J. J Mumford. "The Morphology of Spray-Dried Particles: The Effect of Process Variables upon the Morphology of Spray-Dried Particles." In: *Chemical Engineering Research and Design* 77.5 (1999), pp. 442–460 (cit. on pp. 16, 17).

[174] Y. Wang, L. Che, N. Fu, X. D. Chen, and C. Selomulya. "Surface formation phenomena of DHA-containing emulsion during convective droplet drying." In: *Journal of Food Engineering* 150 (2015), pp. 50–61 (cit. on p. 24).

[175] Y. Wang, L. Che, C. Selomulya, and X. D. Chen. "Droplet drying behaviour of docosahexaenoic acid (DHA)-containing emulsion." In: *Chemical Engineering Science* 106 (2014), pp. 181–189 (cit. on p. 24).

[176] S. Wanning, R. Süverkrüp, and A. Lamprecht. "Pharmaceutical spray freeze drying." In: *International Journal of Pharmaceutics* 488.1-2 (2015), pp. 136–153 (cit. on p. 8).

[177] J. K. R. Weber, A. Tamalonis, C. J. Benmore, O. L. G. Alderman, S. Sendelbach, A. Hebden, and M. A. Williamson. "Aerodynamic levitator for in situ x-ray structure measurements on high temperature and molten nuclear fuel materials." In: *Review of Scientific Instruments* 87.7 (2016), p. 073902 (cit. on pp. 21, 25).

[178] Y. Wei, W. Deng, and R. H. Chen. "Effects of insoluble nano-particles on nanofluid droplet evaporation." In: *International Journal of Heat and Mass Transfer* 97 (2016), pp. 725–734 (cit. on p. 36).

[179] Y. Wei, W. Deng, and R. H. Chen. "Effects of internal circulation and particle mobility during nanofluid droplet evaporation." In: *International Journal of Heat and Mass Transfer* 103 (2016), pp. 1335–1347 (cit. on pp. 129, 134).

[180] W. D. Wu, W. Liu, T. Gengenbach, M. W. Woo, C. Selomulya, X. D. Chen, and M. Weeks. "Towards spray drying of high solids dairy liquid: Effects of feed solid content on particle structure and functionality." In: *Journal of Food Engineering* 123.February 2014 (2014), pp. 130–135 (cit. on p. 25).

[181] J. Xiao and X. D. Chen. "Multiscale Modeling for Surface Composition of Spray-Dried Two-Component Powders." In: *AIChE Journal* 60.7 (2014), pp. 2416–2427 (cit. on pp. 31, 134).

[182] Wei Xu and Chang-Hwan Choi. "Effects of Surface Topography and Colloid Particles on the Evaporation Kinetics of Sessile Droplets on Superhydrophobic Surfaces." In: *Journal of Heat Transfer* 134.February 2015 (2012), p. 051022 (cit. on pp. 21, 24).

[183] X. Yang, J. Xiao, M.-W. Woo, and X. D. Chen. "Three-Dimensional Numerical Investigation of a Mono-Disperse Droplet Spray Dryer: Validation Aspects and Multi-Physics Exploration." In: *Drying Technology* 33.February 2015 (2014), p. 141217112010003 (cit. on p. 31).

[184] A. L. Yarin, G. Brenn, O. Kastner, and C. Tropea. "Drying of acoustically levitated droplets of liquid-solid suspensions: Evaporation and crust formation." In: *Physics of Fluids* 14.7 (2002), pp. 2289–2298 (cit. on pp. 21, 25).

[185] J. F. Zayas. "Foaming Properties of Proteins." In: *Functionality of Proteins in Food.* Springer, Berlin, Heidelberg, 1997. Chap. 6 (cit. on p. 42).

[186] S. Zellmer, G. Garnweitner, T. Breinlinger, T. Kraft, and C. Schilde. "Hierarchical Structure Formation of Nanoparticulate Spray-Dried Composite Aggregates." In: *ACS Nano* 9.11 (2015), pp. 10749–10757 (cit. on pp. 16, 17).

Contents

Contents

Abstract

Drying droplets as a template for multi-component solid particles: experimental study and modeling at the droplet scale

Liquid droplets are one of the major means of generation of solid particles with controlled. These templates are encountered with a variety of industrial processes, among them, spray drying. These tailored structures would meet the demand for particles with controlled properties, like improved kinetics, sustained release or controlled reactivity. The major scientific obstacle is the detailed description of the components distribution inside the droplet during drying, besides prediction of the final particle morphology. An experimental/modeling approach is undertaken in this thesis to understand how the drying conditions and the liquid formulation impact the final structure of the powders. The drying systems studied were sucrose-dextran and lactose-whey protein isolate aqueous solutions. The experimental work was firstly carried out at the lab-scale spray-dryer giving a reference picture of the possible particle morphologies for the drying systems. An experimental set-up was designed and developed to suspend a liquid droplet by a filament, from which the droplet mass variation over time could be accurately measured, giving fundamental insight into the drying process and allowing the analysis of the modification of the solid structures. A novelty explored at the droplet scale with an acoustic levitator was to apply an in situ Raman spectroscopy to assess the evolution of the spatial distribution of two components in drying droplets. Finally, a 2-D droplet drying model using Computational Fluid Dynamics was developed for allowing the assessment of the spatial distribution of the droplet components under a convective drying, until the formation of a crust. A sensitivity analysis was performed in order to show the influence of the experimental conditions on the drying kinetics and the component spatial distribution.

KEYWORDS: Drying droplet, Spray drying, Multi-component drying systems, Particle morphology, Experimental and modeling approaches, Amorphous solid.

Résumé

Séchage de gouttes comme vecteur pour les particules solides multi-constituants : étude expérimentale et modélisation à l'échelle de la goutte

Les gouttes liquides se sont avérées l'un des principaux vecteurs pour la génération de particules solides à propriétés contrôlées. Ce type de vecteur est utilisé dans plusieurs domaines industriels, y compris le séchage par atomisation. Le développement de ces particules structurées est poussé par la demande pour des particules à propriétés contrôlées, comme la cinétique de dissolution, le relargage contrôlé ou la réactivité. Le principal verrou scientifique est la description détaillée de la distribution des constituants au sein de la goutte pendant le séchage, en plus de la prédiction de la morphologie de la particule finale. L'objectif de cette thèse est de comprendre, par une approche couplée modélisation/expérimentation, comment les conditions de séchage et les formulations liquides impactent la structure de la poudre. L'étude expérimentale a d'abord été réalisée dans un sécheur par atomisation à l'échelle laboratoire pour la création d'une cartographie représentant les morphologies obtenues pour les deux systèmes de séchage. Un dispositif expérimental a été conçu de manière à étudier la formation d'une particule solide à partir d'une goutte suspendue par un filament, ce qui permet d'appréhender des éléments fondamentaux relatifs au séchage de la goutte ainsi que des aspects sur la modification de la structure solide. Une nouveauté explorée à l'échelle de la goutte avec un lévitateur acoustique consistait à appliquer la spectroscopie Raman in situ afin d'évaluer l'évolution de la distribution spatiale de deux composants lors du séchage de la goutte. Enfin, un modèle de séchage de goutte en 2-D avec la Dynamique des Fluides Numérique est conçu, ce qui permet de quantifier la distribution spatiale des composants de la goutte sous un séchage convectif, jusqu'à la formation de la croûte. Une analyse de sensibilité est réalisée de manière à montrer l'influence des conditions expérimentales sur la cinétique de séchage et la distribution spatiale des solutés.

MOTS-CLÉS : Séchage de goutte, Séchage par atomisation, Systèmes de séchage multi-constituants, Morphologie de particules, Approches expérimentation et modélisation, Solide amorphe.